Development of a novel Kalman filter and its application to neutrino interaction measurements in next-generation time projection chambers

Federico Battisti

Pembroke College

University of Oxford

A thesis submitted for the degree of

Doctor of Philosophy

Michaelmas 2024

Acknowledgements

The thesis you are about to read has been the product of four very challenging years. My DPhil journey started in the oddest possible way, with professor Farrukh Azfar (which would have later become my co-supervisor) calling me from the UK to offer me the position, a week into the first Italian quarantine period. By the time me and my cohort got into Oxford, I naively thought (or hoped) that the worst of the COVID-19 pandemic was behind us and that we were gonna enjoy a relatively normal Michaelmas. Unfortunately, as the reader will know, that wasn't to be the case. These turbulent years were also marked for me by the passing of two close family members, whose love and affection was sourly missed during the second half of my DPhil journey.

Despite these hardships, I'm still able to describe this experience as a nourishing and fulfilling one. If this is the case, it is in great part thanks to the exceptional people that I'm lucky to share my life with and that I would like to thank in these acknowledgements. Firstly, I would like to thank my parents and grandparents. Their unwavering support and affection made me able to surpass many difficulties and gave me the safety and strength to follow my passions and pursue a career in physics. I'd like to thank my partner Meghi, who I wouldn't have met if it wasn't for this DPhil and without whom I now can't imagine my life without. Without her I would have never been able to finish and my years in Oxford would have been meaningless in comparison. I'd like to thank Xianguo, my supervisor, who saw potential in me from the very first interview and provided me with invaluable guidance and experience. I would also like to thank my co-supervisor Farrukh who always offered a friendly face and was my guide through the horrors of Oxford bureaucracy. I'd like to also thank my other less official supervisors, Tom from the ND-GAr group and Marian from the ALICE group, without whom this project would have never taken full shape. Finally, I'd like to thank the Oxford neutrino group for creating such a relaxed and friendly work environment, and all my friends in the UK and Italy who enrich my life and have provided me with much laughter and affection throughout the years.

I dedicate this thesis to Giorgio and Irma, who are no longer with us, but whose love and humanity will forever guide me.

Statement of originality

I hereby declare that this thesis is the result of my own original work, and I have not used any sources other than those duly acknowledged. Any quotes or ideas borrowed from other authors have been appropriately referenced within the thesis.

Federico Battisti, 18th September 2024

Abstract

The Deep Underground Neutrino Experiment (DUNE) is a next-generation neutrino oscillation experiment designed to achieve new levels of precision in the study of neutrino flavour oscillations. Its primary goals include measuring charge-parity violation in neutrinos and determining the neutrino mass hierarchy. To achieve these objectives, DUNE relies on a near detector complex to constrain systematic uncertainties, including those related to neutrino flux and interaction cross-sections. A key component of the near detector is a high-pressure gas time projection chamber called ND-GAr, whose novel application in neutrino physics enables low tracking thresholds and high precision, critical for addressing systematic uncertainties arising from nuclear effects. A novel momentum reconstruction algorithm, based on the Kalman filter technique, was developed for ND-GAr, facilitating the reconstruction of low energy tracks. This algorithm significantly improves the detector's performance in momentum reconstruction, eliminating bias and achieving a relative momentum resolution of approximately 2.6% for muons and 5.3% for protons. Its effectiveness was demonstrated through an evaluation of ND-GAr's performance in applying the transverse kinematic imbalance (TKI) technique. The double transverse kinematic imbalance, δp_{TT}, can be used to isolate neutrino-hydrogen interactions, providing a sample free from nuclear effects. The novel Kalman filter enhances ND-GAr's ability to implement the TKI technique, achieving a δp_{TT} resolution of (11.9 ± 0.7) MeV/c. These improvements will extend ND-GAr's capabilities in studying nuclear effects and will provide stronger support for DUNE's scientific goals.

Contents

List of Figures

1 Introduction

The Deep Underground Neutrino Experiment (DUNE) [1] will be a new generation accelerator oscillation neutrino experiment. It will include three main components: a powerful wide-band neutrino beam situated at Fermilab, a multi-instrumented near detector (ND) positioned a few hundred meters from the neutrino source and a far detector (FD) situated 1300 km away from the source in South Dakota. The key goal of the DUNE experiment will be to initiate a new era of precision in the field of neutrino flavour oscillations by performing a complete range of measurements using both neutrino and antineutrino beams. Particular emphasis will be put on the measurement of charge-parity violation in neutrino oscillations and determining the order of the neutrino mass eigenstates.

In order to perform neutrino oscillation measurements, a prediction for the expected signal and background at the FD as a function of the oscillation parameters, needs to be produced. The prediction is then compared with the measured flavour-tagged neutrino spectra at the FD, in order to produce estimates for the parameters that regulate the oscillation probability. Producing this prediction requires the determination of the neutrino flux at production, the neutrino interaction cross sections and the response of the detector: all of these factors are affected by systematic uncertainties that need to be constrained. The DUNE ND has been designed to specifically address each element [2].

The DUNE ND will include as one of its main components a high pressure gas time projection chamber (HPgTPC) based on argon, called ND-GAr. The TPC technology has enjoyed ample success in high-energy particle physics. Since its original proposal by Nygren in 1975 [3], it has been used in various experiments and setups [4, 5]. One of the most notable TPC detectors in modern particle physics is the one used by the ALICE experiment at CERN [6]. The design of ND-GAr is heavily inspired by ALICE, to the point that the multiwire proportional chambers that will be used by ND-GAr will be repurposed from the ALICE detector after its recent upgrade [7]. The use of such a large gas TPC in a neutrino experiment is unprecedented and it is motivated by the low tracking thresholds and extreme levels of precision achievable using this technology. These features will be particularly useful in the modelling of neutrino interactions and nuclear effects, which are one of the key sources of systematic uncertainty in the oscillation measurement.

In this thesis we present the conception, development and testing of what is now the standard momentum reconstruction algorithm used by the TPC component of the ND-GAr detector. The algorithm is based on the Kalman filter technique, which is an iterative Bayesian technique often used in the field of particle tracking. This Kalman filter application presents some novel features which allow it to reconstruct very long "looping" tracks, which is particularly beneficial to a neutrino experiment such as ND-GAr. The method was developed in collaboration with experts of the ALICE collaboration and is envisioned to be used by both experiments. A similar more simple algorithm was also developed for ND-GAr-Lite, a now abandoned temporary muon spectrometer design centred on a multi-layer scintillator tracker,that would have substituted ND-GAr in the early days of the experiment's lifetime.

The impact of this novel Kalman filter was tested in a significant physics application: as already mentioned, one of the key roles of the ND-GAr detector will be to act as a laboratory for the study of nuclear effects in neutrino interactions. One of the key techniques that will be used by the experiment is transverse kinematic imbalance (TKI) [8–12], a method inspired by the missing energy concept in high

energy physics. It has been suggested that TKI could be used in a HPgTPC to isolate a sample of neutrino-hydrogen interactions present in the gas mixture. Hydrogen interactions are devoid of nuclear effects and represent an ideal testing ground for the characterization of these crucial sources of systematic uncertainty. The efficacy of the technique is in large part determined by the resolution of the detector, making the impact of the novel Kalman filter very directly detectable.

This thesis is structured as follows:

- Chapter 2 offers an introduction to neutrino physics and some key experimental particle physics concepts.
- Chapter 3 provides a description of the DUNE experiment and its physics goals, with particular focus on the near detector and ND-GAr.
- Chapter 4 introduces the key concepts behind the Kalman filter technique and offers a description of a Kalman filter application developed for the ND-GAr-Lite temporary muon spectrometer.
- Chapter 5 introduces the novel Kalman filter developed for the ND-GAr detector and investigates its performance.
- Chapter 6 describes a study on the capability of the ND-GAr detector of using transverse kinematic imbalance to isolate a sample of neutrino-hydrogen interactions, exploring the impact of the new Kalman filter algorithm.

2

Theoretical Background

Contents

2.1 Introduction

This chapter summarizes key aspects of neutrino physics. It begins with theoretical topics, covering the role of neutrinos in the Standard Model (Sec. 2.2), their interactions with matter (Sec. 2.3), neutrino masses (Sec. 2.4), and flavour oscillations (Sec. 2.5). It then follows with an historical overview, offering a more experimental perspective (Sec. 2.6). The chapter also discusses experimental topics central to this thesis, including neutrino flux production (Sec. 2.7) and the use of tracking detectors in neutrino physics (Sec. 2.8). Finally, a brief review of the behaviour of charged particles in matter is given (Sec. 2.9), providing context for later discussions.

2.2 Neutrinos in the Standard Model

The Standard Model (SM) of particle physics is a gauge theory defined by the symmetry $SU(3)_C \times SU(2)_L \times U(1)_Y$ where the sub-scripts C, L and Y refer to the colour, left-handed chirality and hypercharge respectively [13]. $SU(3)_C$ is the gauge symmetry of strong interactions, which affects the quark sector, while $SU(2)_L \times U(1)_Y$ is the gauge symmetry of the electro-weak force.

The particles which compose the SM are divided into bosons of spin 1 that mediate the fundamental interactions (photons for the electromagnetic interactions, $W^{\pm}$ and Z^0 for the weak force and 8 gluons for the strong force), the spin 0 Higgs boson and the fundamental fermions which have spin 1/2. The fermions can be divided into quarks and leptons. Quarks are elementary components of hadrons but do not exist as free particles. Both quark and leptons are divided into three generations with identical properties, except different masses. Fermions can be organized according to whether or not they are affected by weak interactions, in $SU(2)_L$ left-handed doublets and right-handed singlets (see Table 2.1).

Neutrinos are electrically and colour neutral fermions that can only interact weakly, either via neutral current (NC) processes, mediated via Z^0 bosons, or

$\begin{pmatrix}\nu_e\\ e\end{pmatrix}_L$	$\begin{pmatrix}u\\ d\end{pmatrix}_L$	e_R	u_R	d_R
$\begin{pmatrix}\nu_\mu\\ \mu\end{pmatrix}_L$	$\begin{pmatrix}c\\ s\end{pmatrix}_L$	μ_R	c_R	s_R
$\begin{pmatrix}\nu_\tau\\ \tau\end{pmatrix}_L$	$\begin{pmatrix}t\\ b\end{pmatrix}_L$	τ_R	t_R	b_R

Table 2.1: Irreducible fermion representations in the SM

charged current (CC) processes, mediated via $W^\pm$ bosons. The flavour of the neutrino is defined by the charged lepton which is connected to the same CC vertex:

$$\begin{aligned} W^+ &\to e^+ + \nu_e, \\ &\to \mu^+ + \nu_\mu, \\ &\to \tau^+ + \nu_\tau. \end{aligned} \tag{2.1}$$

The weak interaction is parity violating, meaning that only left-handed particles or right-handed antiparticles participate in the interaction. Neutrinos have been observed to be maximally parity violating, which implies that only left-handed neutrinos ν_L and right-handed antineutrinos $\bar{\nu}_R$ should exist. In the SM, fermions gain their mass through the Higgs mechanism which gives rise to the Dirac mass term:

$$\mathcal{L}_{mass}^{Dirac} = m_D(\bar{\psi}_L\psi_R + \bar{\psi}_R\psi_L), \tag{2.2}$$

where $\psi_{L(R)}$ is the left-handed (right-handed) chiral component. Under these conditions neutrinos are expected to be massless.

The electroweak part of the SM Lagrangian, which determines neutrino interactions in the SM, can be treated by only considering the $SU(2)_L \times U(1)_Y$ part of the SM symmetry group [14]. The $SU(2)_L$ symmetry group is called weak isospin and has three generators I_a, with $a = 1, 2, 3$, which satisfy the angular momentum commutation relations:

$$[I_a, I_b] = i\varepsilon_{abc}I_c, \tag{2.3}$$

where ε_{abc} is the Levi-Civita tensor.

The symmetry group $U(1)_Y$ is called hypercharge and is generated by the weak hypercharge operator Y, which is connected to the electric charge operator Q and I_3 by the Gell-Mann-Nishijima relation:

$$Q = I_3 + \frac{Y}{2} \tag{2.4}$$

The CC weak interaction Lagrangian for the three generations of leptons and quarks, can be written as:

$$\mathcal{L}_I^{(CC)} - \frac{g}{2\sqrt{2}} j_W^\rho W_\rho + \text{H.c.}, \tag{2.5}$$

where H.c. stands for Hermitian conjugate and g is the coupling constant associated with the $SU(2)_L$ symmetry group. W_ρ is a field operator that annihilates W^+ bosons and creates W^- bosons and is defined as:

$$W^\mu = \frac{A_1^\mu - iA_2^\mu}{\sqrt{2}}. \tag{2.6}$$

j_W^ρ is the fermion charged current, which is the sum of the leptonic and quark charged-currents:

$$j_W^\rho = j_{W,L}^\rho + j_{W,Q}^\rho, \tag{2.7}$$

given by:

$$j_{W,L}^\rho = 2 \sum_{\alpha=e,\mu,\tau} \bar{\nu}'_{\alpha L} \gamma^\rho \ell'_{\alpha L}, \tag{2.8}$$

$$j_{W,Q}^\rho = 2(\bar{u}'_L \gamma^\rho d'_L + \bar{c}'_L \gamma^\rho s'_L + \bar{t}'_L \gamma^\rho b'_L), \tag{2.9}$$

where the primes on the fermion fields are used to emphasize that, in general, they don't have definite masses, but are linear combinations of the fields with definite mass (see Sec. 2.5).

The neutral-current weak interaction Lagrangian can be written as:

$$\mathcal{L}_I^Z = -\frac{g}{2\cos\theta_W} j_Z^\rho Z_\rho, \tag{2.10}$$

where θ_W is the weak mixing angle. The value of θ_W determines the coefficients of the linear combinations of A_3^μ and B_μ, that define the electro-magnetic field A^μ

and the neutral vector boson field Z^μ:

$$A^\mu = \sin\theta_W A_3^\mu + \cos\theta_W B^\mu, \tag{2.11}$$

$$Z^\mu = \cos\theta_W A_3^\mu - \sin\theta_W B^\mu. \tag{2.12}$$

The neutral current j_Z^ρ is given by the sum of a quark and a lepton component:

$$j_Z^\rho = j_{Z,L}^\rho + j_{Z,Q}^\rho \tag{2.13}$$

given by:

$$\begin{aligned} j_{Z,L}^\rho = {} & 2g_L^\nu \sum_{\alpha=e,\mu,\tau} \bar{\nu}'_{\alpha L}\gamma^\rho \nu'_{\alpha L} \\ & + 2\sum_{\alpha=e,\mu,\tau}\left(g_L^l \bar{\ell}'_{\alpha L}\gamma^\rho \ell'_{\alpha L} + g_R^l \bar{\ell}'_{\alpha R}\gamma^\rho \ell'_{\alpha R}\right), \end{aligned} \tag{2.14}$$

$$\begin{aligned} j_{Z,Q}^\rho = {} & 2\sum_{\alpha=u,c,t}\left(g_L^U \bar{q}'_{\alpha L}\gamma^\rho q'_{\alpha L} + g_R^U \bar{q}'_{\alpha R}\gamma^\rho q'_{\alpha R}\right) \\ & + 2\sum_{\alpha=e,\mu,\tau}\left(g_L^D \bar{q}'_{\alpha L}\gamma^\rho q'_{\alpha L} + g_R^D \bar{q}'_{\alpha R}\gamma^\rho q'_{\alpha R}\right). \end{aligned} \tag{2.15}$$

where U and D stand for up-type and down-type quarks and the g_L^f and g_R^f coefficients are:

$$g_L^f = I_3^f - q_f \sin^2\theta_W, \tag{2.16}$$

$$g_R^f = -q_f \sin^2\theta_W, \tag{2.17}$$

with $f = (\nu, \ell, U, D)$.

The spontaneous breaking of the $SU(2)_L \times U(1)_Y$ symmetry through the Higgs mechanism, gives rise to the masses of weak vector bosons, which can be written as:

$$M_W = \frac{gv}{2} \sim 80 \text{ GeV/c}^2, \tag{2.18}$$

$$M_Z = \frac{gv}{2\cos\theta_W} \sim 91 \text{ GeV/c}^2 \tag{2.19}$$

where v is the Higgs field vacuum expectation value. In general, most neutrino interactions which are experimentally relevant (with the exception of those involving extremely high energy cosmogenic neutrinos), happen well below this energy scale. In these low energy processes, the internal gauge boson lines in the Feynman diagrams can be contracted and the interaction can be treated as if it were point-like.

In the case of the CC processes, this contraction leads to an effective four-fermion interaction which can be described with the effective CC Lagrangian:

$$\mathcal{L}_{\text{eff}}^{(CC)} = -\frac{G_F}{\sqrt{2}} j_{W\mu}^{\dagger} j_W^{\mu} \tag{2.20}$$

where $G_F = \sqrt{2}g^2/8M_W^2 \simeq 1.166 \times 10^{-5}$ GeV^{-2} is the Fermi constant. Similarly, the effective NC Lagrangian can be written as:

$$\mathcal{L}_{\text{eff}}^{(CC)} = -\frac{G_F}{\sqrt{2}} j_{Z\mu}^{\dagger} j_Z^{\mu}. \tag{2.21}$$

2.3 Neutrino interactions

In the SM, neutrino interactions are described by the leptonic charged current defined in Eq. 2.9 and the neutrino part of the leptonic neutral current in Eq. 2.14. The phenomenology of neutrino interactions, however, strongly depends on the energy and the target of the interaction. In this section, we describe the main types of neutrino interactions, as well as the complications brought by the complex structure of the nuclei.

2.3.1 Neutrino electron scattering

Neutrino-electron interactions are the simplest form of interactions that neutrinos undergo with matter. At the lowest order, they involve only free leptons, allowing their amplitudes to be computed exactly using Feynman rules. Depending on whether or not the final-state particles are the same as the ones in the initial state, they can be divided into elastic and quasi-elastic (QE).

Elastic scattering

Low energy neutrinos and anti-neutrinos with flavour $\alpha = e, \mu, \tau$, interact with electrons via elastic scattering:

$$\begin{aligned} \nu_\alpha + e^- &\to \nu_\alpha + e^- \\ \bar{\nu}_\alpha + e^- &\to \bar{\nu}_\alpha + e^- \end{aligned} \tag{2.22}$$

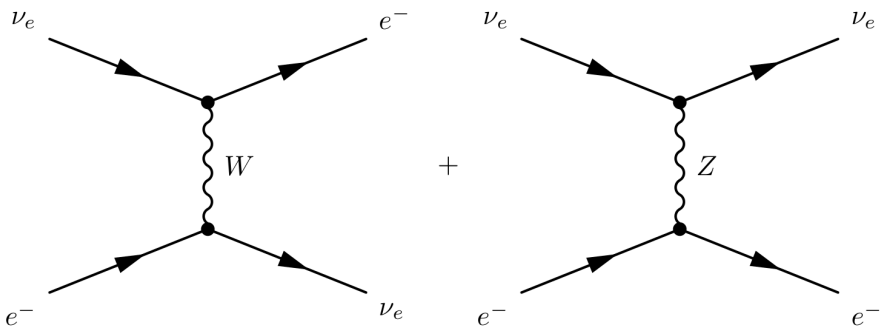

Figure 2.1: The two tree-level Feynman diagrams for the elastic scattering process $\nu_e + e^- \to \nu_e + e^-$: charged current (left) and neutral current (right). [14]

This process has no threshold energy, as the final-state particles are identical to those in the initial state; the only effect is a redistribution of the total energy and momentum between the two participating particles.

For ν_e, electron elastic scattering has both a CC and a NC component. Both are shown as tree-level Feynman diagrams in Fig. 2.1. For $\bar{\nu}_e$, the process is very similar, with the only difference being that the CC diagram is a t-channel, rather than s-channel. For other neutrino flavours, the electron elastic scattering process receives contribution only from the NC diagram.

In the low energy limit, where the W and Z propagators can be neglected, the effective Lagrangian for the ν_e (and $\bar{\nu}_e$) electron elastic scattering, can be derived from Eqs. 2.20 and 2.21 and is given by:

$$\begin{aligned}\mathcal{L}_{\text{eff}}(\nu_e e^- \to \nu_e e^-) = -\frac{G_F}{\sqrt{2}}\{&[\bar{\nu}_e\gamma^\rho(1-\gamma^5)e][\bar{e}\gamma^\rho(1-\gamma^5)\nu_e] \\ &+[\bar{\nu}_e\gamma^\rho(1-\gamma^5)\nu_e][\bar{e}\gamma^\rho(g_V^\ell - g_A^\ell\gamma^5)e]\},\end{aligned} \tag{2.23}$$

where the first term is the CC contribution and the second one is the NC contribution; $\gamma^5 = i\gamma_1\gamma_2\gamma_3\gamma_4$ is the chirality matrix, which is used to define the left-handed projector $P_L = (1-\gamma_5)/2$; g_V^f and g_A^f are the vector and axial couplings, which can be defined as combinations of the terms in Eqs. 2.16 and 2.17:

$$g_V^f = g_L^f + g_R^f = I_3^f - 2q_f \sin^2\theta_W, \tag{2.24}$$

$$g_V^f = g_L^f + g_R^f = I_3 \tag{2.25}$$

The Lagrangian for other neutrino flavours has a similar form, but only a NC component:

$$\mathcal{L}_{\text{eff}}(\nu_\alpha e^- \to \nu_\alpha e^-) = -\frac{G_F}{\sqrt{2}}[\bar{\nu}_\alpha \gamma^\rho (1-\gamma^5)\nu_\alpha][\bar{e}\gamma^\rho (g_V^\ell - g_A^\ell \gamma^5)e]. \tag{2.26}$$

From the Lagrangians, it can be derived that the total neutrino-electron cross-section follows $\sigma \propto G_F^2 s$ where $s = (p_\nu + p_e)^2$ is one of the three Mandelstam variables. The differences between the cross-sections arise form the different values of the coupling coefficients and produce the ratios:

$$\sigma_{\nu_e} : \sigma_{\bar{\nu}_e} : \sigma_{\nu_{\mu,\tau}} : \sigma_{\bar{\nu}_{\mu,\tau}} \simeq 1 : 0.42 : 0.16 : 0.14, \tag{2.27}$$

where $\sigma_{\nu_e} \simeq 93\ s/\text{MeV}^2$, in the limit $\sqrt{s} \gg m_e$.

Quasi-elastic scattering

Muon neutrinos with energy above the μ production threshold can interact with electrons through the quasi-elastic CC process:

$$\nu_\mu + e^- \to \nu_e + \mu^-. \tag{2.28}$$

An analogous process exists for ν_τ neutrinos, at much higher energies. In general, the threshold for a scattering process with a target particle with mass m_A can be calculated by considering that the centre of mass energy s, must be bigger that the total mass energy squared of the exiting particles $(\sum m_X)^2$. This produces the neutrino energy threshold:

$$E_\nu = \frac{(\sum m_X)^2}{2m_A} - \frac{m_A}{2}. \tag{2.29}$$

The effective Lagrangian of the QE process has a form that is analogous to the CC component of the Lagrangian in Eq. 2.23 . The total cross-section of the process is given by:

$$\sigma = \frac{G_F^2 s}{\pi}\left(1 - \frac{m_\mu^2}{s}\right). \tag{2.30}$$

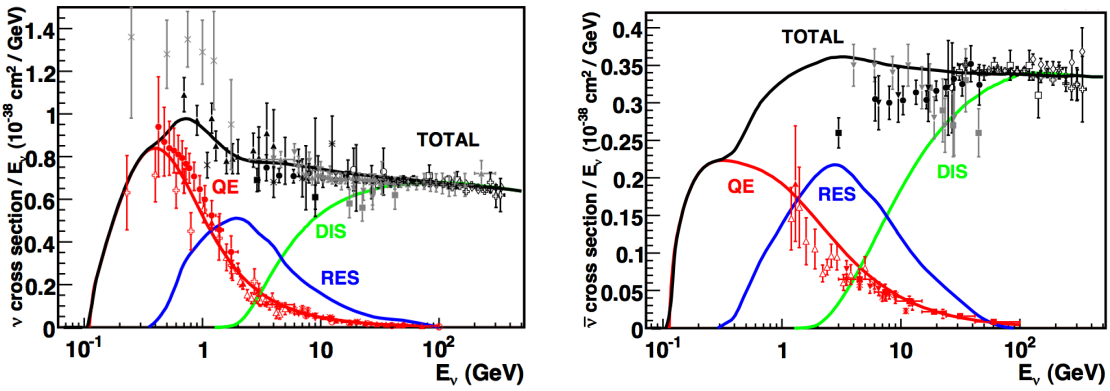

Figure 2.2: Muon neutrino (left) and antineutrino (right) charged-current cross-section measurements and predictions as a function of neutrino energy. The contributing processes in this energy region include quasi-elastic (QE) scattering, resonance production (RES), and deep inelastic scattering (DIS). The error bars in the intermediate energy range reflect the uncertainties in these cross-sections (typically 10 40%, depending on the channel). [15]

2.3.2 Neutrino nucleon interactions

Neutrino interactions with nucleons are significantly more complex and diverse than neutrino-electron interactions, and are characterized by much higher cross-sections. These processes can be divided broadly into elastic, where the recoiling nucleon recoils from the interaction intact, and inelastic. The elastic processes dominate at low four-momentum transfer Q^2. In the case of CC interactions, where the nucleon changes charge and mass is transferred to the final-state lepton, they are more properly referred to as quasi-elastic.

For inelastic interactions, at low Q^2, the cross-section is dominated by resonance (RES) production, where the nucleon is excited into a baryonic resonance, such as Δ, before decaying, typically into one ore more pions. The other non-resonant inelastic scattering modes can be divided in shallow and deep inelastic scattering (SIS and DIS respectively) based on their Q^2. SIS interactions are found at $Q^2 < 1$ GeV^2 and they occupy the whole allowed invariant mass (W) range. DIS interactions dominate at higher Q^2, where neutrinos have a small enough wavelength to be able to resolve individual quarks, and fragment the nucleon. In general, the higher the Q^2, the more the internal structure of the nucleon is revealed

by the interaction. While the study of DIS is fairly advanced at both a theoretical and experimental level [16], softer inelastic processes are not well understood. This includes the entire realm of SIS, as well as the transition regions between RES and SIS and SIS and DIS, which are particularly problematic. The different cross-section contributions for CC QE, RES and DIS muon neutrino and antineutrino processes are shown in Fig. 2.2.

While nucleons are fundamentally composed of three quarks, the constant gluon exchanges, which in turn can produce other temporary quark/anti-quark pairs, give rise to a much more complex internal structure. For this reason it is not possible, for neutrino-nucleon interactions, to calculate exact cross-sections using simple Feynman diagram rules. The general approach consists in representing a nucleon (i.e. hadronic) current $H_\mu^{CC/NC}$ by vector (V_μ), axial-vector (A_μ) and iso-scalar (V_μ^S) currents [17, 18]:

$$H_\mu^{CC} = V_\mu^\pm + A_\mu^\pm, \tag{2.31}$$

$$H_\mu^{NC} = (1 - 2\sin^2\theta_W)V_\mu^0 + A_\mu^0 - 2\sin^2\theta_W V_\mu^S. \tag{2.32}$$

These currents are composed of several form-factors F, which are functions of Q^2, representing the different contributing terms. The selection of the necessary form factors, as well as the functions used to describe them, are fully interaction dependent.

NC elastic and CC quasi-elastic scattering

At the lowest Q^2, the dominant interactions are those in which the nucleon is recoiled intact. When this occurs via NC, these are elastic interactions where the final-state and initial state particles are identical:

$$\nu_\alpha + N \to \nu_\alpha + N \tag{2.33}$$

If the neutrino has a Q^2 that is high enough to create the relevant charged lepton mass, then the CC QE interactions also become available:

$$\nu_\alpha + n \to p + \ell^-, \tag{2.34}$$

$$\bar{\nu}_\alpha + p \to n + \ell^+. \tag{2.35}$$

Due to their relative simplicity, CC QE interactions are particularly important experimentally. Due to the fact that the nucleon recoils intact, they are the best interaction with which to measure weak nucleon form-factors, which are difficult or inaccessible for other scattering probes. Additionally, their two-body nature enables the kinematics to be completely reconstructed, and hence the initial neutrino energy determined. If the target nucleon is considered at rest, the neutrino energy E_ν can be fully determined just by the exiting lepton momentum p_ℓ and angle θ_ℓ with respect to the incoming neutrino:

$$E_\nu = \frac{m_n E_\ell (m_p^2 - m_n^2 - m_\ell^2)}{m_n - E_\ell + p_\ell \cos\theta_\ell}. \tag{2.36}$$

These assumptions, however, are not entirely valid if the nucleon is part of a nuclear environment (see Sec. 2.3.3).

Resonance Production

Resonance production is at its most dominant in the transition region between CC QE and DIS, at energies 0.5 GeV $< E_\nu <$ 10 GeV. In these types of interactions the target nucleon is "excited" into a baryonic resonance, such as a N^* or Δ, with the available resonances being determined by the neutrino energy. These resonances then decay, most commonly into a nucleon and a single pion (Fig. 2.3). A variety of other final states are however available, depending on the resonance, including multiple pions, kaons or photons.

Resonant production is available to all neutrino and anti-neutrino flavours and can happen through NC and CC channels, off neutrons and protons. For example CC single π^+ production can occur on both neutrons ($\nu_\ell + n \to \ell^- + n + \pi^+$) and protons ($\nu_\ell + p \to \ell^- + p + \pi^+$). Of particular experimental interest is π^0 production, for which the decay photons can mimic the signal produced by a ν_e CC electron.

Deep Inelastic Scattering

At higher energies ($E_\nu >$ 10 GeV) the dominant CC process becomes DIS. In these interactions the neutrino is capable of transferring enough momentum that the internal structure of the nucleon can be resolved and the scattering process can

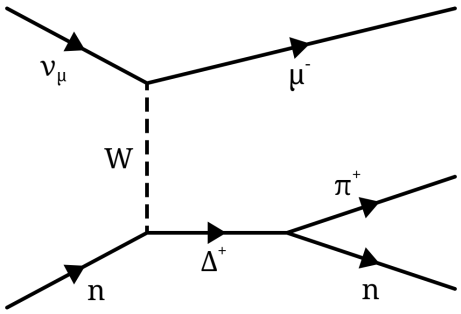

Figure 2.3: Feynman diagram for an example of resonance: ν_μ CC resonance single-pion interaction. [18]

be treated as if happening between the neutrino and an individual quark. The types of quarks that the neutrino can scatter with, depends on the available Q^2. At lower energies the nucleons contain mostly u, d and some s quarks, while at higher Q^2 the higher mass quarks become available.

As a result of the DIS interaction, the struck nucleon breaks up into fragments, which hadronise producing jets of strongly interacting particles. The DIS cross-section, rises linearly until E_ν approaches M_Z and M_W.

2.3.3 Nuclear effects

The description of neutrino-nucleon interactions provided so far, applies exactly, only to hydrogen nuclei, which consist of a single proton. In heavier nuclei, these interactions become significantly more complex due to various nuclear effects. This complexity is particularly relevant in modern neutrino experiments, where the need for higher interaction rates has led to the use of heavier nuclear targets such as carbon, water, or argon. Understanding and accurately modelling these nuclear effects is crucial for interpreting experimental results and reducing systematic uncertainties.

The first type of nuclear effects, is related to the initial state of the nucleons. Nucleons are not stationary, but they move isotropically inside the nucleus through Fermi motion (FM). The direction and momentum of the nucleon can affect the kinematics and cross-section of the interactions, especially at low Q^2. In first

approximation the motion of the nucleons can be described through a relativistic Fermi-gas model, under which all nucleons have total momentum $p_n \sim 0.2$ MeV/c. At low E_ν, however, this assumption is no longer valid and more complex models involving spectral functions become more appropriate [19].

Bound nucleons are also subjected to a secondary effect known as "Pauli blocking", which is a direct consequence of the Pauli exclusion principle. As fermions, final-state nucleons are not permitted to be in a state which is already occupied by another nucleon, which reduces the available phase-space as well as the cross-section of the interaction. In the case of a relativistic Fermi-gas model this requires the final-state nucleon's momentum to exceed the Fermi-momentum.

Nucleons inside the nuclear medium can also behave as correlated nucleon pairs, alpha particles, or any combination of nucleons in a quasi-bound state. These correlations arise mostly from pion-exchanging currents and can be either long or short-range. All nucleons experience long-range correlations to some extent, while short-range correlations affect $\sim 20\%$ of the nucleons [20]. When a neutrino interacts with a correlated proton-neutron pair, the momentum exchange is shared by both nucleons leading to a 2-particle 2-hole (2p2h) process.

Finally, when final-state hadrons propagate through the nuclear medium they can undergo strong interactions with the other nucleons in the medium. These final-state interactions (FSI) can modify significantly the apparent topology of the event. They can affect the momentum and direction of the final-state particles, as well as their type and number: pions and nucleons can be absorbed and never escape the nucleus, or their collisions with other nucleons can generate additional particles. For example, there is a finite probability that a pion produced in a RES process is absorbed inside the nucleus, mimicking a CC QE event.

While nuclear effects affect all neutrino-nucleon interactions, they are particularly relevant at lower E_ν (i.e. in the RES region and below) where the individual quarks cannot be resolved and the target nucleon's momentum is of similar magnitude to the neutrino's.

2.3.4 Coherent scattering

At very low Q^2, neutrinos can interact with nuclei through coherent scattering. In this type of interactions, the nucleus recoils as a whole without fragmenting or changing its composition. The coherent scattering cross-section is proportional to the square of atomic mass number A^2, because the neutrino-nucleon amplitudes sum coherently.

At low E_ν, coherent scattering is only available as an NC channel, while at higher energies both NC and CC processes are possible. In the first case the only effect of the interaction is a slight recoil of the nucleus, while in the second case additional final-state particles, such as π, ρ or K mesons, can be produced.

The kinematics of coherent scattering processes are strongly constrained by the low Q^2 requirement, resulting in relatively low cross-sections. Despite this, certain types of coherent pion production, are experimentally important. For example, the decay photons resulting from coherent π^0 production, can mimic ν_e signals.

2.4 Neutrino masses

While under the SM, neutrinos are treated as massless particles, experimental evidence for neutrino flavour oscillations, contradicts this hypothesis (see Sec. 2.6). Many mechanisms exist that would allow neutrinos to have mass. Arguably the most minimal expansion of the SM would be for neutrinos to be Majorana particles, for which their matter and antimatter states are the same [21]. This would allow for a Majorana mass term to be constructed, having only one chiral component:

$$\mathcal{L}_{mass}^{Majorana} = \frac{m_M}{2}\left(\psi_L^T C^{-1}\psi_L + \text{H.c.}\right), \tag{2.37}$$

where C is the charge conjugation operator. The existence of a new mechanism of mass generation, besides the Higgs mechanism, could explain naturally the smallness of ordinary neutrino masses, compared to other leptons and quarks.

Experimentally, this hypothesis can be tested by searching for a hypothetical rare nuclear transition known as neutrino-less double beta decay ($0\nu\beta\beta$) [22].

This process consists in the transformation of an even-even nucleus into a lighter isobar containing two more protons, accompanied by two electrons and no other particle, resulting in a total change of lepton number by two units: $(\mathrm{A}, \mathrm{Z}) \rightarrow (\mathrm{A}, \mathrm{Z}+2) + 2e^-$. This lepton number violation could be explained by neutrinos being Majorana particles.

In order to observe $0\nu\beta\beta$, experiments aim at the detection of two emitted electrons sharing the total transition energy (i.e. the Q-value) of the process. The signature therefore consists in a peak at the Q-value in the sum-energy spectrum of the two electrons. Current experiments have been able to set limits on the half-life of the process, with the most stringent being set by the KamLAND-Zen experiment at 3.8×10^{26} yr [23]. Under the assumption that neutrinos are Majorana particles, a limit can also be set on the effective Majorana neutrino mass $m_{\beta\beta}$. KamLAND-Zen's results set the upper limit $\langle m_{\beta\beta} \rangle < (28 - 122)$ MeV/c^2 at 90% confidence level (C.L.).

An alternative minimal SM expansion could consist in the introduction of one or more right-handed neutrinos ν_R, which would be completely sterile singlets under the $SU(2)_L$ SM gauge-group, unaffected by all the fundamental forces. If the masses of these right-handed neutrinos were to be large, the small-ness of other neutrino masses could be naturally explained by a "Seesaw" mechanism, for which many models exist [24].

On top of $0\nu\beta\beta$, several other experimental methods can be used to measure neutrino masses. The most direct technique consists in studying the kinematics of β-decay electrons. Neutrino masses lead to a reduction of the maximal observed energy of the decay and a small spectral shape distortion close to the kinematic endpoint of the β-spectrum. To date, the most sensitive measurements using this method have been produced by the KATRIN experiment, which set the limit at $m_\nu < 0.8$ eV at 90% C.L. [25].

Tighter constraints on the sum of all neutrino masses can be obtained from cosmological measurements. The density of relic neutrinos from the Big Bang is large and can impact the evolution of the universe. Recent cosmological measurements

on the large scale structure of the universe set this limit at $\sum_i m_i \leq 0.12$ eV at a 95% C.L. [26]. These results are however strongly reliant on the underlying cosmological assumptions.

2.5 Theory of neutrino oscillations

The stationary states of the free-particle Hamiltonian are the mass eigenstates of the particle and they satisfy the equation:

$$\hat{H}\psi = i\frac{\partial\psi}{\partial t} = E\psi. \tag{2.38}$$

The time evolution of the mass eigenstates takes the form:

$$\psi(\mathbf{x}, t) = \phi(\mathbf{x})e^{-iEt}. \tag{2.39}$$

The neutrinos have three mass eigenstates ν_1, ν_2 and ν_3. In weak interactions however, neutrinos are produced as their weak eigenstates ν_e, ν_μ or ν_τ alongside their respective flavour of charged lepton (see Eq. 2.1). The neutrino mass eigenstates do not correspond to the weak eigenstates. Each neutrino flavour has to be described as a coherent linear super-position of the ν_1, ν_2 and ν_3 states. The relationship between the weak and mass eigenstates can be described using the Pontecorvo-Maki-Nakagawa-Sakata (PMNS) unitary mixing matrix U_{PMNS} as [13]:

$$\begin{pmatrix}\nu_e\\ \nu_\mu\\ \nu_\tau\end{pmatrix} = U_{\text{PMNS}}\begin{pmatrix}\nu_1\\ \nu_2\\ \nu_3\end{pmatrix} = \begin{pmatrix}U_{e1} & U_{e2} & U_{e3}\\ U_{\mu1} & U_{\mu2} & U_{\mu3}\\ U_{\tau1} & U_{\tau2} & U_{\tau3}\end{pmatrix}\begin{pmatrix}\nu_1\\ \nu_2\\ \nu_3\end{pmatrix}, \tag{2.40}$$

with the unitarity condition being:

$$UU^\dagger = \begin{pmatrix}U_{e1} & U_{e2} & U_{e3}\\ U_{\mu1} & U_{\mu2} & U_{\mu3}\\ U_{\tau1} & U_{\tau2} & U_{\tau3}\end{pmatrix}\begin{pmatrix}U^*_{e1} & U^*_{\mu1} & U^*_{\tau1}\\ U^*_{e2} & U^*_{\mu2} & U^*_{\tau2}\\ U^*_{e3} & U^*_{\mu3} & U^*_{\tau3}\end{pmatrix} = \begin{pmatrix}1 & 0 & 0\\ 0 & 1 & 0\\ 0 & 0 & 1\end{pmatrix}. \tag{2.41}$$

If we consider an electron neutrino flavour eigenstate, its wave function will be a linear combination of the three mass eigenstates defined by their relative weak interaction couplings U_{ei} as:

$$|\nu_e\rangle = U_{e1}|\nu_1\rangle + U_{e2}|\nu_2\rangle + U_{e3}|\nu_3\rangle. \tag{2.42}$$

The neutrino state then propagates as a linear combination of the mass eigenstates until it interacts, collapsing into a weak eigenstate and producing a specific lepton flavour. If the three neutrino masses are not the same, phase differences are generated between the different wave function components, giving rise to the phenomenon of neutrino oscillations.

2.5.1 Two flavour scenario

While neutrinos in the standard model have three flavours and mass eigenstates, flavour oscillations can be more easily derived in a two-flavour scenario, without losing many of the key features of the phenomenon. Let's consider the weak eigenstates ν_e and ν_μ which are linear superpositions of the mass eigenstates ν_1 and ν_2. The weak eigenstates are related to the mass eigenstates by a unitary 2×2 matrix which can be written as a function of a single mixing angle θ:

$$\begin{pmatrix} \nu_e \\ \nu_\mu \end{pmatrix} = \begin{pmatrix} \cos\theta & \sin\theta \\ -\sin\theta & cos\theta \end{pmatrix} \begin{pmatrix} \nu_1 \\ \nu_2 \end{pmatrix}. \tag{2.43}$$

The propagation of a ν_e wave function through space can be written according to the time dependence of the mass eigenstates:

$$|\nu_e(L,T)\rangle = \cos\theta\,|\nu_1\rangle\, e^{-i\phi_1} + \sin\theta\,|\nu_1\rangle\, e^{-i\phi_2}, \tag{2.44}$$

where the phases of the two eigenstates can be written as:

$$\phi_i = p_i \cdot x = E_i T - \mathrm{p}_i L \quad (c = 1), \tag{2.45}$$

with p_i and x being the 4-momenta and 4-positions of the mass eigenstates, E_i and p_i their energies and total momenta, and T and L the time passed and distance travelled since production. By rewriting the mass eigenstates as a linear combination of weak eigenstates Eq. 2.44 can be rewritten as:

$$\begin{aligned} |\nu_e(L,T)\rangle &= e^{-i\phi_1}[(\cos^2\theta + e^{i\Delta\phi_{12}}\sin^2\theta)\,|\nu_e\rangle - (1 - e^{i\Delta\phi_{12}})\cos\theta\sin\theta\,|\nu_\mu\rangle] \\ &= c_e\,|\nu_e\rangle + c_\mu\,|\nu_\mu\rangle\,, \end{aligned} \tag{2.46}$$

where $\Delta\phi_{12} = \phi_1 - \phi_2$ is the difference between the phases. If $\Delta\phi_{12} = 0$ the neutrino remains a pure electron neutrino state, while if $\Delta\phi_{12} \neq 0$ a muon neutrino

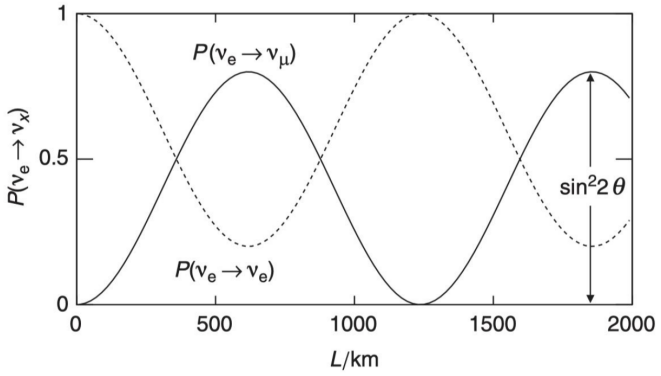

Figure 2.4: The two-flavour oscillation probability $P(\nu_e \rightarrow \nu_\mu)$ and the survival probability $P(\nu_e \rightarrow \nu_e)$ plotted as function of L for $E_\nu = 1$ GeV, $\Delta m^2 = 0.0002$ eV^2 and $\sin^2(2\theta) = 0.8$ [13].

component is introduced in the wave function. The probability that the neutrino which was produced as a ν_e will interact as a ν_μ is $P(\nu_e \rightarrow \nu_\mu) = c_\mu c_\mu^*$. Conversely the probability of the particle maintaining the initial flavour, sometimes referred to as survival probability, is simply $P(\nu_e \rightarrow \nu_e) = 1 - P(\nu_e \rightarrow \nu_\mu)$. From Eq. 2.46 $P(\nu_e \rightarrow \nu_\mu)$ can be written as:

$$P(\nu_e \rightarrow \nu_\mu) = \sin^2(2\theta) \sin^2\left(\frac{\Delta\phi_{12}}{2}\right). \tag{2.47}$$

The probability then depends on the mixing angle θ and the difference between the phases of the neutrino mass eigenstates $\Delta\phi_{12}$. The phase difference can be re-written as a function of the neutrino masses. If we assume that the momenta of the two mass eigenstates are equal $\mathrm{p}_1 = \mathrm{p}_2 = \mathrm{p}$ the phase difference becomes:

$$\Delta\phi_{12} = (E_1 - E_2)T = \left[\mathrm{p}\left(1 + \frac{m_1^2}{\mathrm{p}^2}\right)^{1/2} - \mathrm{p}\left(1 + \frac{m_2^2}{\mathrm{p}^2}\right)^{1/2}\right] T. \tag{2.48}$$

Under the assumption that neutrinos are very light and thus $m \ll E$, one can use the first order approximation $\sqrt{1+x^2} \approx 1 + x^2/2$ and re-write the phase difference as:

$$\Delta\phi_{12} \approx \frac{m_1^2 - m_2^2}{2\mathrm{p}} L. \tag{2.49}$$

Eq. 2.47 can finally be re-written as:

$$P(\nu_e \rightarrow \nu_\mu) = \sin^2(2\theta) \sin^2\left(\frac{\Delta m^2 L}{4E_\nu}\right), \tag{2.50}$$

where $p = E_\nu$ and $\Delta m^2 = m_1^2 - m_2^2$. An illustrative example of the evolution of the oscillation probabilities as a function of distance is shown in Fig 2.4. For small values of Δm^2, neutrino flavour oscillations can only develop over very large distances. The amplitude of the oscillation is determined by $\sin^2(2\theta)$, with mixing being maximal when $\sin^2(2\theta) = 1$ i.e. when $(\theta = \pi/4)$.

2.5.2 Three flavour scenario

In the three flavour scenario the PMNS mixing matrix, which describes the relationship between the flavour and mass eigenstates contains three mixing angles θ_{12}, θ_{23} and θ_{13} and one phase δ_{CP}.

$$\begin{aligned} U_{\mathrm{PMNS}} &= \begin{pmatrix} 1 & 0 & 0 \\ 0 & c_{23} & s_{23} \\ 0 & -s_{23} & c_{23} \end{pmatrix} \begin{pmatrix} c_{13} & 0 & s_{13}e^{-i\delta_{CP}} \\ 0 & 1 & 0 \\ -s_{13}e^{i\delta_{CP}} & 0 & c_{13} \end{pmatrix} \begin{pmatrix} c_{12} & s_{12} & 0 \\ -s_{12} & c_{12} & 0 \\ 0 & 0 & 1 \end{pmatrix} \\ &= \begin{pmatrix} c_{12}c_{13} & s_{12}c_{13} & s_{13}e^{-i\delta_{CP}} \\ -s_{12}c_{23} - c_{12}s_{23}s_{13}e^{i\delta_{CP}} & c_{12}c_{23} - s_{12}s_{23}s_{13}e^{i\delta_{CP}} & s_{23}c_{13} \\ s_{12}s_{23} - c_{12}c_{23}s_{13}e^{i\delta_{CP}} & -c_{12}s_{23} - s_{12}c_{23}s_{13}e^{i\delta_{CP}} & c_{23}c_{13}, \end{pmatrix} \end{aligned} \tag{2.51}$$

where c_{ij} and s_{ij} stand for $\cos\theta_{ij}$ and $\sin\theta_{ij}$ respectively. The derivation of the neutrino oscillation probability can be done following a procedure that is fully analogous to what was described in the 2-flavour scenario. If we consider an electron neutrino, the time evolution of its wave function can be described as the superposition of the time evolution of the mass eigenstates:

$$|\nu_e(x,t)\rangle = U_{e1}\,|\nu_1\rangle\, e^{-i\phi_1} + U_{e2}\,|\nu_2\rangle\, e^{-i\phi_2} + U_{e3}\,|\nu_1\rangle\, e^{-i\phi_3}. \tag{2.52}$$

We can then re-write the mass eigenstates as a linear superposition of the three weak eigenstates. By doing this and grouping the terms for each weak eigenstate we obtain:

$$\begin{aligned} |\nu_e(x,t)\rangle =& (U_{e1}^* U_{e1} e^{-i\phi_1} + U_{e2}^* U_{e2} e^{-i\phi_2} + U_{e3}^* U_{e3} e^{-i\phi_3})\,|\nu_e\rangle + \\ & (U_{e1}^* U_{\mu 1} e^{-i\phi_1} + U_{e2}^* U_{\mu 2} e^{-i\phi_2} + U_{e3}^* U_{\mu 3} e^{-i\phi_3})\,|\nu_\mu\rangle + \\ & (U_{e1}^* U_{\tau 1} e^{-i\phi_1} + U_{e2}^* U_{\tau 2} e^{-i\phi_2} + U_{e3}^* U_{\tau 3} e^{-i\phi_3})\,|\nu_\tau\rangle = \\ & = c_e\,|\nu_e\rangle + c_\mu\,|\nu_\mu\rangle + c_\tau\,|\nu_\tau\rangle\,. \end{aligned} \tag{2.53}$$

The oscillation probability can be obtained similarly to the 2-flavour scenario and is defined in terms of the flavours of the charged leptons produced in the weak interactions and the relevant PMNS matrix elements:

$$P(\nu_e \to \nu_\mu) = c_\mu c_\mu^* = |U_{e1}^* U_{\mu 1} e^{-i\phi_1} + U_{e2}^* U_{\mu 2} e^{-i\phi_2} + U_{e2}^* U_{\mu 2} e^{-i\phi_2}|^2. \tag{2.54}$$

If the phases were all the same then the unitarity condition $U_{e1}^* U_{\mu 1} + U_{e2}^* U_{\mu 2} + U_{e3}^* U_{\mu 3} = 0$ would imply that the oscillation probability is null. Neutrino oscillations can only occur if neutrinos have masses and these masses are different. Using the approximation outlined Eq. 2.49 and generalizing the results of Eq. 2.54 the oscillation probability between two generic flavour eigenstates $P(\nu_\alpha \to \nu_\beta)$ can be written as:

$$\begin{aligned} P(\nu_\alpha \to \nu_\beta) = \delta_{\alpha\beta} &- 4 \sum_{j>k} \Re \left[U_{\alpha j}^* U_{\beta j} U_{\alpha k} U_{\beta k}^* \right] \sin^2 \left(\frac{\Delta m_{jk}^2 L}{4E_\nu} \right) \\ &+ 2 \sum_{j>k} \Im \left[U_{\alpha j}^* U_{\beta j} U_{\alpha k} U_{\beta k}^* \right] \sin \left(\frac{\Delta m_{jk}^2 L}{2E_\nu} \right), \end{aligned} \tag{2.55}$$

where $\Re$ and $\Im$ stand for the "real" and "imaginary" parts, respectively. It's important to note that the second sum in the expression is non-zero only if the δ_{CP} phase is non-zero.

2.5.3 Charge-parity symmetry violation

The three most fundamental discrete symmetries that govern particle physics are: charge conjugation $\hat{C}$, which turns a particle into an antiparticle; parity $\hat{P}$, which reverses the spatial component of the wave function; time $\hat{T}$, which reverses the time component of the interaction. It has been demonstrated experimentally that the weak interaction violates both the $\hat{P}$ and $\hat{C}$ symmetries [27]. Let's consider for example the pion decay $\pi^- \to \mu^- + \bar{\nu}_\mu$ illustrated in Fig. 2.5. The parity operator $\hat{P}$ inverts the direction of the particle but not the spin, resulting in a left-handed antineutrino, which is not allowed. Charge conjugation $\hat{C}$ transforms a particle into its own antiparticle, resulting in the decay $\pi^+ \to \mu^+ + \nu_\mu$ where the neutrino is right-handed, which is also not allowed. The application of $\hat{C}\hat{P}$ changes left-handed particles into right-handed antiparticles and the resulting decay can happen.

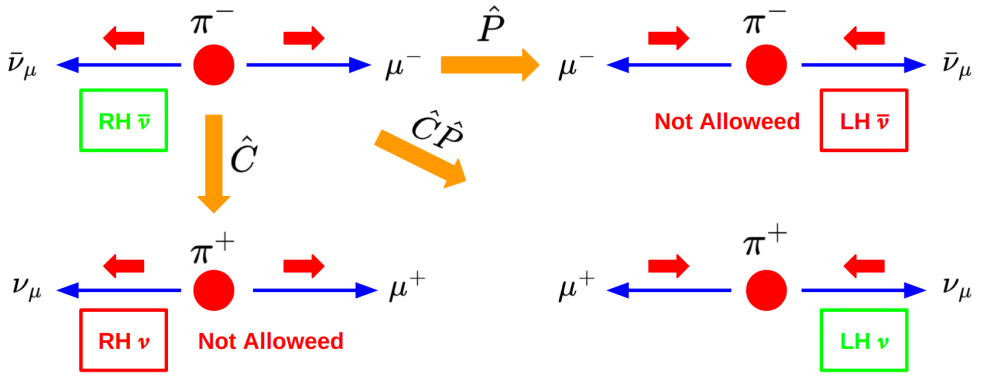

Figure 2.5: $\hat{C}$ and $\hat{P}$ violation in pion weak decay. The blue arrows are the particle, and the red arrows show the spin vectors of each particle [27].

The conservation of the CP symmetry implies that the probability of a particular interaction happening is identical to the probability of the CP transformed interaction occurring. It is known that CP conservation is not respected in the quark sector [28]. In the context of neutrino oscillation CP invariance would imply:

$$P(\nu_\alpha \to \nu_\beta) = P(\bar{\nu}_\alpha \to \bar{\nu}_\beta). \tag{2.56}$$

The unitarity conditions of the PMNS matrix, however, allow for a CP-violating phase δ_{CP} to exist. If $\delta_{\mathrm{CP}} \neq 0$, the imaginary component of the oscillation probability in Eq. 2.55 is also non zero and changes sign when the $\hat{C}\hat{P}$ operator is applied, breaking the symmetry and resulting in $P(\nu_\alpha \to \nu_\beta) \neq P(\bar{\nu}_\alpha \to \bar{\nu}_\beta)$. The CP-asymmetry can be quantified as the difference between the two probabilities:

$$\begin{aligned} \mathcal{A}^{\mathrm{CP}}_{\alpha\beta} &= P(\nu_\alpha \to \nu_\beta) - P(\bar{\nu}_\alpha \to \bar{\nu}_\beta) = \\ &= 4 \sum_{j>k} \Im \left[U^*_{\alpha j} U_{\beta j} U_{\alpha k} U^*_{\beta k} \right] \sin \left(\frac{\Delta m^2_{jk} L}{2E_\nu} \right), \end{aligned} \tag{2.57}$$

which is often written in terms of the Jarlskog invariant J_{CP} as:

$$\begin{aligned} &\mathcal{A}^{\mathrm{CP}}_{\alpha\beta} = 16 \sin \left(\frac{\Delta m^2_{21} L}{4E_\nu} \right) \sin \left(\frac{\Delta m^2_{32} L}{4E_\nu} \right) \sin \left(\frac{\Delta m^2_{31} L}{4E_\nu} \right) J_{\mathrm{CP}} \sum_\gamma \varepsilon_{\alpha\beta\gamma} \\ &\text{with } J_{\mathrm{CP}} \sum_{\gamma,l} \varepsilon_{\alpha\beta\gamma} \varepsilon_{jkl} = \Im \left[U^*_{\alpha j} U_{\beta j} U_{\alpha k} U^*_{\beta k} \right]. \end{aligned} \tag{2.58}$$

Current measurements of δ_{CP} lack the precision necessary to definitively determine whether the neutrino oscillation CP violation exists. The determination of the CP violating phase is thus a major topic of research in modern neutrino physics.

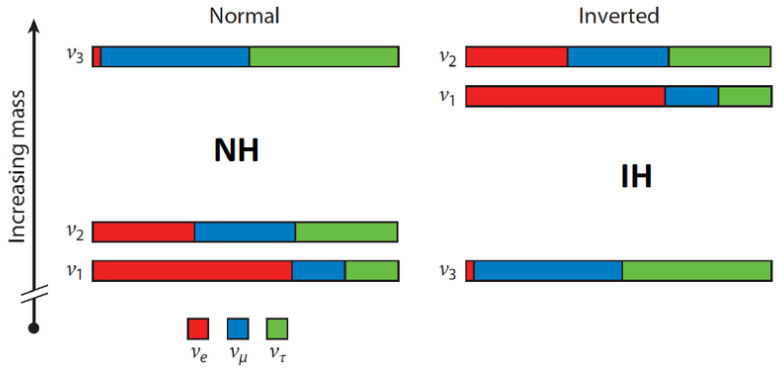

Figure 2.6: Illustration of the neutrino mass ordering for the two hypotheses, Normal Hierarchy (NH) and Inverted Hierarchy (IH). The flavour sharing due to the mixing is also drawn for each mass eigenstate. [29]

2.5.4 Mass ordering

An important aspect of modern neutrino oscillation physics is the determination of the neutrino mass ordering (MO) and mass hierarchy (MH). MO refers to the ordering of the three neutrino mass eigenstates, while MH refers more properly to the hierarchical structure between the mass differences. Regardless of the absolute mass scale of the lightest neutrino, two possible hierarchies (and thus orderings) exist, as shown in Fig. 2.6. The scenario in which the lightest mass eigenstate is ν_1, followed in order by ν_2 and ν_3 is referred to as the normal hierarchy (NH), while the alternative scenario in which ν_3 is the lightest, followed by ν_1 and ν_2 is referred to as the inverted hierarchy (IH).

2.5.5 Neutrino oscillations in matter

When neutrinos travel through matter they interact with electrons and nuclei in the medium. These interactions effectively modify the oscillation probabilities in a way that depends on the flavours of the neutrinos. This is due to the fact that while ν_es take part in both NC and CC interactions with electrons, ν_μs and ν_τs only participate in NC interactions (see Sec. 2.3). This matter effect is known as the Mikhaev, Smirnov and Wolfenstein (MSW) effect [30–32].

The MSW effect can be easily described in the 2-flavour scenario [33]. The time evolution Schrödinger equation in eq. 2.38 can be re-written using the 2-

flavour mixing matrix as:

$$\hat{H}\begin{pmatrix}\nu_e\\ \nu_\mu\end{pmatrix} = i\frac{d}{dt}\begin{pmatrix}\nu_e\\ \nu_\mu\end{pmatrix} \text{ where } \hat{H} = \left(\frac{\Delta m^2}{4E_\nu}\right)\begin{pmatrix}-\cos 2\theta & \sin 2\theta\\ \sin 2\theta & \cos 2\theta\end{pmatrix}. \tag{2.59}$$

The enhanced interaction probability experienced by ν_es can be effectively described by an extra potential $V_e = \pm\sqrt{2}G_F N_e$, where N_e is the electron density, G_F is the Fermi constant and the positive (negative) sign applies to electron neutrinos (antineutrinos). Using this potential we can construct an effective Hamiltonian $\hat{H}_M$ which describes the propagation of neutrinos in matter:

$$\hat{H}_M = \hat{H} + \begin{pmatrix}V_e & 0\\ 0 & 0\end{pmatrix} = \left(\frac{\Delta m^2}{4E_\nu}\right)\begin{pmatrix}-\cos 2\theta & \sin 2\theta\\ \sin 2\theta & \cos 2\theta\end{pmatrix} + \begin{pmatrix}V_e & 0\\ 0 & 0\end{pmatrix}. \tag{2.60}$$

In the simple case where the matter density is constant, the effective Hamiltonian $\hat{H}_M$ can be re-diagonalised to obtain a new mixing matrix:

$$\hat{H}_M = \left(\frac{\Delta m^2_M}{4E_\nu}\right)\begin{pmatrix}-\cos 2\theta_M & \sin 2\theta_M\\ \sin 2\theta_M & \cos 2\theta_M\end{pmatrix}. \tag{2.61}$$

where θ_M and Δm^2_M are the new effective oscillation parameters. They can be written as:

$$\begin{aligned}\Delta m^2_M &= M\Delta m^2,\\ \sin 2\theta_M &= \frac{\sin 2\theta}{M},\end{aligned} \tag{2.62}$$

with the coefficient M being

$$M = \sqrt{\left(\cos 2\theta - \hat{A}\right)^2 + \sin^2 2\theta}, \tag{2.63}$$

and

$$\hat{A} = \pm\frac{2\sqrt{2}G_F N_e E_\nu}{\Delta m^2}. \tag{2.64}$$

The sign of $\hat{A}$ is positive for neutrinos and negative for antineutrinos. Using the new effective parameters the oscillation probability in matter becomes

$$P(\nu_e \to \nu_\mu) = \sin^2 2\theta_M \sin^2\left(\frac{\Delta m^2_M L}{4E_\nu}\right). \tag{2.65}$$

The MSW effect modifies neutrino oscillation probabilities in some crucial ways. Due to the $\pm$ sign in front of $\hat{A}$, a difference in behaviour between neutrinos

and antineutrinos is introduced without CP violation. This MSW-induced CP violation is dependent on the MH, making the experimental determination of δ_{CP} also dependent on it (see Fig. 2.13 for and example of different δ_{CP} distributions dependent on the MH). The fact that the MH is not yet experimentally established is a major limitation to the determination of δ_{CP}.

Another important consequence of matter effects is that a resonant condition exists, for which the oscillation probability is significantly enhanced with respect to the one in vacuum, which is when $\hat{A} = \cos 2\theta$. The resonant condition can be met only if $\hat{A} > 0$, which in turn depends on the sign of the squared mass difference Δm^2. This fact can be exploited to study the neutrino mass ordering. However, either long travel distances or high matter densities are necessary in order for the MSW effects to be appreciable. In the case where $\Delta m^2_M L/4E_\nu \ll 1$ the neutrino oscillation probabilities are indistinguishable from the ones in vacuum.

2.6 History of neutrinos and current status

The first appearance of neutrinos in modern physics can be traced back to Pauli [34], who hypothesized the existence of a very weakly interacting particle to explain the continuity of the energy spectrum measured for β-decay electrons. Neutrinos were given their name (meaning "small neutrons" in Italian) by Fermi, who was the first to develop a theory of β-decay which effectively incorporated the new particle as one of the four fermions involved in the interaction [35]. Using Fermi's theory, Bethe and Peierls produced the first estimation of the cross-section for a weak antineutrino interaction with a proton [36]. The smallness of the cross-section (e.g. $\sigma \sim 10^{-44}$ cm^2) led the two scientists to conclude that detecting the interaction would be almost impossible.

Pontecorvo was the first to recognize that neutrinos could be detected experimentally with a sufficiently intense neutrino flux [37]. He estimated that a flux of about 10^{11} ν/cm^2/s, achievable from a nuclear reactor, combined with a ton-scale detector, could yield several antineutrino interaction events per day via the channel $\bar{\nu}_e p \to n e^+$. Pontecorvo proposed detecting neutrinos through inverse β-decays on

specific elements, which would produce radioactive nuclei whose β-decays could then be measured. One such reaction involved inducing inverse β-decays on chlorine to produce radioactive argon: $\nu_e\ ^{37}\mathrm{Cl} \rightarrow e^-\ ^{37}\mathrm{Ar}$. Decades later, this method was implemented in radiochemical detectors used in solar neutrino experiments.

The experimental setup proposed by Pontecorvo, involving a nuclear reactor source and a ton-scale detector, was realized by Reines and Cowan, who discovered the electron antineutrino $\bar{\nu}_e$ in 1956 [38]. At the time, neutrino flavours were not yet understood, so the main achievement of the experiment is more accurately described as the discovery of the antineutrino. Their detector used water tanks enriched with cadmium chloride ($CdCl_2$), placed between scintillator tanks equipped with photomultiplier tubes (PMTs). The antineutrino interaction signature consisted in two prompt photon showers from positron annihilation, followed by a delayed photon shower from neutron capture on cadmium nuclei, several microseconds later.

A year after the discovery of the electron neutrino, the Wu experiment demonstrated that the weak interaction violates parity [39]. The experiment measured the β-decay of cobalt-60 (^{60}Co) nuclei in a paramagnetic crystal. The nuclei were polarized by cooling the crystal to 0.003 K above absolute zero and applying a magnetic field. If parity were conserved, β-emission would have been equally intense in both directions along the spin axis. Instead, the experiment observed that electrons were preferentially emitted opposite to the nuclear spin.

Shortly after, the helicity of neutrinos was measured in the Goldhaber experiment [40]. This experiment studied europium-152 undergoing electron capture, producing an excited samarium-152 nucleus and an electron neutrino: $e^- + ^{152}\mathrm{Eu} \rightarrow ^{152}\mathrm{Sm}^* + \nu_e$. The samarium nucleus de-excites by emitting a gamma ray. By measuring the circular polarization of these gamma rays, which is dependent on the recoil direction of the nucleus and the helicity of the neutrino, the experiment confirmed that neutrinos are exclusively left-handed.

In 1962, a second flavour of neutrino was discovered by Lederman, Schwartz, and Steinberger at the Brookhaven National Laboratory [41]. Named the muon

neutrino (ν_μ), it was associated with the muon in the primary decay mode of the pion: $\pi^- \rightarrow \mu^- \bar{\nu}_\mu$. The experiment was the first to utilize an accelerated proton beam, which collided with a beryllium target to produce pions and other charged hadrons that decayed into neutrinos. A thick steel absorber separated the neutrinos from all other charged particles, and a 10-ton aluminium spark chamber behind the absorber detected neutrino interactions. The detector could distinguish muons, which produced straight, long tracks, from electrons, which induced electromagnetic showers. If electron and muon neutrinos were identical, the detector would have observed similar numbers of muon tracks and electron showers. Instead, the experiment found a significant excess of single-muon events, demonstrating that neutrinos from β-decays and those from pion decays are distinct, and producing the first direct measurements of muon neutrinos.

The discovery of the τ lepton at SLAC in the 70s motivated the search for a third neutrino flavour [42]. Additional experimental backing came from the study of the decay of the Z_0 boson produced at the large electron positron collider (LEP) in e^+e^- collisions [43]. These measurements showed that the number of light neutrinos coupled to the neutral weak boson had to be equal to three. The tau neutrino ν_τ was finally directly observed at Fermilab in 2000 at the DONUT experiment, completing the 3-flavour paradigm which still stands today [44].

2.6.1 Neutrino oscillation discovery

Around the same time as the discovery of the last neutrino flavour, data from experiments measuring the solar and atmospheric neutrino fluxes, were providing compelling experimental evidence for the phenomenon of neutrino flavour oscillations, initiating a new era in neutrino physics. Hints of this phenomenon had existed since the earliest measurements of solar neutrino fluxes in the 1970s and theoretical speculation on the phenomenon had been initiated by Pontecorvo in the 1950s [45] .

Neutrinos are produced in large quantities through a number of distinct fusion processes in the Sun. The solar neutrino spectrum is shown in Fig 2.7. Despite

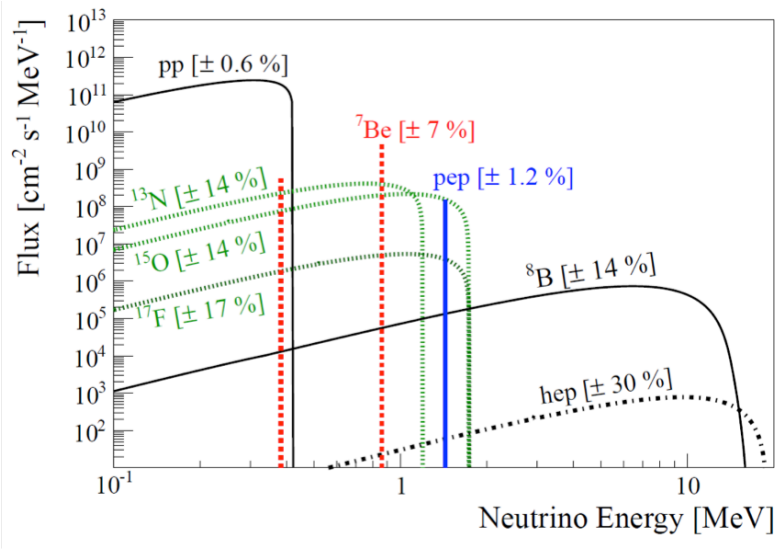

Figure 2.7: Solar neutrino spectrum [46].

the small neutrino interaction cross-sections and the large distance from the Sun, the flux of solar neutrinos is so intense that given a large detector it is possible to detect them. The main hydrogen burning process in the Sun, which is known as the pp-cycle, produces electron neutrinos through the reaction:

$$4p \rightarrow^{4} \mathrm{He} + 2e^{+} + 2\nu_e + E \ (27 \ \mathrm{MeV}). \tag{2.66}$$

The earliest solar neutrino experiment, which was based in the Homestake Mine in South Dakota, used the radiochemical method proposed by Pontecorvo to measure the solar neutrino flux [47]. The detector consisted of a 615-tonne massive tank of C_2Cl_4. The electron neutrinos interacted with the Cl nuclei through inverse β-decay, producing radioactive ^{37}Ar nuclei which could then be counted through their decay products. The observed rate of interactions was 0.48 ± 0.04 ν/day which represented a significant deficit compared to the expected 1.7 ν/day. This anomaly became known as the solar neutrino problem.

The Homestake experiment was not sensitive to low-energy neutrinos from the pp-cycle ($E_\nu < 0.5$ MeV) but only to those produced in rarer processes, such as the β-decay of ^{8}B nuclei ($E_\nu \simeq 15$ MeV). Predictions of the ^{8}B neutrino flux rely heavily on solar models, scaling as $\propto T^{24}$ with the solar core temperature T. In

contrast, pp-cycle neutrino flux predictions depend on T as $\propto T^{-1}$ and are well constrained by solar luminosity.

Later radiochemical experiments, such as GALLEX [48] and SAGE [49], used Gallium as a target, enabling the detection of low-energy pp-cycle neutrinos. Both experiments confirmed the solar neutrino anomaly.

The 50-kton Super Kamiokande water Cherenkov experiment provided additional proof of the solar neutrino deficit [50]. The detector consists of a large vessel containing water, surrounded by photomultipliers capable of detecting Cherenkov radiation from relativistic charged particles. Solar neutrinos were detected through neutrino-electron elastic scattering. The final-state electrons produced Cherenkov radiation that could be identified as a ring of hits on the sides of the detector. The number of photons gave a measure of the neutrino energy, while the orientation of the ring provided information on the direction of the particle.

The angular distribution of the exiting electrons is isotropic with the centre of mass frame with respect of the incoming neutrino. Since the center of mass frame is boosted in the laboratory frame, the scattering electron follows roughly the direction of the ν_e. Consequently, the directional correlation with the Sun is maintained, allowing the Super-Kamiokande experiment to provide clear evidence of a flux of ν_e from the Sun. This measurement confirmed the solar anomaly from the radiochemical experiments, as the flux of electron neutrinos was measured to be half that expected.

While the Super-Kamiokande experiment provided clear evidence for a deficit of solar neutrinos coming from the Sun, it gave no information regarding other neutrino species. The Sudbury Neutrino Observatory (SNO) was designed to measure both the ν_e flux and the total neutrino flux [51]. SNO was a Cherenkov detector consisting of a vessel containing 1000 tons of heavy water and 9600 PMTs. The use of heavy water was motivated by the low binding energy of deuteron, which gave access to nuclear CC interactions, something that is not possible in standard water and that was unavailable to the Super-Kamiokande experiment. The CC channel $\nu_e + \mathrm{D} \rightarrow e + \mathrm{p} + \mathrm{p}$ where deuteron is broken up into nucleons,

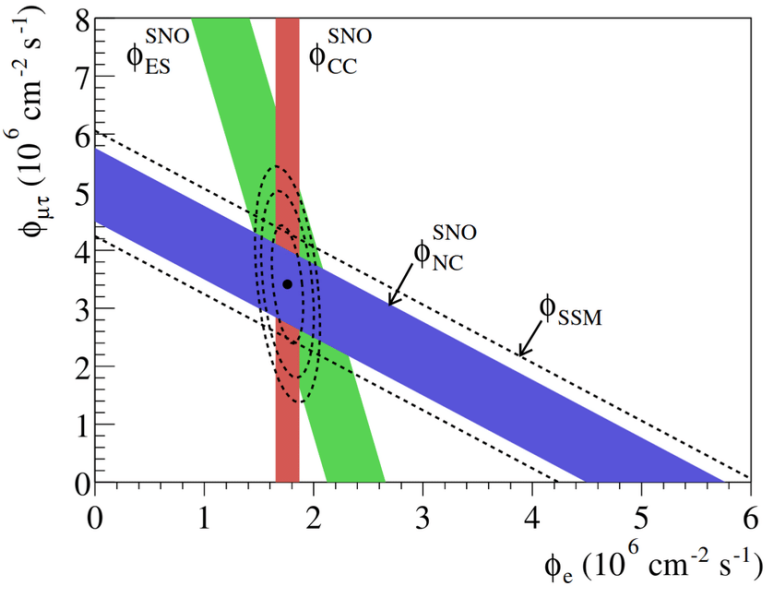

Figure 2.8: Flux of $8B$ solar neutrinos which are μ or τ flavour vs flux of electron neutrinos deduced from the three neutrino reactions in SNO. The diagonal bands show the total 8B flux as predicted by the standard solar model (SSM) (dashed lines) and that measured with the NC reaction in SNO (solid band). The intercepts of these bands with the axes represent the $\pm 1\sigma$ errors. [51]

is only sensitive to the electron neutrino flux, making it possible to isolate it from the other flavours:

$$\text{CC rate} \propto \phi(\nu_e). \tag{2.67}$$

The NC channel with consequent break-up of the deuteron nucleus ν_l+D $\rightarrow p$+n+e was instead sensitive to the flux of all neutrino flavours. The neutron in the final state could be detected by measuring the electromagnetic shower produced by the de-excitation photon ejected by a capturing deuteron nucleus through the reaction: $\mathrm{n} + \mathrm{D} \rightarrow {}^3_1\mathrm{H} + \gamma$. The NC process is sensitive to the total neutrino flux:

$$\text{NC rate} \propto \phi(\nu_e) + \phi(\nu_\mu) + \phi(\nu_\tau). \tag{2.68}$$

Neutrinos can also interact with atomic electrons through electronic scattering (ES). While for ν_e this process is available both through CC and NC interactions, it is only possible for ν_μ and ν_τ through NC interactions. The channel is thus sensitive to all neutrino fluxes but to differing degrees:

$$\text{ES rate} \propto \phi(\nu_e) + 0.154\,[\phi(\nu_\mu) + \phi(\nu_\tau)]\,. \tag{2.69}$$

Since the electrons from ES maintain the directional information of the original neutrino, these interactions could be separated from the CC sample. Using all three processes SNO was capable of providing constraints on and separate the ν_e and $\nu_\mu + \nu_\tau$ fluxes obtaining the overall results:

$$\begin{aligned} \phi(\nu_e) &= (1.76 \pm 0.10) \times 10^{-6} \text{cm}^{-2}\text{s}^{-1}, \\ \phi(\nu_\mu) + \phi(\nu_\tau) &= (3.41 \pm 0.63) \times 10^{-6} \text{cm}^{-2}\text{s}^{-1}. \end{aligned} \tag{2.70}$$

The SNO flux constraints are shown in Fig. 2.8. The total neutrino flux was measured to be consistent with the expected ν_e flux coming from the Sun:

$$\phi(\nu_e)_{\text{exp}} = (5.1 \pm 0.9) \times 10^{-6} \text{cm}^{-2}\text{s}^{-1}. \tag{2.71}$$

The SNO data demonstrated that while the total flux of neutrinos coming from the Sun was consistent with expectation, about a third of it consisted of ν_μ and ν_τ neutrinos rather than ν_e. Since only electron neutrinos can be produced in fusion reactions in the Sun, the SNO experiment was the first to give clear evidence of neutrino flavour oscillation transformation over large distances.

It's important to note that the flavour oscillation of neutrinos is determined by the PMNS matrix mixing angles and mass splittings (see Sec. 2.5 for more detail) and that the neutrino source and where the detectors are located with respect to it, determine the constants to which the experiments are sensitive. Specifically, the condition for an experiment to be sensitive to a specific Δm^2 is:

$$\frac{\Delta m^2 L}{2E} \sim 1, \tag{2.72}$$

where L is the "baseline", or the distance between the source and the detector, E is the energy of the neutrino at production and Δm^2 is the difference between the squared mass of the neutrino mass eigenstates. The solar neutrino experiments described so far, produce samples characterized by very large L and very low E and are sensitive to the Δm^2_{12} mass splitting and the correspondent θ_{12} mixing angle. For this reason the two parameters have historically been referred to as solar mass difference and solar mixing angle $(\Delta m^2_\odot, \theta_\odot)$.

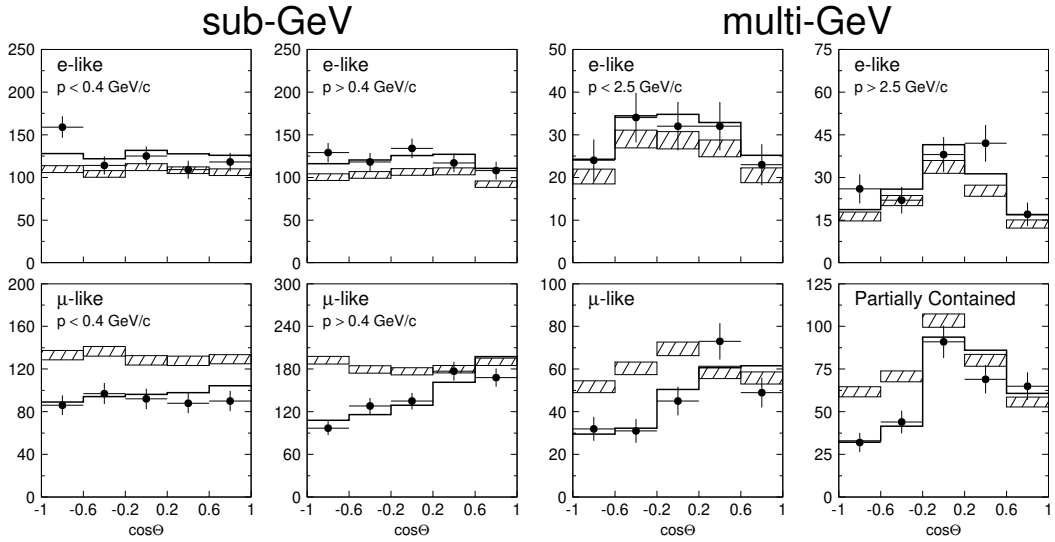

Figure 2.9: Zenith angle distributions of μ-like and e-like events for sub-GeV and multi-GeV data sets. Upward-going particles have $\cos\Theta < 0$ and downward-going particles have $\cos\Theta > 0$. Sub-GeV data are shown separately for $p < 400$ MeV/c and $p > 400$ MeV/c. Multi-GeV e-like distributions are shown for $p < 2.5$ GeV/c and $p > 2.5$ GeV/c and the multi-GeV μ-like are shown separately for FC (fully contained) and PC (partially contained) events. The hatched region shows the Monte Carlo expectation for no oscillations normalized to the data live-time with statistical errors. The bold line is the best-fit expectation for $\nu_\mu \leftrightarrow \nu_\tau$ oscillations with the overall flux normalization fitted as a free parameter. [52]

While solar neutrino experiments provided definitive proof of the neutrino oscillation phenomenon, the first clear observations came from the study of atmospheric neutrinos. Atmospheric neutrinos are produced by the interaction of cosmic rays with the oxygen and nitrogen nuclei present in the atmosphere. These interactions mostly generate positive and negative pions, which can decay as $\pi^+ \rightarrow \mu^+ + \bar{\nu}_\mu$ and $\pi^- \rightarrow \mu^- + \nu_\mu$ respectively. The muons can then further decay, producing an electron, alongside a ν_e and ν_μ. The full chain is expected to produce a ratio of muon neutrinos to electron neutrinos $R = N(\nu_\mu + \bar{\nu}_\mu)/N(\nu_e + \bar{\nu}_e) \sim 2$.

Experiments originally built to look for proton decay in the 70s and 80s, which had atmospheric neutrinos as background, were the first to observe a deficit of the atmospheric muon neutrino flux, leading to the identification of the "atmospheric neutrino anomaly". In 1998, Super-Kamiokande produced the first definitive measurements of the phenomenon, leading to the discovery of neutrino oscillations [52]. As previously mentioned, the detector was capable of distinguishing between

electron and muon induced tracks, as well as measuring the leptons' zenith angle Θ and energy. Super-Kamiokande measured the variation in the number of ν_e and ν_μ induced events as a function of the zenith angle and reconstructed neutrino energy. The μ-like samples were shown to have a θ-dependent deficit in the more energetic regions and a constant deficit in the less energetic regions (Fig. 2.9). The multi-GeV μ-like events were further separated between fully contained (FC) and partially contained (PC) to take into account the varying levels of uncertainty. The results were inconsistent with expectations based on calculations of the atmospheric neutrino flux, and could not be explained by experimental biases and uncertainties in the prediction of neutrino fluxes and cross-sections. The data were instead consistent with two-flavour $\nu_\mu \leftrightarrow \nu_\tau$ oscillation. The experiment also provided some of the first limits on the values of θ_{23} and $\Delta m^2_{23} \simeq \Delta m^2_{13}$. These parameters dominate the oscillation probability at the typical L/E of atmospheric neutrino experiments and have for this reason historically referred to as the atmospheric mixing angle and mass splitting ($\theta_{ATM}, \Delta m^2_{ATM}$). The mass splitting was measured to be $5 \times 10^{-4} < \Delta m^2_{ATM} < 6 \times 10^{-3}$ and $\sin^2 2\theta_{ATM} > 0.82$ at 90% confidence level.

2.6.2 Confirmation from artificial sources

Independent evidence of the flavour oscillation solution to the solar neutrino problem and the atmospheric neutrino problem came from experiments using man-made neutrino sources. The first confirmation of solar neutrino oscillations came in 2002 from KamLAND, a long baseline reactor neutrino experiment [53]. Neutrinos from nuclear reactors are $\bar{\nu}_e$s with energies of the order of a few MeVs. This makes the particles above threshold for electronic CC interactions, but not for other flavours, which means that if the neutrinos oscillate, CC interactions cannot happen. Reactor experiments can measure the disappearance probability of the $\bar{\nu}_e$s in the incoming flux, by comparing the expected rate of interactions predicted through Monte Carlo models, and the observed rate. In general a disappearance measurement involves detecting a reduction in the number of neutrinos of a specific flavour as they travel over a certain distance, compared to what is expected if no

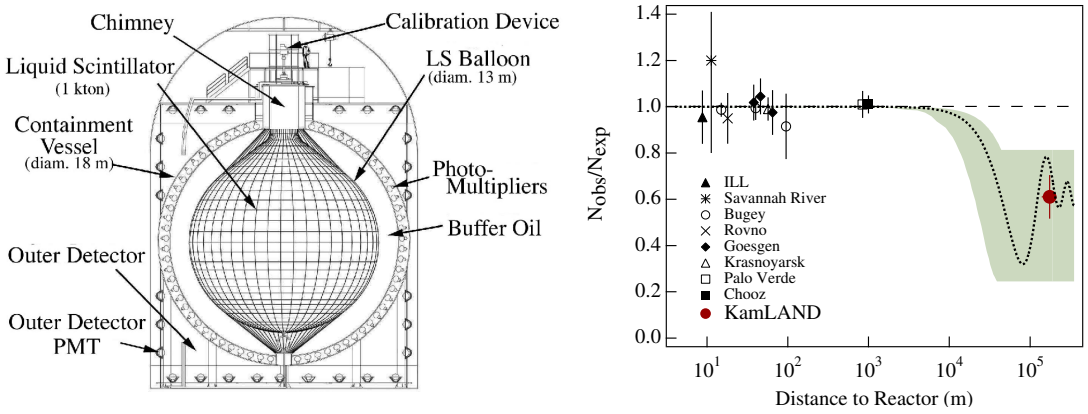

Figure 2.10: (Left) Schematic diagram of the KamLAND detector. (Right) The ratio of measured to expected $\bar{\nu}_e$ flux from reactor experiments. The solid dot is the KamLAND point plotted at a flux-weighted average distance (the dot size is indicative of the spread in reactor distances). The shaded region indicates the range of flux predictions corresponding to the 95% confidence level large mixing angle region found in a global analysis of the solar neutrino data done shortly before the publication of the KamLAND results. The dotted curve corresponds to $\sin^2 2\theta_\odot = 0.833$ and $\Delta m^2_\odot = 5.5 \times 10^{-5}$ eV^2 and is representative of best-fit large mixing angle predictions available at the time, while the dashed curve shows the prediction under the no-oscillation hypothesis. [53]

oscillation occurred, while an appearance measurement refers to the detection of a neutrino flavour that was not present in the initial neutrino beam, .

The KamLAND detector consisted of 1 kton of ultra-pure liquid scintillator contained in a 13 m diameter transparent spherical balloon (see the left image in Fig. 2.10 for a schematic representation). The balloon was placed in a containment vessel filled with buffer oil and instrumented with over 1800 wall-mounted PMTs. The containment vessel was surrounded by an outer water Cherenkov detector, used to absorb γ-rays and neutrons coming from the rock, and to tag cosmic rays. The detector was located 180 km from the reactor source, in the cavern previously used by the Kamiokande experiment; this baseline, combined with the MeV energy range of reactor antineutrinos, made the experiment sensitive to the same type of oscillations measured by the solar neutrino experiments. The main channel used by the experiments was the $\bar{\nu}_e$ inverse β-decay. The signature consisted in a prompt e^+ detection followed by a delayed neutron capture, much like the Reines and Cowan experiment 50 years prior. With an exposure of 162 ton$\cdot$year KamLAND observed

a ratio between the number of observed β-decay events and the expected number of events without disappearance of $0.611 \pm 0.085(\text{stat}) \pm 0.041(\text{syst})$ for $\bar{\nu}_e$ energies > 3.4 MeV (see the right plot in Fig. 2.10). The deficit excluded the non-oscillation hypothesis at a 99.95% confidence level and was consistent with a "large mixing angle" solution to the solar neutrino problem.

The atmospheric neutrino anomaly was confirmed by the first generation of neutrino accelerator experiments. All such experiments produced muon neutrino beams using the same method pioneered by Lederman at al. at the Brookhaven laboratories in the 50s. A proton beam, accelerated by a synchrotron, is extracted and directed onto a target, generating secondary particles. Magnetic focusing horns select pions of a specific charge and direct them into a decay tunnel, where $\pi^+ \rightarrow \mu^+ + \bar{\nu}_\mu$ and $\pi^- \rightarrow \mu^- + \nu_\mu$. A beam dump at the tunnel's end absorbs all remaining particles except neutrinos.

This technique yields highly pure $\nu_\mu/\bar{\nu}_\mu$ beams, with only a small ν_e contamination from kaon decay. All accelerator experiments use a near detector, placed close to the beam source to characterize the initial flux, and a far detector, positioned several kilometres away to measure $\nu_\mu/\bar{\nu}_\mu$ disappearance and the appearance of other neutrino flavours. The exact position of the far detector is chosen to optimize the sensitivity to oscillations.

The first long baseline accelerator experiment in operation was the KEK to Kamioka long-baseline neutrino oscillation experiment (K2K). The experiment used a neutrino beam derived from a 12 GeV proton beam from the KEK proton synchrotron. The neutrinos produced from the proton collisions and subsequent decays were 98% pure muon neutrinos with a mean energy of 1.3 GeV. The K2K experiment used Super Kamiokande as its far detector, having a flight distance of 250 km. The L/E of the experiment was optimized to probe the atmospheric mass splitting, which at the time was estimated to be $\Delta m^2_{ATM} \sim 3 \times 10^{-3}$ eV^2. K2K also employed a set of near detectors (ND) placed 300 m from the proton target. The ND included a 1 kiloton water Cherenkov detector (1KT) and a fine-grained detector (FGD) system. The measurements performed at the ND were

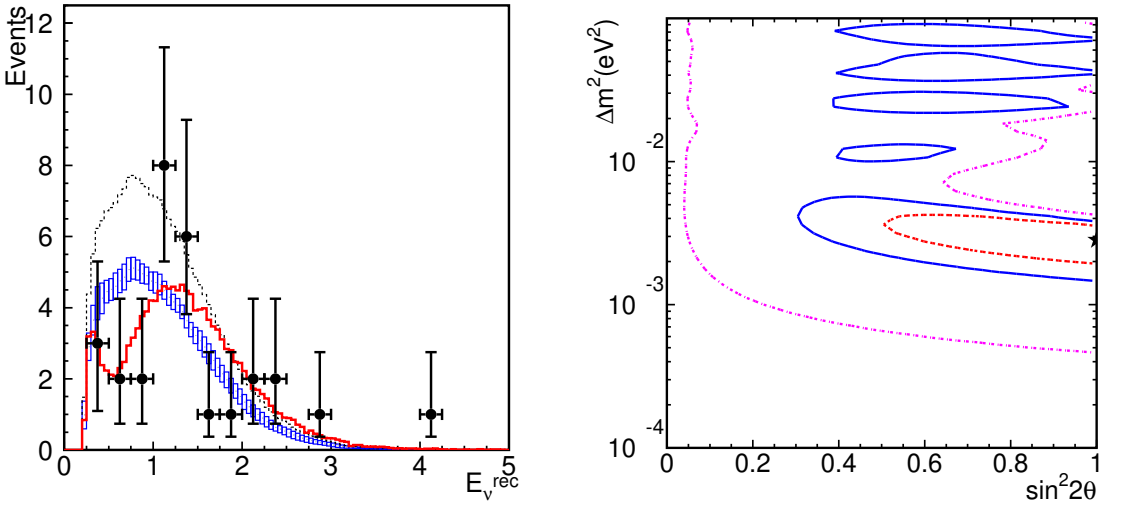

Figure 2.11: (Left) Reconstructed E_ν distribution from the first three years of data taking by K2K. Points with error bars are data. Box histogram is expected spectrum without oscillations, where the height of the box is the systematic error. The solid line is the best fit spectrum. These histograms are normalized by the number of events observed (29). In addition, the dashed line shows the expectation with no oscillations normalized to the expected number of events (44). (Right) Allowed regions of oscillation parameters. Dashed, solid and dot-dashed lines are 68.4%, 90% and 99% C.L. contours, respectively. The best fit point is indicated by the star. [54]

used to verify the stability and direction of the beam as well as determine the flux normalization and the energy spectrum at production. The flux at Super Kamiokande was estimated by multiplying the estimated ratio between the flux at the far and near detector and multiplying by the flux measured at the near detector. The use of a similar technology at the near and far detectors (water Cherenkov) allowed to mostly eliminate the systematic uncertainties related to the flux normalization measurement. A similar detector setup is used by all modern accelerator experiments.

The first measurements of neutrino oscillations compatible with the atmospheric neutrino measurements came from an analysis published in 2002, which included data taken between June 1999 and July 2001, corresponding to 4.8×10^{19} protons on target [54]. The experiment observed a reduction of ν_μ flux, together with a distortion of the energy spectrum. Super Kamiokande observed 56 neutrino events with an expectation of $80.1^{+6.2}_{-5.4}$. Additionally, the neutrino energy spectrum

was found to better match the expected spectrum with neutrino oscillation than without. Combining the two results, the no oscillation hypothesis was rejected at a 99% confidence level. The comparison between the measured spectrum and the expectation under the oscillation and no-oscillation hypothesis is shown in the left plot in Fig. 2.11. The best fit for the values of the oscillation parameters was $(\Delta m^2_{ATM}, \sin^2 2\theta_{ATM}) = (2.8 \times 10^{-3}\ \text{eV}^2, 1.0)$ which was also consistent with the atmospheric oscillation measurements. The confidence level contours are shown in the right plot in Fig. 2.11.

Further support came from the Main Injector Neutrino Oscillation Search (MINOS) experiment, the first Fermilab based neutrino experiment, which started operation in 2005. It employed a wide-band neutrino beam peaked at 1-3 GeV, produced at the Neutrino at the Main Injector (NuMI) facilities. The experiment followed the same near/far detector structure pioneered by K2K, with a ND situated at Fermilab and a FD placed 735 km away from the source in the Soudan iron mine in Minnesota. Both MINOS detectors consisted of several steel-scintillator tracking calorimeters with toroidal magnetic fields averaging 1.3 T and were placed along the beam axis. After a year of data taking, the experiment found 215 ν_μ CC events with energies below 30 GeV at the FD, where the expectation would have been of 336 ± 14.4 events [55]. The data was found to be consistent with ν_μ disappearance via oscillation with $\Delta m^2_{ATM} = 2.74^{+0.44}_{-0.26} \times 10^{-3}$ eV^2 and $\sin^2 2\theta_{ATM} > 0.87$ at a 68 % confidence level.

2.6.3 Modern measurements

Results from the first generation of oscillation experiments in the early 2000s established the three-flavour paradigm described by the PMNS matrix as the most plausible one. This model had two key implications: the expectation of a third oscillation mode governed by the θ_{13} mixing angle and, if $\theta_{13} \neq 0$, the potential for measuring CP violation in the lepton sector via the δ_{CP} phase. The CHOOZ [56] and Palo Verde [57] reactor neutrino experiments set the first upper limits on

$\sin^2\theta_{13} < 0.15$. Both used pressurized water reactors as neutrino sources, with detectors positioned at a $\sim$ 1 km baseline.

A second generation of θ_{13} focused reactor experiments was established in the early 2010s. The Double Chooz (DC) experiment provided the first positive evidence in 2012, by measuring a rate of electron antineutrino disappearance consistent with neutrino oscillations [58]. The deficit could be interpreted as an indication of a non-zero value of $\sin^2\theta_{13}$. The definitive proof came from the Daya Bay experiment a year later [59]. This was among the first reactor experiments to employ a near/far detector configuration, which allowed for a much higher degree of control over the systematics (note that in later years the DC experiment would also employ a ND). As illustrated in the left diagram of Fig. 2.12 the experiment used six pressurized water reactors, as antineutrino sources. Two near (flux-weighted baseline 470 m and 576 m) and one far (1648 m) underground experimental halls (EHs) were excavated and connected by tunnels. Each hall contained a varying number of identical liquid scintillator antineutrino detectors (ADs) designed to detect inverse β-decays: two in EH1, one in EH2 and three in the far hall EH3, close to the oscillation maximum.

The $\bar{\nu}_e$ rate in the far hall was predicted with a weighted combination of the two near-hall measurements assuming no oscillation. The experiment observed a deficit of 6% in the number of observed antineutrino events, corresponding to an observed/expected ratio of $R = 0.940 \pm 0.011$ (stat) $\pm$ 0.004 (syst). A rate-only analysis yielded $\sin^2\theta_{13} = 0.092 \pm 0.016$ (stat) $\pm$ 0.005 (syst), which excluded a $\theta_{13} = 0$ hypothesis with a significance of 5.2 standard deviations. The right plot in Fig. 2.12 shows the measured numbers of events in each detector, relative to those expected assuming no oscillation. The 6.0% rate deficit is obvious for EH3 in comparison with the other EHs, providing clear evidence of a non-zero θ_{13}. The oscillation survival probability at the best-fit values is given by the smooth curve. The χ^2 versus $\sin^2 2\theta_{13}$ is shown in the inset.

These results were confirmed by a new generation of accelerator neutrino experiments. The Tokai to Kamioka (T2K) experiment, still in operation today, was

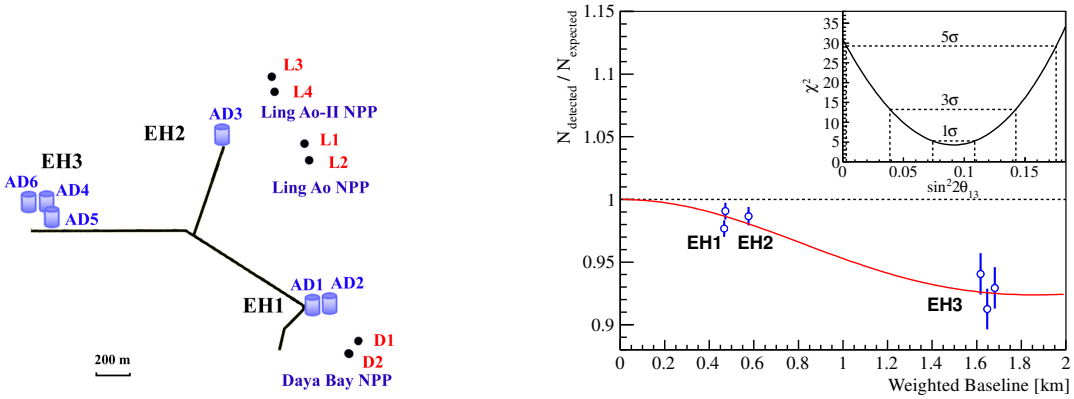

Figure 2.12: (Left) Layout of the Daya Bay experiment. The dots represent reactors, labelled as D1, D2, L1, L2, L3 and L4. Six ADs, AD1-AD6, are installed in three EHs (Right) Ratio of measured versus expected signal in each detector, assuming no oscillation. The error bar is the uncorrelated uncertainty of each AD, including statistical, detector-related, and background related uncertainties. The expected signal is corrected with the best-fit normalization parameter. Reactor and survey data were used to compute the flux-weighted average baselines. The oscillation survival probability at the best-fit value is given by the smooth curve. The AD4 and AD6 data points are displaced by -30 and +30 m for visual clarity. The χ^2 versus $\sin^2 2\theta_{13}$ is shown in the inset. [59]

the first one to observe ν_e appearance in a ν_μ flux. This channel was of particular interest at the time (and still today), because it is sensitive to both θ_{13} and δ_{CP}.

T2K is a direct successor of the K2K experiment, sharing with it its FD, Super Kamiokande. It uses a neutrino beam produced at JPARC and directed $\sim 2.5°$ off-axis, with a far detector baseline of 295 km. This configuration produces a narrow band beam, tuned at the first oscillation maximum $E_\nu = \Delta m^2_{23} L/(2\pi) \simeq 0.6$ GeV to reduce backgrounds from higher energy neutrino interactions. Depending on the polarity of the horn current, either positively or negatively-charged mesons are focused, resulting in a beam largely composed of muon neutrinos or antineutrinos. The first iteration of the T2K ND complex included the on-axis interactive neutrino grid (INGRID), and the ND280 off-axis detector. INGRID consists of several layers of iron-absorber / scintillator tracker arranged in crossed horizontal and vertical layers. Its main function is to accumulate neutrino interactions with high statistics to monitor the beam intensity, direction and profile. ND280 was used to reconstruct exclusive final states to study neutrino interactions and beam properties

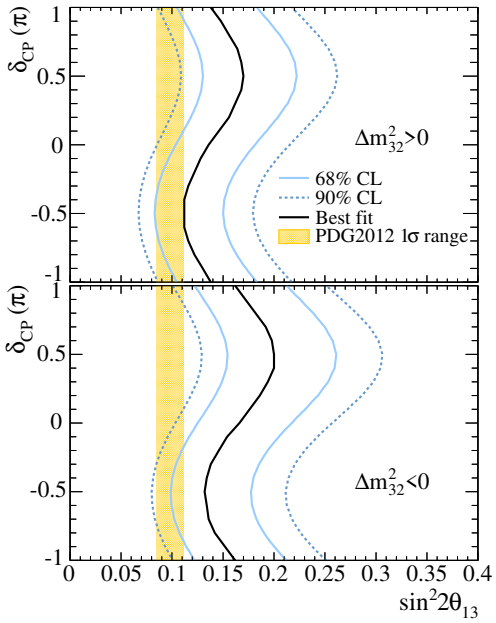

Figure 2.13: The 68% and 90% CL allowed regions for $\sin^2 2\theta_{13}$, as a function of δ_{CP} assuming normal hierarchy (top) and inverted hierarchy (bottom). The solid line represents the best fit $\sin^2 2\theta_{13}$ value for given δ_{CP} values. The shaded region shows the average θ_{13} value from the PDG 2012 world average. [60]

corresponding to those of the FD. It included a 0.2T super-conducting magnet, three large volume TPCs interleaved with two fine grain detectors (FGDs), a π^0-optimized detector and a surrounding electromagnetic calorimeter. The FGDs served as the neutrino targets, while the momentum and identity of the particles emerging from the interaction were determined by the TPCs.

The first indications of ν_e appearance from T2K came in 2011 [61], leading to a full discovery in 2013, after 3 year of data taking [60]. In both cases the energy spectrum and the neutrino cross-section parameters were constrained using ν_μ CC interactions in ND280. In the 2013 study, T2K observed a total of 28 FD electron neutrino events with an energy distribution consistent with an appearance signal, corresponding to a significance of 7.3σ when compared to 4.92 ± 0.55 expected background events. Fixing the values of the relevant oscillation parameters at the best estimates available at the time, they obtained a best-fit distribution for $\sin^2\theta_{13}$ for all values of δ_{CP} and the two possible signs of Δm^2_{32} i.e. the neutrino mass hierarchy (see Fig. 2.13). Their best fit at a 68% C.L. for $\delta_{\mathrm{CP}} = 0$ and

$\Delta m^2_{32} > 0$ ($\Delta m^2_{32} < 0$) was $\sin^2 2\theta_{13} = 0.140^{+0.038}_{-0.032}$ ($\sin^2 2\theta_{13} = 0.170^{+0.045}_{-0.037}$), which was consistent with T2K's ν_μ disappearance analysis as well as measurements coming from reactor experiments.

Shortly after the OPERA experiment at the Laboratori Nazionali del Gran Sasso (LNGS) reported the discovery of $\nu_\mu \to \nu_\tau$ oscillation in appearance mode [62]. The detector, consisting of a series of emulsion cloud chamber detectors, recorded 5 ν_τ events over 4 years of exposure (2008 to 2012) to the CERN neutrinos to Gran Sasso (CNGS) ν_μ beam, achieving significance of 5.1σ. These results provided an unambiguous confirmation of three-flavour neutrino oscillations in the atmospheric sector.

The discovery of non-zero θ_{13} and $\nu_\mu \to \nu_e$ at T2K opened up the possibility of measuring CP violation in neutrino oscillations. This could be directly achieved by comparing electron neutrino and antineutrino appearance probabilities in the form of the $\mathcal{A}^{\mathrm{CP}}_{\mu e}$ variable defined in Eq. 2.57. T2K was the first to produce a combined analysis of neutrino and antineutrino oscillations resulting in constraints on the values of δ_{CP} [63]. Marginalizing the $\sin^2\theta_{13}$ using results from reactor measurements, they obtained a best-fit value of $\delta_{\mathrm{CP}} = -1.791$ ($\delta_{\mathrm{CP}} = -1.414$), in normal (inverted) ordering, close to maximal CP violation. These results excluded the hypothesis of CP conservation ($\delta_{\mathrm{CP}} = 0, \pi$) at a 90% confidence level.

In recent years, significant progress has been made in precision measurements of neutrino oscillation parameters. The current world average for all the oscillation parameters are summarized in Table 2.2. Despite these advancements, the present generation of neutrino experiments lacks the necessary sensitivity to fully resolve several critical open questions in neutrino physics. One key issue is the measurement of the mixing angle θ_{23}, which appears to be close to 45°, raising the possibility of maximal mixing. However, the precise octant of θ_{23} remains undetermined. Additionally, the discovery of CP violation in the lepton sector is beyond the reach of existing experiments. Another unresolved question is the neutrino mass ordering, which remains ambiguous with current experimental constraints. To address these fundamental gaps, a new generation of experiments with enhanced

Parameter	World Average	Mass Ordering
$\sin^2\theta_{12}$	0.307 ± 0.013	
$\sin^2\theta_{23}$	0.539 ± 0.022	Inverted
$\sin^2\theta_{23}$	0.546 ± 0.021	Normal
$\sin^2\theta_{13}$	$(2.20 \pm 0.07) \times 10^{-2}$	
Δm^2_{21}	$(7.53 \pm 0.18) \times 10^{-5}$ eV^2	
Δm^2_{32}	$(-2.536 \pm 0.034) \times 10^{-3}$ eV^2	Inverted
Δm^2_{32}	$(2.456 \pm 0.033) \times 10^{-3}$ eV^2	Normal
δ_{CP}	$1.36^{+0.20}_{-0.16}\pi$ rad	

Table 2.2: Summary of best currently available experimental results for neutrino oscillation parameters [64]. When the results are dependent on neutrino mass hierarchy (see Sec. 2.5.4), the ordering is specified.

sensitivity and capabilities is required. DUNE will be one of these experiments, as will be discussed in Chapter 3.

2.7 Accelerator neutrino beams

The essential concept behind the production of neutrino beams from accelerated protons, has not changed much since the early days of the Lederman experiment [41]. In brief, a proton beam strikes a thick nuclear target, producing secondaries, such as pions and kaons. These secondaries leave the target, boosted in the forward direction, but with some divergence given by the production cross section $d^2\sigma/dp_{\mathrm{T}}dx_f$, where p_{T} is the transverse momentum of the meson to the proton beam axis and $x_f \sim p_L/p_{\mathrm{proton}}$ is the ratio between the longitudinal momentum of the secondary particle and the proton beam momentum. The mesons are then permitted to be drifted freely in space until they decay into tertiary daughter neutrinos. The decays of the mesons $\pi^\pm \to \mu + \nu_\mu$ (BR $\sim 100\%$), $K^\pm \to \mu + \nu_\mu$ (BR $= 63.4\%$) and $K^\pm \to \mu + \nu_\mu$ (BR $= 27.7\%$) make the development of $\nu_\mu/\bar{\nu}_\mu$ by far the most profitable and the only one that has been realized in practise. A certain number of electron neutrinos are also generated via $\mu \to e\nu_e\nu_\mu$ and $K_L \to \pi e\nu_e$ decays, producing an irreducible contamination.

Most modern experiments employ a magnet-based focusing system, which enables a great increase in the extraction efficiency, as well as the selection of the

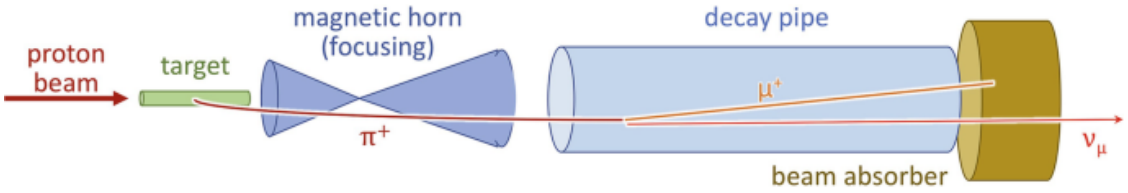

Figure 2.14: A schematic diagram of a typical neutrino beam production procedure. Both neutrino and antineutrino beams can be produced by switching modes of the focusing horns to select pions of the preferred charge [66].

signs of the mesons and, indirectly, the types of tertiary neutrinos i.e. $\nu_\mu/\bar{\nu}_\mu$ [65]. A schematic representation of the essential components of a modern neutrino beam is shown in Fig. 2.14. In the following section we describe some important features of beam production which are relevant to modern neutrino accelerator experiments.

2.7.1 Hadron production and neutrino flux predictions

One of the key challenges in any accelerator neutrino experiment consists in producing an accurate prediction of the neutrino flux. This can be done starting from $dN^2/dpd\Omega$, which is the yield of secondary hadrons, as a function of their momentum and angle emerging from the target. The momentum of the secondaries is directly related to the resulting neutrino energy, while the production angle relates to how well the flux is focused in the direction of the desired neutrino beam.

An important property of hadron production is that both the pion momenta and the mean number of $\pi^\pm$ produced per proton on target, grow linearly with the proton momentum. The transverse momentum components are instead invariant and only depend on the Fermi momentum of nucleons, peaking at $p_\mathrm{T} \sim 280$ MeV/c. The production spectra in transverse momentum p_T are then largely independent of x_F. The fact that p_T does not scale is important because the transverse momentum is what controls the divergence of the secondary beam. This implies that it is possible to significantly increase the momentum of the accelerated protons, and thus the energy and number of the secondaries, without much increasing the spread of the beam.

The geometry of the target is also important in the prediction of the neutrino spectrum. The probability for the secondary particles to re-interact in the target

material, increases with the path length and the proton beam energy. Secondary interactions tend to decrease the relative yield of high energy particles and increase the yield of lower energy particles. For very high energy neutrino beams, the target is often segmented, as to permit small-angle, high-momentum secondaries to escape the target with less path length for re-interaction.

In order to characterize the hadron production yield, neutrino experiments can either measure it directly, reproducing the exact conditions in which the experiment's beam is produced, or rely on models to extrapolate existing data from dedicated hadron production experiments. These kind of experiments are dedicated beam spectrometers that measure the secondary yield of accelerated proton beams on a variety of targets. Hadron production experiments, however are often limited in the range of proton momenta, p_{T} and x_f that they are able to examine. Additionally the dimensions and material of the target can vary widely, making a direct extrapolation often challenging.

2.7.2 Beam focusing

Focusing of the secondaries from the target is essential for increasing the neutrino flux to the detectors on axis with the beam line. In pion decay, the flux of neutrinos at a given decay angle θ with respect to the pion direction is:

$$\phi_\nu = \frac{A}{4\pi z^2}\left(\frac{2\gamma}{1+\gamma^2\theta^2}\right), \tag{2.73}$$

where A is the size of the detector, z is its distance from the pion decay point and γ is the pion boost factor. If no focusing is employed, the pions diverge from the target with an angle:

$$\theta_\pi \sim \frac{p_{\mathrm{T}}}{p_\pi} \sim \frac{\langle p_{\mathrm{T}}\rangle}{p_\pi} = \frac{2}{\gamma}, \tag{2.74}$$

where a typical $p_{\mathrm{T}} = 280$ MeV/c was assumed and $p_\pi \sim E_\pi = \gamma m_\pi$. This angle is larger than the typical angle of neutrinos from pion decay by a factor of 2, making it crucial to correct, in order to enhance the flux.

Magnetic focusing horns are one of the most widely used techniques in beam focusing today. These devices consist in two axially-symmetric conductors with

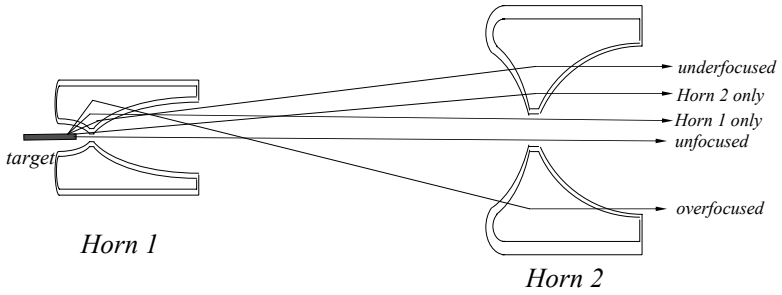

Figure 2.15: Two-lens focusing system: a second lens, significantly further from the target than the first, improves the collection efficiency of particles over or under-focused by the first lens. The horns shown are for the Fermilab NuMI line. The scale transverse to the beam axis is 4 times the scale along the beam axis. [65]

a current sheet running down he inner conductor and returning on the outer conductor. Between the conductors a toroidal magnetic field is produced whose $q\vec{v} \times \vec{\mathrm{B}}$ force focuses the particles of one sign and defocuses those of the other sign, enhancing the ν_μ component of the beam and reducing the $\bar{\nu}_\mu$ component or vice-versa. Hadrons of the opposite sign propagating at the centre of the beam, where no magnetic field is present, will decay into neutrinos of the opposite sign producing "wrong-sign" impurities. Designs of horns now are quite refined and employ full analyses of the vibrations and strains on the horn.

Many different designs have been developed through the years, each with different focusing characteristics. Some of the most commonly used are conical horns, which are effective at focusing all momenta for a given angle of pion into the horn, and parabolic horns, which are specialized in focusing a given momentum for all possible angles of entry. Often, multiple horns are combined into a single focusing system. Subsequent focusing elements can be used to rescue pion trajectories improperly focused by the first focusing element. A schematic representation of the multi-horn system used by the Fermilab NuMI line in its first iteration, is shown in Fig. 2.15. In this case both horns are of the parabolic type.

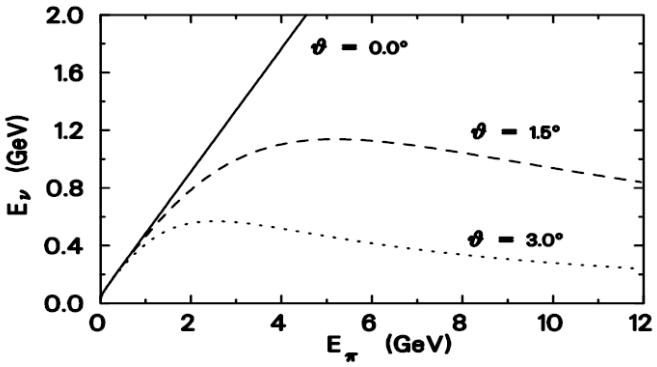

Figure 2.16: Neutrino energy from pion decay as a function of pion energy, for several choices of decay angle between the neutrino and pion direction.[65]

2.7.3 Off-axis beams

In many experiments it is desirable to produce neutrino beams with smaller fluxes but more carefully-selected properties. It might be desirable, for example, to select neutrinos of a given energy for study of energy-dependence of cross sections or neutrino oscillation phenomena at a particular neutrino energy. One of the techniques developed to achieve this, is to use an off-axis neutrino beam, as seen for example for the T2K experiment in Sec. 2.6. The reduction of the flux at off-axis angles, is directly related to the tertiary decay kinematics of the neutrinos, following Eq. 2.73. The narrowing of the energy spectrum is also a consequence of the decay kinematics. The decay of a secondary pion results in a neutrino energy:

$$E_\nu = \frac{(1-(m_\mu/m_\pi))^2 E_\pi}{1+\gamma^2\theta^2}, \tag{2.75}$$

where θ is the angle between the neutrino and the meson direction , and $\gamma = E_\pi/m_\pi$. The neutrino and meson energy are linearly related for on-axis decays ($\theta = 0°$). This produces "wide-band" neutrino beams, where the spectrum of the resulting neutrinos is as wide as that of the secondary mesons that produce them. For off-axis decays, the relationship is more complex, due to the denominator. In Fig. 2.16 we show the relationship expressed in Eq. 2.75 for several decay angles. For large off-axis angles, nearly any pion energy makes about the same energy of neutrino, making it possible to use a broad-band pion beam to generate a narrow-band neutrino spectrum.

2.8 Tracking detectors in neutrino physics

In neutrino physics, tracking detectors are used to reconstruct the paths of charged particles produced in neutrino interactions, either measuring the ionization they cause or the energy deposited (see Sec. 2.9) [67]. They often include a magnetic field which bends the particle trajectories, allowing for measurement of momentum via curvature. These detectors are most common in high energy experiments where long tracks can be produced. For the same reason, they tend to perform particularly well in the reconstruction of muons, which produce long, clean tracks. If the detector is constituted of a high density material, electrons tend to produce electromagnetic showers which are easily distinguished from muons. More challenging is the distinction between photons and electrons which depends on the specific detector technology.

A notable category of tracking detectors is represented by segmented scintillator trackers. An historical example is the MINERνA experiment, which used a high-intensity beam to study neutrino interactions on many nuclear targets [68]. The experiment's detector included a central tracker which consisted of 200 hexagonal detector panels, each one comprised of 127 triangular scintillator plastic strips with fibre optic cable running down their centres. A charged particle passing through the scintillator would produce an amount of light proportional to the energy deposition, providing important information for energy reconstruction and particle identification. The many scintillator strips enabled the detector to reconstruct three-dimensional tracks and pinpoint the origin of the neutrino interaction. Other notable examples are given by the near and far detectors of the NOνA experiment [69]. Both detectors consist of cells of extruded, highly reflective plastic PVC filled with liquid scintillator. The high level of granularity of the scintillator cells allow both detectors to reconstruct entire event topologies.

Another important tracking technology used in neutrino physics is the TPC. Historically, the most common type of TPC's have been cylindrical and gas-based [4, 5]. In a gas TPC, signal and track formation are achieved through the production of ionization electrons induced by the energy deposition of passing charged particles.

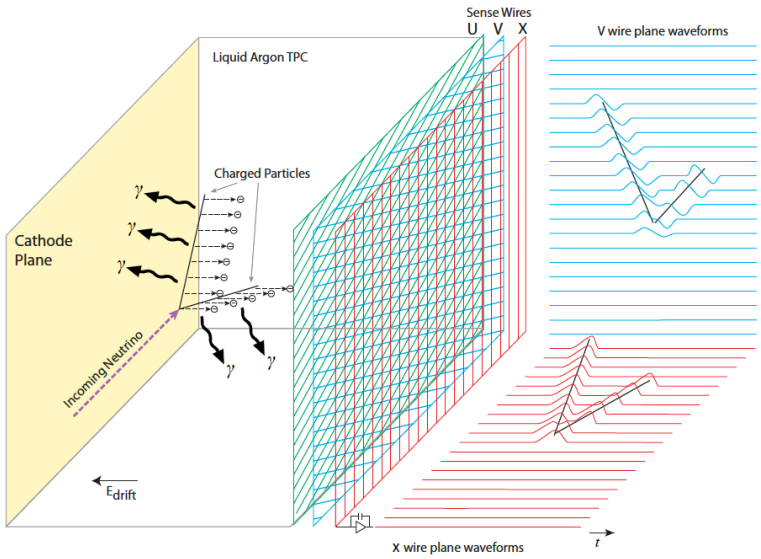

Figure 2.17: Schematic representation of the detection method of liquid argon time projection chambers [1].

The electrons then drift towards a sensor region in an electric field produced through an electrode plane. Subsequently, the electrons undergo multiplication through electromagnetic avalanches and are read out using technologies such as multi-wire proportional chambers (MWPCs) [70] or gas electron multipliers (GEMs) [71]. Additionally, the TPC is usually equipped with a magnetic field, enabling momentum measurement by curvature and charge identification. The avalanche-induced signals provide hit coordinates in two dimensions, while the drift time provides the third.

While gaseous TPC's provide excellent tracking resolution and coverage, their low mass has made them seldom used in neutrino physics. A notable exception is represented by the TPC trackers in the ND280 detector, which were used as trackers for charged particles produced on much more dense scintillator tracker modules [72]. Additionally, some notable examples of HPgTPC proposals exist. These detectors are functionally analogous to the more traditional gas TPCs, but operate in a pressurized environment. One example is the detector currently being developed by the NeXT collaboration for the study of $0\nu\beta\beta$ [73]. The central tracker of the ND-GAr detector will also employ this technology, as will be discussed in detail in Sec. 3.3.

The most widely used type of TPCs in neutrino physics are liquid argon time projection chambers (LArTPCs). First proposed by Carlo Rubbia in 1977 [74], this technology combines elements of both tracking and scintillator detectors. The LArTPC is now a mature detector technology within the neutrino experiment community, being employed in detectors such as MicroBooNe[75] and SBND[76] at Fermilab as well as the ProtoDUNE [77] prototypes tested at the CERN neutrino facilities. In a LArTPC, as charged particles travel trough the detector, they produce ionization electrons and prompt vacuum ultra-violet (VUV) scintillation photons. The electrons are drifted by an electric field and collected by a wire plane placed at the anode. The information from several wire planes is combined to produce a 3D image. The start time is given by the prompt scintillation light, which can be collected by photo-sensors within a few nanoseconds, whereas the drift time is of the order of the microsecond. The basic functioning principles of a LArTPC are illustrated in Fig. 2.17. The measurement of the collected ionization electrons also provides information on the dE/dx of the charged particles, which is what enables both calorimetry and particle identification (PID).

The choice of liquid argon as a medium is motivated by several key advantages. LAr has a high density, making it a good target for neutrinos. It also exhibits low electron attachment and high electron mobility, allowing for long drift volumes and effective charge transport and collection. Additionally, argon is relatively inexpensive, easy to purify and liquefy, and largely chemically inert. LArTPCs are extremely powerful in particle identification, as they produce almost photographic renditions of interaction events, which can be combined with energy loss information. This, for example, makes it possible to distinguish between photon and electron showers, which is extremely valuable in neutrino oscillation experiments.

2.9 Passage of particles through matter

When a relativistic charged particle moves through a medium, it undergoes electromagnetic interactions with the atomic electrons, leading to energy loss via ionization of the atoms. The energy loss per unit distance travelled dE/dx, also

known as the stopping power, is described by the Bethe-Bloch formula [78]. The stopping power varies weakly between materials and only depends on their densities ρ. It can thus be written as:

$$-\frac{\mathrm{d}E}{\rho \mathrm{d}x} = 4\pi N_A r_e^2 m_e c^2 z^2 \frac{Z}{A}\frac{1}{\beta^2}\left(\frac{1}{2}\ln\frac{2m_e c^2\beta^2\gamma^2 T_{\max}}{I^2} - \beta^2 - \frac{\delta}{2}\right), \tag{2.76}$$

where N_A is Avogadro's number, r_e is the classical electron radius, $m_e c^2$ is the electron mass energy, z is the charge of the particle, Z and A are the atomic number and mass of the absorbing material, $\beta = v/c$ and $\gamma = 1/\sqrt{1-\beta^2}$ are the usual relativistic factors for the passing particle, I is the material mean excitation energy, $T_{\max}$ is the maximum kinetic energy which can be imparted to a free electron in a single collision and $\delta/2$ is a density effect correction factor. The mean energy loss rate for charged particles in different materials is shown in Fig. 2.18 as a function of the particle velocities $\beta\gamma$ and different particle momenta.

The stopping power is independent of the mass of the particles and depends on the charge of the incident particle squared Z^2. At relatively small velocities $\beta\gamma < 3.5$ the dE/dx falls off as $1/\beta^2$. As β gets smaller the $\beta^2\gamma^2 = 1/(1-\beta^2)$ term in the logarithm halts the decrease of the stopping power. A minimum is reached at $3 \leq \beta\gamma \leq 4$ at which a particle is said to be minimally ionizing (MIP). Beyond the minimum the logarithmic component of the Bethe formula becomes dominant, and the stopping power begins to rise again. This is due to the fact that, as the incident charged particle reaches relativistic energies, its transverse electric field increases, leading to more of the material's atoms being within range of the particle's electric field. However, the slope eventually shallows out, due to the fact that long-distance atomic electrons are screened from the electric field of the incident particle by the dielectric effect of the intervening atoms in the material. This phenomenon is known as the "density effect" and is encapsulated in the $\delta/2$ term in the formula.

From the Bethe-Bloch formula the range R of a charged particle entering a material with an initial energy E_0 can be calculated as:

$$R = \int_{E_0}^{0} \frac{dE}{dE/dx} \tag{2.77}$$

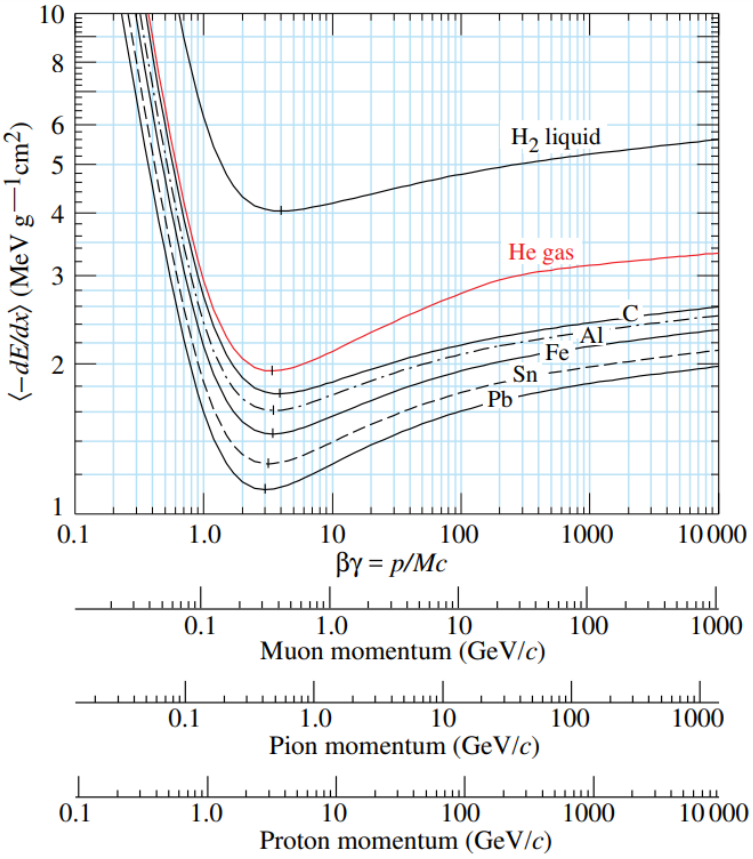

Figure 2.18: Mean energy loss rate in liquid (bubble chamber) hydrogen, gaseous helium, carbon, aluminium, iron, tin, and lead. Radiative effects, relevant for muons and pions, are not included. Taken from [78].

Following the calculation [79], the formula gives:

$$R \propto E_0^{3/2}/\sqrt{m} \tag{2.78}$$

$$R \propto m(\beta c)^3 \tag{2.79}$$

From this it follows that, if two particles have the same velocity, the heavier one will travel further, while if they have the same initial kinetic energy, the lighter one will. However, it is important to note that since energy loss is a statistical process, particles starting with the same kinetic energy will produce a spread of different final energies and ranges leading to the phenomenon of range straggling.

A charged particle travelling through a medium will not only lose energy through ionization, but it will also be deflected in its path by a series of small scatters. This behaviour is mostly due to Coulomb scattering from nuclei and is usually referred

to as multiple Coulomb scattering or simply multiple scattering (MS). For most small angle scatters the net scattering and displacement distributions are Gaussian in virtue of the central limit theorem.

We can define the projection on a plane $\theta_{\text{plane}}^{\text{rms}}$ of the three-dimensional displacement in space $\theta_{\text{space}}^{\text{rms}}$ as:

$$\theta_M = \theta_{\text{plane}}^{\text{rms}} = \frac{1}{\sqrt{2}}\theta_{\text{space}}^{\text{rms}} \tag{2.80}$$

If we approximate the projected angular distribution to be Gaussian, its spread is well defined by the Molière angle θ_{M}, which can be calculated using the formula [80]:

$$\theta_{\text{plane}}^{\text{rms}} \simeq \theta_{\text{M}} = \frac{13.6 \text{ MeV}}{\beta pc} z \sqrt{\frac{\Delta d}{X_0}} \left[1 + 0.038 \ln\left(\frac{\Delta d}{X_0}\frac{z^2}{\beta^2}\right)\right], \tag{2.81}$$

where Δd is the total distance travelled between two steps, and X_0 the radiation length in cm.

3

The Deep Underground Neutrino Experiment

Contents

3.1 Introduction

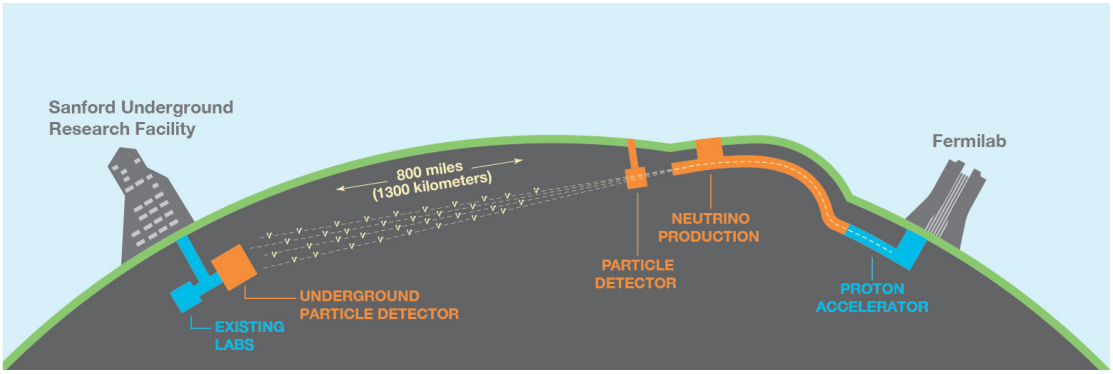

Figure 3.1: Schematic representation of the DUNE experiment with its main components [1].

The Deep Underground Neutrino Experiment (DUNE) will be a next generation long baseline neutrino oscillation experiment [1]. Its main goal will be to measure the parameters governing neutrino and antineutrino oscillations, with particular emphasis on the CP violation (CPV) phase δ_{CP} and the neutrino mass ordering (MO). The experiment will consist of three main components: a wide-band high-intensity neutrino beam situated at Fermilab, which will be capable of producing both a ν_μ and a $\bar{\nu}_\mu$ flux; a tens-of-kt-scale, underground, liquid-argon-based far detector (FD), situated at the Sanford Underground Research Facility (SURF) in South Dakota, approximately at 1300 km from the source; a modular near detector (ND) situated approximately at 500 m from the source.

In this chapter we start by providing an overview of DUNE's facilities in Sec. 3.2. A dedicated discussion of the muon spectrometer component of the experiment's ND, which is the focus of this thesis, is then provided in Secs. 3.3 and 3.4. An overview of the experiment's scientific program is then offered in Sec. 3.5 with a discussion dedicated to the physics goals of the ND in Sec. 3.6. Finally, an overview of DUNE's construction staging plans is given in Sec. 3.7.

3.2 DUNE components and design

In this section we give a brief overview of the components constituting the DUNE experiment, including the neutrino beamline, the Near Detector and the Far Detector. Due to budgetary restrictions DUNE will pursue a staged approach in its construction and operation [81]. The initial composition of the experiment, referred to as Phase I, will include two LArTPC Far Detector modules, both being 10kt in volume, and employing a Vertical Drift (VD) [82] and Horizontal Drift (HD) technology [83] respectively. The initial configuration of the ND will include two out of the three originally envisioned detectors: the liquid argon near detector ND-LAr, a modular LArTPC using a similar detection technique to the FD modules and the System for on Axis Neutrino Detection (SAND), whose main function will be to act as a beam monitor [84]. A third ND module will be placed between ND-LAr and SAND to act as a muon spectrometer: this will be called the Temporary Muon Spectrometer (TMS) and will be removed from the ND facilities after Phase I to be replaced by a more capable detector.

In order to pursue its full physics scope, after Phase I DUNE will undertake several key improvements to all of its key components: this second form of the experiment is referred to as Phase II. The FD will be complemented by two extra liquid argon modules for a total fiducial mass of at least 40kt. The proton beam power will augmented from 1.2 MW to 2.3 MW. The TMS will be replaced by a more capable, high-pressure, gaseous-argon magnetized detector called ND-GAr. A dedicated discussion of the staging scenario between Phase I and II, as well as the evolution in sensitivity of the experiment will be given in Sec. 3.7.

3.2.1 The LBNF beamline

The DUNE experiment's neutrino flux will be produced by the LBNF beamline at Fermilab, which is expected to produce the highest power neutrino beam in the world [86, 87]. It will repurpose many of the elements of the Neutrinos at the Main Injector (NuMI) neutrino beam, which was built to provide neutrinos for the NOvA and MINOS experiments and is partially based on the Tevatron collider facilities

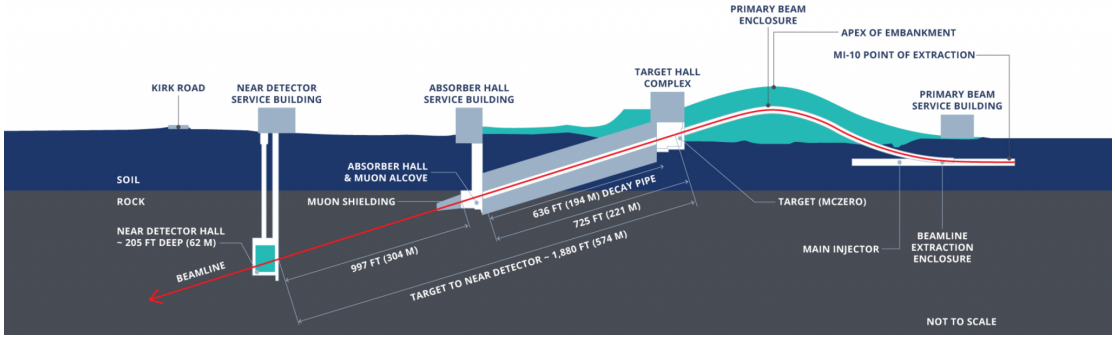

Figure 3.2: Longitudinal section of the LBNF beamline facility at Fermilab. The beam comes from the right, the protons being extracted from the main injector [85].

[88]. For a more general description of the general components and challenges related to the generation on man-made neutrino fluxes see Sec. 2.7.

The production of the neutrino flux begins at Fermilab's linear accelerator (Linac), where protons are originated as H^- ions and accelerated to energies of 400 MeV. The ions are converted into protons in the Fermilab Booster, where they are accelerated to 8 GeV as 1.6 μs batches with a 53 MHz bunch spacing. The bunches are then accelerated in the Main Injector (MI) synchrotron to an energy range of 60-120 GeV. Fermilab's proton accelerator facilities will be upgraded through the Proton Improvement Plan, phase II (PIP-II), in time for the DUNE Phase I data taking period. The new proton beam will reach an average beam power of the order of 1.14 MW, delivering 7.5×10^{13} protons in one MI machine cycle (0.7 sec - 1.2 sec) to the LBNF target. Further improvements are expected as part of the PIP III project, which will allow to reach 2.3 MW of power for DUNE Phase II. All the improvements to the beamline components are being planned to achieve minimal retro-fitting.

Once the primary proton beam reaches the desired energy, it is directed through the use of extraction and transport components over a man-made hill and bent downwards towards a graphite target located at ground level. This constitutes the first element of the proper neutrino beamline (see Fig. 3.2 for a schematic representation). The charged mesons, primarily kaons and pions, produced in the interactions of the protons are sign selected and focussed by two magnetic horns

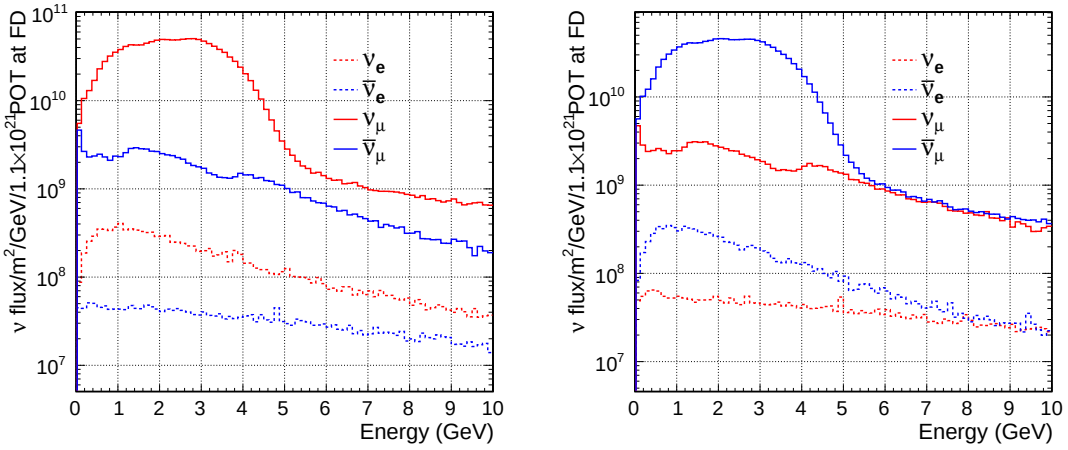

Figure 3.3: Neutrino fluxes at the FD for neutrino mode (Left) and antineutrino mode (Right). [89]

(see Fig. 2.15) into a decay pipe towards the FD. The target and focusing horns are all located inside a heavily shielded vault called the target chase, that is isolated from the decay pipe at its downstream end by a metallic window.

The mesons generated in the proton interactions are short-lived and decay, producing a combined flux of ν_μ, $\bar{\nu}_\mu$, ν_e and $\bar{\nu}_e$. If the main neutrino type being produced is ν_μ, the beam is said to be in forward horn current (FHC) mode, otherwise it is said to be in reverse horn current (RHC) mode. Both polarities produce high purity fluxes, with an expected contamination from the "incorrect" neutrino type (i.e. ν_μ in RHC mode and vice-versa) of less than 10% in the oscillation energy region. The neutrino fluxes at the FD, produced in FHC and RHC are shown in Fig. 3.3. At the end of the decay pipe, an absorber is placed to remove the residual hadrons. The absorber core consists of replaceable aluminium and steel water-cooled blocks. Approximately 40% of the beam power is deposited in the target chase and surrounding shielding, 30% in the decay pipe and 30% in the absorber.

The wide-band neutrino beam produced by the LBNF facility, is needed to cover the first and second neutrino oscillation maxima, which for a 1300 km baseline are expected to be approximately at 2.4 and 0.8 GeV. For this reason the beamline design is optimized for neutrino energies between 0.5 and 5 GeV.

3.2.2 The far detector

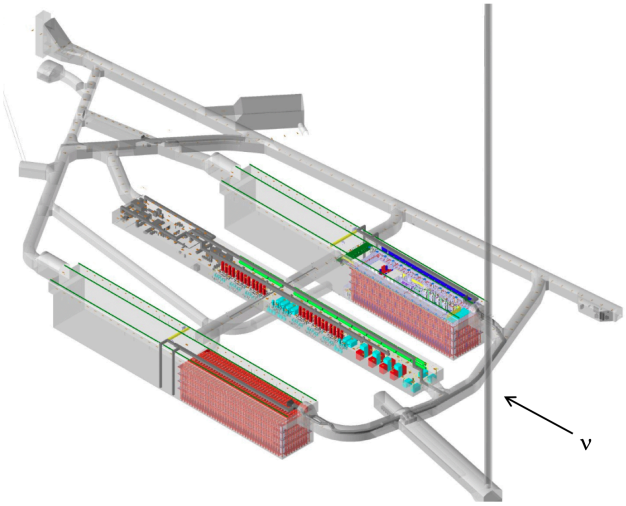

Figure 3.4: Underground caverns for DUNE FD and cryogenics systems at SURF, in South Dakota. The drawing, which looks towards the northeast, shows the first two far detector modules in place. [89].

The DUNE FD will include four LArTPC detector modules, each containing a 10kt fiducial liquid argon mass and a total liquid argon mass of 17.5kt. Each module will fit inside a cryostat. Of the four modules only the first two will be available during DUNE Phase I, the first one using an horizontal drift technology (originally identified as single phase (SP) [83]) will be called FD1-HD and the second one using a vertical drift technology[82] (evolved from the dual phase (DP) technology [90]) will be called FD2-VD. The last two modules will be employed during Phase II and their exact technology is yet to be determined [81]. For a general description of the functioning principles of a LArTPC see Sec. 2.8.

The FD1-HD design combines a several-tens-of-kt level fiducial mass with a sub-cm spatial resolution. Both are crucial to achieve DUNE's scientific goals of measuring CPV, while searching for nucleon decay and being capable of observing neutrinos from supernova bursts. An example of the design of the detector being directly informed by the physics requirements of the experiment, comes from the ν_e appearance channel in the oscillation analysis. In order to correctly identify a ν_e CC interaction, a detector needs to be able to identify the presence of a high-energy

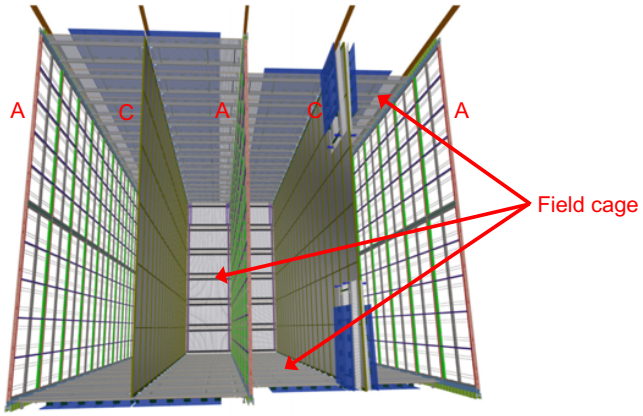

Figure 3.5: Schematic of a 10 kt DUNE FD horizontal drift module, showing the alternating anode (A) and cathode (C) planes that divide the LArTPC into four separate drift volumes. The red arrows point to one top and one bottom field cage module and to the rear end-wall field cage.[89].

electron, while avoiding misclassification of high energy photons as electron, since both electrons and photons can induce electro-magnetic showers in the LAr medium. The FD modules are capable of distinguishing between these two signals by using dE/dx information combined with spatial information. Photon induced showers have an initial non ionized gap of the order of one radiation length ($\sim$ 14 cm). This gap can be easily measured by the FD modules thanks to their 0.5 cm spatial resolution. Additional dE/dx separation based on pre-electro-magnetic-shower depositions, can be achieved, thanks to the charge resolution of the FD modules.

Each FD1-HD detector module consists of 4 separate liquid argon drift volumes with a maximum drift length of 3.5 m (Fig. 3.5). Each volume is instrumented with a vertical cathode plane and an anode plane, for a total of three module-long (58.2 m) anode planes and two cathode planes. A field cage surrounds the drift region between the two, producing a stable 500 V/m electric field in the horizontal direction. The drift ionization electrons reach the anode planes within a few milliseconds.

Each anode plane is instrumented with a total of 50 anode plane assemblies (APAs) which consist of an aluminium frame with three layers of active wires and an additional shielding layer wrapped around them. The first two active layers are identified as the U and V induction layers. These layers are angled

at $\pm 37.5^{\circ}$ in order to enable precise 3-dimensional reconstruction. The relative voltage between the layers is chosen so that the drift electrons pass through them and produce a bipolar induction signal on both planes. The drifting electrons are finally collected in the final X wire plane, where they produce a mono-polar signal. In the X collection plane, as well as in the G shielding plane, the wires run vertically. The spacing between the wires in each layer is of 0.5 cm, and defines the spatial resolution of the APAs.

The scintillation photons produced by the passing charged particles in the liquid argon in the very ultraviolet (VUV) spectrum are collected by modules of a photon detector (PD) systems called X-ARAPUCA [91]. Liquid argon produces $\sim$24000 per MeV of deposited energy. These photons reach the detectors in a time-frame of the order of a nanosecond. The X-ARAPUCA modules are mounted between the sets of wire-planes and consist of layers of dichroic filter and wavelength shifters, that shift the VUV scintillation light into the visible range, trap the visible photons, and transport them to a silicon photo-multiplier (SiPM). The signals produced in the SiPMs are then combined with the wire signals from the APAs at the data acquisition (DAQ) level.

The FD2-VD design was developed from the R&D experience accumulated by the DUNE collaboration with the ProtoDUNE-SP and ProtoDUNE-DP prototypes at the neutrino research facilities at CERN [82]. The detector consists of several vertical drift modules enclosed in a large cryostat structure. Each module is divided into two vertical drift regions 6.5 m in height by an horizontal cathode, and feature two anode planes, one close to the cryostat top, just below the surface of the liquid argon region and one close to the bottom of the cryostat. Field cage modules hang vertically around the module's perimeter. The 450 V/cm electric field drifts the ionisation electrons, either upwards or downwards depending on the drift region. The vertical design of the FD2-VD offers a slightly larger instrumented module compared to FD1-HD and it's more cost-effective thanks to its high-modularity and general structure and geometry.

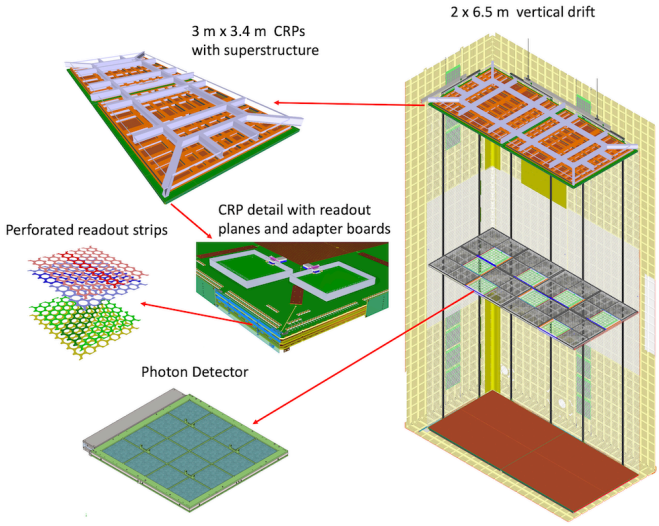

Figure 3.6: Schematic view of a vertical drift module concept with PCB-based charge readout. Corrugations on cryostat wall shown in yellow; PCB-based CRPs shown in brown at the top and bottom; cathode shown in violet, at mid-height with openings for photon detectors; field cage modules shown in white, hung vertically around the perimeter; photon detectors, placed in the openings on the cathode and on the cryostat walls, around the perimeter in the vertical regions near the anode planes. [82].

The anode planes in the FD2-VD design consist of two double-sided perforated printed circuit boards (PCBs) that are connected to form a charge-readout unit (CRUs). The perforation holes allow the electrons to pass through the PCB's. The first PCB is instrumented with two sets of induction strips, while the second one hosts the collection strips. The three planes of strips are segmented at about 7.5 mm pitch for the induction planes and 5 mm pitch for the collection plane, and are set at 60° angles relative to each other to maximize information in the charge readout from different projections. Two CRUs are connected to a frame to form a Charge Readout Plane (CRP). Each anode plane consists of 80 CRPs. Much like in the FD1-HD design the anode plane signal allows for a two-dimensional reconstruction of any given event, while the third dimension is given by the drift time information obtained from the scintillation light.

The photo-detectors implemented in the FD2-VD follow the same general design of the ARAPUCA-X modules developed for FD1-HD. The PDs will be mounted on the four cryostat membrane walls and on both sides of the central cathode structure. This configuration offers a uniform light measurement coverage across the entire

LArTPC volume. Additionally, the FD2-VD liquid argon will be doped with a small quantity of xenon. This has no impact on the TPC operation but significantly enhances the photon detection performance. A schematic representation of the vertical drift modules' design is shown in Fig. 3.6.

3.2.3 The near detector

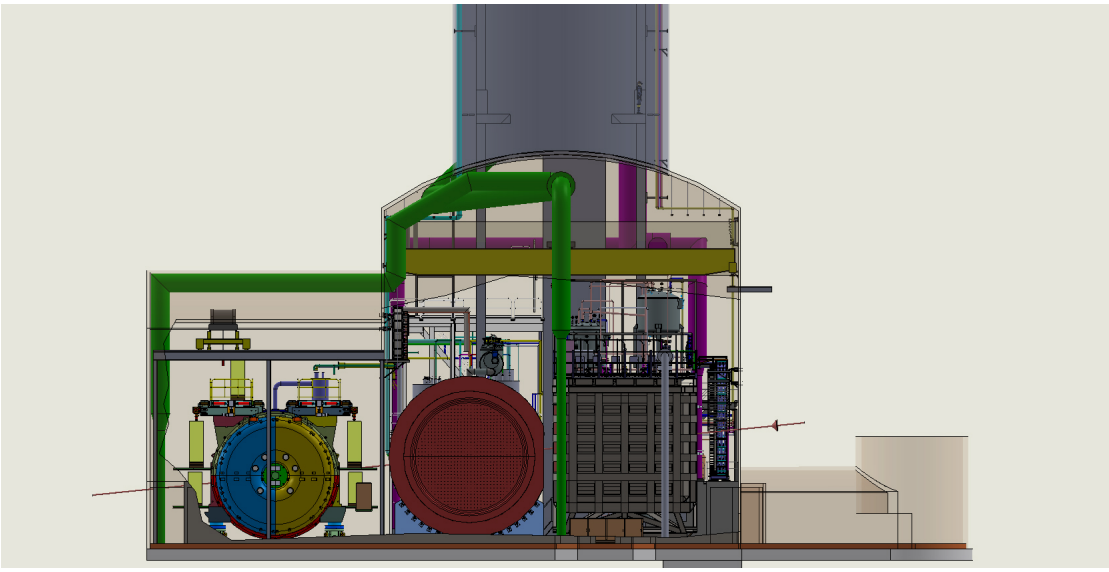

Figure 3.7: Schematic side-view of DUNE's ND hall. The neutrino beam direction is given roughly by the red arrow and from right to left the detectors ND-LAr, ND-GAr and SAND are shown [84].

To enable oscillation measurements, DUNE must first predict the anticipated signal and background at the FD, for any given set of oscillation parameters, followed by a comparison with measured flavour-tagged neutrino spectra. To generate this prediction, one must determine the neutrino flux at production, the neutrino-argon interaction cross-sections, and the detector response, all of which have systematic uncertainties that need to be constrained (see Sec. 3.6 for a more detailed discussion). The near detector (ND) is tailored to address each prediction component [2]: it will gauge the unoscillated neutrino beam flux both on-axis and at varying off-axis angles; refine models of neutrino interactions through cross-section and final state topology measurements; model detector responses relative to neutrino energy. Additionally, the ND is designed for operation within a high

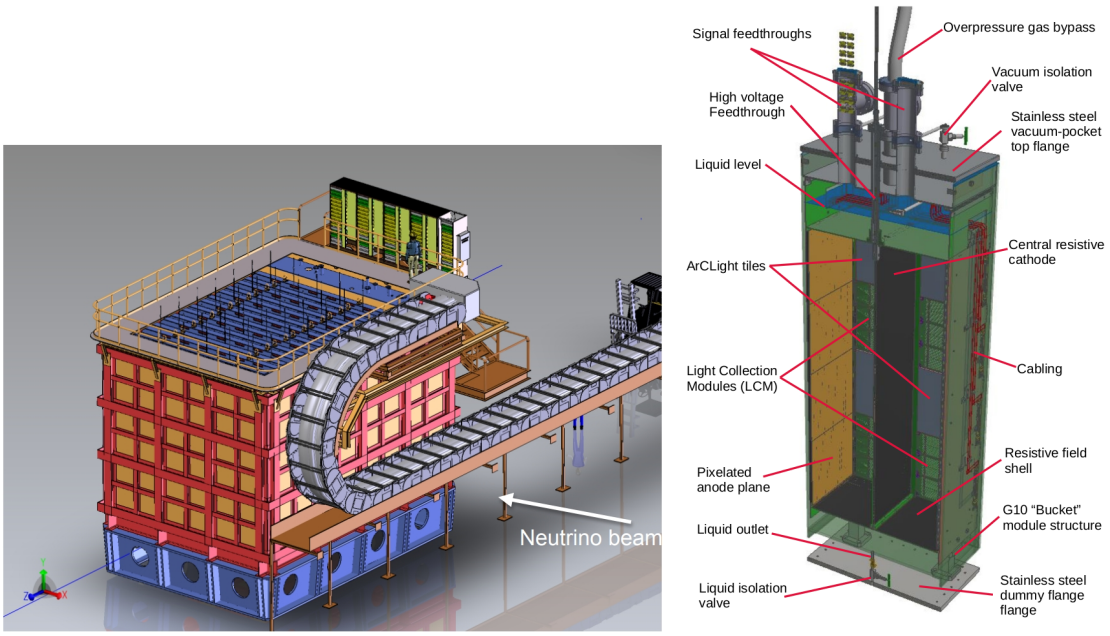

Figure 3.8: (Left) Schematic view of the external components of ND-LAr, including the cryostat and the system for the DUNE-PRISM movement (Right) Schematic drawing of a single ND-LAr module with its major components individually highlighted [84].

event rate environment, ensuring the requisite statistical coverage across the full phase-space. The ND will consist of three detectors with complementary functions: ND-LAr, which will use a LArTPC technology similar to the FD modules; ND-GAr, a gaseous argon TPC detector; and SAND, a magnetized beam monitor. ND-LAr and ND-GAr can be moved to different off-axis positions, while SAND remains fixed on-axis. A schematic depiction of the ND, inclusive of all detectors, is presented in Fig. 3.7. The ND-GAr detector will become available only during Phase II, with a much simpler detector named the temporary muon spectrometer (TMS), replacing it during Phase I.

ND-LAr will be a LArTPC detector engineered for operation within a high-rate environment. Utilizing the same argon target and similar detector technology as the FD modules, ND-LAr is essential for modelling nuclear response on argon and the impact of the dense LAr medium. ND-LAr is comprised of 35 distinct TPC modules, mirroring the design of the ArgonCube prototype [92]. Despite the relatively modest dimensions of the detector, this modular architecture is

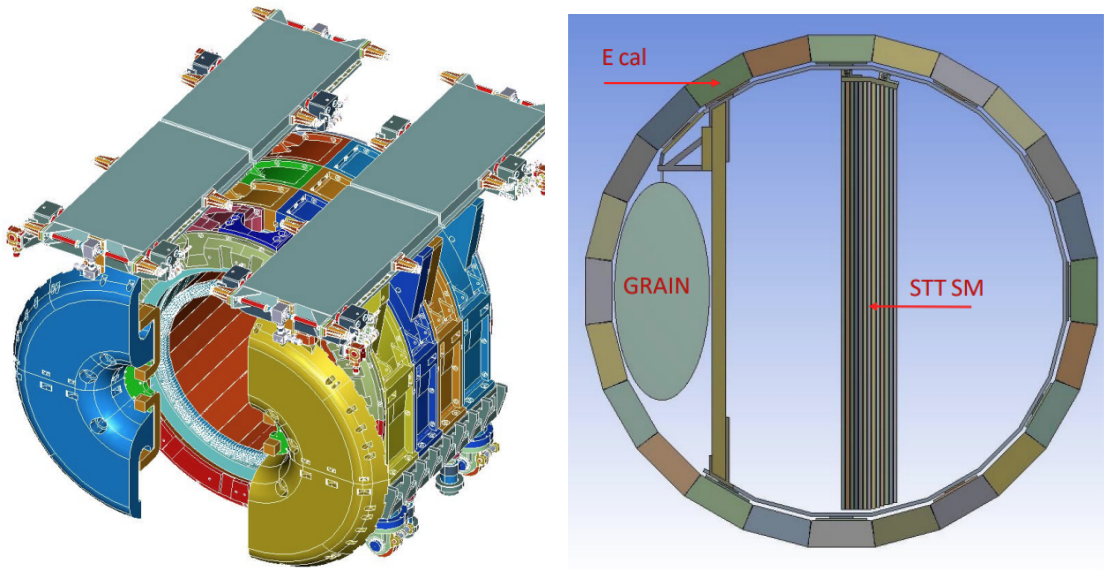

Figure 3.9: (Left) Schematic view of the external components of SAND, including its cryostat and its solenoid magnet (Right) Side view of the internal components of SAND, including its active liquid argon target called GRAIN, one of the straw tube tracker modules and the electro-magnetic calorimeter [84].

indispensable for managing the high event rate, facilitating a smaller drift region of the order of 50 cm, enhanced light separation, and increased sensor pixelation. Each module encompasses two optically isolated TPCs outfitted with a LArPix-based pixelated charge readout system [93], alongside a light readout for rapid timing data from prompt scintillation light, and a field structure ensuring minimal field non-uniformity throughout the active volume. Given the relatively compact dimensions of its active volume, ND-LAr cannot fully contain the majority of muons generated in ν_μ Charged Current (CC) interactions within liquid argon. Hence, precise momentum reconstruction of this muon sample necessitates an external spectrometer component, a role fulfilled by ND-GAr and the TMS.

ND-LAr and ND-GAr possess the capability to be translated up to 30 meters perpendicular to the neutrino beam axis, spanning angles $0° < \theta < 3°$, a feature named Precision Reaction Independent Spectrum Measurement (PRISM). With increasing off-axis angles, the mean energy of the neutrino flux diminishes while its energy dispersion narrows (see Sec. 2.7.3). Consequently, the ND gains access to diverse unoscillated neutrino flux profiles, which can be combined to predict

the oscillated flux at the FD. This data-centric methodology mitigates reliance on models. Moreover, a key feature of the DUNE-PRISM program is that the off-axis fluxes will vary in mean energies and spreads and will thus be dominated by distinct interaction types (e.g. quasi-elastic, resonant etc.). Access to this variety of samples will facilitate the disentanglement of flux and cross-section uncertainties, enhancing flux and interaction modelling.

The System for On-axis Neutrino Detection (SAND) will function as a constant on-axis monitor of the neutrino beam, a crucial role for the DUNE-PRISM program. It will ensure that any differences in flux measured by ND-LAr and ND-GAr result from their off-axis position rather than anomalies in beam production. SAND's main structural components, along with its solenoid magnet, cryostat, and electromagnetic calorimeter, will be repurposed from the KLOE experiment (Fig. 3.9). The nominal internal tracker design of SAND will feature a Straw Tube Tracker (STT) divided in modules, although other options are still being investigated by the DUNE collaboration [84]. The modules will include a series of tunable passive slabs interleaved with tracking layers of 5 mm diameter tubes. SAND will provide various targets, such as CH_2 and C. The interplay between CH_2 and C targets will offer the possibility of studying neutrino-on-hydrogen interactions, which are devoid of nuclear effects, by statistical "subtraction" . Additionally, SAND will incorporate its own active target of liquid argon called Granular Argon for Interaction of Neutrinos (GRAIN), whose design is currently being finalized.

3.3 The ND-GAr detector

ND-GAr will be a magnetized detector with a magnetic field of 0.5 T, mainly constituted of a high-pressure gas time-projection chamber (HPgTPC) surrounded by an electro-magnetic calorimeter (ECAL). A simple cut-away schematic of the detector is shown in Fig. 3.10. ND-GAr will fulfil two main goals: firstly it will act as a spectrometer measuring the charge and momentum of particles exiting ND-LAr; secondly it will offer its own sample of neutrino interactions inside the HPgTPC. The high pressure gas environment will offer relatively low tracking thresholds

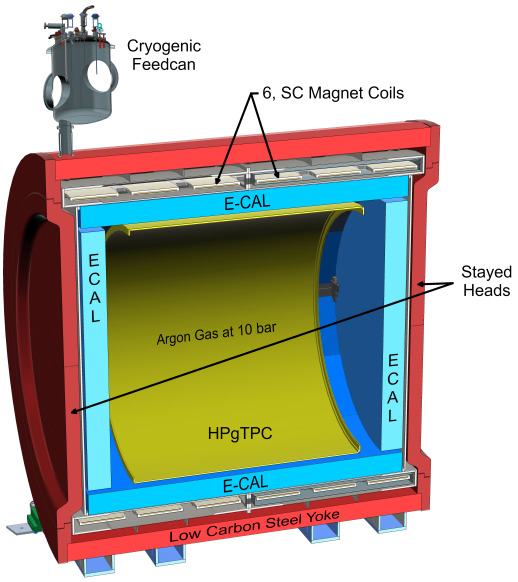

Figure 3.10: Cut-away view showing the various components of ND-GAr [94].

and enhanced particle identification performance when compared to LArTPCs, especially for pion-proton separation. The PID capabilities of ND-GAr specifically derive from a combination of dE/dx measurements in the HPgTPC, E/p measurements in the ECAL and the curvature momentum and sign measurements available from the magnetization of the TPC, alongside range measurements in the ECAL.

ND-GAr's spectrometer role mostly consists in identifying the sign and measuring the momentum of muons exciting ND-LAr. This is done to measure the spectrum of ν_μ and $\bar{\nu}_\mu$ reaching the near detector, through their CC interaction products. This is crucial to reach the oscillation measurement sensitivity desired by the experiment.

ND-GAr's lower tracking thresholds as well as its superior PID capabilities and acceptance, will make kinematic regions not accessible to a LAr detector, available to the ND complex. The relationship between proton tracking threshold and tracking material can be seen in Fig. 3.11. This is particularly important to enhance the ability of the ND of clarifying the relationship between the true and reconstructed energy in neutrino interactions on argon. Nuclear effects can introduce significant systematic uncertainties in the reconstruction of the neutrino energy. Theoretical studies suggest for example that final state interactions (FSIs)

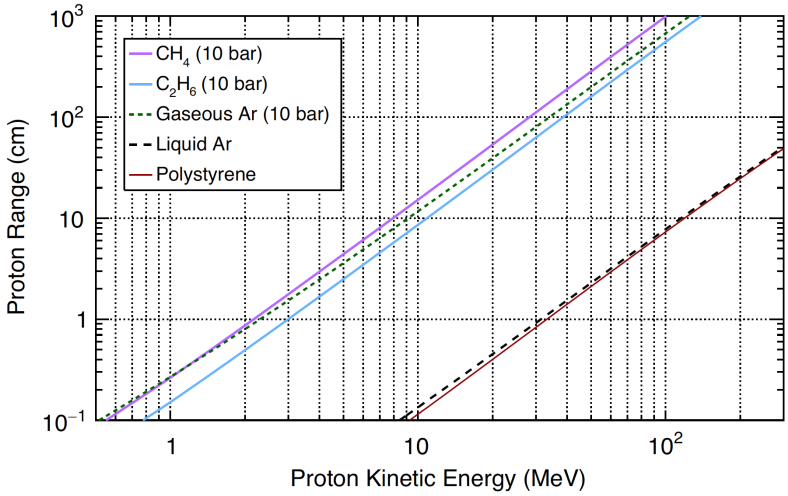

Figure 3.11: Plot showing proton range in cm as a function of kinetic energy in MeV in double logarithmic scale. The different curves show the range dependency in different gaseous, liquid or solid media [12].

can increase dramatically the number of final state protons in the kinetic range of tens of MeVs and it's thus crucial for the ND to be able to measure them and identify them. This is possible with a HPgTPC which has lower tracking thresholds, but not in a LAr or solid detector such as ND-LAr or SAND.

It is also important for ND-GAr to characterize the spectrum of charged pions coming from ν_μ and $\bar{\nu}_\mu$ CC interactions. At very low momenta, down to 20 MeV/c, this is essential because this is the region where FSI is more prevalent. Only a gaseous detector has low enough energy thresholds to do it with a sufficient efficiency. At higher momenta above 100 MeV/c, ND-GAr becomes essential in distinguishing the pion multiplicity, since in LAr the same pions tend to produce hadronic showers, while in ND-GAr's TPC they are more likely to produce distinguishable tracks. Measuring neutral pions from ν_μ and $\bar{\nu}_\mu$ CC interactions in the same momentum range is also possible for ND-GAr thanks to its ECAL.

3.3.1 The HPgTPC

The design of the ND-GAr HPgTPC is closely related to the design of the ALICE experiment TPC [95]. The basic detection mechanisms of ALICE's and ND-GAr's TPCs are identical (see Sec. 2.8). The primary ionization electrons are formed

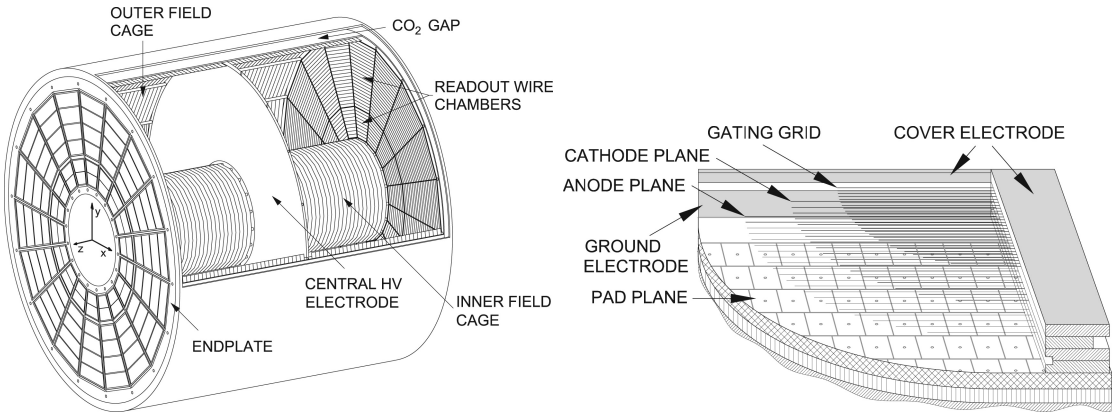

Figure 3.12: (Left) Diagram of the ALICE TPC .(Right) Schematic diagram of the ALICE MWPC-based ROC with pad plane readout. [2]

by the energy deposition of passing charged particles, and drifted towards the end-caps by an electric field produced by a high voltage (HV) central electrode plane. The total drift region has a cylindrical shape with a diameter of $\sim$ 5 m and a length of $\sim$ 2.5 m per side. The electric field is oriented in parallel to the 0.5 T magnetic field, in order to reduce transverse diffusion. At the end-caps, multi-wire proportional chambers (MWPCs) induce electron avalanches which produce a signal on an anode pad plane. Read-outs of the pad signals give hit coordinates in two dimensions, while the drift time provides the third. A schematic representation off the ALICE TPC is given in the left diagram in Fig. 3.12.

The read-out chambers or ROCs used in ALICE, contain the MWPCs and read-out pad planes and are divided in 18 trapezoidal regions, each including a smaller inner chamber (IROC) and an outer chamber (OROC). A schematic representation of the ROCs is given in the right diagram in Fig. 3.12. All of ALICE's ROCs will be re-installed in ND-GAr, as they have been replaced in the original detector by GEM-based ROCs [96]. An additional central region of ROCs (CROCs) will fill the central regions of the read-out planes, which in ALICE was occupied by a silicon based central tracker and an inner field cage.

Despite all the common elements, some key differences between the design of the two TPCs exist: the two detectors will use different gases, with ALICE's base gas being a mixture $Ne/CO_2/N_2$ and ND-GAr using a mixture of Ar-CH_4 at 90%-10%

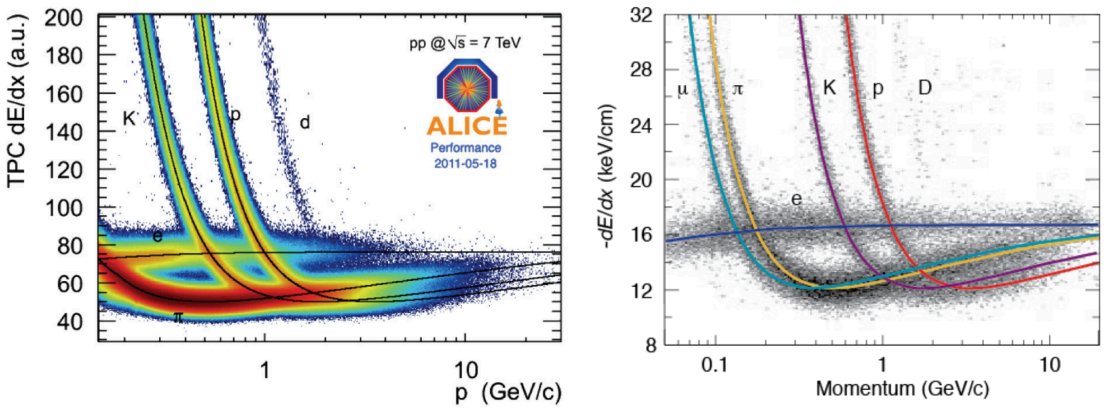

Figure 3.13: (Left) ALICE TPC dE/dx-based particle identification as a function of momentum [97]. (Right) PEP-4/9 TPC (80:20 Ar-CH4, operated at 8.5 Atm, from [98]) dE/dx-based particle identification.

molar fractions; ND-GAr will operate at a pressure 10 times larger than ALICE; the electronics and data acquisition systems will be completely redesigned to be closer to the LArPix technologies used in DUNE's LArTPCs; the field cage will only include an outer component, since the central region in ND-GAr will be part of the active volume of the detector, while in ALICE it was occupied by the beam pipe and a silicon-based tracker.

The HPgTPC is oriented so that the neutrino beam is perpendicular to the electric and magnetic fields. This is the most favourable orientation for measuring charged particles travelling along the neutrino beam direction. In ALICE the track reconstruction is done by combing ROC hits to form tracks following the trajectories of charged particles in the TPC. This is done for ND-GAr through the `GArSoft` software package which handles the simulation and reconstruction for the detector. A comprehensive description of this tool will be given later in Secs. 4.4 and 5.4.

In ALICE the ionization induced by charged particle tracks can be used to estimate the particle dE/dx. When combined with a curvature momentum estimate, this can be used for PID. In the left plot in Fig. 3.13 we show the characteristic PID curves for charged particles produced in proton-proton collisions at $\sqrt{s} = 7$ TeV. The band resolution of the different particle types dE/dx curves is expected to

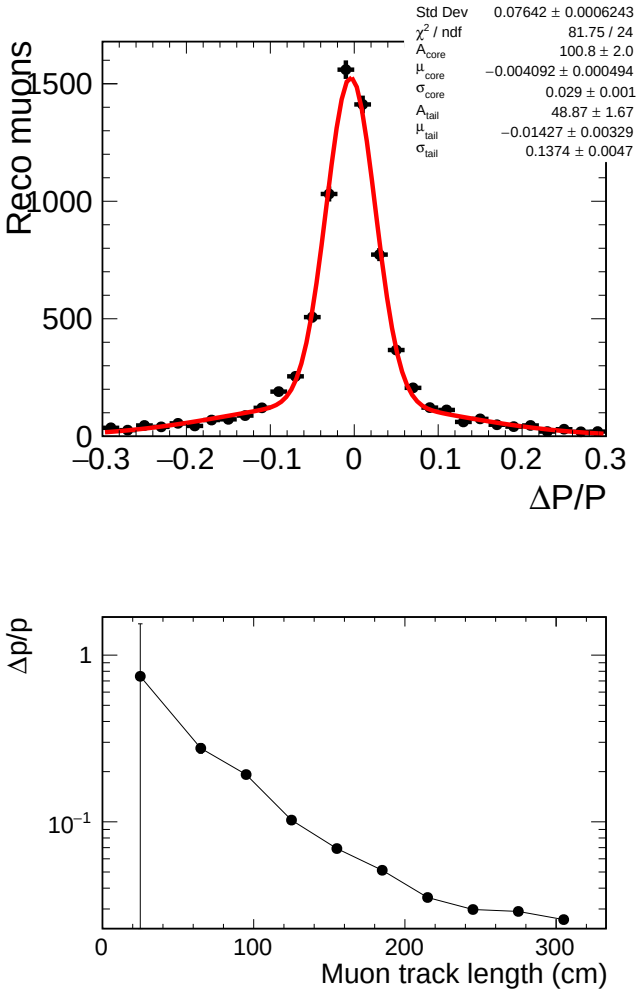

Figure 3.14: (Top) Momentum resolution for reconstructed muons in `GArSoft`, in a sample of ν_μ CC events. The events were generated using the LBNF flux. The portion of the double-Gaussian fit which defines the central core of the $\Delta p/p$ distribution, contains 2/3 of events and has a width of 2.7%. The tails are well described by a 12% resolution. (Bottom) Momentum resolution as a function of track length [2].

be significantly improved in ND-GAr. The 10 times higher gas pressure in ND-GAr will result in a correspondent increase in ionization per unit track length. A better comparison can be made with the performance of the PID capabilities of PEP-4/9, which operated at 8.5 atmospheres: the experiment's dE/dx curves are shown in the right plot Fig. 3.13 showing good separation between particle types below a few GeV, including pions and muons which are problematic for TPCs with lower material budgets.

The resolution of a curvature momentum measurement in a TPC depends on the

pad resolution as well as the multiple coulomb scattering (MS) degradation. The characteristics of the track and of the neutrino event also influence the curvature resolution. These include the particle transverse momentum p_T the track length as well as the detector occupancy at the time of the track formation (see Sec. 5.5.2). Given the randomized nature of particle track formation in a neutrino experiment, the track length distribution is expected to have a significant component of short tracks. For this reason fiducial cuts are imposed inside the TPC. Note that low energy particles that stop within the detector (primarily protons) would be reconstructed via their track length rather than their curvature. Within the fiducial volume ND-GAr will have a 4π acceptance. This includes particles crossing the central cathode region, which is very thin (25 μm of mylar).

An early study was done using the `GArSoft` software suite, on the momentum resolution for muons coming from ν_μ CC interactions in the HPgTPC using the LBNF flux. A fiducial cut was imposed on the interaction vertexes requiring a distance of at least 50 cm from the barrel walls and 30 cm from the end-caps. The momentum resolution was calculated in terms of fractional residuals defined as:

$$\frac{\Delta p}{p_{\text{true}}} = \frac{p_{\text{reco}} - p_{\text{true}}}{p_{\text{true}}} \tag{3.1}$$

where p_{true} is the true initial momentum of the particle while p_{reco} is the reconstructed one. The distribution was fitted with a sum of two Gaussian functions, defining a "core" and a tails resolution. The resolution defined by the σ of the residual distribution is of 2.7% for the core distribution and 12% for the tails as shown in the top plot in Fig. 3.14. The single Gaussian resolution is shown as a function of the muon track length in the bottom plot in Fig. 3.14.

3.3.2 The electro-magnetic calorimeter

The main role of the ECAL in ND-GAr, will be to reconstruct electrons and photons coming from neutrino interactions. The ability of detecting photons and identifying their production point makes the reconstruction of π_0 from inside the HPgTPC possible. This will be especially important in the reconstruction of ν_e events for

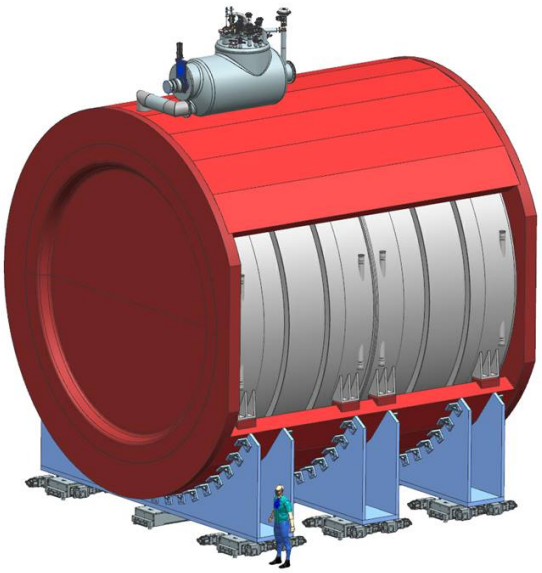

Figure 3.15: Schematic representation of the outer layer of the SPY magnet, showing parts of the cryostat sytem at the top, the outer steel yoke in red, the low material budget muon window cut-out in grey and a human figure for size reference at the bottom [94].

which the missed identification of π_0 produces important systematic uncertainties. The ECAL will also be important in determining the t_0 for particles coming from ND-LAr and rejecting external background such as rock muons and neutrons. It will offer a time precision at the sub-nanosecond level.

The reference design of the ECAL is heavily inspired by the CALICE hadron calorimeter from the ALICE experiment [99] as well as the ECAL of the ND280 modules at T2K [100]. It will have an octagonal shape fully contained in the pressure vessel, with each octant composed of trapezoidal modules. The modules will contain alternating layers of active polystyrene scintillator read out by SiPM detector and absorber sheets. The active layers are segmented in tiles and strip offering an effective space resolution of the order of a few cm.

3.3.3 The SPY magnet system

The current integrated design for ND-GAr's solenoid, pressure vessel and yoke is named the Solenoid with Partial return Yoke (SPY) [94] and is largely based on the magnet system developed for the Multi Purpose Detector (MPD) at the NICA Collider at JINR [101]. The magnet system is composed of a superconducting

magnet surrounded by an iron return yoke. To reduce dimensions and overall costs, the magnet and cryostat system has been designed to serve as the cylindrical component of the pressure vessel for the HPgTPC, while also providing support for the HPgTPC and the ECAL, which will be fully contained inside its volume.

The magnet coil is composed of rectangular superconducting cables bent and grouped to form six identical sub-coils with an internal diameter of 7 m, a length of 0.9 m and a thickness of 20 mm, operating at 5000 A. The coils will be hosted in a cryostat reaching operating temperatures of 4.5 K to 4.7 K. The cooling elements of the cryostat will consist of pipes welded onto the outer surface of the coil formers hosting a flow of liquid helium.

The SPY magnet will produce an overall magnetic field of 0.5 T with a field uniformity of $\pm 1\%$. These field characteristics surpass the requirements necessary to achieve the particle reconstruction performance desired by ND-GAr. These include a minimum 3% momentum resolution for muons exiting from ND-LAr and a performance at least as good as the FD for particles produced in neutrino interactions on gas. The yoke has also been designed to reduce the amount of material between ND-LAr and ND-GAr to a minimum by removing a portion of the downstream barrel. This is important to ensure that the muons coming from ND-LAr loose as little energy as possible in uninstrumented portions of the detectors, reducing the relative uncertainties to a minimum.

SPY is completed by a carbon steel return yoke, which presents several unique characteristics. The pole faces of the yoke have been designed to offer sufficient mechanical strength to act also as the end-caps of the detector's pressure vessel. This removes the necessity for the large domed heads that would normally be required for a pressure vessel of such a diameter, shortening the overall dimensions of the system by about 4 m. A schematic view of the outer components of the SPY magnet are shown in Fig. 3.15.

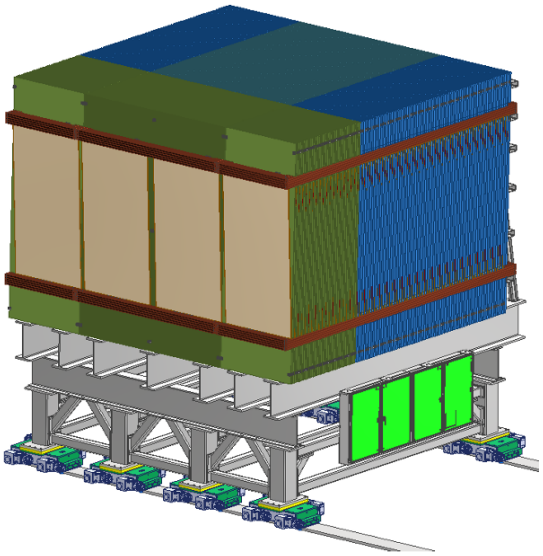

Figure 3.16: Schematic view of the temporary muon spectrometer's current official design [84].

3.4 The temporary muon spectrometer

As mentioned in Sec. 3.2, due to budgetary restrictions, the DUNE experiment will follow a staged approach to its construction. During Phase I the muon spectrometer component of the ND complex will consist of a Temporary Muon Spectrometer (TMS) which will act as a place-holder for the ND-GAr detector, only fulfilling the minimal goals necessary for the early life of the experiment. In this section we discuss the official TMS design chosen by the collaboration (Sec. 3.4.1), as well as an alternative design named ND-GAr-Lite (Sec. 3.4.2). While the latter design has now been abandoned by the collaboration, the studies described in Chapter 4 are centred on it, making a description of the detector necessary.

3.4.1 TMS

The TMS is a magnetized steel range stack detector which is set to become operative during DUNE Phase I. Its main role will be to measure the momentum and charge of muons exiting ND-LAr. This will increase the acceptance of ND-LAr making the performance of the two combined detectors comparable to that of the FD [102].

Both the argon target and the technology of ND-LAr are essential to predict the rate and spectrum of neutrino-argon interactions expected at the FD and achieve the level of control over the systematics necessary for the Phase I physics goals. The inclusion of a magnetized muon catcher to ND-LAr is important to improve the muon momentum reconstruction performance in the key energy range between 0.5 and 5 GeV reaching a resolution of the order of $\delta p/p \sim 5\%$. The sign selection, which is not available using ND-LAr alone, is crucial in the δ_{CP} measurement. This is especially true in reverse horn current where the beam will experience a large contamination of neutrino interactions comparable to the desired antineutrino interactions.

TMS consists of 3 rows, each containing 100 alternating layers of magnetized steel absorber and plastic scintillator. A schematic representation of the detector is shown in Fig. 3.16 . Each scintillator layer consists of four panels divided into 48 strips, all 300 cm long and 3.5 cm wide. The strips in each layer are tilted in an alternating pattern by $\pm 3^{\circ}$ with respect to the vertical direction, providing U and V views. Each row of steel will be magnetized by two electrified coils. The coils which surround the central block produce a magnetic field which faces downwards, while the two lateral blocks have a magnetic field pointing in the opposite direction. The thickness of the steel plates is of 15 mm for the first 40 layers upstream and of 40 mm in all the others. The thickness of the steel layers was chosen in order to optimize the particles' energy deposition.

In TMS the muon momentum will be measured by range, while the charge sign will be determined based on the curvature of the particle trajectory. The scintillator layers are instrumented with ADCs and can provide calorimetric information as well as position measurements. This information can be used in many ways: the Bragg peak can be used to identify stopping muons more effectively; muons experiencing very high energy loss via Bremsstrahlung can be selected and more effectively reconstructed; the stopping point can be more effectively found by studying the evolution of $1/\beta^2$ along the track. Calorimetric measurements of

muon energy can also be made but they are not expected to be competitive with the range measurements.

The capabilities of TMS will be sufficient to reach the physics goals of the DUNE collaboration during Phase I, where the uncertainties will be dominated by the lack of statistics. This won't be true for Phase II where the impact of the systematics will be much larger (see Sec. 3.7). This is why TMS will be substituted by a more capable module, the leading design currently corresponding to ND-GAr.

3.4.2 ND-GAr-Lite

ND-GAr-Lite was an alternative Phase I muon spectrometer design for the ND which would have become possible in the case that early funds for the construction of the SPY magnet had become available [103] (see Fig. 3.17 for a schematic representation of the design). The detector would have included all the components of the SPY system while the central volume of the magnet would have been instrumented with a minimal amount of scintillator tracking planes. The advantage of this approach was to provide a natural staging to the construction of ND-GAr, reducing overall cost and waste compared to the nominal TMS design, which is set to be fully removed from the ND in the transition between Phase I and II. The ND-GAr-Lite design was eventually abandoned by the collaboration as it became clear that the funds necessary to build the SPY magnet were not going to be available for Phase I.

Two plans were originally envisioned for the transition between ND-GAr and ND-GAr-Lite. The first approach was the most straightforward and consisted in building the ECAL and HPgTPC above ground and lowering them in the ND chamber at the same time. They would have been then mounted inside the already functioning SPY magnet and enclosed inside the pressure vessel. The estimated shut-down for such a scenario would have been of the order of 8 months, similar to the 6 months estimated for the TMS to ND-GAr transition between Phase I and II. The second plan consisted in a staged approach where the ECAL would have been inserted first, while keeping the tracking planes in place. The HPgTPC would

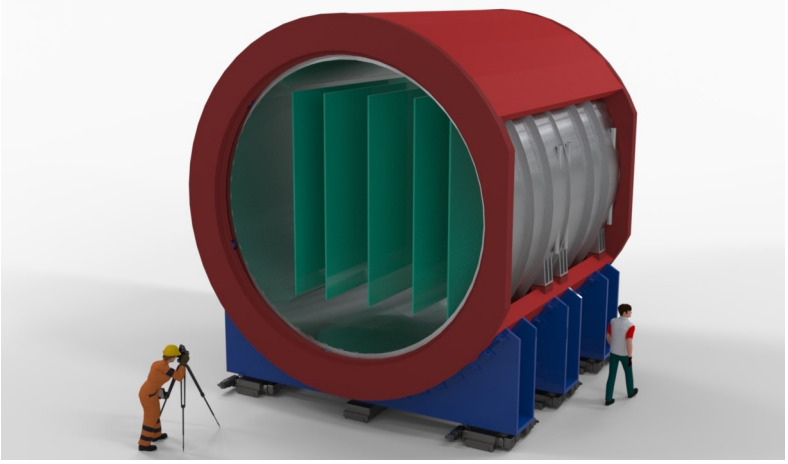

Figure 3.17: Rendering of the ND-GAr-Lite TMS design. The return yoke end caps are removed to show the inner region [103].

have been inserted soon after completing the design. This staged approach had the potential to reduce beam shut-down to a minimum but was never fully studied.

The nominal design for the ND-GAr-Lite tracker consisted of a series of rectangular tracking stations, all roughly 5.8 m tall and 5.1 m tall, positioned perpendicularly to the beam direction. Each plane would have included a x-plane and a y-plane composed of triangularly shaped scintillator bars, approximately 4 cm wide and 2 cm tall (Fig. 3.18). Each bar would have been equipped with a detector module called quad-counter, which would have included a motherboard reading out 4 SiPMs which could detect the light from 4 wavelength-shifting fibres.

In order to form a track, ND-GAr-Lite required at least three hits in three unique planes. The nominal tracker design included 5 planes, placed symmetrically about the centre of the internal cylinder of the detector. This configuration was eventually substituted by a new design which used 6 unequal planes, mostly placed in the upstream half of the ND-GAr cryostat. The nominal design had a tracking momentum threshold for muons exiting ND-LAr of 1 GeV/c and an angular acceptance of $\sim$ 20 deg. The new arrangement extended the tracking capability to cover nearly all of the muon kinematic phase space, improved the overall tracking efficiency, and lowered the threshold to track muons with initial momenta as low as 700 MeV/c. Regardless of the planes disposition, the relative momentum resolution for ND-LAr muons was estimated to be between 2% and 4%

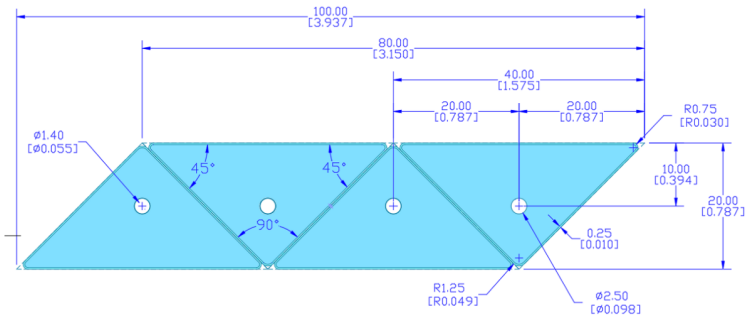

Figure 3.18: Dimensions of the triangular scintillator bars for the tracking planes of ND-GAr-Lite with measurements given in millimetres [103].

over a wide range of momenta. These results satisfied the $\leq 4\%$ ND requirements for a Phase I muon spectrometer.

3.5 DUNE scientific program

The primary scientific goal of the DUNE experiment consists in performing a comprehensive set of neutrino oscillation measurements using the ν_μ and $\bar{\nu}_\mu$ beams coming from LBNF at Fermilab. Particularly central amongst these measurements, are the determination of CPV in neutrino oscillations, the charge parity phase δ_{CP}, the MO (i.e. the sign of Δm^2_{31}) and the octant in which the mixing angle θ_{23} lies. Other key goals of the experiment include the search for proton decay in several decay modes and the detection and measurement of ν_es from a core-collapse supernova within the Milky Way, were that to occur during the lifetime of the experiment. DUNE will also pursue a series of secondary research topics such as beyond the Standard Model (BSM) searches and measurements of neutrino oscillations using atmospheric neutrinos. All these topics will be introduced and discussed in this section. The DUNE ND will offer its own complementary physics program, which will be discussed separately in Sec. 3.6.

3.5.1 Neutrino oscillation measurements

The central aim of DUNE is to test the three flavour neutrino oscillation paradigm at extreme levels of precision. It will do this by performing a complete set of neutrino oscillation parameter measurements. In long-baseline experiments such as

DUNE, that have access to horn-focussed beams producing either ν_μ or $\bar{\nu}_\mu$ dominant fluxes, the oscillation parameters can be studied either through disappearance or appearance measurements. Due to the almost maximal value of θ_{23} the $\nu_\mu \to \nu_\tau$ is the dominant flavour oscillation. Since the oscillation maxima occur at energies below the threshold for τ-lepton production in ν_τ CC interactions, these types of oscillations can only be studied through disappearance measurements. On the other hand the sub-dominant channel $\nu_\mu \to \nu_e$ allows for the detailed study of many oscillation properties through the measurement of the ν_e and $\bar{\nu}_e$ spectra.

If we assume a constant matter density the oscillation probability $\nu_\mu \to \nu_e$ can be written as:

$$\begin{aligned} P(\nu_\mu \to \nu_e) = & \sin^2\theta_{23}\sin^2 2\theta_{13}\frac{\sin^2(\Delta_{31}-aL)}{(\Delta_{31}-aL)^2}\Delta_{31}^2 \\ & + \sin 2\theta_{23}\sin 2\theta_{13}\sin 2\theta_{12}\frac{\sin(\Delta_{31}-aL)}{(\Delta_{31}-aL)}\Delta_{31} \\ & \times \frac{\sin(aL)}{(aL)}\Delta_{21}\cos(\Delta_{31}+\delta_{\mathrm{CP}}) \\ & + \cos^2\theta_{23}\sin^2 2\theta_{12}\frac{\sin^2(aL)}{(aL)^2}\Delta_{21}^2 \end{aligned} \tag{3.2}$$

where $\Delta_{ij} = \Delta m^2_{ij} L/4E_\nu$ is the phase difference, $a = G_F N_e \sqrt{2}$ is the matter effect coefficient, G_F is the Fermi constant, N_e is the number density of electrons in the Earth, L is the baseline in km, and E_ν is the neutrino energy in GeV. In the equation above, both δ_{CP} and a switch signs going from the $\nu_\mu \to \nu_e$ to the $\bar{\nu}_\mu \to \bar{\nu}_e$ channel which implies that a neutrino-antineutrino asymmetry is introduced both by CPV (δ_{CP}) and the matter effect (a). As explained in Sec. 2.5.5 the matter effect asymmetry arises from the presence of electrons in the Earth's matter, with which ν_es have a higher interaction probability than $\bar{\nu}_e$s and other neutrino flavours. In the few GeV range the interaction probability of ν_es and thus the impact of matter effect increase with the amount of matter traversed by the neutrino. Experiments with longer baselines are thus more sensitive to matter effects and consequently to the MO [104].

The measurement of δ_{CP} in DUNE benefits from the use of a wide-band neutrino beam. In Fig. 3.19 we show the $P(\nu_\mu \to \nu_e)$ as a function of neutrino energy at

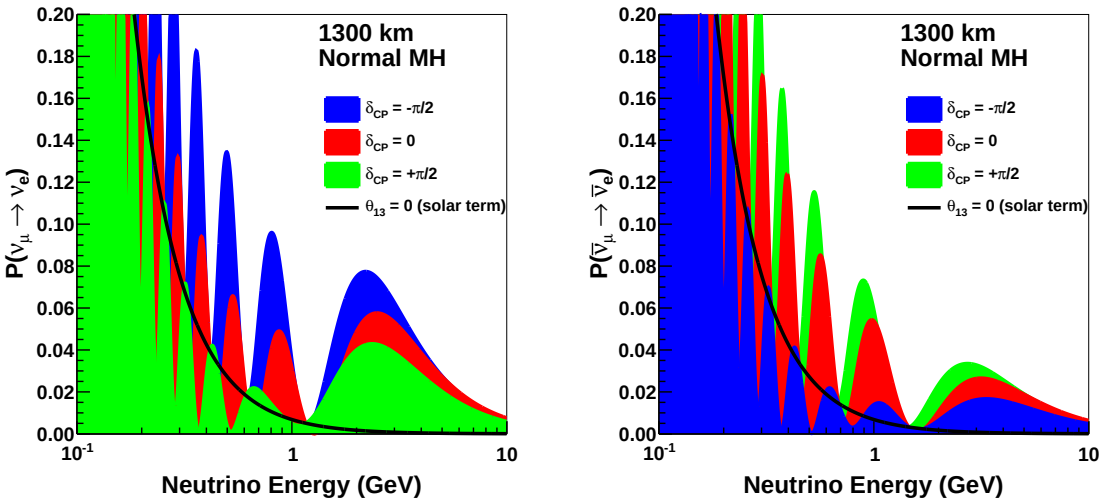

Figure 3.19: The appearance probability at a baseline of 1300 km, as a function of neutrino energy, for δ_{CP} (blue), 0 (red), and $\pi/2$ (green), for neutrinos (left) and antineutrinos (right), for normal ordering. The black line indicates the oscillation probability if θ_{13} were equal to zero. Note that DUNE will be built at a baseline of 1300 Km [1].

a 1300 Km baseline for three maximal values of $\delta_{\text{CP}} = -\frac{\pi}{2}, 0, \frac{\pi}{2}$. The various oscillation nodes are clearly visible, with the main one being peaked at 2.4 GeV, where DUNE's neutrino flux will also be peaked. The value of δ_{CP} impacts both the amplitude and the phase of the oscillation nodes: for this reason, being capable of measuring the rate of ν_e appearance as a function of the neutrino spectrum is highly desirable. In particular the impact of δ_{CP} on the amplitude of the oscillation probability peaks is higher at nodes below neutrino energies of 1.5 GeV, making the ability of DUNE of measuring ν_e appearance down to at least 500 MeV highly impactful.

Fig. 3.20 shows DUNE's sensitivity to MO and CPV as a function of the true value of δ_{CP} for a given exposure, and the sensitivity as a function of exposure for a given δ_{CP} value or range of values. These estimates were produced by the DUNE collaboration through a series of analyses which included full, end-to-end simulation, reconstruction, and event selection of FD MC and parametrised ND MC, considering the Phase II ND composition [105]. DUNE will be able to establish the MO at 5σ for 100% of δ_{CP} values with 100 kt-MW-years exposure. With the

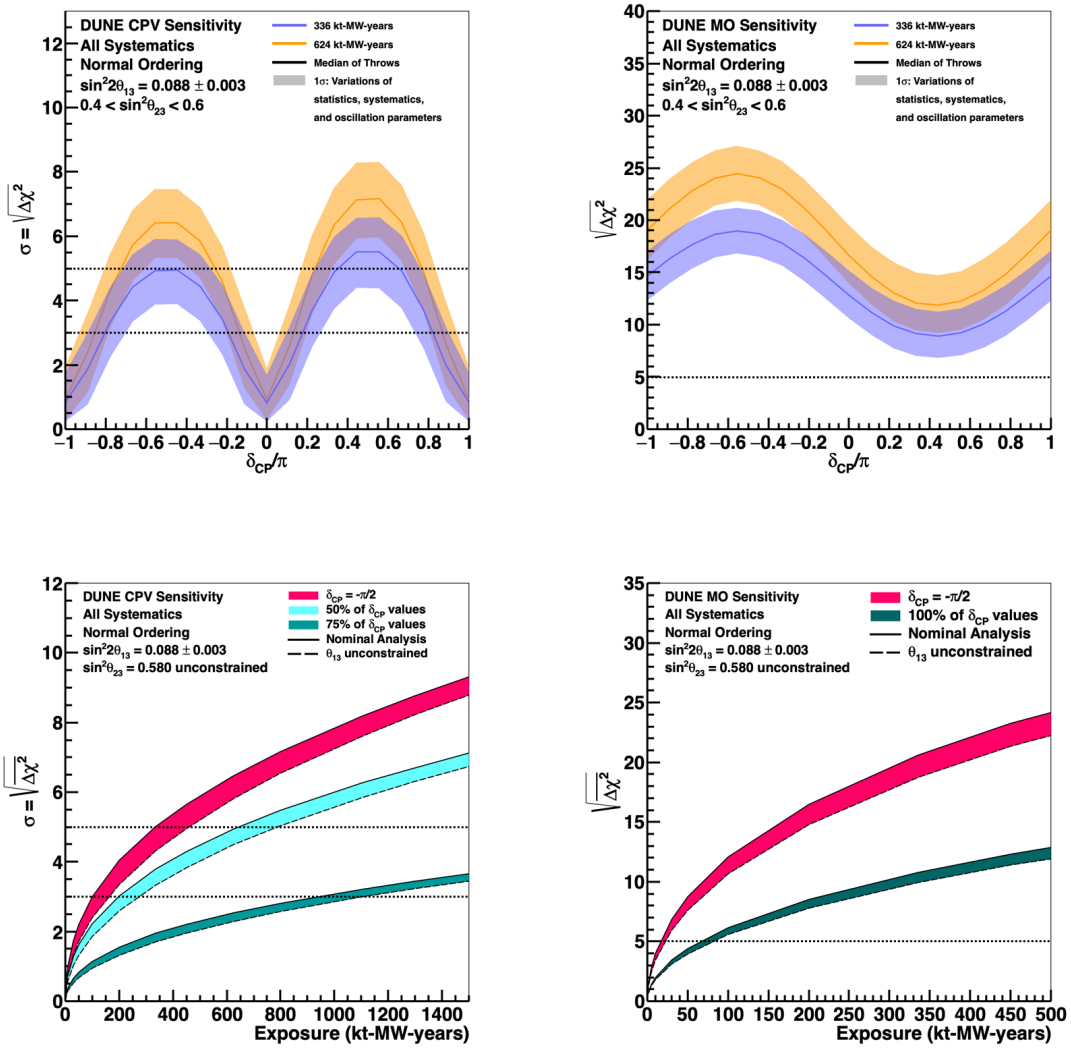

Figure 3.20: Sensitivity to the neutrino MO (Left) and CP violation (Right) as a function of the true value of δ_{CP} for several exposures (Top) or as a function of exposure in kt-MW-years (Bottom), with the Phase II near detector. For the top plots, the solid line shows the median sensitivity while the width of the band represents 68% of variations of statistics, systematics, and oscillation parameters. In the bottom plots, only the Asimov sensitivity is considered and the width of the bands represents the difference between an analysis which uses the external constraint from reactor antineutrino experiments on $\sin^2\theta_{13}$ and one without this constraint. Curves are shown for maximal CP violation ($\delta_{\mathrm{CP}} = \pm\pi/2$) and for different fractions of δ_{CP} values [81].

same exposure, DUNE will be able to observe CPV with 3σ significance if δ_{CP} is maximal. To observe CPV at 5σ an exposure of ∼350 kt-MW-years will be needed if δ_{CP} is maximal, of ∼700 kt-MW-years to cover 50% of possible values and ∼1000 kt-MW-years to cover 75%. Conversion of exposures to calendar years depends

upon the staging scenario, which is discussed in Sec. 3.7.

While the determination of the MO and the discovery of CPV in the leptonic sector will be the main goals of DUNE's oscillation program, the measurements of all the other parameters regulating the oscillation probability will also be a key focus. Particular importance will be given to the measurement of the mixing angles θ_{13} and θ_{23}. The θ_{13} mixing angle has been accurately measured in reactor experiments, which will provide constraint to the DUNE oscillation analysis in the early stages of the experiment. However, to reach the desired levels of systematics constraint, DUNE will have to perform a measurement of θ_{13} which is independent from and competitive with the reactor results. The measurement in DUNE will be done using a ν_e and $\bar{\nu}_e$ appearance channel, whereas in reactor experiments it is performed through $\bar{\nu}_e$ disappearance.

The measurement of $\sin^2\theta_{23}$ in DUNE will help disambiguate its value, potentially pointing to a previously unknown symmetry between the ν_2 and ν_3 mass eigenstates. Current world measurements are ambiguous on whether the values of θ_{23} lies in the lower octant ($< 45°$) or the higher octant ($> 45°$) and allow for the maximal value $\sin^2\theta_{23} = 0.5$ [106]. This would implicate that the ν_τ flavour eigenstate receives equal contributions from the mass eigenstates ν_2 and ν_3, which would point towards a previously unknown symmetry.

Fig. 3.21 shows the two-dimensional 90% C.L. regions in $\sin^2 2\theta_{13} - \delta_{\mathrm{CP}}$ and $\sin^2 2\theta_{13} - \Delta m^2_{32}$ planes for three different levels of exposure, with equal running in neutrino and antineutrino mode, with the Phase II ND. The 90% C.L. region for the NuFIT global fit is shown in yellow for comparison. At large exposures DUNE is capable of determining both δ_{CP} and $\sin^2\theta_{13}$, with the precision on $\sin^2\theta_{13}$ similar to the current world average dominated by reactor neutrino experiments. DUNE will also have significant sensitivity to the θ_{23} octant for values of $\sin^2\theta_{23}$ less than about 0.47 and greater than about 0.55.

Overall, obtaining measurements of all the oscillation parameters within a single wide-band oscillation experiment has great value, because it provides a clear analysis of the neutrino oscillation pattern allowing for a detailed test of the three

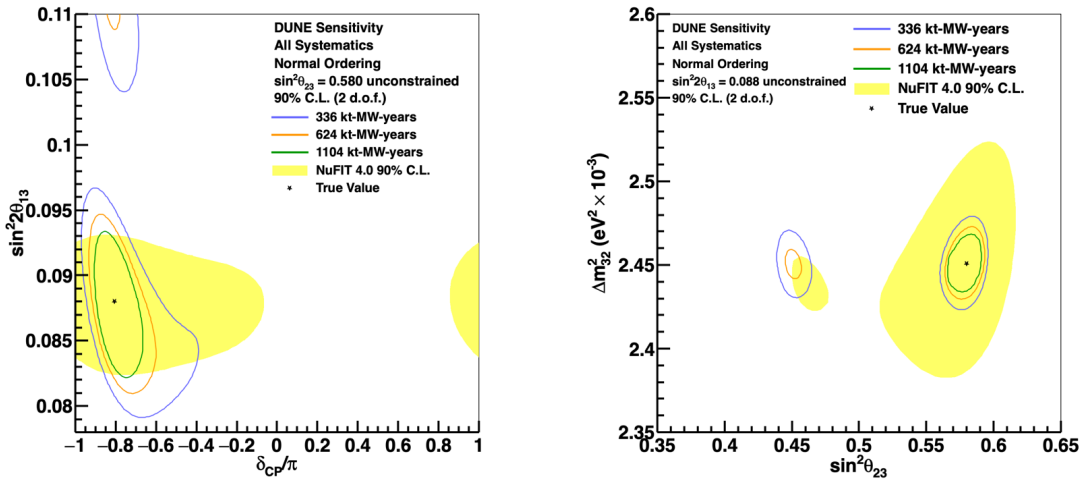

Figure 3.21: Two-dimensional 90% C.L. regions in $\sin^2 2\theta_{13} - \delta_{\mathrm{CP}}$ (Left) and $\sin^2 2\theta_{13} - \Delta m^2_{32}$ (Right) planes for three different levels of exposure, with equal running in neutrino and antineutrino mode, with the Phase II ND. The 90% C.L. region for the NuFIT global fit is shown in yellow for comparison. The true values of the oscillation parameters are assumed to be the central values of the NuFit global fit and the oscillation parameters governing long-baseline oscillation are unconstrained [81].

flavour neutrino model. Additionally, precise measurements of the PMNS mixing values, allow for comparison with mixing patterns in other areas of the standard model such as quarks. The question of why the quark mixing angles are smaller than the lepton mixing angles remains unanswered and constitutes an important part of the flavour pattern question [107].

3.5.2 Nucleon decay

Many BSM theories propose the unification of the strong, electromagnetic and weak interactions. These grand unified theories (GUTs) extend the standard model introducing a unified gauge symmetry at very high energies ($> 10^{15}$ GeV) [108]. One of the experimentally verifiable predictions that GUTs have in common is nucleon decay [109]. The dominant modes for proton decays predicted by GUTs are $p \to K^+ + \bar{\nu}$ and $p \to e^+ + \pi^0$. The first and second mode are dominant in supersymmetric and non-supersymmetric GUTs respectively. While no evidence of supersymmetry has been found at the electroweak scale, despite extensive efforts

at the large hadron collider (LHC), the main appeal of GUTs, which consists in gauge-coupling unification, remains intact.

Many experiments have performed searches of nucleon decay, imposing lifetime limits which already constrain the viability of several GUT models. Currently the best limits on most nucleon decay modes are set by the Super Kamiokande experiment, which features the largest mass and exposure time (more than 30 years) of any detector to date [110–112]. The lifetime τ limits on the two most important decay channels are:

$$\tau(p \to e^+\pi^0) > 1.4 \times 10^{34} \text{ yrs}, \qquad \tau(p \to \bar{\nu}K^+) > 5.9 \times 10^{33} \text{ yrs} \tag{3.3}$$

Extending the lifetime limits will require detectors to feature long exposure times combined with either large sensitive masses or improved detection efficiency or background rejection. The FD LArTPCs feature all these characteristics. Their excellent imaging, calorimetric and particle identification capabilities, combined with their large liquid argon mass, make them ideal detectors for a nucleon decay search.

The LArTPC technology is particularly well suited for the $p \to K^+ + \bar{\nu}$ or any decay mode that involves charged kaons, because it allows one to observe the entire decay chain. In a water Cherenkov detector such as Super Kamiokande the kaons emerging from these decay modes are usually below threshold, but in a LArTPC they can be identified both by their distinctive dE/dx as well as their decay. Therefore, this mode can be tagged in a LArTPC by looking for single kaons within a suitable energy range, with their point of origin lying within the fiducial volume, followed by its decay products. The background induced by cosmic ray muons can be contained imposing fiducial volume cuts and stringent kaon identification requirements. The dominant background is produced by atmospheric neutrino CC interactions where a muon and a recoiling proton are produced. In this case the proton can be misreconstructed as a positive kaon and the primary vertex for neutrino interaction can be mislabelled as a secondary vertex where the kaon decays.

The DUNE FD will not limit its search to a single mode or a few dominant channels, but it will feature a broad program covering many decays. These efforts are made all the more interesting by the fact that during the DUNE lifetime, two other large detectors, Hyper-Kamiokande [113] and JUNO [114] are set to perform searches for nucleon decays. If any of the experiments were to observe a signal, having confirmation from other experiments using drastically different detector technologies and thus different backgrounds would be very powerful.

3.5.3 Atmospheric neutrinos

Atmospheric neutrinos offer a complementary sample which includes all neutrino and antineutrino flavours and a wide range of L/E. This will allow for a measurement of all oscillation parameters which is independent from the one performed with the neutrino beam. Furthermore, the atmospheric sample will be available at all times, even before the ND or the LBNF neutrino beam become operative, offering an ideal training ground for the development of reconstruction software, analysis methodologies, and calibrations at the FD.

The FD modules, thanks to their large mass and overburden, which protects them from the atmospheric muon sample, are well equipped to study the atmospheric neutrino sample. Additionally, atmospheric neutrinos produce event topologies which are highly overlapping with those produced by neutrinos from the beam. The only additional requirements that are needed to make the study of atmospheric neutrinos possible are a self trigger and a more stringent demand on the neutrino direction reconstruction. The LArTPC technology is well equipped to accommodate both, thanks to its scintillation fast timing properties and its photographic reconstruction capabilities.

The atmospheric sample is especially suited to determine the neutrino MO, both in the electron neutrino appearance as well as muon neutrino disappearance channels. This is due to the fact that the atmospheric neutrinos can travel through the entire Earth before reaching the detectors, and are thus much more impacted by the MSW matter effect. This makes the determination of the MO highly independent

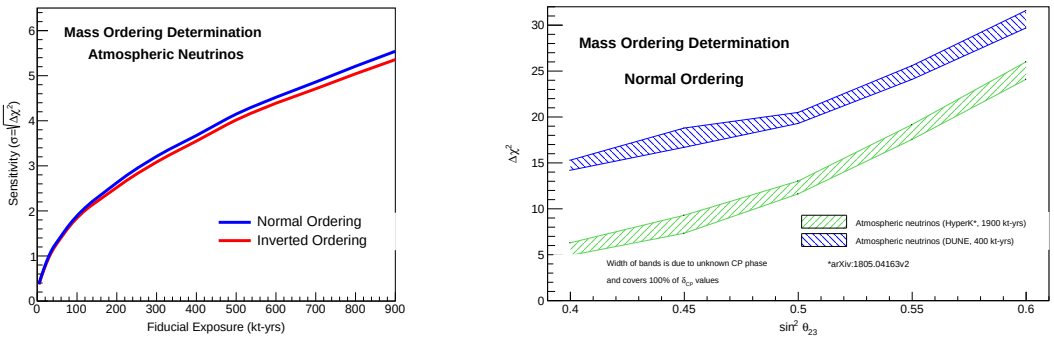

Figure 3.22: Sensitivity to mass ordering using atmospheric neutrinos as a function of fiducial exposure in DUNE (Left) and as a function of the true value of $\sin^2\theta_{23}$ (Right). For comparison, HyperKamiokande with a 1900 kt $\cdot$ yrs $\cdot$ exp sensitivities are also shown [89].

from the measurement of δ_{CP}. Fig. 3.22 shows the MO sensitivity as a function of the fiducial exposure and $\sin^2\theta_{23}$, with a comparison to HyperKamiokande. The sensitivity is proportional to the square root of the exposure [1, 115], indicating that the measurement is not systematics-limited. This is in stark contrast with the MO determination that can be achieved with the beam measurements, for which the control of the systematic uncertainties is the main limiting factor. The sensitivity also strongly depends on the true value of $\sin^2\theta_{23}$.

The sensitivity to MO using the atmospheric sample can be greatly improved if separation between neutrinos and antineutrinos can be achieved. This is not straight-forward in the DUNE FD modules, since they lack magnetization. However thanks to their high resolution imaging capabilities, particle/anti-particle statistical discrimination can be achieved through topological tagging, including proton tagging and decay electron tagging.

Many other important measurements can be made using atmospheric neutrinos at the DUNE FD. Studies have indicated that it could be possible to use a sample of sub-GeV atmospheric neutrinos to exclude some regions of δ_{CP} independently from the beam measurements [116]. Additionally, atmospheric neutrinos can act as a probe for many BSM scenarios, potentially allowing DUNE to place competitive limits on Lorentz and charge-parity-time symmetry (CPT) violation (similarly

to what has been done by the IceCube [117, 118] and Super-Kamiokande [119] collaborations) non-standard interactions [120] and sterile neutrinos [121].

3.5.4 Supernova neutrinos

A core-collapse supernova is an end of life event which occurs when all the nuclear fuel present in a massive star is consumed. In the late stages of such a star's life, as an effect of nucleogenesis and nuclear burning, its core assumes a concentric structure, with iron at the centre and progressively lighter elements moving outwards. Once temperatures of $T \sim 10^{10}$ K are reached, the iron core loses energy by neutrino emission through pair annihilation and plasmon decay. Simultaneously, the Fe nuclei are too heavy to be further burned for energy production, and thus the core contracts and heats up while also increasing its mass through additional nucleogenesis. Once the critical Chandrasekhar mass of 1.4 solar masses is reached, the pressure imposed by the external layers of the star can no longer be balanced and the star almost immediately collapses. The central core bounces and produces an initial shock wave. At the same time the iron core reaches nuclear levels of density storing most of the gravitational energy in the form of a degenerate Fermi sea of electrons and electron neutrinos. Eventually the trapped energy is released mostly in the form of $\sim 10^{58}$ ν_es with energies of ~ 10 MeV. The central object then settles to a neutron star or a black hole and the remaining energy is absorbed by beta reactions behind the shock wave that blasts away the rest of the star, resulting in the supernova explosion.

As the majority of the energy in a supernova core-collapse is released through the expulsion of ν_es in its early stages, neutrinos represent an essential probe in the study of these phenomena. This was proven when electron antineutrinos from the SN 1987a core collapse were detected via Cherenkov and scintillation detectors [122, 123]. While the amount of statics gathered during this event was sparse, the observations provided a qualitative validation of the basic physical structure of the supernova collapse phenomenon. The current generation of detectors will make a high statistics observation of a nearby supernova possible, with sensitivity to

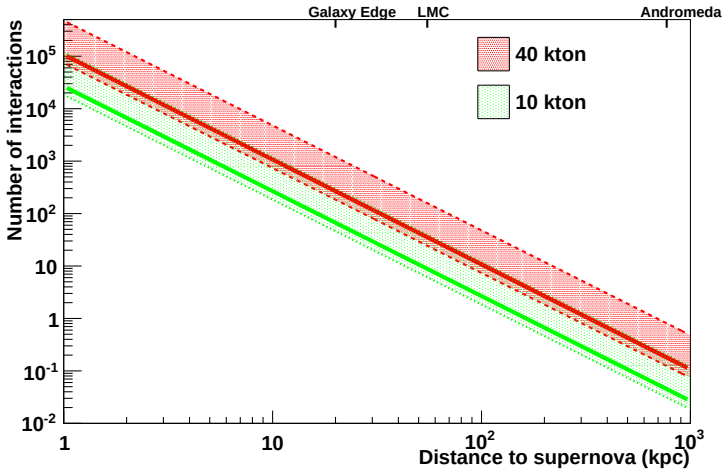

Figure 3.23: Estimated numbers of supernova neutrino interactions in DUNE as a function of distance to the supernova, for different detector masses (ν_e events dominate). The red dashed lines represent expected events for a 40-kton detector and the green dotted lines represent expected events for a 10-kton detector [103].

different flavour components of the flux. This is particularly important because the different phases of the core-collapse neutrino production are expected to produce distinct neutrino flavour and energy spectra, the evolution of which can be studied to shed light on the supernova process and the nature of neutrinos themselves.

The DUNE FD will be sensitive to supernova neutrinos with energies from tens of MeVs to 5 MeV. The estimated numbers of supernova neutrino interactions in the DUNE FD modules as a function of distance to the supernova, for different detector masses, are shown in Fig. 3.23. The FD LArTPCs are particularly sensitive to the ν_e component of the supernova burst through the CC absorption channel $\nu_e + {}^{40}Ar \rightarrow e^- + {}^{40}K^*$, where the ${}^{40}K^*$ represents a potassium nucleus in an excited state. The exiting electron combined with the de-excitation products of the ${}^{40}K^*$ nucleus provide a particularly clean signature which is not available to other neutrino detector technologies. Other electron flavour channels available to the FD include $\bar{\nu}_e$ CC interactions and elastic electron scattering. Additionally it is possible that other core-collapse neutrino flavours will be accessible through NC interactions such as $\nu + {}^{40}Ar \rightarrow \nu + {}^{40}Ar^*$ where the products of the de-excitation of the argon nucleus can be used for tagging. This possibility is however yet to be investigated.

3.5.5 Beyond the standard model physics

The combination of the high intensity wide-band LBNF neutrino beam with a highly capable ND and a massive LArTPC FD make DUNE an ideal experiment for many searches of new physics. In this sub-section we summarize some of the key searches that have already been proposed and in some cases investigated by the DUNE collaboration.

An important field of study in neutrino physics, consists in exploring the possibility of extending the standard three flavour paradigm. Experimental results exist which are in tension with the SM and can be interpreted as mixing between the currently known neutrino flavours and one or more sterile states [124, 125]. These results have produced a wide field of searches for sterile neutrinos through many different experiments and methodologies. DUNE will be able to search for a wide range of sterile neutrino masses by looking for missing NC and CC interactions both at the FD and ND. Additionally, anomalies pointing towards the expansion of the three flavour paradigm in the standard model could be found by measuring deviations from the unitarity of the PMNS matrix, something that can be done by DUNE by measuring the oscillation parameters at unprecedented levels of precision. These deviations would be particularly sizeable if the masses of the extra states are relatively small.

If the DUNE data is consistent with the three flavour hypothesis, non-standard interactions (NSIs) could still affect the propagation of neutrinos through the Earth [126]. Thanks to its very long baseline and wide-band beam, DUNE could be sensitive to these anomalies if the parameters that regulate the new physics are large enough. One of the ways in which DUNE will investigate the existence of NSIs, is through the measurement of neutrino-induced di-lepton production in the Coulomb field of a heavy nucleus, also known as neutrino trident interactions [127]. This channel, while extremely rare, is a particularly sensitive probe into the existence of new gauge symmetries beyond the SM. Thanks to the high intensity of the LBNF beam a relatively large amount of these interactions are expected at the ND ($\sim$ 100

trident interactions per year), making DUNE capable of measuring deviations from the SM rates and test the presence of new gauge symmetries.

The characteristics of the DUNE experiment also make it particularly well positioned to test various models of light dark matter (LDM). The existence of dark matter is very strongly supported by many cosmological and astrophysical observations, however no direct detection of weakly interactive massive particles has been done so far [128]. It has been proposed that if the DM is much lighter than the electroweak scale, then DM candidates could exist that interact with regular matter through a "vector portal" mediator [129]. It has been shown that high flux neutrino beam experiments such as DUNE could be sensitive to such DM candidates [130], whereas collider experiments such as the LHC are not. Another important category of dark matter that could be accessible to DUNE though its large LArTPC FD, is boosted dark matter (BDM) [131]. Many models exist that contain both a heavy and light DM component, in which the lighter one can be produced from the annihilation of the heavier one in environments with high DM concentrations such as the Sun or galactic centres. Due to the large mass difference between the two DM components, the lighter one is produced with a relativistic boost, making it energetic enough to be detected by the DUNE FD in a wide range of parameter space.

3.6 Near detector physics

The design of the DUNE ND is completely informed by the necessities of the experiment's oscillation measurement program. The ND will serve as the experiment's control: it will establish the reference unoscillated event rate spectra, measure and monitor the beam, constrain systematic uncertainties and provide essential input to interaction models.

The oscillation measurement directly depends on the neutrino spectra that are established at the ND. Only using these measurements it is possible to predict the unoscillated neutrino energy spectra at the FD and obtain a measurement of the oscillation parameters through a fit. The picture is complicated by the fact that the

reconstructed neutrino spectrum at the FD is an unresolved convolution of cross section, flux, and energy response. The ND must independently constrain all of these components and provide information which can improve the precision of the models. For this reason the ND must significantly outperform the FD: multiple methods to determine neutrino fluxes with differing dependencies on the cross-sections need to be available, and the cross sections need to be measured to a high degree of precision. Additionally the ND needs to be capable of measuring events in a similar way to the FD, mitigate environmental differences and confidently predict the FD event rates, while also operating in a much higher rate environment. The ND is designed to achieve all these scientific goals while also providing its own independent program of BSM and SM physics.

3.6.1 Flux measurements

In order to understand the importance of the ND in achieving the DUNE scientific program it is useful to illustrate how the oscillation measurement is made. The oscillation probability cannot be measured directly, so its determination relies on a measurement of the neutrino interaction rate for different neutrino flavours as a function of the reconstructed neutrino energy. At the FD this measurement can be formalized as [1]:

$$\frac{dN_x^{\mathrm{FD}}}{dE_{\mathrm{rec}}}(E_{\mathrm{rec}}) = \int \Phi_{\nu_\mu}^{\mathrm{FD}}(E_\nu) P_{\nu_\mu \to x}(E_\nu) \sigma_x^{Ar}(E_\nu) T_x^{\mathrm{FD},Ar}(E_\nu, E_{\mathrm{rec}}) dE_\nu \qquad (3.4)$$

where E_{rec} is the reconstructed neutrino energy, $\Phi_{\nu_\mu}^{\mathrm{FD}}$ is the unoscillated muon neutrino flux at the FD, E_ν is the true neutrino energy, $P_{\nu_\mu \to x(E_\nu)}$ is the oscillation probability from ν_μ to $x = \nu_e, \nu_\mu$ and $T_x^{\mathrm{FD},Ar}(E_\nu, E_{\mathrm{rec}})$ is the true to reconstruction response function. It is clear from this, that in order to extract a measurement of the oscillation probability, one needs to deconvolve and constrain the systematics related to the beam flux, the neutrino cross sections and the detector response. The main role of the ND is to do this in the most comprehensive way possible.

The FD unoscillated neutrino flux cannot be well constrained directly, however, the near-to-far flux ratio can be, by using existing hadron production data and

knowledge of the beamline's optics. The FD flux can then be understood as:

$$\Phi_{\nu_\mu}^{\mathrm{FD,estimate}}(E_\nu) = \Phi_{\nu_\mu}^{\mathrm{ND,measured}}(E_\nu) \times R^{\mathrm{MC}}(E_\nu) \tag{3.5}$$

where $\Phi^{\mathrm{ND,measured}}$ is the unoscillated muon neutrino flux measured at the ND, and $R^{\mathrm{MC}} = \Phi_{\nu_\mu}^{\mathrm{FD,MC}}(E_\nu)/\Phi_{\nu_\mu}^{\mathrm{ND,MC}}(E_\nu)$ is the near-to-far ratio obtained from Monte Carlo simulation.

The spectral composition of the neutrino flux needs to be constantly monitored in order to detect changes in the beam that might be caused by a malfunction in the LBNF beamline. This role will be fulfilled by the SAND detector.

Measuring the flux in the beam at the ND is not sufficient. In order to make a prediction on $R(E_\nu)$ the flux has to be predicted at different locations, including those where measurements cannot be made directly. A comprehensive model of the neutrino beam needs to be produced in order to do that. A beam model needs to incorporate all the elements of the neutrino beam production from the proton beam, to the target geometry, the prediction for the hadron production from the target, geometries and electromagnetic structure of the focusing system, geometry of the decay and beam dump regions, and a model for the decay of the hadrons produced from the target. The flux prediction output produced by the beam model is greatly affected by systematic uncertainties connected to each element. An extremely powerful way to reduce these systematics is to tune the model's outputs to agree with the neutrino event spectrum as measured at the ND. The prediction for $\Phi_{\nu_\mu}^{\mathrm{FD,estimate}}$ then becomes a combination of direct measurement and beam modelling. It is important to note that since it is based on the events observed in the ND, this tuning involves aspects of the beam model, cross section model, and the detector response model.

An additional strategy that is used by the DUNE ND to reduce the model dependence in the unoscillated FD flux prediction is the PRISM program, which was briefly described in Sec. 3.2. This technique involves making a linear combination of predicted ND fluxes to mimic the expected oscillated FD flux. The effect of this procedure is to effectively remove the spectral differences between the analysed

beam at the near and the far detectors. This extends the benefits of tuning the beam models to ND measurements to the whole spectrum covered by the FD.

The extraction of the incident neutrino flux from the ND data can be done through a combination of different measurements and techniques. One of the key flux measurements that is performed early in the life of any accelerator experiment due the high statistics available, is a reconstruction of the neutrino event spectrum from the inclusive ν_μ CC. The weakness of this method consists of the fact that the measured event rate convolves flux, cross section, beam, and detector effects. However, the sample itself can be used to constrain the parameters in the flux along with the beam and cross section model. Additionally, if the detector response of the ND and FD are comparable the uncertainty stemming from detector effects can be minimized and an event rate prediction at the FD can be made directly. This has been demonstrated by the NOνA experiment [132] and will be applicable to DUNE thanks to the ND-LAr detector.

A cleaner characterization of the flux can be obtained using neutrino-electron scattering events $\nu_x e \to \nu_x e$. These are pure electro-weak processes for which the cross section is calculable at tree level. The measurement sample is dominated by ν_μ NC interactions but also includes ν_e NC and CC interactions. The signal is then effectively independent of nuclear effects and cross-section uncertainties. The final state electron is kinematically constrained as:

$$1 - \cos\theta = \frac{m_e(1-y)}{E_e} \tag{3.6}$$

where θ is the angle between the exiting electron and the incoming neutrino, m_e and E_e are the electron mass and energy, and y is the fraction of the neutrino energy transferred to the electron. For DUNE energies $E_e \gg m_e$ and θ is small which implies $E_e\theta^2 < 2m_e$. These kinematic constraints make the background rejection relatively simple, with the main one composed of ν_e CC nuclear interactions, for which the energy transfer and $E_e\theta^2$ happen to be small. The main caveat of this technique consists in the limited statistical availability of neutrino-electron scattering events when compared to the much more prevalent neutrino interactions

on nuclei. With the DUNE flux however, roughly 100 events per year per ton of fiducial mass are expected at the ND. This implies that both SAND and ND-LAr are expected to accumulate thousands of events per year.

It is possible through careful sample selection to perform flux measurements that are mostly energy and/or nuclear effect independent. One sample that provides energy independent flux determination is the inclusive neutrino CC scattering channel in the limit that the energy transfer to the nucleus is very low (e.g. less that a few 100 MeV) [133]. In this limit, the event rate is proportional to the flux, and by measuring the rate as a function of energy, one can derive the flux "shape". Another strategy that allows for nuclear effect free and energy independent measurements is to use a sample of neutrino interactions on hydrogen. Studies have been done looking into the possibility of isolating such a sample using transverse kinematic imbalance (TKI) from materials containing a variety of nuclear targets. For a more in depth discussion of this topic see Chapter 6 where such a study is performed for the ND-GAr detector.

An irreducible background for any flux measurement and consequently any oscillation measurement, consists of unoscillated ν_es that are produced in the beam through kaon and muon decay. The LBNF has been designed to minimize the presence of ν_es and maximize the ν_μ flux. However a small portion of ν_e which varies between 0.5% to 1.2% depending on the energy is still expected. The systematic uncertainty on the beam ν_e flux is expected to be non-negligible but subdominant.

3.6.2 Cross section measurements

The measured event rates at the FD arise from a convolution of flux, cross sections and detector effects. An important source of uncertainties comes from the limited quality of neutrino interaction models at the energy ranges and with the heavy nuclear targets (e.g. argon) that interest DUNE. While previous cross section measurements on different nuclei from experiments such as MINERνA and Argoneut exist and additional ones are expected to come from the SBN program at Fermilab, none are sufficient to reach the level of precision required by DUNE

[2]. A comprehensive program of cross section measurement at the DUNE ND will be needed to mitigate this issue.

A major source of cross section related uncertainty comes from the fact that the ND and FD neutrino spectra are expected to be quite different. As already discussed, the PRISM program is expected to mitigate this issue by allowing to effectively construct the FD spectrum from a combination of measured ND fluxes. However, the spectral matching in the PRISM analysis will not be perfect and significant cross section model dependent uncertainties will remain. Additionally, the fact that DUNE plans to use argon as its main interaction target further complicates the picture. Neutrino scatters on such a heavy nucleus will inevitably be heavily affected by nuclear effects. An extensive program of studies is needed at the ND to constrain and mitigate the impact of nuclear effects in the oscillation analysis.

In the DUNE energy range many types of neutrino interactions are important (see Sec. 2.3). Charge current quasi elastic interactions (CCQE) are crucial to any oscillation experiment due to the simplicity of the final state. Most available models, however, have relied on measurements of neutrino interaction on deuterium, which are unaffected by multi-nucleon effects. This lack of knowledge induces large systematic uncertainties for heavier nuclear environments such as argon.

Multi-pion productions in resonant (RES) interactions, are thought to have only a small effect in the determination of the cross section. This assumption, however, has not been tested in the energy ranges relevant to DUNE. Additionally it is known that current available models for charged pion production are in disagreement with the available data from several important experiments such as MINERνA [134], MiniBooNE [135] and T2K [136] and no tests for RES model on nuclei $A > 20$ exist. Nuclear effects further add to the complexity as pion absorption through FSI can mask RES events as CCQE.

Improving our understanding of RES cross sections will be crucial for DUNE's scientific program, since they constitute a $\sim 40\%$ of the total interactions that are expected to be seen by the experiment. The DUNE ND will be capable of effectively study RES pion production, thanks to its technological capabilities, high statistics

and wide energy range. In particular ND-LAr will measure well the hadronic component of neutrino interactions with good liquid argon TPC resolution and will use the information provided by ND-GAr to reconstruct the muon kinematics. ND-GAr, on the other hand, will be able to measure charged particles with a very low energy threshold and unmatched PID.

The energy region where soft inelastic scattering (SIS) is relevant, as well as the transition regions between RES and SIS and SIS and deep inelastic scattering (DIS), are particularly problematic. As current model struggle to include these types of interactions effectively, the experimental input that the ND will be able to provide, will be essential for DUNE's precision goals to be achieved.

Finally, coherent pion production is also an important sector of study for the DUNE ND. While this interaction type is relatively uncommon compared to scattering from nucleons, and is relevant only at the lower end of the DUNE energy range, its ability to mimic the interactions used to measure ν_μ disappearance and ν_e appearance means that it is important to evaluate this background. While some models of coherent neutrino scattering have been implemented in MC generators, the only measurements of coherent pion production in the DUNE energy range, which were made in MINERνA, show disagreements with the predictions [137].

3.6.3 BSM physics at the ND

Thanks to its highly capable suite of detectors, in combination with the high intensity of the LBNF beam and its short-baseline the DUNE ND will be a powerful laboratory for the study of many BSM topics. Thanks to the combination of the ND-LAr and ND-GAr detectors the DUNE-ND will be able to achieve excellent momentum resolution and charge separation for tracks produced in the ND-LAr active volume that traverse the ND-GAr tracker region. The lower density the ND-GAr HPgTPC should also give access to BSM signatures that wouldn't be available in liquid argon. The ability of ND-LAr and ND-GAr to move off axis for the PRISM program will also be useful in BSM searches as it will allow to reduce the intensity of the neutrino interaction background.

Some of these BSM topics, including light dark matter, neutrino tridents and non standard interactions have already been mentioned in Sec. 3.5.5. Additionally, the DUNE ND can be used to search for topologies arising from a variety of very-weakly interacting long-lived particles such as heavy neutral leptons (HNL). Many models predict that HNLs could be produced in the decay of charmed mesons, which are expected to be generated in significant amounts in the high intensity LBNF beam. The only accessible HNLs will be the ones that are the lightest particles in their hidden sector, and thus will decay into SM particles. Due to the expected small mixing angles, the particles can be stable enough to travel from the LBNF target to the ND and decay inside the active fiducial region of the detector. Other very-weakly interacting particles that are accessible to the DUNE ND include sterile neutrinos. In particular these could be searched for by looking into short-baseline oscillation anomalies in the L/E range of 0.01 to 1 eV^2. These searches would be motivated by previous experimental results that show tension with the three-neutrino-flavour paradigm such as the LSND anomaly. Measurements of short-baseline neutrino oscillations could also be used as a probe into large extra dimension theories, in which right-handed sterile neutrinos are expected to exist.

3.6.4 Additional standard model opportunities

The combination of the high intensity LBNF beam and the highly capable DUNE ND enable a variety of SM physics measurements that go beyond the cross section measurements discussed in Sec. 3.6.2.

A particularly precise measurement of the electroweak mixing angle $\sin^2\theta$ could be made using neutrino-nucleon scattering and neutrino-electron scattering. The latter measurement is particularly advantageous as it is not affected by the theoretical uncertainties arising from the modelling of the nucleus structure. These uncertainties are the main limiting factor in the precision of current state-of-the-art measurements performed on DIS cross sections. The DUNE ND is particularly well positioned to perform such a measurement thanks to the combination of the

relatively high statistics available in ND-LAr and the constrain of systematics achievable through the use of ND-GAr's and SAND's light trackers.

The proton decay search at the FD (see Sec. 3.5.2) can be aided by measurements performed at the ND. The proton decay mode $p \to K^+\bar{\nu}$ is heavily impacted by a background of K^+ produced by atmospheric neutrinos. The DUNE ND will be able to measure the production of K^+ and K^0 by beam neutrinos and place constraints on the proton decay background.

3.7 DUNE staging

Parameter	Phase I	Phase II	Impact
FD mass	2 FD modules (20 kt fiducial)	4 FD modules (40 kt fiducial LAr equivalent)	FD statistics
Beam power	1.2 MW	Up to 2.3 MW	FD statistics
ND configuration	ND-LAr+TMS, SAND	ND-LAr, ND-GAr, SAND	Systematics

Table 3.1: A high-level description of the two-phased approach to DUNE. The ND-LAr detector, including its capability to move sideways (PRISM), and the SAND are present in both phases of the ND [138].

As discussed throughout this chapter, budgetary constraints will require the DUNE experiment to pursue its physics program in two distinct phases. The overall configurations of the experiment in Phases I and II are summarized in Tab. 3.1.

DUNE Phase I is expected to begin taking physics data with the FD in the late 2020s, with the beam and ND becoming operational by 2032 [81, 138]. The average beam power during the first year of beam operation will be 1.2 MW, increasing to 1.6 MW in the second year. Further optimizations are planned in subsequent years, with the beam power reaching 2.3 MW after approximately 15 years.

Regarding the fiducial mass of the FD, the experiment will operate with two FD modules (providing a total fiducial mass of 20 kt) during the first three years. The third and fourth modules (FD3 and FD4) are expected to become fully operational in years 4 and 6, respectively, ultimately providing a nominal fiducial mass of 40 kt.

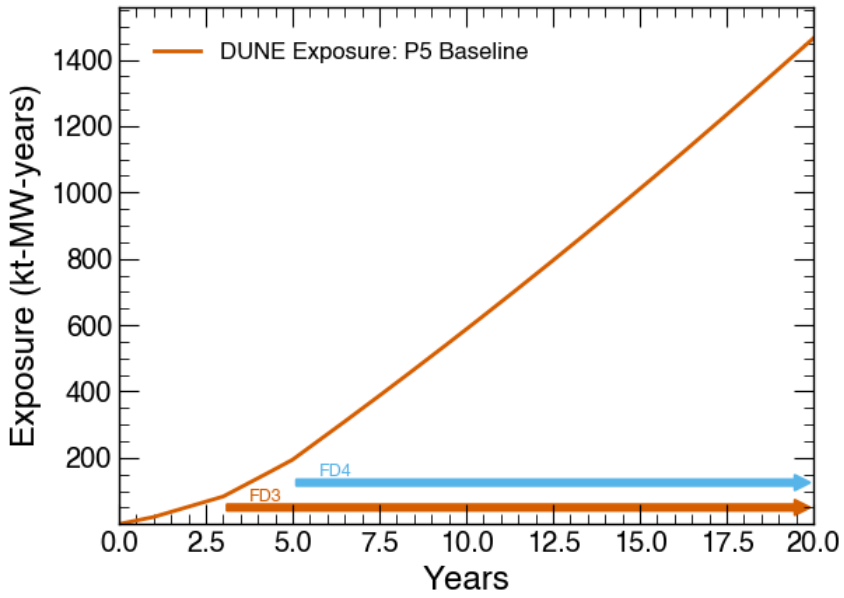

Figure 3.24: DUNE integrated exposure, in kt · MW · yr units, as a function of time [138].

The accumulated exposure, expressed in kt·MW·yr, as a function of time under this staged deployment scenario is shown in Fig. 3.24. Systematic constraints derived from the Phase I ND will apply through year 6, after which they will be gradually superseded by improved constraints from the Phase II ND, starting in year 7. These improved constraints, as they evolve over approximately two years, will retroactively be applied to all previously collected FD data.

During Phase I, DUNE is expected to collect approximately 100 kt · MW · yr of data over 5 years of operation. This corresponds to approximately 400 ν_e and 150 $\bar{\nu}e$ candidates in the FD, depending on the oscillation parameters and assuming equal running time in neutrino and antineutrino mode.

Although these data sets will remain statistically limited, once systematic constraints from the Phase I ND are applied, they will be sufficient to determine the neutrino MO with a significance exceeding 5σ, independent of the true values of the oscillation parameters, as shown in the left panel of Fig. 3.25a. If CPV is close to maximal (δCP $\simeq \pm\pi/2$), DUNE will also be able to establish CPV at the 3σ level during Phase I (see right panel of Fig. 3.25). In addition, DUNE

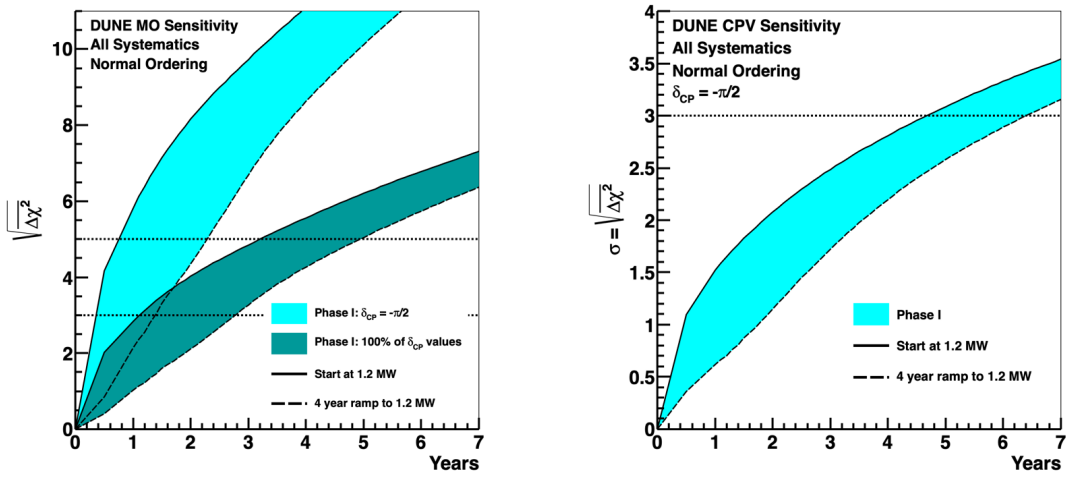

Figure 3.25: Sensitivity to the neutrino mass ordering (left) and CP violation for $\delta_{\mathrm{CP}} = -\pi/2$ (right) in Phase I. The cyan bands show the sensitivity if $\delta_{\mathrm{CP}} = -\pi/2$ and the green band in the left plot shows the sensitivity for 100% of δ_{CP} values. The width of the bands shows the impact of potential beam power ramp up; the solid upper curve is the sensitivity if data collection begins with 1.2 MW beam power and the lower dashed curve shows a conservative beam ramp scenario where the full power is achieved after 4 years.[81].

will provide improved measurements of the disappearance parameters Δm^2_{32} and $\sin^2 2\theta_{23}$ compared to current uncertainties. However, the statistical precision of Phase I data will be insufficient to resolve the θ_{23} octant or to establish CPV, except in the most favourable scenarios.

Achieving the oscillation physics program foreseen for the DUNE experiment (see Sec. 3.5.1) will require an exposure of 600 to 1000 kt·MW·yr, depending on the specific measurement. This exposure can be reached by operating the experiment for $6-10$ additional calendar years with a beam power exceeding 2 MW and a FD with a fiducial mass equivalent to 40 kt of liquid argon, provided that the systematic uncertainties can be controlled at the level enabled by the Phase II ND. In the absence of the increased FD mass and beam power, achieving the same exposure would require $24-40$ years of operation.

The sensitivity of DUNE to establish CPV as a function of time is shown in Fig. 3.26. With the full Phase II exposure of 1000 kt $\cdot$ MW $\cdot$ yr, DUNE will be able

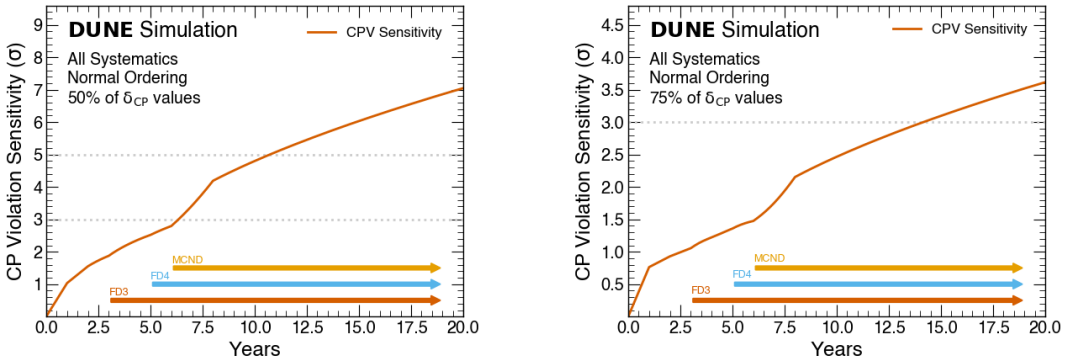

Figure 3.26: The significance for DUNE to establish CPV for 50% (Left) and 75% (Right) of CP values as a function of running time.[138].

to establish CPV at the 3σ level for 75% of possible values of δ_{CP}, and determine its value with a precision between 6° and 16°, depending on the true value of δ_{CP}.

4

Kalman filter reconstruction for ND-GAr-Lite

Contents

4.1 Introduction

ND-GAr-Lite was a proposed muon spectrometer for the DUNE ND complex, to be used during Phase-I of the experiment. As described in Sec. 3.4.2 the key design principle behind the detector was to include the structural components of ND-GAr, but to exclude the active detector elements: the gas TPC and the ECAL. In their place a simple tracker composed of segmented tracking planes would be

built. Significant effort was dedicated to this design by the ND-GAr group, which was able to produce official geometries for the detector, and code which allowed to fully simulate the passage of particles through it, down to the signal formation, track finding and reconstruction.

A relatively well developed simulation and reconstruction chain for ND-GAr-Lite, was available at the time of the writing of this thesis. However, several aspects of the track reconstruction algorithm were known not to be at a state-of-the-art level. No treatment of energy loss or multiple scattering was put in place and no estimate of the uncertainties from the measurement was produced by the algorithm.

As a key part of this thesis project, a collaboration with experts from the ALICE experiment tracking group was established, to produce a Kalman filter (KF) based on the one used for the ALICE TPC (see Chapter 5 for a full description). This new algorithm was set to improve on the existing one and fit the needs of both the new geometry of the ALICE detector as well as ND-GAr. In this context, an additional goal of this thesis project became to produce a similar algorithm, also based on the pre-existing ALICE KF, that could be applied to ND-GAr-Lite's tracker.

The first step in the development of the algorithm, consisted in creating a simple toy Monte Carlo (MC) simulation which allowed for a high degree of control over many aspects of particle propagation and signal formation. This was achieved by developing many aspects of the simulation modularly and somewhat independently from one another. Most of the development stage in the algorithm's life consisted in producing different samples with this toy MC tool and then testing the performance of the algorithm and whether it conformed to expectations. Once the KF was thought to be at a good level of maturity, it was tested on the more complete simulation already available from the ND-GAr group.

This Chapter will be divided as follows: in Sec. 4.2 we give a brief overview of the KF technique as it applies to track fitting; in Sec. 4.3 we introduce the KF algorithm developed for ND-GAr-Lite; in Sec. 4.4 we give a full description of the simulation software developed by the ND-GAr group; in Sec. 4.5 we describe the toy Monte Carlo tool specifically developed for the testing of the KF; in Sec. 4.6

we present some selected results from the tests done using the toy Monte Carlo tool; in Sec. 4.7 we show the performance of the algorithm when applied to the more complete simulation developed by the ND-GAr group and we compare with the results obtained with the previously existing algorithm; in Sec. 4.8 we give a summary of the results.

4.2 The Kalman filter technique

In this section we offer a brief review of the KF technique, specifically in the context of track fitting [139, 140]. Track fitting consists in estimating track parameters; filtering consists in analysing (linear) dynamic systems, defined as any system in which a (linear) function can describe its time dependence in an ambient space. By viewing a track in space as a dynamic system, we can use filtering techniques for track fitting, including KFs. This can be achieved by uniquely describing the conditions of the particle with a number of parameters grouped into a true state vector, s^{true} (a function of a suitable coordinate, x_k, known as the free parameter) at each trajectory point k, $s^{\text{true}}(x_k) \equiv s_k^{\text{true}}$.

Assuming that the system is linear, the propagation of s_k^{true} can be described by a linear transformation, F_k. The propagation of the system can be corrupted by inherent processes, such as multiple scattering for a charged particle moving across a medium. This random disturbance can be encapsulated in a process noise vector, w_k, and can affect all or only some of the state vector variables. The propagation of the system can then be written as:

$$s_k^{\text{true}} = F_{k-1} s_{k-1}^{\text{true}} + w_{k-1}. \tag{4.1}$$

By using a detector we are able to measure some properties of the particle at specific intervals of x_k, where the trajectory and the detector intersect. We can encapsulate these properties in a measurement vector, m_k, which is a linear combination of the properties in s_k^{true}. If the detection process is affected by

noise, m_k will also be corrupted by a measurement noise vector, ϵ_k. The whole measurement operation can be written as :

$$m_k = H_k s_k^{\text{true}} + \epsilon_k, \tag{4.2}$$

where H_k is a linear transformation.

We assume that all components of w_k and ϵ_k are Gaussian distributed, unbiased, and uncorrelated. The expectation values and covariances for the k^{th} step are defined as:

$$\mathrm{E}\left[w_k\right] = \vec{0},\ \mathrm{Cov}\left[w_k\right] = Q_k, \tag{4.3}$$

$$\mathrm{E}\left[\epsilon_k\right] = \vec{0},\ \mathrm{Cov}\left[\epsilon_k\right] = R_k. \tag{4.4}$$

The KF is a iterative algorithm which produces an estimate, s_k, of the true state vector, s_k^{true}, at each trajectory point. It combines *a priori* knowledge of the system, condensed in the track propagator, F_k, and the measurement information from m_k to produce an optimized *a posteriori* estimate. In this sense the KF procedure can be said to be "Bayesian" in nature. The covariance matrix associated with the estimated state vector, s_k, is defined as:

$$\mathrm{Cov}\left[s_k\right] = C_k. \tag{4.5}$$

The KF procedure can be divided into discrete operational steps, that are applied iteratively:

1. Seeding: Produce an initial estimate for the state vector and covariance matrix, s_0 and C_0, respectively, using a certain technique.

2. Propagation: Produce an *a priori* estimate for the state vector and the covariance matrix, $\widetilde{s}_k$ and $\widetilde{C}_k$, respectively, at the next x_k ($k \geq 1$) step, using only the track propagator and no measurement knowledge:

$$\widetilde{s}_k = F_{k-1} s_{k-1}, \tag{4.6}$$

$$\widetilde{C}_k = F_{k-1} C_{k-1} F_{k-1}^T + Q_{k-1}, \tag{4.7}$$

where the process noise matrix Q_k is added as a correction to the covariance matrix and T stands for transpose. Note that no correction is added to $\widetilde{s}_k$ because the expectation value of w_k is is assumed to be null, as defined in Eq. 4.3.

3. Update: Produce an updated estimate for the state vector and the covariance matrix, s_k and C_k, respectively, using information from the current measurement:

$$s_k = \widetilde{s}_k + K_k \left(m_k - H_k \widetilde{s}_k \right), \tag{4.8}$$

$$C_k = \left(\mathbb{1} - K_k H_k \right) \widetilde{C}_k, \tag{4.9}$$

where K_k is the Kalman gain. The expression for K_k is:

$$K_k \equiv \widetilde{C}_k H_k^T \left(R_k + H_k \widetilde{C}_k H_k^T \right)^{-1}, \tag{4.10}$$

and is obtained by requiring that the covariance in Eq. 4.9 is minimized. To proceed to the next point, the algorithm is repeated from the propagation step, using the current updated estimate, s_k, as the input.

An illustration of the basic functioning of the KF algorithm is provided in Fig. 4.1. The machinery described so far, assumes that the evolution of the dynamic system is determined by linear transformations, however, the propagation of a charged particle in a magnetic field is non-linear. Equation 4.6 in this case takes the more general form:

$$\widetilde{s}_k = f_{k-1} \left(s_{k-1} \right), \tag{4.11}$$

where f_{k-1} is a non-linear function. In order to apply the KF technique, the track propagator in Eq. 4.7, F_{k-1}, has to be approximated by the Taylor expansion coefficient defined as follows:

$$f_{k-1} \left(s^* \right) \simeq f_{k-1} \left(s_{k-1} \right) + F_{k-1} \cdot \left(s^* - s_{k-1} \right), \tag{4.12}$$

$$F_{k-1} = \frac{\partial f_{k-1}}{\partial s^*}, \tag{4.13}$$

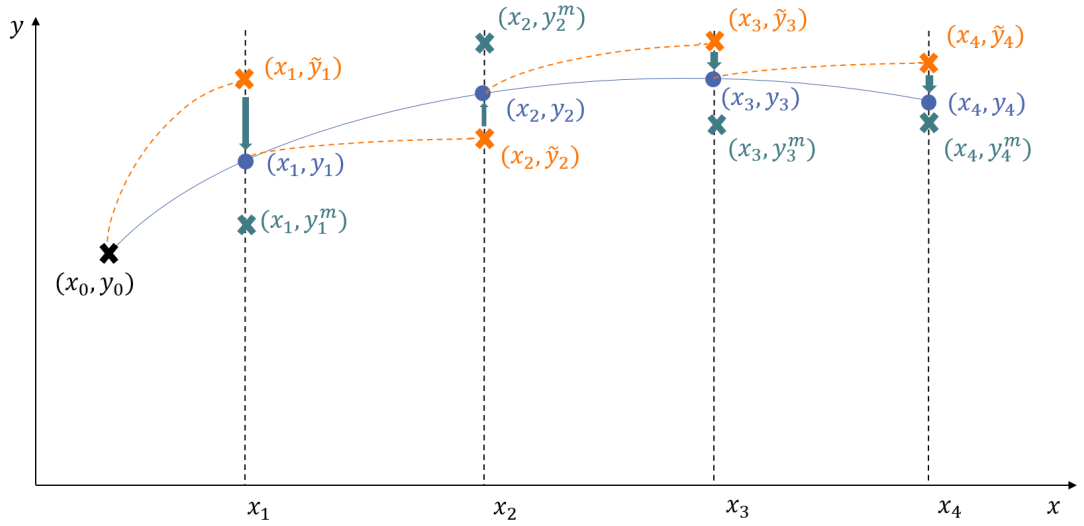

Figure 4.1: Schematic representation of a Kalman filter (KF): y represents one of the variables of the state vector s which is a function of the free parameter x. The coordinates of the free parameter x_k are taken at the points of intersection between the detector and the particle trajectory. Starting from the first estimate (x_0, y_0), which is obtained from a seeding algorithm, the KF produces an *a priori* estimate at the following point $(x_1, \tilde{y_1})$, shown in orange. The result is compared with the measurement (x_1, y_1^{m}) shown in green and the filtering step is applied, producing an updated estimate (x_1, y_1). The procedure is repeated until no more track points are available [141].

where s^* is a generic state vector coordinate near the point of expansion, s_{k-1}. All the other KF steps (Eqs. 4.9-4.10) remain identical to the linear procedure. This technique is known as extended KF.

4.3 The Kalman filter applied to ND-GAr-Lite

The KF developed for ND-GAr-Lite was largely based on the parametrisation utilized by the ALICE collaboration for their own TPC KF, which can be considered the state of the art in the field [142, 143]. This includes the definition of the state vector and of the evolution functions. The code produced to apply and test the custom KF, however, was largely produced as a custom tool to accommodate the peculiarities of ND-GAr-Lite's tracking system, which is a dis-homogenous detector, unlike the ALICE TPC. The KF algorithm developed for ND-GAr-Lite will be referred to as `KF-Lite`.

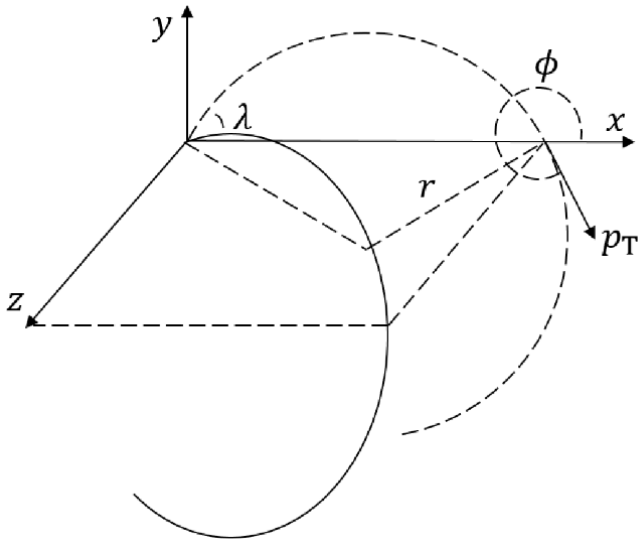

Figure 4.2: Diagram illustrating the definition of the coordinates defining the evolution of the custom KFs produced for ND-GAr-Lite as well as ND-GAr.

We assume that an ideal magnetic field is applied along the direction perpendicular to the neutrino beam, which is identified by the coordinate x. The z coordinate coincides with the direction of the magnetic field, while the y coordinate identifies the vertical direction. The spatial information in the zy plane is assumed to be given by the detector's tracking planes. The information regarding the x coordinate is given by the central position of the triangular scintillator bar in which the hit was formed.

The algorithm is evolved along the free parameter, x, and its state vector is defined as:

$$s(x) = (y, z, \sin\phi, \tan\lambda, q/p_{\mathrm{T}})\,, \tag{4.14}$$

where y is the vertical direction; z is the drift direction; ϕ is the azimuthal angle of the transverse momentum, i.e. the component of the momentum vector transverse to the drift direction; λ is the "dip angle" between the transverse momentum and the total momentum vector; q is the charge sign of the particle and p_{T} is the modulus of the transverse momentum. Note that the inverse transverse momentum can also be written in terms of track curvature $1/r$. The conversion is easily obtained

using the standard formula for charged particles moving in a magnetic field:

$$p_{\mathrm{T}}\ (\mathrm{GeV}/c) = 0.3\ B\,(\mathrm{T})\ r\,(\mathrm{m})\,. \tag{4.15}$$

A visual representation of the coordinates is given in Fig. 4.2.

The state vector is evolved along the trajectory using a propagator function, as described in Eq. 4.6:

$$\widetilde{s}_k = f_{k-1}(s_{k-1}) = \begin{cases} \widetilde{y}_k = y_{k-1} + \dfrac{\sin\phi_{k-1} + \sin\widetilde{\phi}_k}{\cos\phi_{k-1} + \cos\widetilde{\phi}_k}\Delta x_k, \\ \widetilde{z}_k = z_{k-1} + \left(\widetilde{\phi}_k - \phi_{k-1}\right)\dfrac{r}{q}_{k-1}\tan\lambda_{k-1}, \\ \sin\widetilde{\phi}_k = \sin\phi_{k-1} + \dfrac{q}{r}_{k-1}\Delta x_k, \\ \tan\widetilde{\lambda}_k = \tan\lambda_{k-1}, \\ \dfrac{\widetilde{q}}{p_{\mathrm{T}}}_k = \dfrac{q}{p_{\mathrm{T}}}_{k-1} \times \dfrac{p_{k-1}}{\Delta p_k + p_{k-1}}, \end{cases} \tag{4.16}$$

where Δx_k is the distance in the x direction between the previous and current points, p_k is the total momentum and Δp_k is the total momentum loss. In order to obtain the propagation matrix F_k analytically, one only needs to calculate the Taylor expansion coefficient $\partial f_k/\partial s_k$, as described in Eqs. 4.12 and 4.13, with the exception of the q/p_{T} term, which is treated separately.

In order to compute the momentum loss, Δp_k, at each trajectory point, the ionization energy loss, $-\mathrm{d}E/(\rho \mathrm{d}x)$ (where ρ is the density of the material in $\mathrm{g/cm^3}$), of the particle is evaluated using the standard Bethe-Bloch formula as defined in Eq. 2.76.

The differential energy loss, $-\mathrm{d}E/(\rho \mathrm{d}x)$, is calculated using the properties of the most abundant gas present in the gas mixture in standard conditions and then multiplied by the material's density to obtain a reasonable approximation of the $\mathrm{d}E/\mathrm{d}x$ [144]. The total momentum loss between two steps is then calculated by numerical integration [145].

In the evaluation of F_k, the q/p_{T} parameter is treated as if it were static (e.g. $\Delta p_k = 0$). A correction term, c_k is added to the q/p_{T} diagonal element of the

covariance matrix, $\widetilde{C}_k$, after the propagation step:

$$c_k = \left(a \cdot \frac{\Delta p_k}{p_{k-1}} \cdot \frac{q}{p_{\mathrm{T}\,k-1}} \right)^2 , \tag{4.17}$$

where $a = 3.162 \times 10^{-3}$ is a constant multiplicative factor which is directly taken from the ALICE TPC framework [146].

Multiple scattering is treated through the noise correction matrix, Q_k. At each step the scattering angle can be treated as emerging from a Gaussian distribution with a root mean square equal to the Molière angle θ_{M}, as defined in Eq. 2.81. The Q_k terms relative to $\sin\phi$, $\tan\lambda$ and q/p_{T} are evaluated through error propagation [147]. Let's consider two uncorrelated scattering angles (θ_1, θ_2), which are the projections of the 3D scattering angle θ_{space} defined in Eq. 2.80, on two perpendicular planes crossed by the particle along the momentum direction. Assuming that they follow a Gaussian distribution, their average value will correspond to the Molière angle θ_M defined in Eq. 2.81, with a corresponding covariance matrix:

$$V = \begin{bmatrix} \theta_M^2 & 0 \\ 0 & \theta_M^2 \end{bmatrix} . \tag{4.18}$$

We can then convert the scattering angles to cylindrical coordinates:

$$\begin{cases} \lambda = \theta_1, \\ \phi = \theta_2 / \cos\lambda. \end{cases} \tag{4.19}$$

Using error propagation as defined in Eq. 4.27, we can propagate to the state vector s_k:

$$\begin{aligned} Q_k &= \left(\frac{\partial s_k}{\partial(\theta_1, \theta_2)} \right) V \left(\frac{\partial s_k}{\partial(\theta_1, \theta_2)} \right)^T = \\ &= \left(\frac{\partial s_k}{\partial(\lambda, \phi)} \right) \left(\frac{\partial(\lambda, \phi)}{\partial(\theta_1, \theta_2)} \right) \begin{bmatrix} \theta_M^2 & 0 \\ 0 & \theta_M^2 \end{bmatrix} \left(\frac{\partial(\lambda, \phi)}{\partial(\theta_1, \theta_2)} \right)^T \left(\frac{\partial s_k}{\partial(\lambda, \phi)} \right)^T . \end{aligned} \tag{4.20}$$

Following the calculation one gets the matrix:

$$Q = \begin{bmatrix} 0 & 0 & 0 & 0 & 0 \\ 0 & 0 & 0 & 0 & 0 \\ 0 & 0 & \theta_{\mathrm{M}}^2 \cdot \frac{\cos^2\phi}{\cos^2\lambda} & 0 & 0 \\ 0 & 0 & 0 & \frac{\theta_{\mathrm{M}}^2}{\cos^4\lambda} & \frac{q}{p_{\mathrm{T}}} \cdot \theta_{\mathrm{M}}^2 \cdot \frac{\tan\lambda}{\cos\lambda} \\ 0 & 0 & 0 & \frac{q}{p_{\mathrm{T}}} \cdot \theta_{\mathrm{M}}^2 \cdot \frac{\tan\lambda}{\cos\lambda} & \left(\frac{q}{p_{\mathrm{T}}}\right)^2 \theta_{\mathrm{M}}^2 \tan^2\lambda \end{bmatrix} , \tag{4.21}$$

which is added to the covariance matrix $\widetilde{C}_k$ as described in Eq. 4.7.

Note that in the case of ND-GAr-Lite the material budget corrections are applied only between points that are inside the same tracking plane. When the `KF-Lite` needs to be moved between two consecutive points which lie in separate planes, the state vector is propagated in three separate steps: first the state vector is propagated to the edge of the first plane and the correspondent material budget corrections are applied; then it is propagated to the next plane applying no corrections, since the space between the planes is considered to be empty; finally the state vector is propagated to the following point and both the material budget corrections and the filtering step of the `KF-Lite` algorithm are applied.

Each step in the evolution of the `KF-Lite` can potentially fail, in which case the algorithm is stopped. This can happen mainly in two scenarios: $\sin\phi$ can be calculated to be out of range, i.e. $|\sin\phi| > (1 - 10^{-7})$, even if more measurement points exist (see Sec. 5.2), or the particle can lose all its remaining kinetic energy. Once the `KF-Lite` is stopped, the information for each of the reconstructed points is saved. Flags are used to preserve information on which of the reconstruction steps have been successful and which have failed.

4.3.1 Seeding algorithms

One of the limitations of the KF technique is that it requires an initial estimate to be externally provided, both for the state vector s_0 and the covariance matrix C_0. As mentioned in Sec. 4.2 this procedure is often referred to as "Seeding" and the initial estimates are referred to as the algorithm's "Seed". Two seeding methods have been tested for this work: the first is taken directly from the ALICE infrastructure, while the second coincides with the algorithm originally used by ND-GAr-Lite for its track reconstruction.

The seeding strategy originally used by the ALICE experiment consists in a simple three-point circle finding algorithm and will be referred to from now on simply as `Seed`. In the plane perpendicular to the magnetic field, the trajectory of a charged particle is a circle. Since only one circumference will pass through

any three points, one can find a point which is roughly at the start of the particle trajectory, one at the end and one in the middle and obtain the properties of the circle that passes though them. This equates to solving a system of three linear equations for three unknown variables: the coordinates of the centre of the circumference (x_C, y_C) and its radius r. After translating the coordinate system to the first of the three points (x_0, y_0) the equations can be written as:

$$\begin{cases} x_C^2 + y_C^2 = r^2, \\ (x_1 - x_C)^2 + (y_1 - y_C)^2 = r^2, \\ (x_2 - x_C)^2 + (y_2 - y_C)^2 = r^2, \end{cases} \tag{4.22}$$

where (x_C, y_C) and (x_n, y_n) are the translated centre of the circle and the three trajectory points respectively and r is the radius. From the circle properties (x_C, y_C) and r and the coordinates of the three points, one can find an estimate for the state vector s_0 at the starting point (x_0, y_0, z_0). Apart from y_0 and z_0 which are taken as the measured values the other elements are estimated as:

$$\begin{cases} 1/p_{\mathrm{T}} = 1/(0.3Br) \\ \sin\phi = x_C/r \\ \tan\lambda = z_1/\Delta xy \end{cases} \tag{4.23}$$

where Δxy is the arch between the first and second point and is calculated as:

$$\Delta xy = 2r \arcsin\left(\frac{\sqrt{y_1^2 + x_1^2}}{2r}\right) \tag{4.24}$$

The charge sign q is determined as:

$$q = \frac{x_3 y_2 - x_2 y_3}{|x_3 y_2 - x_2 y_3|} \tag{4.25}$$

The three-point method for the estimation of the initial-state vector s_0 can be written as:

$$s_0 = h\left[(x_0, x_1, x_2); (y_0, y_1, y_2, z_0, z_1, z_2)\right] \equiv h(\zeta; \eta), \tag{4.26}$$

where x_i, y_i and z_i are the measured coordinates of the three points, all taken to be independent and uncorrelated. In order to compute an estimate for C_0 one can use the matrix expression for error propagation [148]:

$$C_0 = gVg^T \tag{4.27}$$

$$g_{ij} = \frac{\partial h_i}{\partial \eta_j}, \tag{4.28}$$

where V is the covariance matrix of the vector η, which is determined by the resolution of the detector in y and z. The coordinate x is taken to be the free parameter and thus is not considered in the error propagation. The partial derivatives are estimated numerically as:

$$\frac{\partial h_i}{\partial \eta_j} \approx \frac{h(\zeta; \eta_{i\neq j}, \eta_j + \sigma_{\eta_j}) - h(\zeta; \eta_{i\neq j}, \eta_j)}{\sigma_{\eta_j}}, \tag{4.29}$$

where σ_{η_j} is the resolution of the vector element η_j. The `Seed` estimation for both the covariance matrix C_0 and the state vector s_0 is adjusted for energy loss and multiple scattering using the same method as the KF. The q/p_{T} ratio is corrected with the factor described in Eq. 4.16, and the relative covariance matrix element is updated by adding the c_k factor from Eq. 4.17. To handle multiple scattering, the Q matrix calculated in Eq. 4.21 is added to the covariance. The total distance travelled, needed to calculate total energy loss and the scattering angle $\theta_{\mathtt{M}}$, is given by the length of the portion of the trajectory of the particle inside the scintillating planes.

The second seeding algorithm consists in the iterative linear regression method for circle fits (`ILRM`) outlined in [149]. It was originally used as ND-GAr-Lite's full reconstruction algorithm and has so far only been tested as a seeding method on ND-GAr-Lite. The algorithm is closely related to the least squares method, where the centre of the circle trajectory in the xy plane and its radius r are found by minimizing the functional:

$$L(x_C, y_C, r) = \sum_{i=1}^{n} (\sqrt{(x_i - x_C)^2 + (y_i - y_C)^2} - r)^2 = \sum_{i=1}^{n} \rho_i^2 \tag{4.30}$$

where (x_i, y_i) are the coordinates of all the points along the track. Due to the non-linear dependence of the functional L on the circle parameters, applying the least square method leads to very cumbersome computations. One can then linearize the system by introducing the new variable $Z_i = x_i^2 + y_i^2$ and rewriting the circle equation as:

$$Z = 2x_C x + 2y_C y + \gamma \tag{4.31}$$

where $\gamma = r^2 - x_C^2 - y_C^2$. This linear regression method (LRM) is equivalent to minimizing the functional:

$$M(x_C, y_C, r) = \sum_{i=1}^{n}((x_i - x_C)^2 + (y_i - y_C)^2 - r^2)^2 \tag{4.32}$$

While the LRM method is much faster than the non-linear method, it is only reliable in the cases where $\rho_i \ll r$. This is because the LRM is based on the assumption that all points included in the fit, roughly lie on the same circle. The `ILRM` method solves this instability issue by utilizing a slightly different functional:

$$K(x_C, y_C, r) = M(x_C, y_C, r)r^{-2} \tag{4.33}$$

Using the numerical methods outlined in App. A.1, it is possible to find values of (x_C, y_C, r) which minimize K, maintaining the computational agility of the LRM method, and the stability of the non-linear methods.

Starting from the circumference properties, all the components of the state vector can be calculated as described in Eq. 4.23. The covariance matrix C_0 is estimated as in Eq. 4.27, reapplying the fit only to three points, at the start, end and middle of the particle trajectory. This approximation is not completely correct and tends to overestimate the uncertainties, since in reality, all the points in the track are used. However, since only a rough estimate of C_0 is needed by the `KF-Lite`, no other method has been explored. As in the case of the application of the ALICE algorithm to ND-GAr-Lite, only the diagonal elements of C_0 are considered.

4.4 The ND-GAr software suite: `GArSoft`

`GArSoft` is a software toolkit used to handle the simulation and reconstruction of events inside ND-GAr and ND-GAr-Lite [150]. It is largely based on the `LArSoft` toolkit [151, 152] which is used by the DUNE experiment to handle the simulation and reconstruction for all its liquid argon based detectors i.e. the ND-LAr detector and the FD modules. `GArSoft`, as well as `LArSoft`, are based on the `art` event processing framework [153], which is shared by most of the modern Fermilab experiments. The `art` framework allows for the different simulation and reconstruction steps to be handled modularly through the use of simple text files.

4.4.1 Particle generation and propagation in GArSoft

In GArSoft the simulation of neutrino interactions inside the detector geometries is handled through the use of the Generator of Events for Neutrino Interaction Experiments (GENIE) [154]. The main component of GENIE is the GENIE Generator, which provides software tools which support a state-of-the-art comprehensive physics model for neutrino interaction simulations in realistic experimental setups. GENIE also offers extensive data archives to allow for MC/data comparisons as well, as a generator tuning framework. GENIE can be used in GArSoft by providing the generator with a neutrino flux file, which comes in the form of ROOT [155] n-tuples, containing entries describing neutrino-producing decays, with one entry for every neutrino recorded. Additionally, GENIE requires a detector geometry in the form of a ROOT-readable gdml [156] file and, optionally, a list of neutrino types and interactions that one wants to simulate, as well as the portion of the detector geometry in which the user desires the interaction to occur. This framework allows for the neutrino interaction generation to be handled identically independently from the detector that one wants to simulate.

In addiction to the GENIE event generator, GArSoft also supports a particle gun generator. This tool allows the user to generate individual particles inside the detector geometry, specifying their type, starting position, 3-dimensional momentum and energy. This particle gun tool is directly adapted from Geant4 [157]. Geant4 is a software package composed of tools for the simulation of the passage of particles through matter. The toolkit is capable of handling all aspects of the simulation, which include: the geometry of the detector and the materials involved, which in GArSoft are specified through a ROOT-readable gdml file; the fundamental particles of interest and the tracing of particles through materials and electromagnetic fields; the physics processes governing particle interactions as well as the response of sensitive detector components; the generation of event data, the storage of events and tracks, the visualization of the detector and particle trajectories, and the capture and analysis of simulation data at different levels of detail and refinement. In GArSoft the standard physics lists provided by Geant4 are used.

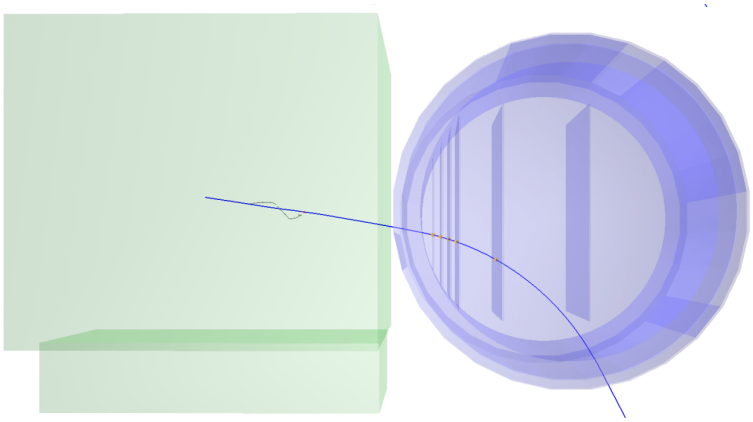

Figure 4.3: ND-GAr-Lite tracker station layout with the 6-plane optimized design. The transparent green box depicts ND-LAr with an exiting muon that enters ND-GAr-Lite [103].

In `GArSoft`, Geant4 is used to handle all aspects of the simulation up to the signal formation and digitization steps which are handled through custom-made software which is detector-specific. Geant4 is also used in `GArSoft` to support a simple event-display application. Fig. 4.3 shows an example of a particle-gun generated muon starting in ND-LAr's volume, shown in light green and crossing the whole volume of the 6-plane configuration of ND-GAr-Lite shown in light blue. The energy deposits in the scintillator planes are highlighted in red.

4.4.2 Digitization, track formation and reconstruction in `GArSoft` for ND-GAr-Lite

The signal formation on ND-GAr-Lite's scintillator planes is handled through custom-made software integrated in `GArSoft`. The hit cluster positions are simulated in the scintillator planes by taking the energy deposits produced by Geant4 and mapping them onto the correspondent strips. Each hit cluster is defined as a collection of all Geant4 energy deposition hits mapped on a single strip. Each plane is formed by two sub-planes, which are segmented either along the y or z direction into triangularly shaped strips. If the strip belongs to the y-segmented sub-plane, the y is given by the centre of the strip and the z is taken as the energy deposit's position, normally smeared according to the strip's space resolution which is $\sigma_s = 0.3$ cm; vice-versa if the strip belongs to the z-segmented sub-plane. Note that more than a

hit per sub-plane per particle track can be produced depending on the trajectory of the particle. For example a particle with a trajectory perpendicular to a tracking plane, will on average produce two hits per sub-plane. This is a direct consequence of the disposition of the triangular scintillator strips. The energy deposition is converted to photo-electron counts via a simple response function and the timing information is smeared according to the time resolution of the strips.

To produce a track candidate, the hit clusters are ordered using the time information, then a set of three hit clusters in three separate tracking planes is found, forming the initial track candidate. An `ILRM` fit is applied to the triplet and hit clusters are added to the track candidate, based on their vicinity to the helix trajectory defined by the fit. Every time a cluster is added, the track is refitted until the final track candidate is produced. All possible triplets are tested until the best track candidate is found. The original track finding algorithm only produced one track candidate per event. The track finding algorithm has been updated as part of this thesis project; now all the points that haven't been added to the main track candidate are collected and a new track candidate is looked for. This process is repeated until no unmatched clusters are left. The clusters that don't pass the "closeness" criteria with any of the candidate track trajectories are discarded.

Once all the track candidates are formed, they are fitted once again with the `ILRM` algorithm to provide estimates for the track parameters (x_C, y_C, r, λ). These are then converted and saved in the form of 3-dimensional position and momentum together with all the hit cluster points forming the track. The information regarding the Monte Carlo true trajectory and properties of the particle are saved separately. No "back-tracker" algorithm which could match the ND-GAr-Lite reconstruction results with the MC truth information, was available at the time of the production of this thesis. These had to be matched separately using positional arguments.

4.5 Toy Monte Carlo simulation

A toy MC tool was developed to test and study the new custom `KF-Lite` algorithm. The simulation was constructed with extreme modularity in mind, so that each of

its aspects could be tested separately. The simulation procedure for each track can be divided in the following steps:

1. **Definition of a simplified detector geometry.** The cylinder dimensions of the inner tracker region are specified, together with the position, dimensions, spatial resolution and material properties of the scintillator planes, which are approximately treated as solid rectangular slabs. The space in between the scintillator slabs is considered to be empty.

2. **Particle Generation.** A particle is defined by specifying its type, charge, transverse momentum p_T, azimuthal angle ϕ, dip angle tangent $\tan\lambda$ and starting position. From this information, the initial true MC state vector s_0^t is built.

3. **Propagation of the particle.** The state vector is propagated as described in Equation 4.16. This is done along the x direction in a fixed coordinate frame at 0.25 cm increments.

4. **Application of energy loss and multiple scattering.** The magnitude of the corrections are calculated using the Bethe-Bloch and Molière formulas respectively, analogously to what was described in Sec. 4.3. Note that these corrections are applied only when the particle is moving inside the scintillator planes.

5. **Particle stopping.** The propagation is stopped if: the particle reaches the edges of the detector cylinder; the particle gets close enough to the Bragg Peak, that the basic Bethe-Bloch model no longer well describes the energy loss; one of the propagation steps fails.

6. **Hit clusters generation**. All points inside the scintillator planes are recorded and grouped. For each scintillator a random amount of the recorded points, between 1 and 4, is saved as the hit clusters.

7. **Simulation of the measurement noise.** Once the hit clusters are generated, the measurement noise is simulated by smearing the y and z coordinates of the trajectory points with Gaussian distribution having a width equal to the resolution of the detector planes.

Once a track is generated, no additional track finding step is applied and the `KF-Lite` is applied on top of one of the possible seeding strategies. The energy loss, multiple scattering and point smearing, determine the process and measurement noise of the simulation; they can all be controlled by the user event by event, both in their magnitude and in whether or not they are applied at all.

4.6 The toy Monte Carlo studies

The toy MC tool described in Sec. 4.5 was employed to construct several test particle samples used for the development of the `KF-Lite` algorithm. The tests focussed on the reconstruction of forward going muons in the few-GeVs range, crossing the full detector, which are the key particle types for ND-GAr-Lite. The first step for each test, consisted in producing a sample of muons to apply the reconstruction to. Each particle would have either a fixed total momentum, or one chosen randomly from a range selected by the user. All particles were simulated to have a forward going momentum, with randomized small y and z components. The initial position could also either be fixed and set in the middle and front of the first scintillator plane, or placed randomly within a fiducial volume. Two different geometries were considered: the nominal 5-planes geometry and an optimized 6-plane geometry, both described in Sec. 3.4.2.

In the toy MC simulation for each production, the energy loss, multiple scattering and measurement smearing could be set by the user independently from one another. Specifically, each of the elements could be switched on and off entirely, a Landau or Gaussian smearing on the energy loss could be applied, and the magnitude of the measurement smearing could be modified. Once the tracks were formed, the reconstruction was applied. For the seeding portion of the algorithm,

(cm)	Plane-1	Plane-2	Plane-3	Plane-4	Plane-5	Plane-6	Fiducial
x_1	-307	-287	-267	-247	-147	53	-317
x_2	-303	-283	-263	-243	-143	57	-307
y_1	-133	-172	-199.5	-224.5	-249.5	-249.5	-149.5
y_2	134	173	200.5	225.5	250.5	250.5	150.5
z_1	-300	-300	-300	-300	-300	-300	-200
z_2	300	300	300	300	300	300	200

Table 4.1: Table showing the positions of the edges of the tracking planes in the 6-plane configuration of ND-GAr-Lite as well as the fiducial volume box from which the particles in the toy Monte Carlo Uncorrected (U) and Corrected (C) samples, defined in the text, are generated.

only the `Seed` method, described in Sec. 4.3.1 was fully implemented in the toy MC tests. Finally the `KF-Lite` was applied once in the forward direction and once backwards, producing estimates at both ends of the track. For both the seeding and KF applications, the energy loss and multiple scattering corrections could be applied or not, independently from one another.

The series of independently set conditions just described, generated a vast amount of sample simulation and reconstruction combinations, most of which have been produced and tested. A summary of all the sample combinations considered for ND-GAr-Lite is provided in Tab. A.1 in App. A.2.

In this section we focus on two specific tests numbered 13.5c and 13.5.2c in the table. For these two tests the same simulation conditions were applied. We considered a sample of 5×10^3 forward going muons with initial momenta distributed uniformly between 0.5 GeV/c and 4 GeV/c inside the 6-plane geometry of ND-GAr-Lite. Their starting positions are distributed inside a block shaped fiducial volume placed immediately in front of the first plane. A summary of the positions of the six planes and of the starting fiducial volume is shown in Table 4.1. Note that the coordinate frame has its origin in the centre of the tracking section cylinder, which has a radius of 349.9 cm and a length of 669.6 cm. The scintillator planes were simulated to be made of polyvinyltoluene, a plastic polymer scintillator having a radiation length of $X_0 = 42.54$ cm and a density of $\rho = 1.032$ g/cm^3. All the

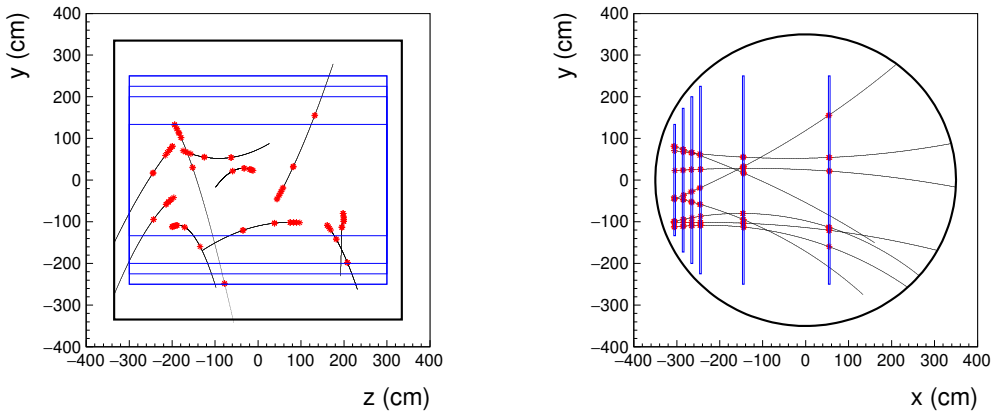

Figure 4.4: Toy Monte Carlo event display showing 8 muon tracks from the simulated sample in (a) zy and (b) xy view. The edges of the cylindrical tracking region are outlined in black, while the tracking planes are outlined in blue. The simulated trajectories are traced in black, while the plane hits are highlighted with red markers.

scintillator planes are set to have equal spatial resolution resolution in both the y and z direction of $\sigma_{yz} = 0.3$ cm.

The difference between the two samples stems from the reconstruction. In both cases the `Seed` algorithm followed by the `KF-Lite` algorithm are used sequentially, but only in the second case the energy loss and multiple scattering corrections are applied to both portions of the algorithm (i.e. the `Seed` algorithm and the KF). The purpose of comparing the two samples is to show the impact that the energy loss and multiple scattering corrections have on the reconstruction, as well as to verify that the simulation and reconstruction algorithms are internally consistent. We denote the sample in which the material budget corrections are not applied as the Uncorrected sample or U sample and the other sample as the Corrected sample or C sample.

An example event display showing 8 muon tracks from the simulated sample are shown in in Fig. 4.4 both in a zy and xy view. The edges of the cylindrical tracking region are outlined in black, while the tracking planes are outlined in blue. The simulated trajectories are traced in black, while the plane hits are

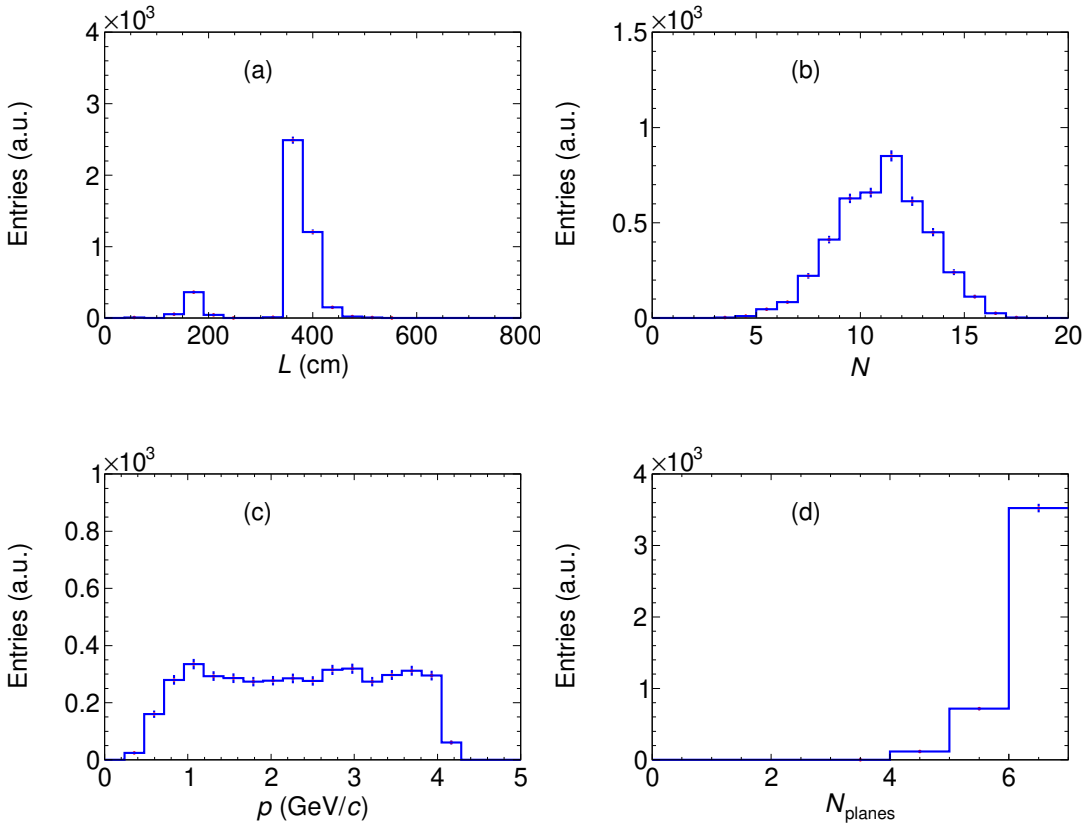

Figure 4.5: Properties of the particles simulated for the U and C toy MC samples: (a) length of the particle tracks L (cm) measured as the summed distances between the hit clusters; (b) number of hit clusters belonging to the tracks N; (c) initial momentum of the particles p (GeV/c); (d) total number of tracking planes traversed by the particle N_{planes}.

highlighted with red markers.

Some key quantities that describe the properties of the two samples are shown in Fig. 4.5. Fig. 4.5a shows the distribution of the track length L in cm, defined as the total distance between the scintillator plane hit clusters. The distribution shows two clear peaks: one between 100 and 200 cm and the other around 400 cm. The two-peaked distribution is easily explained by considering the disposition of the tracking planes in the 6-plane geometry for ND-GAr-Lite. In the 6-planes geometry the first 5 planes are disposed within the first 200 cm of the detector cylinder in the beam direction, while the last one is set 200 cm apart from all the others. This is confirmed by Fig. 4.5d which shows the number of plains which are traversed by each particle in the samples. Most tracks in the samples cross the

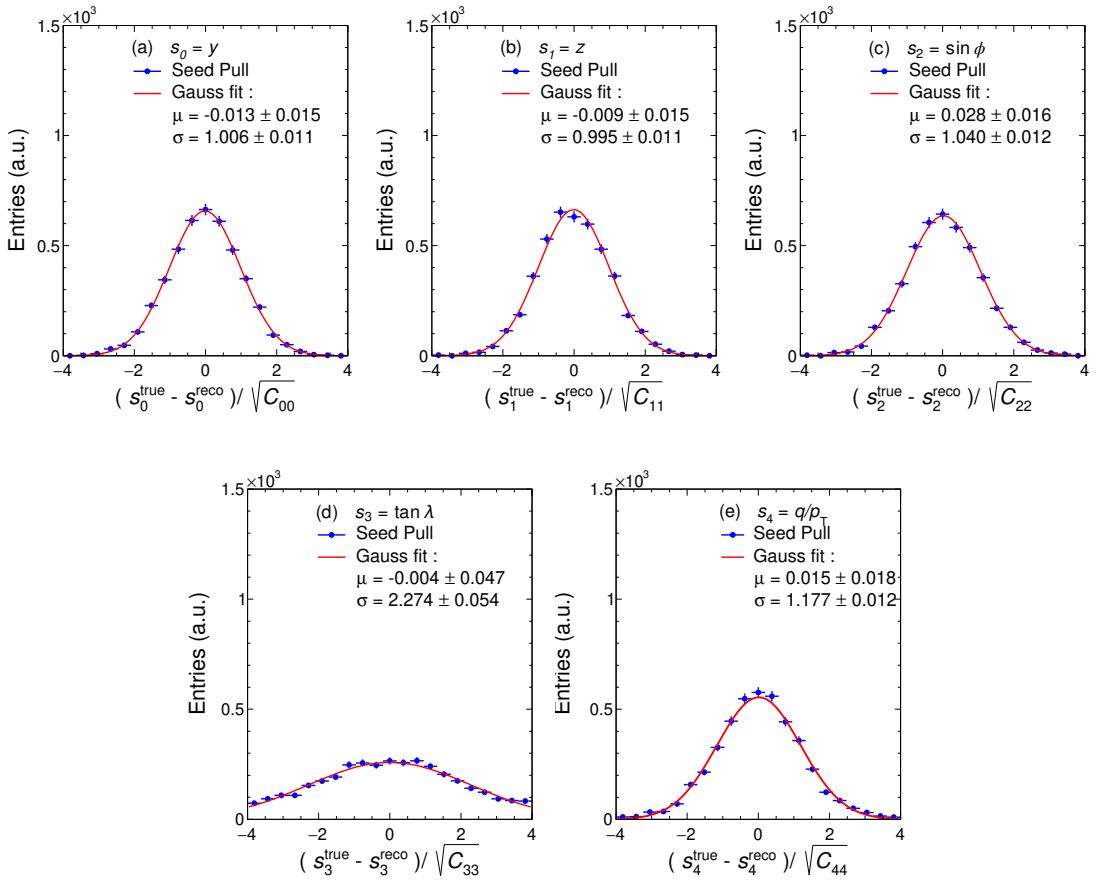

Figure 4.6: Pull distributions for the `Seed` algorithm over the Uncorrected sample. All distributions were fitted to a Gaussian function. Results for parameters s_0 to s_4 (i.e. y, x, $\sin\phi$, $\tan\lambda$ and q/p_{T}) are shown from left to right and labelled from (a) to (e) accordingly.

whole 6 planes and some cross either 4 or 5, explaining the two peaks in the L distribution. Additionally Fig 4.5b shows the number of hit clusters N associated with each track and Fig. 4.5c the initial true momentum p of the particles.

The first test performed on both the U and C samples was a "pull" test. A pull, Π, is defined as the difference between the true value and the reconstructed value of one of the state vector parameters $s = (y, z, \sin\phi, \tan\lambda,\ q/p_{\mathrm{T}}) = (s_0, s_1, s_2, s_3, s_4)$, normalized by the square root of the correspondent diagonal element of the covariance matrix C_{ii}:

$$\Pi_i \equiv \frac{s_i - s_i^{\mathrm{true}}}{\sqrt{C_{ii}}}. \tag{4.34}$$

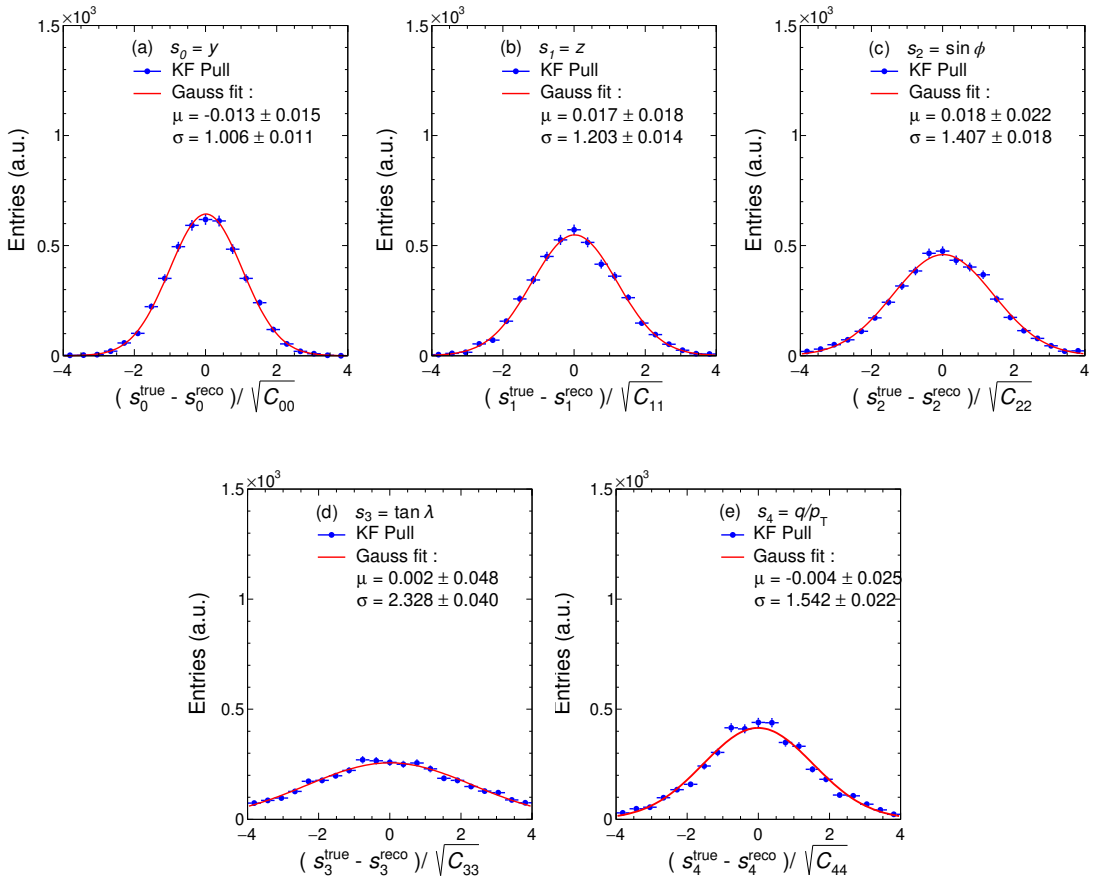

Figure 4.7: Pull distributions for the `KF-Lite` algorithm over the Uncorrected sample. All distributions were fitted to a Gaussian function. Results for parameters s_0 to s_4 (i.e. y, x, $\sin\phi$, $\tan\lambda$ and q/p_{T}) are shown from left to right and labelled from (a) to (e) accordingly.

If the covariance matrix is well defined, the distributions of the pulls should be normal, centred at 0 with $\sigma \simeq 1$.

The U sample pulls were tested, both for the `Seed` and the `KF-Lite` results were fitted to a standard Gaussian distribution. Note that the pulls for the `Seed` algorithm were tested at the start of the particle trajectory, while for the `KF-Lite` they were tested at the end after the full propagation. The resulting U sample distributions for all the state vector parameters are shown in Figs. 4.6 and 4.7 for the `Seed` and the `KF-Lite` results respectively. A very significant underestimation of the uncertainty of the $\tan\lambda$ parameter can be seen in the `Seed` results for which we obtain a value of σ which is roughly double the expectation. This is not corrected

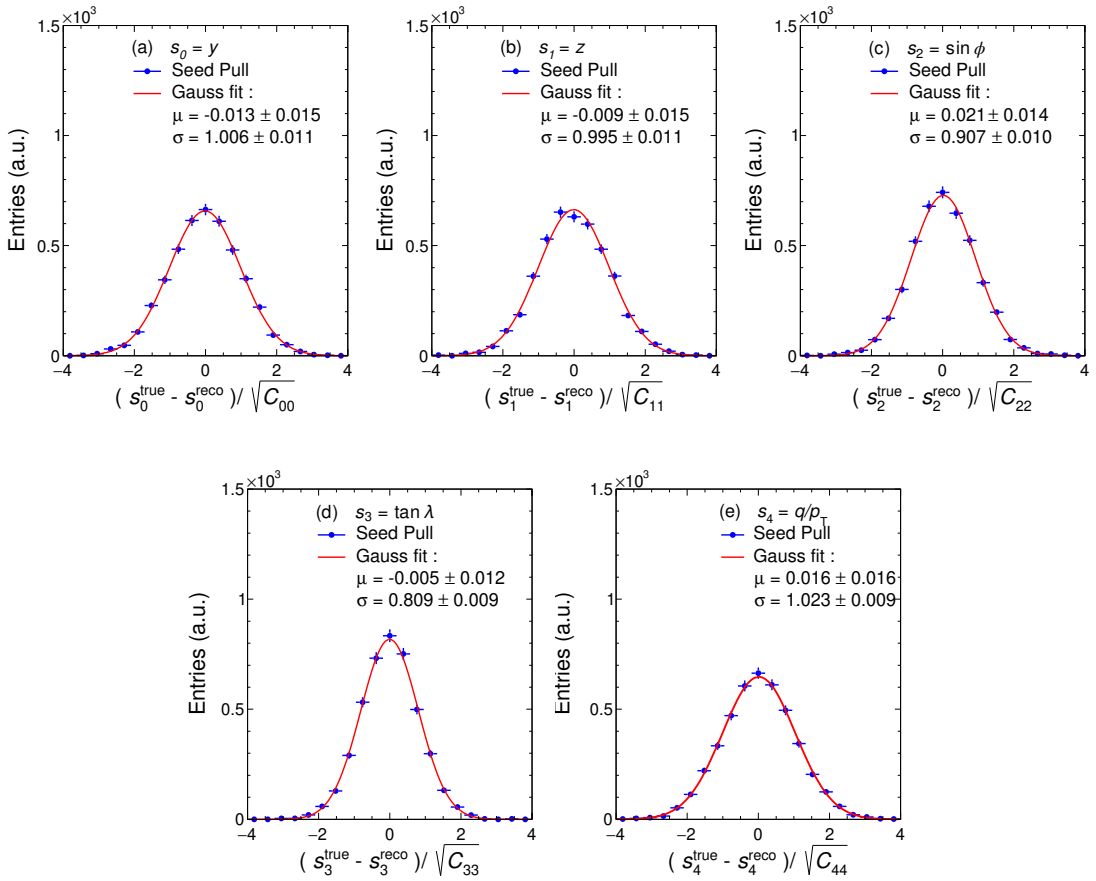

Figure 4.8: Pull distributions for the `Seed` algorithm over the Corrected sample. All distributions were fitted to a Gaussian function. Results for parameters s_0 to s_4 (i.e. y, x, $\sin\phi$, $\tan\lambda$ and q/p_{T}) are shown from left to right and labelled from (a) to (e) accordingly.

after the `KF-Lite` propagation, for which significant underestimations can also be seen for $\sin\phi$ and q/p_T parameters. This to be expected, given that the uncertainty contributions that arise from the particles' multiple scattering and energy loss have not been accounted for.

The C sample pulls were tested in an analogous manner and the resulting distributions are shown in in Figs. 4.8 and 4.9 for the `Seed` and the `KF-Lite` results, respectively. The `Seed` algorithm produces small overestimations on the $\sin\phi$ and $\tan\lambda$ uncertainties. After the propagation of the `KF-Lite` the underestimation in $\tan\lambda$ is removed, while the one in $\sin\phi$ is slightly over-corrected for. Additionally, an underestimation on the uncertainty of q/p_{T} is introduced. In both

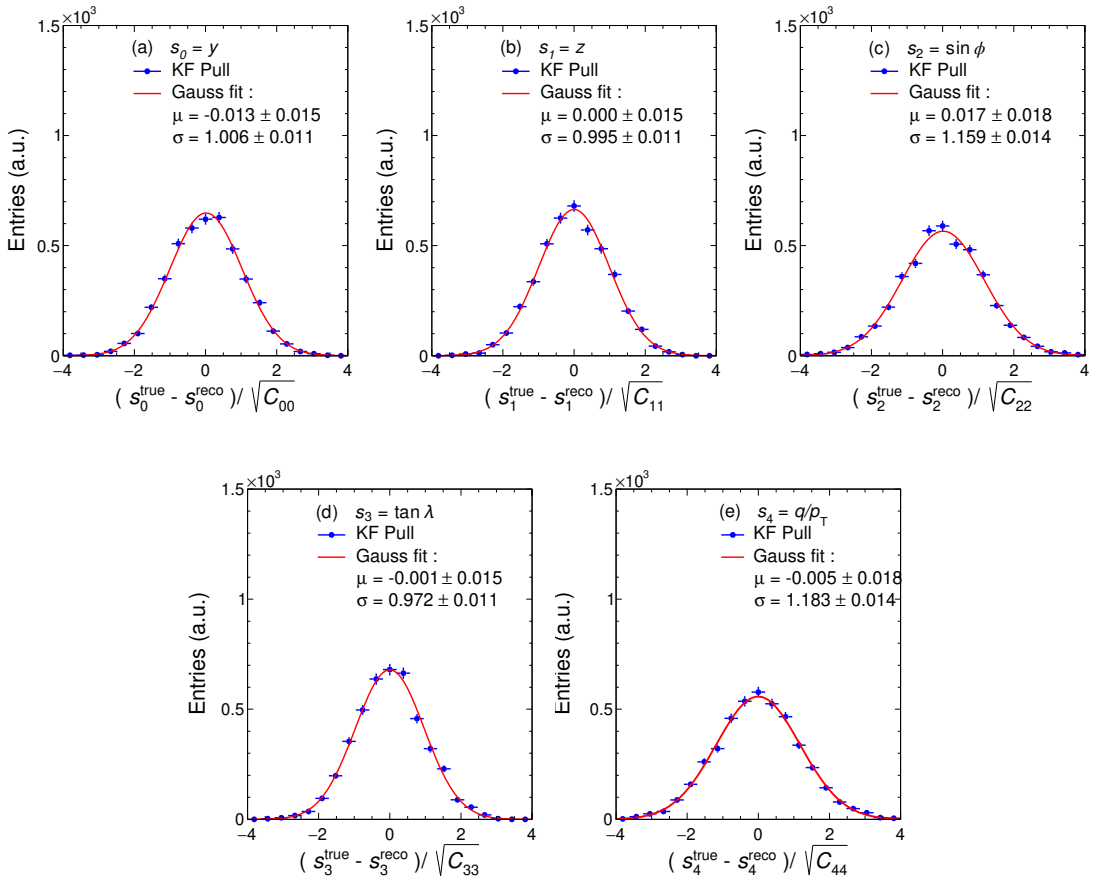

Figure 4.9: Pull distributions for the `KF-Lite` algorithm over the Corrected sample. All distributions were fitted to a Gaussian function. Results for parameters s_0 to s_4 (i.e. y, x, $\sin\phi$, $\tan\lambda$ and q/p_{T}) are shown from left to right and labelled from (a) to (e) accordingly.

cases, however, the imperfections are much less significant that in the case of the U sample and the pulls can be said to have $\mu \sim 0$ and $\sigma \sim 1$. This means that the energy loss and multiple scattering corrections that we apply to the algorithm are internally consistent with the simulation and allow us to produce correct estimates of the uncertainties of the reconstructed state vector parameters.

For both the U and C samples we focussed on figures of merit such as the total momentum resolution and bias. Both of these quantities can be defined as the standard deviation and mean of a Gaussian distribution fitted to the momentum fractional residuals:

$$R = \frac{p_{\mathrm{reco}}}{p_{\mathrm{true}}} - 1. \tag{4.35}$$

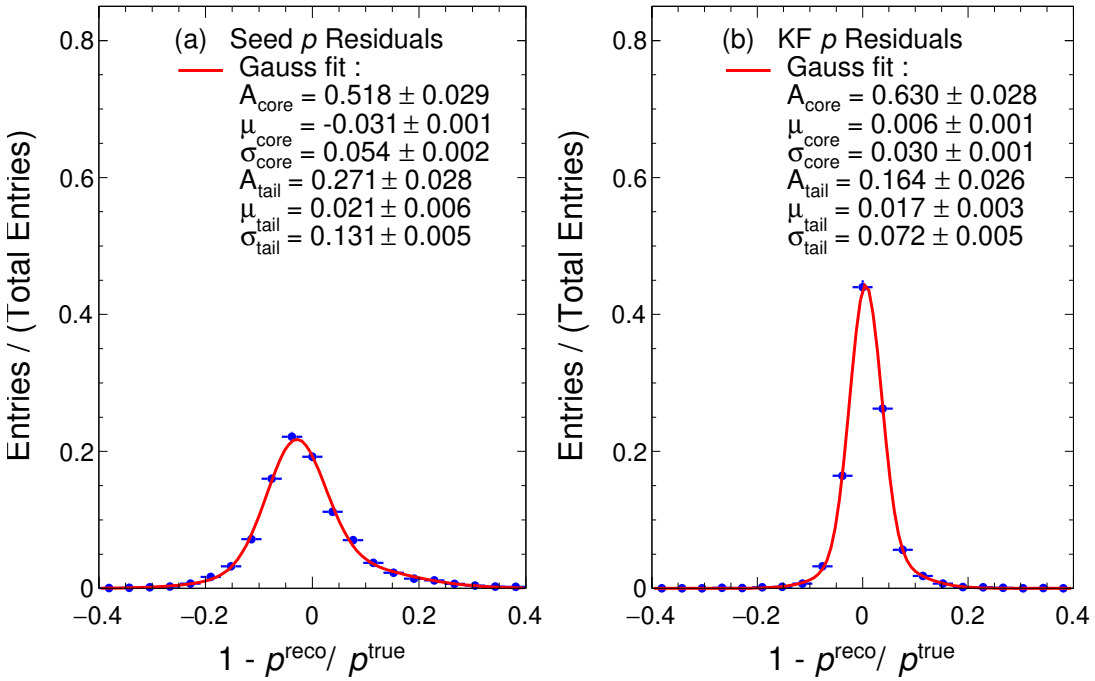

Figure 4.10: Momentum fractional residuals $R = p_{\text{reco}}/p_{\text{true}} - 1$ for the (a) `Seed` and (b) `KF-Lite` algorithms in the U toy Monte Carlo sample. In both cases the distributions were fitted with a double Gaussian function defining a core and a tail distributions.

In Fig. 4.10 we show the momentum fractional residual distributions obtained for the `Seed` and `KF-Lite` algorithms in the U sample, where the energy loss and multiple scattering corrections haven't been applied. In both cases the distributions were fitted with a double Gaussian function $g(x)$ defining core and tails sub-sets:

$$g(x) = \frac{1}{\sqrt{2}}\left[\frac{A_{core}}{\sigma_{core}} e^{-\frac{1}{2}\left(\frac{x-\mu_{core}}{\sigma_{core}}\right)^2} + \frac{A_{tail}}{\sigma_{tail}} e^{-\frac{1}{2}\left(\frac{x-\mu_{tail}}{\sigma_{tail}}\right)^2}\right] \tag{4.36}$$

The `Seed` algorithm is shown to produce a significant negative bias $\mu_{\text{core}} = (-3.1 \pm 0.1)\%$ in the momentum estimation. This is due to an underestimation of the momentum brought by the lack of energy loss correction imparted to the algorithm's estimate. Similarly the `KF-Lite` residuals shows a positive but much less significant bias $\mu_{\text{core}} = (0.6 \pm 0.1)\%$. The opposite direction of the bias is to be expected, since the estimate is produced at the end of the particle trajectory rather than at the start.

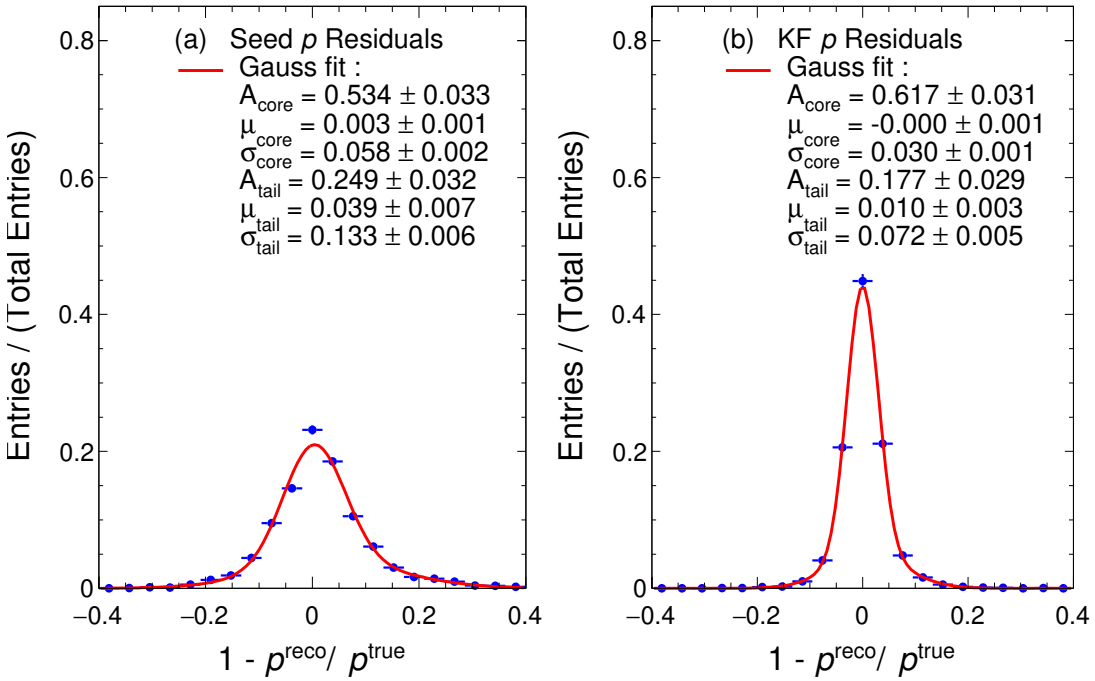

Figure 4.11: Momentum fractional residuals $R = p_{\text{reco}}/p_{\text{true}} - 1$ for the (a) `Seed` and (b) `KF-Lite` algorithms in the U toy Monte Carlo sample. Similar to Fig. 4.10.

In Fig. 4.11 we show the momentum fractional residual distributions obtained for the `Seed` and `KF-Lite` algorithms in the C sample where the energy loss and multiple scattering corrections have been applied. In both cases the distributions were fitted with a double Gaussian function analogously to what was done for the U sample. The bias seen for the `Seed` algorithm in the U sample is now almost completely corrected, having $\mu_{\text{core}} = (0.3 \pm 0.1)\%$. Similarly the `KF-Lite` residuals shows no bias having $\mu_{\text{core}} = (0.0 \pm 0.1)\%$. The energy loss correction that we apply to both algorithms is shown to be perfectly consistent with the simulation.

For a more complete view of the results we also show the relative momentum resolution and bias produced by the `KF-Lite` algorithm as a function of some key track properties. The results for the U and C samples are shown in black and blue respectively. In Fig. 4.12 we show the two quantities as a function of the number of hit clusters belonging to the track N (Figs. 4.12b and 4.12a)the particle's initial true momentum $p^{\texttt{true}}$ (Figs. 4.12d and 4.12c). Note that in both of these cases the μ

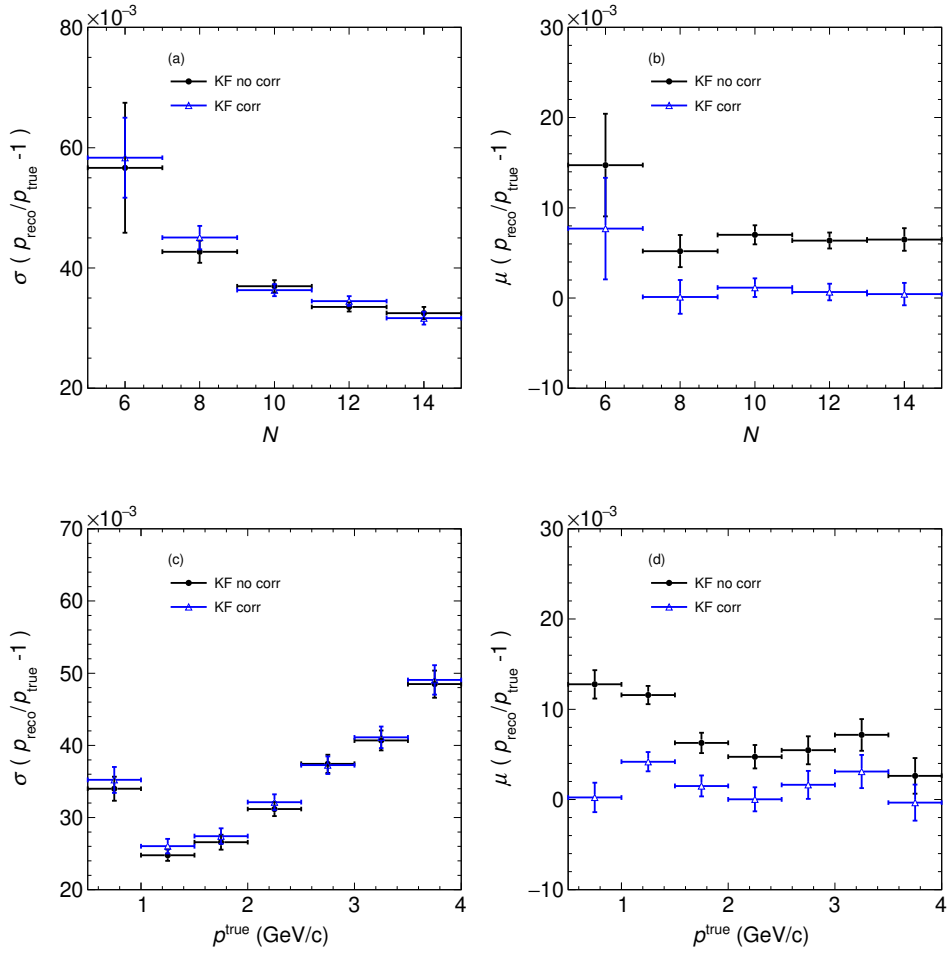

Figure 4.12: Relative momentum resolution σ and bias μ as a function of (a), (b) the number of hit clusters belonging to the track and (c), (d) the initial true momentum of the particle. The results for the U sample are shown in black while for the C sample are shown in blue

and σ values are taken from a simple Gaussian fit, rather that a double Gaussian fit as was done for Figs. 4.10 and 4.11. It is clear from a direct comparison of the two samples that while the results are comparable in terms of resolution, a significant bias correction in the momentum reconstruction is achieved by the application of the energy loss correction step to the `KF-Lite`.

The dependency of the momentum resolution on p and N can be predicted by using the Gluckstern formulas, which describe the dependency of a curvature measurement resolution on several track parameters [158]. Adapting the formulas

to get the total momentum dependency we get:

$$\frac{\sigma_{\mathrm{H}}(p)}{p} = \frac{\cos\lambda\ p\ \sigma_{r\phi}}{0.3BL^2_{\mathrm{Arm}}}\sqrt{\frac{720}{N+4}}. \tag{4.37}$$

$$\frac{\sigma_{\mathrm{MS}}(p)}{p} = \frac{0.016\ (\mathrm{GeV}/c)}{0.3Bl\beta\cos\lambda}\sqrt{\frac{l}{X_0}}, \tag{4.38}$$

where $\sigma_{r\phi}$ is the spatial resolution in the radial direction, l is the length of the track, $\sigma_{\mathrm{H}}(p)$ is the point resolution component of the total momentum resolution and $\sigma_{\mathrm{MS}}(p)$ is the multiple scattering component. The total resolution is expected to be:

$$\sigma_{\mathrm{tot}}(p) = \sqrt{\sigma^2_{\mathrm{H}} + \sigma^2_{\mathrm{MS}}} \tag{4.39}$$

The multiple scattering component σ_{MS} is dominant at lower momenta, while the hit component σ_{H} is dominant at higher momenta. This dependency can be clearly seen in Fig. 4.12c where at lower momenta the resolution has an inverse proportionality on the momentum, which directly derives from the β at the denominator present in Eq. 4.38, while at higher momenta the direct proportionality seen in Eq. 4.37 dominates. In Fig. 4.12a on the other hand we clearly see the $\propto 1/\sqrt{N}$ dependency that we expect from Eq. 4.37

4.7 The `GArSoft` simulation studies

The `GArSoft` software suite described in Sec. 4.4 was used to generate a particle sample to test the performance of the new `KF-Lite` algorithm and compare it to the `ILRM` algorithm which represented the standard reconstruction at the time. The simulation leveraged the Geant4 particle gun tool and used the 6-plane ND-GAr-Lite geometry. The sample was monoenergetic, containing muons having the same initial momenta $p = 1$ GeV/c and starting position in the front and centre of the first scintillator tracking planes. All particles were simulated to have a forward going momentum, with randomized small y and z components. These limited initial conditions were chosen for the simplicity of production and implementation with the `KF-Lite` algorithm. They were also chosen to be a relatively close match with the conditions of muons coming from ND-LAr which are the main sample

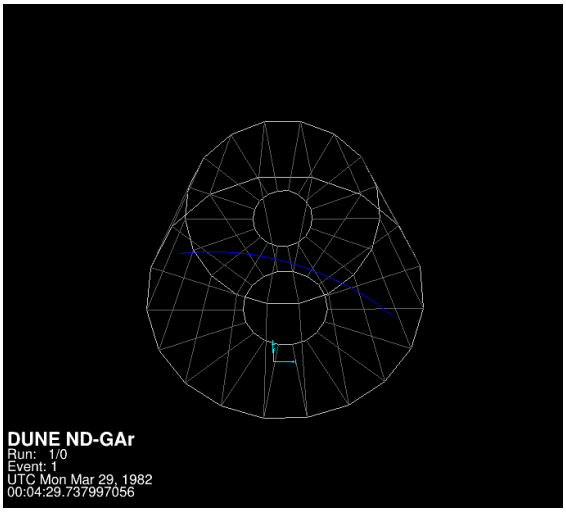

Figure 4.13: `GArSoft` event display showing a muon produced with the particle gun feature and used for the Lite-1 and Lite-2 studies. The layout of the tracker area is outlined in white and the trajectory of the muon is shown in blue.

of interest for ND-GAr-Lite. An example `GArSoft` event display for one of these simulated events is shown in Fig. 4.13 .

Similarly to the toy MC studies described in the previous section many aspects of the reconstruction algorithm could be switched on and off modularly, in order to be tested individually. These features include the energy loss and multiple scattering corrections which can be applied to both the seeding algorithm and the `KF-Lite`. Additionally two separate types of seeding algorithm were implemented: the `Seed` algorithm as well as the `ILRM` algorithm.

In this section we focus on the results obtained for the two most complete and best performing combinations of the algorithm correspond to samples 15.5.2c and 15.6.2c in Tab. A.1 in App. A.2. In both cases we use the same `KF-Lite` algorithm and the full set of material budget corrections are applied, but the two samples are differentiated by the seeding strategy: the `Seed` method in the first case, the `ILRM` in the second. These two test sample conditions will be referred to as Lite-1 and Lite-2 respectively. Some key properties of the particle tracks which are common to both samples are shown in Fig. 4.14, specifically the length of the tracks L as defined in Sec. 4.6 and the number of hit clusters belonging to the particle track N. Comparing the properties with those shown in Fig. 4.5 it's clear that

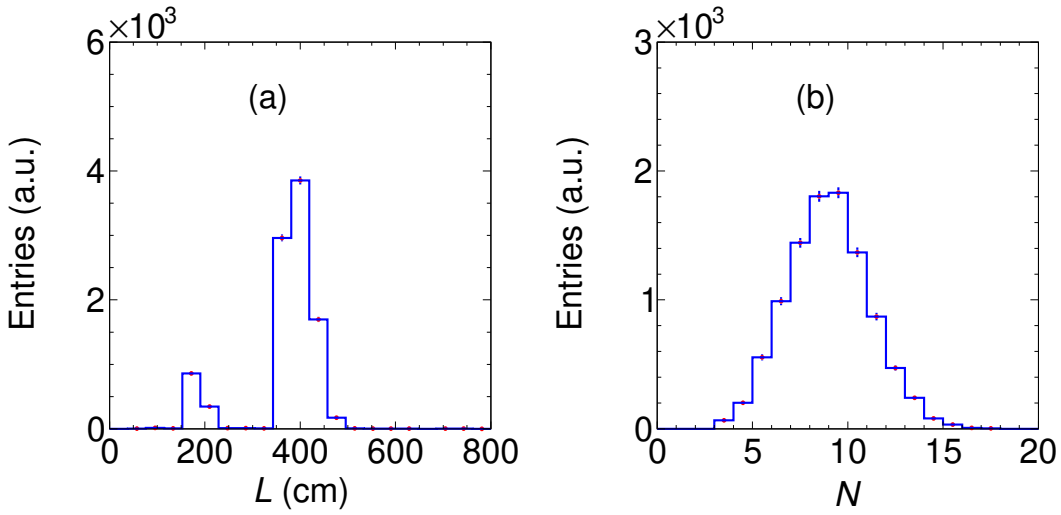

Figure 4.14: Properties of the particles simulated for the `GArSoft` Lite-1 and Lite-2 samples: (a) length of the particle tracks L (cm) measured as the summed distances between the hit clusters; (b) number of hit clusters belonging to the tracks N.

the toy Monte Carlo simulation produced results that are very close to the more complete simulation available in `GArSoft`.

Similarly to what was done within the toy MC study, pull-tests were performed for both seeding algorithms and the `KF-Lite` algorithm after the full propagation. Note that in this case both results are taken at the start of the muon track, for ease of comparison with the `GArSoft` reconstruction results. This is because, while `KF-Lite` was always applied twice, producing estimates at both end of the track, the original `ILRM` reconstruction was only applied once, producing a single estimation at the start of the track.

The pull distributions for all the state vector parameters obtained using the `Seed` algorithm are shown in Fig. 4.15. All pulls are fitted with simple Gaussian distribution showing no biases and $\sigma \sim 1$. A somewhat significant overestimation of the uncertainties can be seen for parameters $s_2 = \sin\phi$ and $s_3 = \tan\lambda$. This was also seen in Fig. 4.8 and is consistent with previous test results.

In Fig. 4.16 we show the pulls obtained after the full propagation of the `KF-Lite` algorithm. In this case the overestimation seen for $s_2 = \sin\phi$ and $s_3 = \tan\lambda$ is

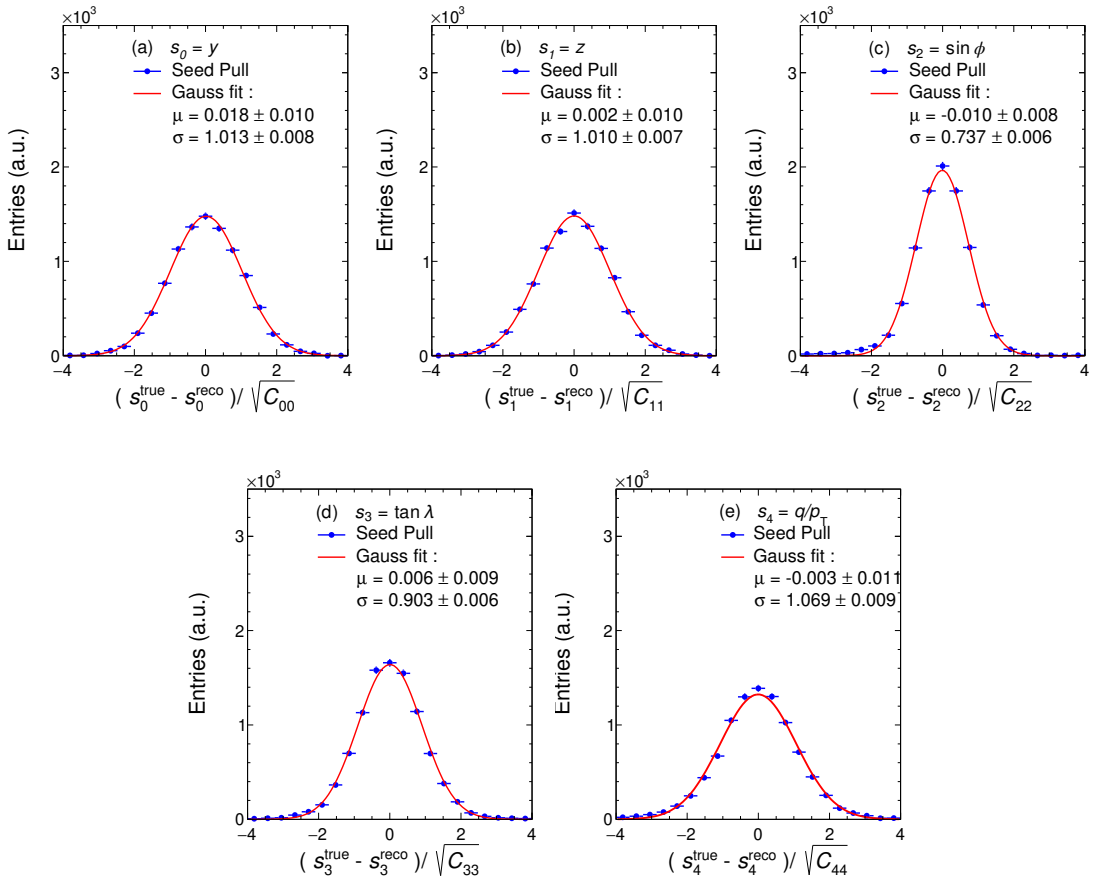

Figure 4.15: Pull distributions for the `Seed` algorithm over the Lite-1 sample. All distributions were fitted to a Gaussian function. Results for parameters s_0 to s_4 (i.e. y, x, $\sin\phi$, $\tan\lambda$ and q/p_{T}) are shown from left to right and labelled from (a) to (e) accordingly.

fully corrected for, but a slight overestimation on parameter $s_4 = q/p_{\mathrm{T}}$ which was not seen in the equivalent toy MC test (see Fig. 4.9) is introduced.

To produce these results an ad-hoc correction to the multiple scattering calculation step of the `KF-Lite` reconstruction was introduced. This correction is applied in those propagation steps where the two consecutive hit clusters belong to different tracking planes and the particle is moving between them. In the toy MC the space between the tracking planes was simulated to be completely empty, while in the more realistic geometry used by `GArSoft`, they are filled with air at atmospheric pressure. The propagation of the particles in these passive portions of the detector produces additional multiple scattering uncertainties that, while small

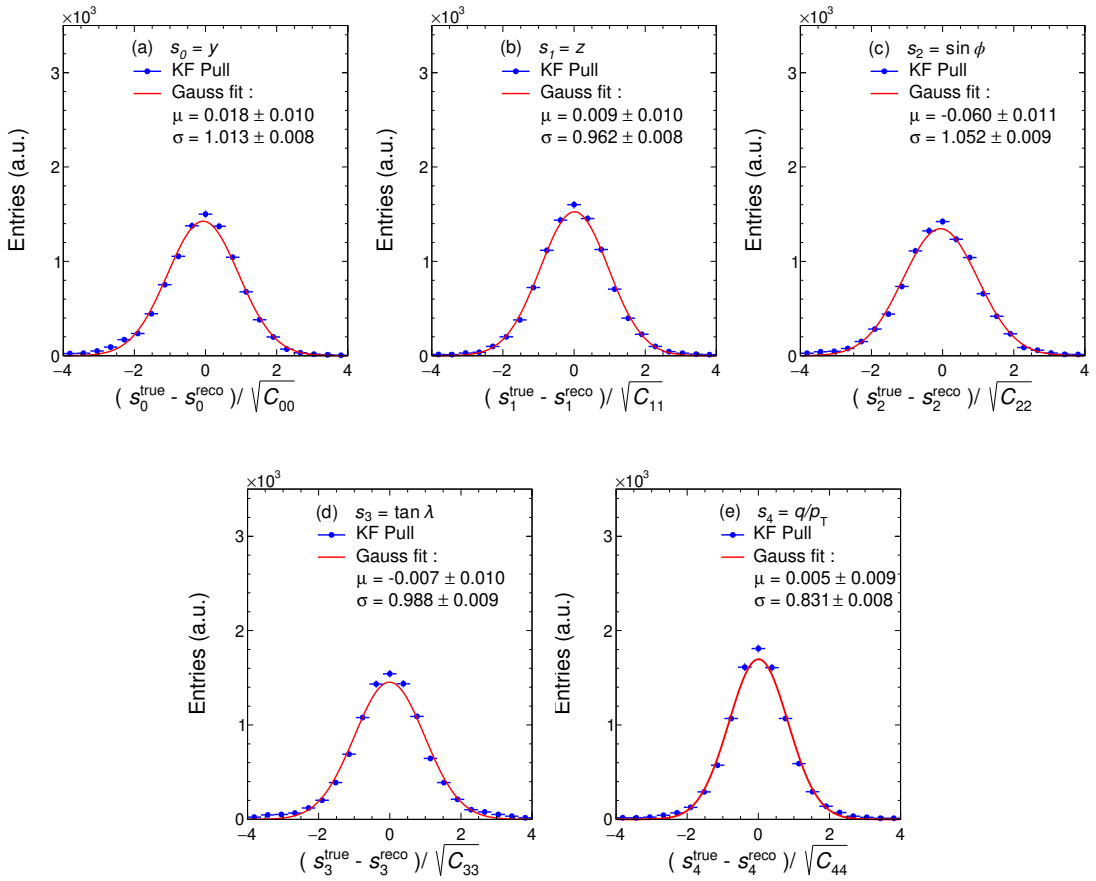

Figure 4.16: Pull distributions for the `KF-Lite` algorithm over the Lite-1 sample where the `Seed` algorithm was used. All distributions were fitted to a Gaussian function. Results for parameters s_0 to s_4 (i.e. y, x, $\sin\phi$, $\tan\lambda$ and q/p_{T}) are shown from left to right and labelled from (a) to (e) accordingly.

compared to the impact of the scintillator planes, are not completely negligible. In order to compensate for this underestimation a multiplicative factor of 4 is applied to the Q matrix described in Eq. 4.21. This factor was found by trial and error and was shown to produce the best pulls overall. A more proper treatment would have required to apply an additional correction step calculating the length of the trajectory between the planes and using the material properties of air. However this was not attempted as the ad hoc correction already showed satisfactory results.

The pull distributions obtained using the `ILRM` algorithm as the seeding algorithm are shown in Fig. 4.17. While the results don't show any bias the σ values for parameters $s_2 = \sin\phi$, $s_3 = \tan\lambda$ and $s_4 = q/p_{\mathrm{T}}$ are largely over-estimated

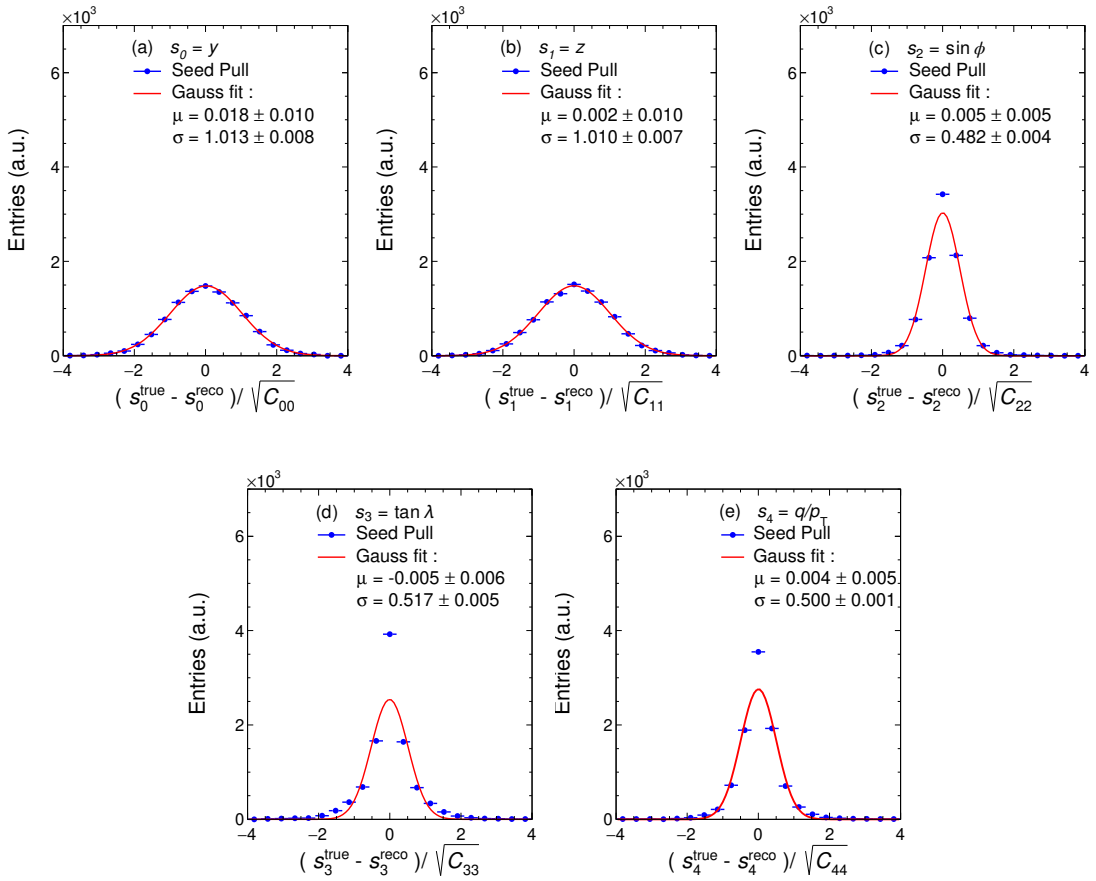

Figure 4.17: Pull distributions for the `ILRM` algorithm over the Lite-2 sample. All distributions were fitted to a Gaussian function. Results for parameters s_0 to s_4 (i.e. y, x, $\sin\phi$, $\tan\lambda$ and q/p_{T}) are shown from left to right and labelled from (a) to (e) accordingly.

by a factor of ~ 2. This is in line with the expectations for the reasons outlined in Section 4.3.1. Specifically the fact that the method used for the calculation of the C_0 matrix is only valid if just three points are used for the estimate, as it was intended for the `Seed` method.

After the full propagation of the `KF-Lite` algorithm the overestimation in the pulls are largely corrected for. This can be seen in Fig. 4.18 were the pulls are shown for the `KF-Lite` algorithm in the Lite-2 sample. All the σ are very close to 1 with the exception of $s_4 = q/p_{\mathrm{T}}$ for which a somewhat significant underestimation is seen. Note that the ad-hoc treatment needed for the propagation in air described for the Lite-1 sample was also used in this case.

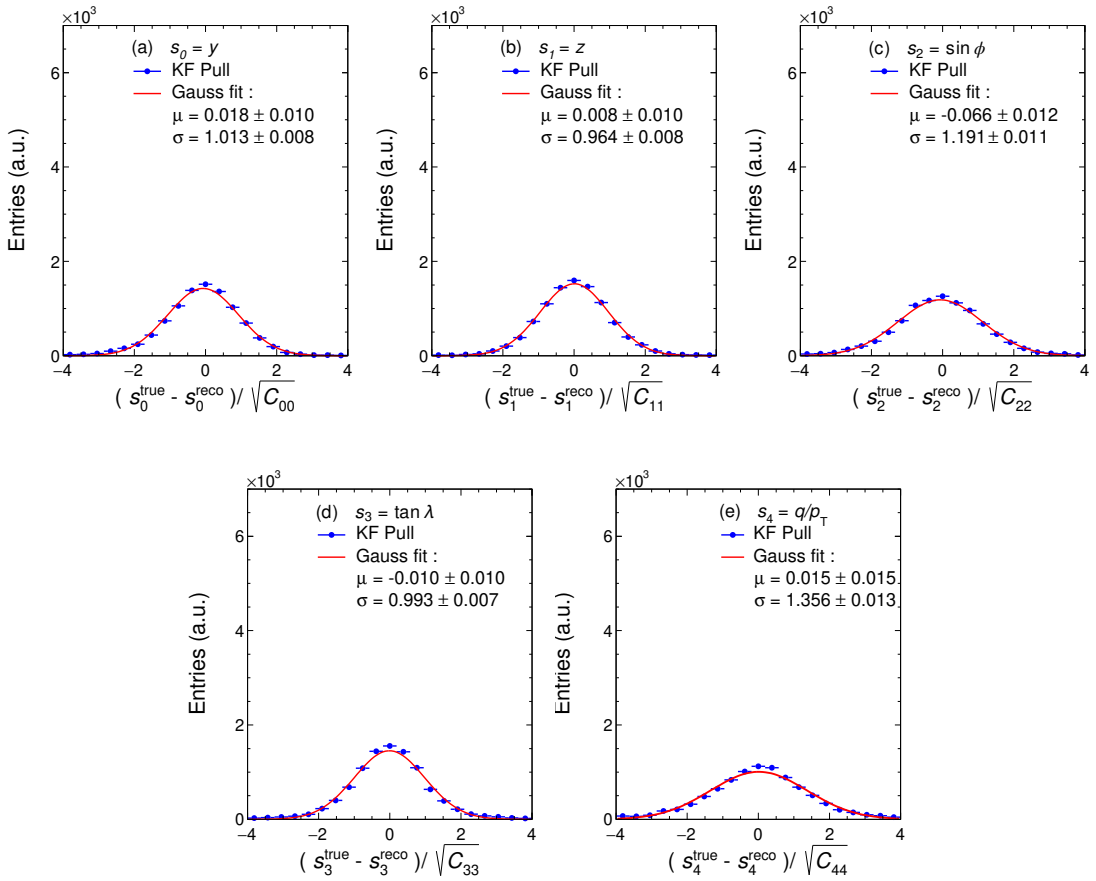

Figure 4.18: Pull distributions for the `KF-Lite` algorithm over the Lite-2 sample where the `ILRM` algorithm was used. All distributions were fitted to a Gaussian function. Results for parameters s_0 to s_4 (i.e. y, x, $\sin\phi$, $\tan\lambda$ and q/p_{T}) are shown from left to right and labelled from (a) to (e) accordingly.

For both the Lite-1 and Lite-2 we studied the total momentum resolution and bias. Both of these quantities can be defined as the σ and μ of a Gaussian fit applied to the momentum fractional residuals R as defined in Eq. 4.35. We also compared the results with the original fit results available from `GArSoft`, which were produced with the `ILRM` algorithm without any material budget correction. In Fig. 4.19 we show the residuals distributions for the Lite-1, Lite-2 and `ILRM` stand-alone algorithms. In all cases the distributions are fitted with a double Gaussian defining a core and tail distribution as it was done for the toy MC results. The residuals produced with the original reconstruction method are presented in Fig. 4.19c and show a very clear bias, that for the core distribution amounts to $\mu_{\mathrm{core}} = -4\%$. This

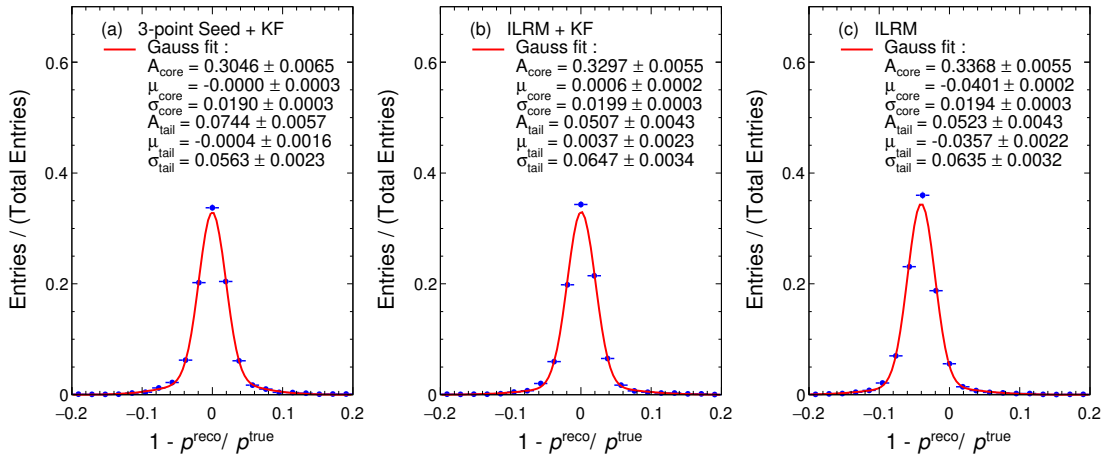

Figure 4.19: Momentum fractional residuals $R = p_{\text{reco}}/p_{\text{true}} - 1$ for the (a) `KF-Lite` paired with the 3-points `Seed` method in the Lite-1 sample (b) `KF-Lite` paired with the `ILRM` algorithm in the Lite-2 sample (c) the original `GArSoft` reconstruction which consists of the `ILRM` algorithm without any material budget corrections. In all cases the distributions were fitted with a double Gaussian function defining a core and a tail distributions.

bias is introduced by the lack of corrections for the energy loss of the particle and it's comparable to what was seen for the U sample `Seed` results in the toy MC study. The residual distributions produced both with the Lite-1 and Lite-2 versions of the algorithm, which are shown in Fig. 4.19a and 4.19b show no significant bias, while maintaining essentially identical resolutions to the original `GArSoft` method.

The relative momentum resolution and bias are also shown as a function of the number of points in the particle tracks N in Fig. 4.20a and 4.20b respectively. The two quantities are taken as the μ and σ of a simple Gaussian fit of the fractional momentum residual distributions. In black we show the results for the Lite-1 algorithm, in blue for the Lite-2 and in red for the original method. It is clear that no difference is present in terms of resolution, while for the bias the new algorithms largely outperform the old one. Additionally a somewhat significant preference is shown in terms of bias reduction with the Lite-1 algorithm compared to Lite-2. This is likely due to the better pulls produced by the `Seed` algorithm, which make the `KF-Lite` more stable.

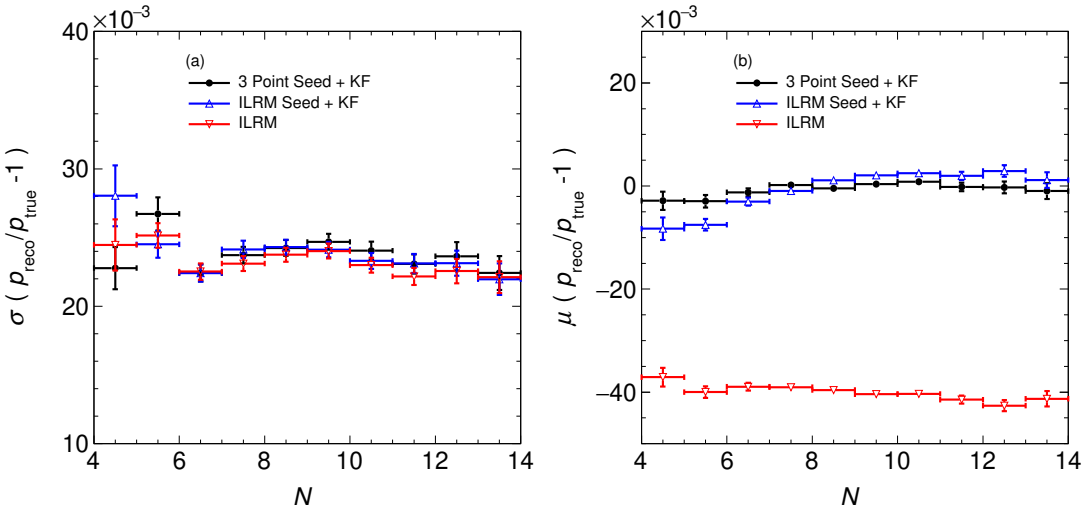

Figure 4.20: Relative momentum resolution σ (a) and bias μ (b) as a function of the number of hit clusters belonging to the track N. The results are shown in black for the Lite-1 sample, in blue for the Lite-2 sample and in red for the original reconstruction produced with GArSoft.

4.8 Results summary

In this chapter, we characterized the performance of the `KF-Lite` algorithm, described in Sec. 4.3. During the initial development phase, a dedicated toy Monte Carlo (MC) simulation (see Sec. 4.5) was used to assess individual components of the algorithm. This simulation supported a series of modular tests (see App. A.2), two of which were discussed in this chapter (tests 13.5c and 13.5.2c in Tab. A.1). For these studies, which were presented in Sec. 4.5, a toy sample of 5×10^3 forward-going muons was generated, with initial momenta uniformly distributed between 0.5 GeV/c and 4 GeV/c, propagating in the 6-plane ND-GAr-Lite geometry. Initial estimates for `KF-Lite` were provided by the `Seed` algorithm.

The goal of these tests was to show the efficacy of the energy loss and multiple scattering corrections applied to `KF-Lite`, as well as the internal consistency of the algorithm. `KF-Lite` was applied to the same data, first without and then with material budget corrections. The state vector estimates produced by the two configurations were evaluated with pull tests, both at the `Seed` and `KF-Lite` stages (Figs. 4.6, 4.7, 4.8 and 4.9). In the uncorrected (U) sample, uncertainties were

found to be underestimated by a factor of ~ 0.5 for $\tan\lambda$ and ~ 0.7 for $\sin\phi$ and q/p_{T}, directly reflecting the absence of material budget corrections. In the corrected (C) sample, the pulls exhibited $\mu \sim 0$ and $\sigma \sim 1$, with deviations no larger than 18%.

The `KF-Lite` corrections were also shown to be successful in improving momentum reconstruction. While both versions of the algorithm achieved the same resolution, the corrections reduced the bias by a factor of ~ 0.6. The results of the double Gaussian fit defined in Eq. 4.36, for the fractional momentum residuals, are summarized in Tab. 4.2 and shown in Figs. 4.10 and 4.11. The momentum resolution and bias were also plotted as a function of some key track characteristics (Fig. 4.12); for both samples, they were shown to qualitatively follow the theoretically expected dependencies expressed in Eqs. 4.37 and 4.38.

After validating `KF-Lite` in a toy MC environment, the algorithm was applied to data simulated with the more sophisticated `GArSoft` software suite, described in Sec. 4.4. The results were compared to those obtained with the uncorrected `ILRM` algorithm, which represented the standard reconstruction at the time, in Sec. 4.7. The simulated sample consisted of mono-energetic, forward-going muons with $p = 1$ GeV/c, chosen to approximate the conditions of muons originating in ND-LAr.

The corrected `KF-Lite` algorithm was tested with two different seeding strategies: the `Seed` and `ILRM` algorithms, described in Sec. 4.3.1. The corresponding results were labelled sample Lite-1 and Lite-2, respectively. In both cases, a full set of pull tests was performed (Figs. 4.15, 4.16, 4.17 and 4.18). For Lite-1, the pulls were shown to be largely successful for both the `Seed` and `KF-Lite`. On the contrary, in the Lite-2 sample, the `ILRM` uncertainties were shown to be overestimated by a factor ~ 2 for all state vector parameters, except the positions. This is attributable to the fact that the method used for the calculation of the C_0 matrix was intended for the `Seed` method, where only three points are considered. After the `KF-Lite` propagation, the estimated uncertainties were shown to be much closer to the correct values, with significant underestimations $\sim 20\%$ and $\sim 30\%$ on $\sin\phi$ and q/p_{T} respectively.

MC	toy		GArSoft		
Reco	U	C	Lite-1	Lite-2	ILRM
A_{core}	0.63 ± 0.03	0.61 ± 0.03	0.305 ± 0.007	0.330 ± 0.006	0.337 ± 0.006
μ_{core} (%)	0.6 ± 0.1	0.0 ± 0.1	0.00 ± 0.03	0.06 ± 0.02	-4.01 ± 0.02
σ_{core} (%)	3.0 ± 0.1	3.0 ± 0.1	1.90 ± 0.03	1.99 ± 0.03	1.94 ± 0.03
A_{tail}	0.16 ± 0.03	0.18 ± 0.03	0.074 ± 0.006	0.051 ± 0.004	0.052 ± 0.004
μ_{tail} (%)	1.7 ± 0.3	1.0 ± 0.3	0.04 ± 0.16	0.4 ± 0.2	-3.6 ± 0.2
σ_{tail} (%)	7.2 ± 0.5	7.2 ± 0.5	5.6 ± 0.2	6.5 ± 0.3	6.3 ± 0.3

Table 4.2: Summary of the momentum reconstruction performance evaluated for the KF-Lite and ILRM algorithms, in the different test configurations described in the chapter. The key parameters arise from double Gaussian fits, defined in Eq. 4.36, applied to fractional momentum residual distributions.

Both versions of the KF-Lite algorithm were shown to outperform the ILRM algorithm in terms of momentum reconstruction, by maintaining a similar level of resolution and completely removing a relative momentum bias of $\sim -3.6\%$. The results of the double Gaussian fits on the relative momentum residuals are summarized in Tab 4.2 and shown in Fig. 4.19. The resolution and bias were also shown as a function of the number of track points in Fig. 4.20.

5

Kalman filter Reconstruction for ND-GAr

Contents

5.1 Introduction

In this chapter we will describe a Kalman filter (KF) algorithm developed for particle tracking in the ND-GAr TPC. As outlined in Sec. 3.3 the ND-GAr TPC design is heavily inspired by ALICE and it will repurpose its MWPCs for signal

formation. ALICE is a nucleus-nucleus collision experiment, designed to study the physics of strongly interacting matter at extreme values of energy density and temperature. The gas TPC technology was chosen by the ALICE collaboration due to its robustness in providing charged-particle momentum measurements with good two-track separation, particle identification, and vertex determination, even at the extreme levels of occupancy reached in Pb-Pb collisions. A similar TPC, but relatively smaller, has been used by the STAR experiment at RHIC [159]. Recently, ALICE has undergone a significant upgrade [7], requiring new R&D in all areas of particle reconstruction.

Given the similarities between the detectors a collaboration was developed with the tracking experts from the ALICE experiment. The tracking algorithm developed for ND-GAr can be described as a KF application for a homogeneous cylindrical gaseous TPC, which is based on and expands the track fitting algorithm developed by the ALICE experiment. Part of the code is directly taken from `AliExternalTrackParam`, the ALICE TPC KF framework [146, 147, 160].

The KF developed by the ALICE experiment for track formation and reconstruction can be considered the state of the art in the field [142, 143], but it has some limitations which make its direct application to a neutrino experiment such as ND-GAr problematic. The parametrisation used by the ALICE experiment's KF is such that it can only follow tracks that describe at most a semicircle in the plane perpendicular to the magnetic field, introducing non-physical breaking points in the reconstruction. Using a simple mirror rotation operation, the new algorithm is capable of following the track indefinitely, especially in the case of low-energy, low-mass (i.e. low energy loss) particles which form several circular trajectories inside the detectors, also known as "loopers". The application of this novel technique is particularly relevant for a neutrino experiment detector such as ND-GAr, for which particles are relatively low energy and are produced in neutrino interactions on gas at random points in the TPC volume. While many points of

contact exist with the ND-GAr-Lite `KF-Lite` algorithm such as the shared ALICE-inspired parametrisation, several differences exist and the ND-GAr KF code was developed mostly independently and treated as a separate project.

The testing of the algorithm proceeded in two stages, much like for the `KF-Lite` algorithm (see Chapter 4). We first produced a modular toy Monte Carlo (MC) tool capable of generating and propagating arbitrary particle tracks in a simplified detector geometry. This tool, which will be referred to as `fastMCKalman`, has been used to develop and test the algorithm [161]. Much like the ND-GAr-Lite toy MC tool, `fastMCKalman` was conceived to be highly modular and allowed to test many features of the algorithm independently. Once the reconstruction algorithm was considered to be fully developed, it was applied to data generated using `GArSoft`, the ND-GAr software suite (see Sec. 4.4), and its performance was compared to the reconstruction already available for the detector. Finally, once the reconstruction improvements were demonstrated, the algorithm was fully integrated in `GArSoft` and proved to behave identically to the independent software contained in `fastMCKalman`.

This Chapter will be organized as follows: in Sec. 5.2 we describe the ND-GAr KF, outlining the difference with the `KF-Lite` algorithm; in Sec. 5.3 we describe the `fastMCKalman` toy MC tool; in Sec. 5.4 we describe the components of `GArSoft` that are unique to ND-GAr, including its original reconstruction algorithm; in Sec. 5.5 we describe the testing done for the algorithm using `fastMCKalman`; in Sec. 5.6 we describe the implementation of the algorithm in `GArSoft`; finally, in Sec. 5.7, we summarize the results.

5.2 The Kalman filter applied to ND-GAr

The KF described in this section has been developed to be used in an homogeneous cylindrical gas TPC. Much of the algorithm is analogous to the one described for ND-GAr-Lite in Sec. 4.3, as both have been based on the same original ALICE TPC KF. However, the code which actualizes the ND-GAr algorithm was developed in the context of the `fastMCKalman` tool largely independently and used directly parts

of the ALICE TPC KF framework `AliExternalTrackParam`. The KF algorithm was also described in a recent publication [141].

The coordinate system defined for the algorithm is the same as the one used for the `KF-Lite` algorithm. Simplifying the geometry of the gas TPC to that of a cylinder, the z coordinate is its height and the xy plane is its base, with the x being the horizontal direction and y being the vertical. We assume that an ideal magnetic field is applied along z which is the drift direction. Deviations from the ideal mono-directional magnetic field lines can be simulated and be accounted for using the infrastructure available in `AliExternalTrackParam`, but were not implemented. The spatial information in the perpendicular xy plane is taken to be given by detector elements disposed in radial layers on the two sides of the cylinder.

The algorithm is evolved along the free parameter, x, and its state vector follows the same parametrisation outlined in Eq. 4.14 for the `KF-Lite` algorithm. A visual representation of the coordinates is given in Fig. 4.2. The evolution of the state vector is divided into two steps: a rotation of the global coordinates to a local frame and a propagation along the helix trajectory. The rotation is applied in the xy plane around the centre of the TPC cylinder. The rotation angle $\alpha = \arctan(y/x)$ is defined so that the x coordinate becomes the radial distance from the centre of the TPC and the y coordinate is ~ 0. After the rotation the state vector is moved along the trajectory using a propagator function, as described in Eq. 4.1. The propagator function used for this algorithm is identical to the one outlined in Eq. 4.16 but is applied in local rotated coordinates. The propagation matrix, F_k, is also similarly calculated to the `KF-Lite` algorithm, as the Taylor expansion coefficient $\partial f_k/\partial s_k$ described in Eqs. 4.12 and 4.13, with the exception of the q/p_{T} term, which is treated separately.

In order to compute the momentum loss, Δp_k, at each trajectory point, the ionization energy loss, $-\mathrm{d}E/(\rho \mathrm{d}x)$ (where ρ is the density of the material), of the particle is evaluated using the standard Bethe-Bloch formula in Eq. 2.76. The differential energy loss, $-\mathrm{d}E/(\rho \mathrm{d}x)$, is calculated using the properties of the most abundant gas present in the gas mixture in standard conditions and then

multiplied by the material's density to obtain a reasonable approximation of the $\mathrm{d}E/\mathrm{d}x$ [144]. The total momentum loss between two steps is then calculated by numerical integration [145].

In the evaluation of F_k, the q/p_T parameter is treated as if it were static. A correction term, c_k is added to the q/p_T diagonal element of the covariance matrix, $\widetilde{C}_k$, after the propagation step (see Eq. 4.17). Similarly, the multiple scattering is treated through the noise correction matrix, Q_k outlined in Eq. 4.21, which is derived from the calculation of the scattering angle.

Each step in the evolution of the KF can potentially fail, in which case the algorithm is stopped. This can happen mainly in two scenarios: $\sin\phi$ can be calculated to be out of range, i.e. $|\sin\phi| > (1 - 10^{-7})$ or the particle can lose all its remaining kinetic energy. Once the KF is stopped, the information for each of the reconstructed points is saved. Flags are used to preserve information on which of the reconstruction steps have been successful and which have failed.

One inherent limitation exists in the propagator function in Eq. 4.16, specifically in the equation describing the evolution of $\sin\phi$. The formula can only be applied within the range of $\sin\phi \in [-1, 1]$, which describes one semi-plane. For $|\sin\phi| \to 1$ the uncertainty on the parameter tends to infinity and the operation is no longer well defined. In radial coordinates this coincides with the moment when the particle is moving parallel to a detector's radial layer and the radial direction of the propagation is inverted. In order to overcome this limitation and further evolve the KF, one can apply a "mirror rotation" or reflection on the state vector [162]. The mirror plane is the one perpendicular to the xy-plane, which connects the coordinate frame's centre (i.e. the centre of the TPC) with the centre of the circular motion of the particle. In the local coordinate frame the mirror rotation is linear and can be written as:

$$\begin{cases} s_k^\mathrm{M} = M s_k, \\ C_k^\mathrm{M} = M C_k M^T, \end{cases} \quad \text{where } M = \begin{bmatrix} 1 & 0 & 0 & 0 & 0 \\ 0 & 1 & 0 & 0 & 0 \\ 0 & 0 & -1 & 0 & 0 \\ 0 & 0 & 0 & -1 & 0 \\ 0 & 0 & 0 & 0 & -1 \end{bmatrix}. \tag{5.1}$$

The angle α, which defines the local coordinate frame, needs to be updated accordingly. This is done by finding the angle α_{C} corresponding to the mirror plane, and updating α as:

$$\begin{aligned} \alpha_k^{\mathrm{M}} &= \alpha_{\mathrm{C}} - \Delta\alpha \\ &= \alpha_{\mathrm{C}} - (\alpha_k - \alpha_{\mathrm{C}}). \end{aligned} \tag{5.2}$$

Finally, to update the z position the angular displacement around the centre of rotation is calculated as:

$$\Delta\phi_C = 2\arcsin\left(\frac{\Delta_{xy}}{2r_k}\right), \tag{5.3}$$

where Δ_{xy} is the distance between the two points in the xy plane. From $\Delta\phi_C$, the correspondent circumference arch in the xy plane, a_{xy}, can be found, and from it, the displacement in the drift direction, Δz_k, reads:

$$\begin{aligned} \Delta z_k &= a_{xy} \cdot \tan\lambda_k \\ &= \Delta\phi_C \cdot r_k \cdot \tan\lambda_k. \end{aligned} \tag{5.4}$$

Once all the mirror operations are complete the closest trajectory point is found and the KF is further evolved from there. From this point onwards we will refer to the KF algorithm, not including the mirroring operation as the Basic KF or `BKF`. We will refer to the full algorithm, which includes both the `BKF` and the mirroring operation as the Corrected KF or `CKF`. A flow chart describing the algorithm is shown in Fig. 5.1.

The seeding strategy used for the `CKF` (as well as for the `BKF`) consists in the simple three-point circle finding algorithm which was also used for the KF algorithm developed for ND-GAr-Lite described in Sec. 4.3.1. Similarly to what was done for the ND-GAr-Lite seeding algorithm, this will be referred to simply as `Seed`. The only notable difference between the two algorithms is that, while for the ND-GAr-Lite algorithm, only the diagonal elements of C_0 were calculated, in this case the off-diagonal terms are also considered.

The `Seed` estimation for both the covariance matrix C_0 and the state vector s_0 is adjusted for energy loss and multiple scattering using the same method outlined the ND-GAr-Lite algorithm. The total distance traveled, needed to calculate total

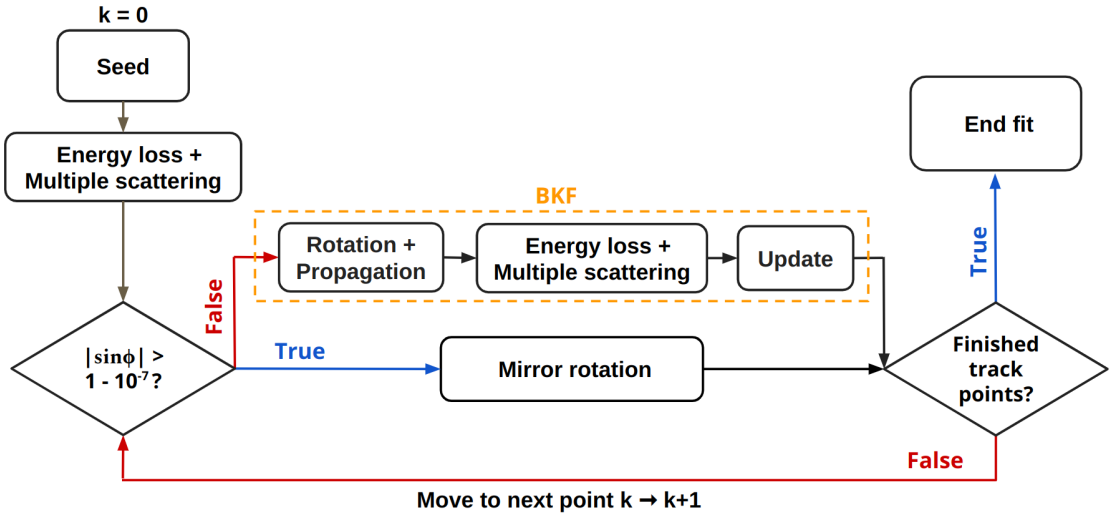

Figure 5.1: Flow chart describing the CKF algorithm. A seeding algorithm is used to obtain an estimate for the status of the system at the start of the trajectory $k = 0$. Energy loss and multiple scattering corrections are applied to the estimate. The fit is then moved to the next point $k \to k+1$ either by applying the BKF procedure or by using the mirror rotation, in the case that the limits of the $\sin\phi$ range have been surpassed. The algorithm is iterated point by point until the end of the trajectory is reached. Other minor modifications have been made to the CKF algorithm compared to the BKF in order to make the mirroring operation more stable.

energy loss and the scattering angle θ_{M}, is determined by summing the distances between the starting and midpoint, and the endpoint used for circle finding.

5.3 The toy Monte Carlo simulation

To generate particle samples and validate the CKF algorithm, we developed a toy MC tool called `fastMCKalman` [161]. This tool, stemming from the `AliExternalTrackParam` framework in the `AliRoot` code-base [160], was designed to be complemented by `RootInteractive` [163], an advanced statistical analysis tool. `fastMCKalman` has been developed with several objectives in mind: conducting rapid MC simulations to evaluate tracking performance metrics, particle identification, and time-of-flight measurements across various detector setups. It was also designed to facilitate detailed studies on signal distortion in the ALICE detector and the derivation of performance metrics for its Run-3 upgrade and future iterations. It's important to note that the studies presented in this Chapter and in Ref. [141], represent the first use of this fast simulation tool and serve as part of its validation process. The

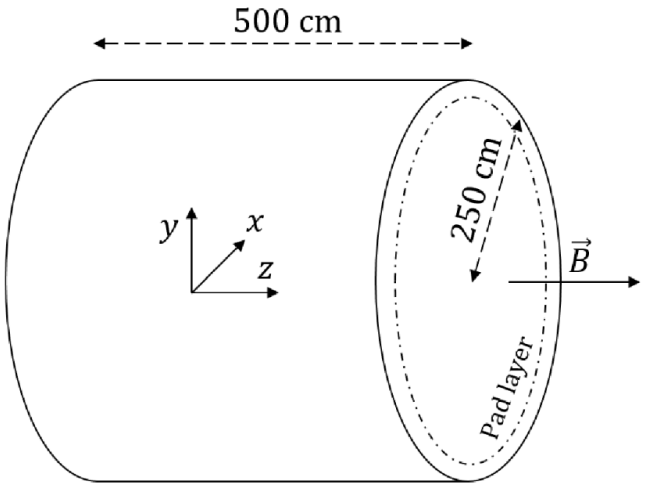

Figure 5.2: Diagram of the simplified detector geometry, showing the direction of the magnetic field and the position of one of the radial pad layers.

use of fast MC tools to complement more extensive generators such as Geant4 [157, 164, 165], are commonplace in high energy physics. The ALICE experiment, for example, implements independent MC components in its simulation pipeline, to model detector effects that would be difficult to simulate using a more standard MC generator [166]. This is the envisioned future use of `fastMCKalman`. However, as of now, only basic effects such as multiple Coulomb scattering and energy loss through ionization have been implemented. In order to ensure the agreement of `fastMCKalman` with more traditional MC generators, the formulas used to simulate these effects are the same implemented by Geant4. Additionally the agreement of the `fastMCKalman` simulation with theoretical expectations is tested as part of the validation of the `CKF` algorithm in Sec. 5.5.2.

The first step in the toy MC simulation consists in defining a simplified detector geometry. The radius and length of the TPC cylinder are specified, together with the number of pad rows, the spatial resolution of the detector in the radial and drift directions (defined as $\sigma_{r\phi}$ and σ_Z respectively) and the gas properties (i.e. the radiation length in cm, X_0, the density in g/cm^3, ρ, and the gas pressure in atm, P_{gas}). A diagram of the detector cylinder is shown in Fig. 5.2.

Each simulated particle is defined by specifying its mass, charge, transverse momentum, p_{T}, azimuth angle, ϕ, dip angle tangent, $\tan\lambda$, and the starting

position. From this information, the initial MC-true (henceforth "true") state vector s_0^{true} is built. The true state vector is moved through the detector by applying the same operations of the propagation steps of `CKF` in reverse, moving from layer to layer of pads.

The propagation of the state vector is obtained by applying Eq. 4.16. At each step the energy loss is calculated using the Bethe-Bloch formula as described in Eq. 2.76 and multiplying by the distance traveled and the material density. The energy loss is then converted in the q/p_{T} multiplicative factor described in Eq. 4.16 and smeared with a Landau distribution having a width equal to the c_k factor described in Eq. 4.17. The multiple scattering effects are simulated by calculating root mean square θ_{M} of the scattering angle distribution and from that the process noise matrix Q. The diagonal elements of the matrix are then used as the widths of smearing Gaussian distributions that are applied to parameters $s_2 = \sin\phi, s_3 = \tan\lambda$ and $s_4 = q/p_{\text{T}}$. To reproduce the measurement noise encapsulated in matrix R, a Gaussian smearing is applied to the position parameters $s_0 = y$ and $s_1 = z$. The widths of the distributions are equal to the position resolutions $\sigma_{r\phi}$ and σ_z respectively. Note that the energy loss and multiple scattering elements of the simulation as well as the relative corrections applied in the reconstruction could be applied and set independently, similarly to what was done for the ND-GAr-Lite toy MC tool described in Sec. 4.5.

The propagation continues until any of the following happens: the particle reaches the edges of the detector cylinder; the particle looses all its remaining kinetic energy; one of the propagation steps fails. Once the track is fully generated, the track fit is done as described in Sec. 5.2. No element of track formation or particle identification is included. After saving all information, a new simulation and track fit start.

5.4 `GArSoft` for ND-GAr

As already described in Sec. 4.4 `GArSoft` is the software toolkit which handles the simulation and reconstruction of events inside ND-GAr and ND-GAr-Lite

[150]. The event generation and particle propagation are shared between the two detectors and are outlined in Sec. 4.4.1. The TPC signal formation, digitization and reconstruction however are completely separate for ND-GAr and will be described in this section.

5.4.1 TPC signal formation, digitization and hit finding

The `GArSoft` signal formation for the ND-GAr TPC takes the energy deposits produced by Geant4 as input (see Sec. 4.4.1). These are used to simulate ionization in the gaseous medium using the untuned Birks' model for recombination [167]. The simulation of the scintillation photons that would be produced by the passing particle is not yet implemented. The ionized electrons drift is simulated by numerically integrating over the longitudinal and transverse diffusion distributions using a constant drift velocity and exponential electron lifetime factor. Electrons are registered on the nearest readout pads after the diffusion simulation has displaced them by a random amount proportional to the square root of the drift time. Note that the readout pads are placed radially at the two ends of the TPC cylinder, similarly to what was described for `fastMCKalman`.

Since the exact electronics to be paired to the MWPC has not yet been decided, no pulse shaping by the readout electronics nor any noise is yet simulated in `GArSoft` and the signal gain is arbitrarily set. The Analogue to Digital Converter (ADC) sampling period is assumed to be 198 ns with an event readout containing 18048 samples. Raw waveforms are saved as "raw digits" with no suppression using a simple thresholding technique.

In `GArSoft` a hit refers to a pulse that has been found and fit on a single channel, following the convention defined by LArSoft. A hit-finding algorithm is used in `GArSoft` to identify the over-threshold blocks in the raw digits that can be mapped onto hits. In the case they surpass a threshold length or the waveform is found to dip below a fraction of their maximum and go back up again, the hits are split. Finally, in order to reduce their number and improve their spacial resolution,

nearby hits in time and space are grouped in hit clusters. The charge centroids of the hit clusters are then found and saved.

5.4.2 Track formation

Track identification in `GArSoft` proceeds in two steps: first the hit clusters are collected into segments called vector hits, then these are combined together into track candidates. Vector hits are identified using linear fits on the hit clusters as a function of (x, y, z). An initial segment of 10 cm is defined by choosing a pair of hit clusters and finding the line passing through them. All hit clusters that lie at most 2cm away from the segment are added to the vector hit. Every time a cluster is added the line segment is refit. Six linear 2D fits are applied, choosing all combinations of coordinate pairs and directions. To define the 3D direction of the vector hit the independent coordinate of the fit is chosen to be the one with the smallest sum of absolute values of slopes. Once all clusters are assigned to vectors, a check on the quality of the fits is performed: if the values of the χ^2 surpass a threshold value, the clusters contained in a vector are released and they are either added to other vector hits or used to form new ones.

Once the vector hits are found they are grouped to form track candidates following a series of criteria. Specifically a vector hit is added to a track candidate if it passes the criteria for at least one of the vector hits already in the track candidate. To describe the test conditions we'll use the following notation: the position and direction vectors of the test vector hit already in the track are written as $\vec{p}_i$ and $\vec{v}_i$ respectively, while the same quantities for the vector hit candidate are written as $\vec{p}_c$ and $\vec{v}_c$.

The first condition is that the dot product between the directions doesn't surpass a threshold of 0.9:

$$|\vec{v}_c \cdot \vec{v}_i| < 0.9. \tag{5.5}$$

A condition is also imposed on the distance between the vector hits, which must be at most 60 cm:

$$|\vec{p}_c - \vec{p}_i| < 60\text{cm}. \tag{5.6}$$

Vector hits must also points towards each other. This can be checked using the "miss distance" which is defined as the cross product between the vector distance between the two centers of the vector hits and their directions. The condition is that the miss-distances must be smaller that 6 cm:

$$\begin{aligned} |(\vec{p}_c - \vec{p}_i) \times \vec{v}_i| < 6 \text{ cm}, \\ |(\vec{p}_c - \vec{p}_i) \times \vec{v}_c| < 6 \text{ cm}. \end{aligned} \tag{5.7}$$

To form a track candidate the vector hits also need to lie on a circle in the xy plane, which is parallel to the direction of the electric and magnetic fields in the TPC. For this to be true the average of the directions must point along the displacement between the centers. We define the xy plane displacement between the vector hit centers as:

$$\vec{t} = \hat{x}(\vec{p}_i - \vec{p}_c) \cdot \hat{x} + \hat{y}(\vec{p}_i - \vec{p}_c) \cdot \hat{y}, \tag{5.8}$$

where $\hat{x}, \hat{y}, \hat{z}$ are the unit vectors along the x, y and z directions respectively. We define the 2D unit vectors pointing along the vector hits in the xy plane as:

$$\begin{aligned} \vec{u}_i &= \frac{\hat{x}\vec{v}_i \cdot \hat{x} + \hat{y}\vec{v}_i \cdot \hat{y}}{|\hat{x}\vec{v}_i \cdot \hat{x} + \hat{y}\vec{v}_i \cdot \hat{y}|}, \\ \vec{u}_c &= \frac{\hat{x}\vec{v}_c \cdot \hat{x} + \hat{y}\vec{v}_c \cdot \hat{y}}{|\hat{x}\vec{v}_c \cdot \hat{x} + \hat{y}\vec{v}_c \cdot \hat{y}|}. \end{aligned} \tag{5.9}$$

We can now define the signed direction sum as:

$$\vec{s} = \vec{u}_i + \frac{\vec{u}_c \cdot \vec{u}_i}{|\vec{u}_c \cdot \vec{u}_i|}\vec{u}_c. \tag{5.10}$$

Finally we can define η as :

$$\eta = \left| \frac{\vec{s}}{|\vec{s}|} \times \vec{t} \right|, \tag{5.11}$$

which is used for the condition $\eta < 1.2$ cm. Unlike the previous criteria which are only applied to individual couples of vectors, the η test is applied between the candidate and test vector as well as all the other vectors belonging to the track candidate within a 20 cm radius; if just one of the tests fails the match is dropped.

The final test is a required match between the vector hits, where λ is computed as:

$$\begin{aligned} \lambda_i &= \tan^{-1}\left(\frac{|\hat{z}\cdot\vec{v}_i|}{\sqrt{(\hat{y}*\vec{v}_i)^2+(\hat{x}\cdot\vec{v}_i)^2}}\right), \\ \lambda_c &= \tan^{-1}\left(\frac{|\hat{z}\cdot\vec{v}_c|}{\sqrt{(\hat{y}*\vec{v}_c)^2+(\hat{x}\cdot\vec{v}_c)^2}}\right), \end{aligned} \tag{5.12}$$

for the test and candidate vector respectively. The match condition is :

$$|\lambda_i - \lambda_c| < 0.05. \tag{5.13}$$

An additional requirement on the relative signs of the slopes is applied only if the absolute value of the z component of $\vec{v}_i$ and $\vec{v}_c$ both exceed 0.01:

$$(\vec{v}_c\cdot\vec{v}_i)(\vec{v}_c\cdot\hat{z})(\vec{v}_i\cdot\hat{z}) > 0. \tag{5.14}$$

Once all the hit clusters are assigned to track candidates their order within the track is defined using a sorting algorithm. The first step in the sorting procedure consists in finding all the distances between the hit clusters. Then two links per point are defined purely based on shortest-distance arguments, avoiding the creation of cyclical loops. Finally a chain is created matching the links. Tracks and hit clusters are assigned to MC-truth particles using a backtracker.

While the current track finding implementation in `GArSoft` is in a relatively mature state, some issues exist that need to be acknowledged. The algorithm has a tendency of adding vector hits to the wrong track or joining two tracks together. This happens most often close to the neutrino interaction vertex, where many particles tracks are formed close in position and direction. The error is also relatively common in the case of the electron and positron tracks produced in photon conversions. The opposite error, consisting in breaking longer tracks

in smaller segments, is also relatively common. This can happen for a variety of reasons: track may have a scatter "kink" partway along it, or a delta ray may be emitted, or some hit clusters from another track may get misassigned to a vector hit, causing it to point in the wrong direction or to be displaced from the track. This effect is again especially noticeable close to the primary interaction vertex, where hit clusters from more than one track can be confused and vector hits may point in the wrong direction. Ways to improve the performance of the pattern recognition could include allowing the track fitter to reassign TPC clusters to tracks, or to make a second pass through hit assignment once the track parameters have been estimated.

5.4.3 Track Fitting

To compute the best estimates of the track parameters on both ends of the track, `GArSoft` employs a pre-existing algorithm based on the KF technique. While several aspects of this fitter are different from what was described in Sec. 5.2, the key operational steps are identical. From now on we will refer to the original `GArSoft` KF algorithm as the `GKF`.

We start by defining the state vector parametrisation used to identify the track helix trajectories in the TPC. As discussed in Sec. 5.2 to uniquely define any helix trajectory produced by a charged particle in a magnetic field, one needs a 5-dimensional state vector which is a function of a sixth free parameter. Keeping the same coordinate system originally defined in Sec. 4.3 and 5.2 the `GArSoft` parametrisation uses z as the free parameter and defines the state vector as:

$$s_G = (y, x, 1/r, \phi, \lambda) \tag{5.15}$$

where all the parameters are defined identically to the parameters in 4.14. The main difference with the ALICE parametrisation used for the `BKF` and `CKF` consists in the choice of z as the free parameter and the use of ϕ instead of $\sin\phi$. The use of z as the free parameter is somewhat problematic. This is because for the tracks produced in ND-GAr, which are expected to be mostly forward going, the motion in the direction of the magnetic field is typically small. Additionally, by choosing the free

parameter x (as for the `CKF` or `KF-Lite`) the algorithm steps are naturally defined by the different pad layers. The identification is less straight-forward if z is chosen. The state vector is evolved along the helix trajectory using the propagator function:

$$\widetilde{s}_G^k = f_{k-1}(s_G^{k-1}) = \begin{cases} \widetilde{y}_k = y_{k-1} + \Delta z_k \cot\lambda_{k-1} \sin\phi_{k-1}, \\ \widetilde{x}_k = x_{k-1} + \Delta z_k \cot\lambda_{k-1} \cos\phi_{k-1}, \\ 1/\widetilde{r}_k = 1/r_{k-1}, \\ \widetilde{\phi}_k = \phi_{k-1} + \Delta z_k (1/r_{k-1}) \cot\lambda_{k-1}, \\ \widetilde{\lambda}_k = \lambda_{k-1}, \end{cases} \tag{5.16}$$

where Δz_k is the distance in the z direction between the previous and current point. The propagation matrix, F_k, is calculated as the Taylor expansion coefficient $\partial f_k/\partial s_k$, as described in Eqs. 4.12 and 4.13.

It's important to note that the evolution equation for the ϕ angle makes use of a small angle approximation $\Delta sin\phi_k \simeq \Delta\phi_k$. Analogously the evolution equations for the y and x parameter approximate an arch motion with a segment linear motion. This is not true for the evolution function described in Eq. 4.16 where all formulas were exact. While this approximation is well justified in the case the consecutive points in the track are very close together, it can produce errors if the condition is not met. These limitations make it so that the `GKF` isn't problematic for tracks confined inside the TPC, but it is in case of large gaps making the connection points from other detector elements (i.e. ND-LAr or the ECAL) complex. By using the angle ϕ rather than its sine, however, the algorithm partially avoids the semi-circle limitation discussed in Sec. 5.2 and is allowed to propagate for an entire circle.

Another key difference with the `CKF` algorithm is that no energy loss treatment is implemented. The $1/r$ parameter is left completely static and no factor such as the one described in Eq. 4.17 is added to F_k. As it will be shown in Sec. 5.6 this omission produces biases in the momentum estimation, especially in the case of heavier particles such as protons. Similarly, no treatment of multiple scattering is implemented in the algorithm. A process noise matrix Q is added to the covariance

matrix as described in Eq. 4.7, but rather than being derived using the Molière angle as described in Eq. 4.21, it is set as a constant arbitrary term:

$$Q = \begin{bmatrix} 0 & 0 & 0 & 0 & 0 \\ 0 & 0 & 0 & 0 & 0 \\ 0 & 0 & 10^{-9} & 0 & 0 \\ 0 & 0 & 0 & 10^{-9} & 0 \\ 0 & 0 & 0 & 0 & 10^{-4} \end{bmatrix}. \tag{5.17}$$

Not evaluating the effects of multiple scattering punctually, is bound to produce an incorrect estimation of the uncertainties related to angle and momentum terms, damaging the precision that the algorithm is able to achieve. The noise matrix R is also left static using the resolution factors $\sigma_y = \sigma_x = 2$cm, which are chosen arbitrarily and don't reflect the actual resolutions of the hit clusters. The filtering step of the algorithm is performed in the standard way as described in Eq. 4.8.

The seeding procedure which was paired to the `GKF` consists in the `ILRM` algorithm described in Sec. 4.3.1. The `ILRM` algorithm only provides an initial estimate for the state vector s_0^G. The initial covariance matrix C_0 is not estimated and is set arbitrarily as:

$$C_0 = \begin{bmatrix} 1 & 0 & 0 & 0 & 0 \\ 0 & 1 & 0 & 0 & 0 \\ 0 & 0 & 0.25 & 0 & 0 \\ 0 & 0 & 0 & 0.25 & 0 \\ 0 & 0 & 0 & 0 & 0.25 \end{bmatrix}. \tag{5.18}$$

While only a very rough estimate of the initial covariance matrix is needed for a KF algorithm to function, if the uncertainties are assigned in a fully arbitrary way ,several steps of the algorithm are wasted determining the general shape of the matrix, reducing the final resolution.

5.4.4 Vertex finding and fitting

The vertex-finding algorithm implemented in `GArSoft` takes as input all the track candidates identified for an event and groups them together based on the position of their endpoints. A track endpoint is a candidate for vertexing with another track endpoint if they are within 12 cm of each other. Vertices are fit with a linear

extrapolation from the endpoints of each track. A list of found vertices and tracks is kept so that a track is not vertexed with itself even if it loops around in the magnetic field, and two tracks cannot be vertexed with each other more than once. Tracks and track ends may contribute to more than one candidate vertex. The vertex fitting algorithm used in `GArSoft` is not fully mature and several improvements are being considered. Using helical extrapolations of tracks from the ends, calculating the covariance matrix of the vertex spatial coordinates, and improving the track association selection criteria are all things that can improve the vertexing.

5.5 The toy Monte Carlo study

Similarly to what was described in Sec. 4.6 The `fastMCKalman` package was firstly used to develop a series of tests that were meant to validate each aspect of the reconstruction separately. These consisted in modifying the simulation conditions, including the particle types, the resolution of the pads, and especially the energy loss and multiple scattering and investigating the performance of the `CKF` and `BKF` algorithms. This series of tests are described summarized in App. A.2.

Once all the aspects of the simulation and reconstruction were considered to be in a mature state, one final summary study was produced and described in a publication for Computer Physics Communications [141]. The study focussed on two specific samples, the first of which included a spectrum of different detector characteristics and particle properties and was used to validate the algorithm across a wide range of parameter space. To analyse this sample, a recently developed interactive data visualization tool called `ROOTInteractive` was used [163]. The second sample was designed to produce performance estimates for a HPgTPC similar to ND-GAr. In this section we will focus on the results of this study, taking most of the material from the publication itself.

5.5.1 Sample Definition

The aforementioned `fastMCKalman` was used to produce two separate samples, simulated in the same simplified gas TPC geometry. The TPC has a cylindrical

form with a radius $r = 250$ cm and the length of the cylinder is taken as $L = 500$ cm. There are 250 circular layers of pads placed radially at each of the two end caps ($z = \pm 250$ cm). A magnetic field of intensity $B = 0.5\ T$ is placed in the drift direction along the cylinder axis.

The first sample, which includes a total of 5×10^5 tracks, contains a wide variety of detector properties, particle types and energies and was used to validate the `CKF` algorithm and its `Seed` in as wide a parameter space as possible. We will refer to this sample as the parameter scan sample or PS sample. The PS sample is composed of two equally large sub-samples with different starting position distributions: a sample of primaries—emulated as in a collider event geometry—starting from the centre of the detector $(x, y, z) = (0, 0, 0)$ cm and a sample of secondaries with randomized starting positions within a fiducial cylinder of radius $r = 200$ cm and length $l = 400$ cm. The initial spatial distribution of the secondaries in the sample is shown in Fig. 5.3.

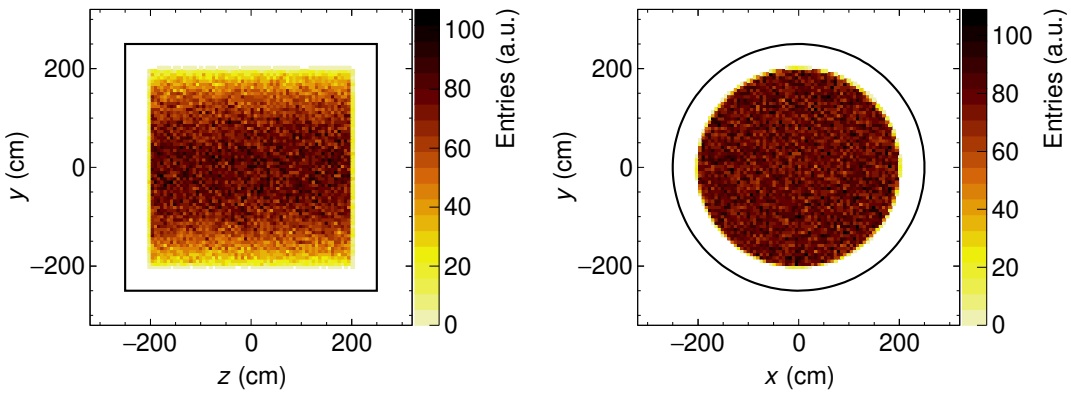

Figure 5.3: Starting positions for secondary particles in the PS sample. The primaries are not shown, as all of their starting positions are in $(x, y, z) = (0, 0, 0)$. The left plot shows the distribution in the zy plane, while the plot on the right shows the distribution in the xy plane. The edges of the TPC are drawn on top.

The tracking pad response as well as the gas properties of the detector are sampled in each simulated event: the resolutions $\sigma_{r\phi} = \sigma_z$ are uniformly distributed

between 0.1 cm and 0.5 cm and the pressure P_{gas} was randomized between 0.1 atm and 10 atm. The gas composition was taken to be the Ne/CO2/N2 (90/10/5) gas mixture used by the ALICE experiment during Run-1 [6]. The radiation length and density of the gas at atmospheric pressure are $X_0 = 1.2763 \times 10^4$ cm and $\rho = 0.0016265$ g/cm^3. The particles produced are equally divided in electrons, muons, pions, kaons and protons, corresponding to the ALICE convention for particle types, t_{ID}, 0, 1, 2, 3, and 4, respectively. The angles ϕ and λ are fully randomized. The initial p_{T} is sampled from a two-component distribution: a high-p_{T} component uniformly distributed in $[0, 20]$ GeV/c, which covers 70% of the total, and a low-p_{T} component flat in $1/p_{\text{T}}$:

$$p_{\text{T}} = \frac{p_{\text{T}_{\text{min}}}}{p_{\text{T}_{\text{min}}}/p_{\text{T}_{\text{max}}} + j}, \tag{5.19}$$

where $p_{\text{T}_{\text{min}}} = 0.01$ GeV/c, $p_{\text{T}_{\text{max}}} = 20$ GeV/c and j is a random variable uniformly distributed between 0 and 1. Some key properties of the tracks composing the PS sample are plotted in Fig. 5.4. These include the p_{T} spectrum, the lever arm L_{Arm} and the number of points per track N separated between primaries and secondaries. The lever arm is defined as the distance in the xy plane between the first and last point in the track. All the tracks included in this and future plots have been successfully reconstructed, unless stated otherwise.

Primaries and secondaries have analogous p_{T}, with the only variations arising from the fact that primaries and secondaries have different reconstruction efficiencies. In particular the reconstruction for low momentum secondaries is more likely to fail than for primaries, resulting in a harder spectrum. This arises from the combination of two factors: the low momentum secondaries have a higher risk of having the start of their track at a $\sin\phi$ angle that is close to the edges of its range, making the application of the mirroring algorithm difficult since not many points are remaining; additionally secondaries are more likely to produce short tracks overall, due to the randomness of their starting points. This is a difficulty which could be at least partially solved, by placing the rotation centre in front of each secondary track, to mimic the geometrical construction of the primaries.

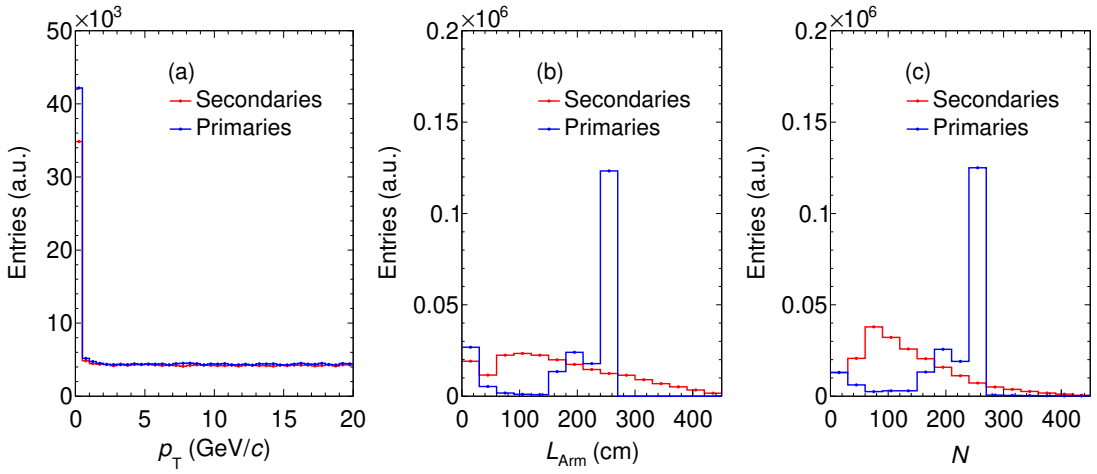

Figure 5.4: Distributions of (a) transverse momentum p_{T}, (b) lever arm L_{Arm} and (c) number of points per track N in the PS sample. In all the plots the distributions for primary and secondary particles are shown separately. The low p_{T} portion of the spectrum is produced via Eq. 5.19. The spikes around $N = 250$ and $L_{\mathrm{Arm}} = 250$ in the primary sample are explained by the simulated geometry having 250 radial pad layers and the particles starting from the centre of the detector.

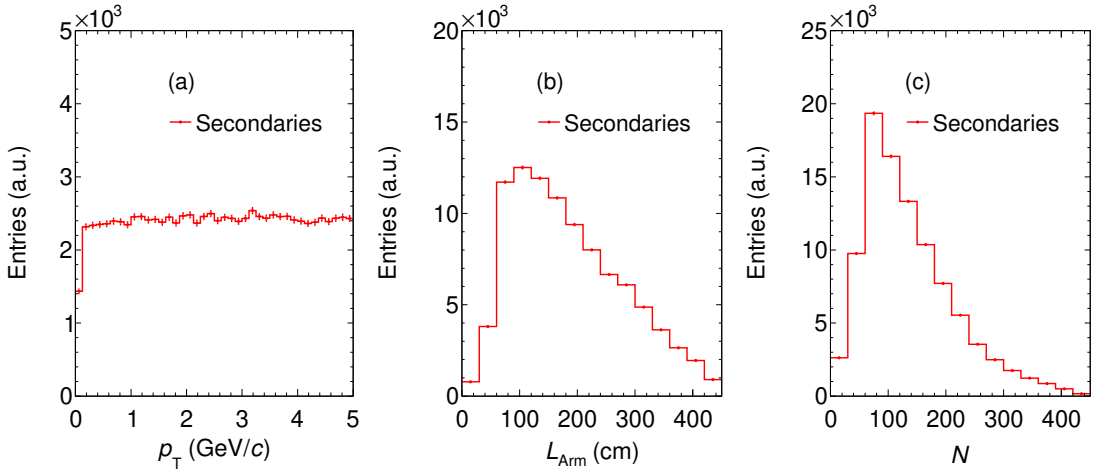

Figure 5.5: Distributions of (a) transverse momentum p_{T}, (b) lever arm L_{Arm} and (c) number of points per track N in the HP sample. For the HP sample only secondaries are produced, to emulate particles produced in neutrino interactions inside the detector.

This solution was however not tested for this study and goes beyond the scope of this work. More significant differences appear in the L_{Arm} and N distributions. Since the primaries all start at the centre of the detector, most tracks will cross the detector exiting from the cylinder's barrel, producing a track with as many

points as the 250 pad layers. In alternative the track can exit from the sides of the detector, producing tracks with a slightly smaller N or be stopped inside the detector having $N < 50$. For the secondaries the spread is much more homogeneous and the chance of producing tracks with $N > 250$ is more significant.

A second sample containing a total of 10^5 particle tracks was produced to recreate conditions analogous to the ones that would be experienced by a HPgTPC in a accelerator neutrino experiment, such as the ND-GAr detector. The goal for this second sample is to explore the potential performance of such a detector, using realistic particle spectra and spatial resolutions. This sample will be referred to as the high-pressure sample or HP sample. The HP sample is produced with randomized starting positions in the same manner as the ones applied to the secondaries in the PS sample. This is done to emulate the randomness of particle track formation in a neutrino experiment. The detector characteristics are fixed, having the same cylinder dimensions and pad distribution of the previous sample. The point resolutions are taken as $\sigma_{r\phi} = \sigma_z = 0.1$ cm, comparable to what is quoted in ALICE [168]. This figure is also used as the benchmark to estimate the point resolution for ND-GAr, given that the MWPC used by the two detectors are going to be the same. The gas is a mixture of argon and methane at a 90 to 10 ratio at 10 atm of pressure, which is the nominal gas suggested for the ND-GAr detector in the DUNE ND CDR [2]. This composition corresponds to a $X_0 = 1.193 \times 10^3$ cm and a density of $\rho = 0.01677$ g/cm^3. Only three particle types are considered in this case: muons, pions and protons. These were chosen because they are the key particles produced in ν_μ charged-current interactions that are the most relevant in an accelerator neutrino experiment such as DUNE. The initial transverse momenta are randomized to be uniformly distributed between 0.01 GeV/c and 5 GeV/c and the angles are randomized over the whole spectrum. The p_{T}, L_{Arm} and N distributions for the sample are shown in Fig. 5.5.

5.5.2 The parameter scan study

The study performed on the PS sample focuses on the validation of the `Seed` and `CKF` algorithms as well as on evaluating the improvement in performance produced by the mirroring technique introduced in Sec. 5.2. The first test performed on the PS sample was a pull test analogous to what was described in Sec. 4.6. The pulls Π are defined in Eq. 4.34 and can be tested to verify that the diagonal elements of the covariance matrix C_{ii} are well defined. Specifically their distributions should be normal, centred at 0 with $\sigma \simeq 1$.

The pulls were tested for the sample, both for the results of the `Seed` and for the estimates evaluated at the start of the track, after the full propagation of the `CKF`: the resulting distributions for all the state vector parameters are shown in Figs. 5.6 and 5.7, respectively. All the pull distributions were fitted to a standard Gaussian distribution and were found to be centred at 0 and have $\sigma \sim 1$; this implies that the diagonal elements of the covariance matrices well describe the uncertainties. The only significant deviations can be seen for $s_4 = q/p_{\mathrm{T}}$ for which $\sigma \sim 1.1$ and to a lesser extent $s_3 = \tan\lambda$. In both cases the underestimations of the matrix elements are likely due to the approximations made during the energy loss correction step. Due to the fact that the dE/dx depends on the momentum of the particle and indirectly its energy, the correction procedure is estimated using a step integration. However this method can only in part compensate for the non-linearity in the energy loss and is not completely reliable over long steps. For this reason the more significant deviations are seen for the `Seed` algorithm.

The standard pull distributions, while being effective at testing the uncertainties associated with the individual parameters, do not provide any information regarding the off-diagonal correlation terms. In order to test the quality of the estimates for the full covariance matrix, the Mahalanobis distance was used [169]. Given a probability distribution, D, on $\mathbb{R}^n$ with mean μ and positive-definite covariance matrix, C, the Mahalanobis distance, M, of a point s from D, is defined as:

$$M = \sqrt{(s-\mu)^T C^{-1} (s-\mu)}, \tag{5.20}$$

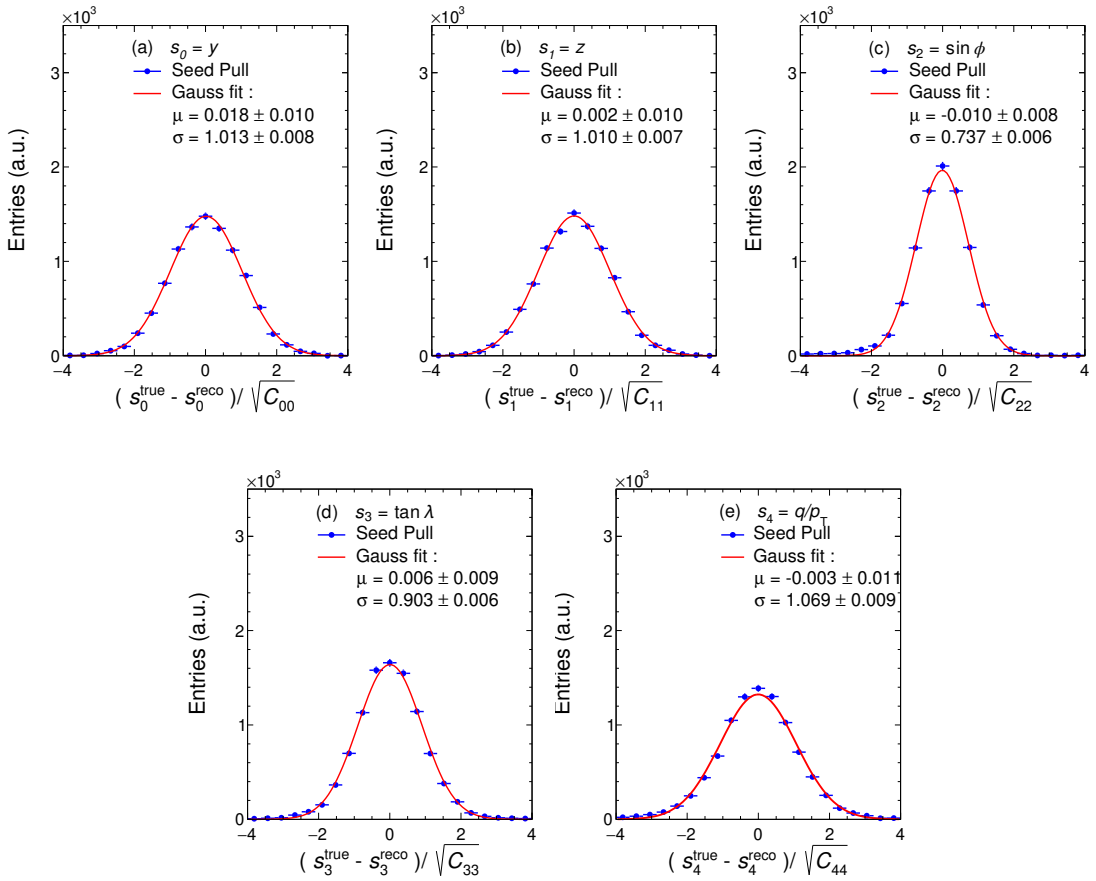

Figure 5.6: Pull distributions for the `Seed` algorithm over the whole PS sample. All distributions were fitted to a Gaussian function. Results for parameters s_0 to s_4 (i.e. y, x, $\sin\phi$, $\tan\lambda$ and q/p_{T}) are shown from left to right and labelled from (a) to (e) accordingly.

where in our case, μ corresponds to the true value of state vector, s^{true}, s and C are the estimates obtained from the reconstruction and $n = 5$. The square of the Mahalanobis distance, M^2, of a set of points belonging to the distribution D, follows a χ^2 distribution with n degrees of freedom. One can check if C is well defined, by verifying that the corresponding M^2 follow a χ^2 distribution with the correct number of degrees of freedom. In Fig. 5.8, we show the results of a χ^2 fit over the M distribution for the whole sample. The plot on the left shows the results obtained from the `Seed` algorithm, while the one on the right shows the results after the full `CKF` propagation. In both cases the n.d.f. obtained with the χ^2 fit are very close to $n = 5$: both `Seed` and `CKF` estimates accurately the covariances

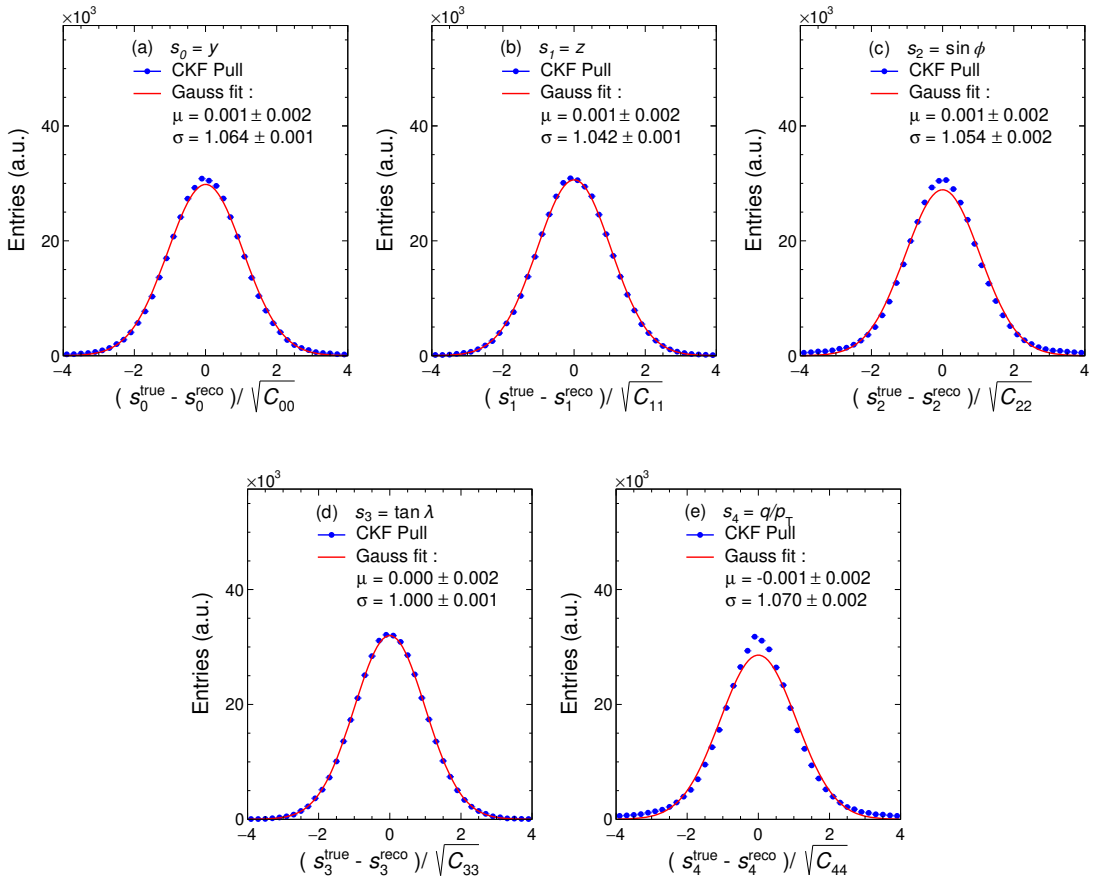

Figure 5.7: Pull distributions obtained after the full propagation of the CKF algorithm over the whole PS sample. All distributions were fitted to a Gaussian function. Results for parameters s_0 to s_4 (i.e. y, x, $\sin\phi$, $\tan\lambda$ and q/p_{T}) are shown from left to right and labelled from (a) to (e) accordingly.

of the reconstructed track parameters in the state vector. The only deviations are caused by the same dE/dx related issue which was pointed out for the Pull test results. It is also important to note that this test is particularly demanding, since all deviations present in the matrix add up to a single figure of merit.

The PS sample was also used to test whether the CKF algorithm produced results that are consistent with the theoretical expectations. The analytical formula for the ideal q/p_{T} resolution, $\sigma_{\mathrm{theo}}(q/p_{\mathrm{T}}) = \sqrt{C_{44}^{\mathrm{theo}}}$, obtainable using a curvature measurement in a TPC, can be written analogously to what was shown for the total momentum in Eqs. 4.37 and 4.38 as [158, 170]:

$$\sigma_{\mathrm{theo}}(1/p_{\mathrm{T}}) = \sqrt{C_{44}^{\mathrm{theo}}} = \sqrt{\sigma_{\mathrm{H}}^2 + \sigma_{\mathrm{MS}}^2}. \tag{5.21}$$

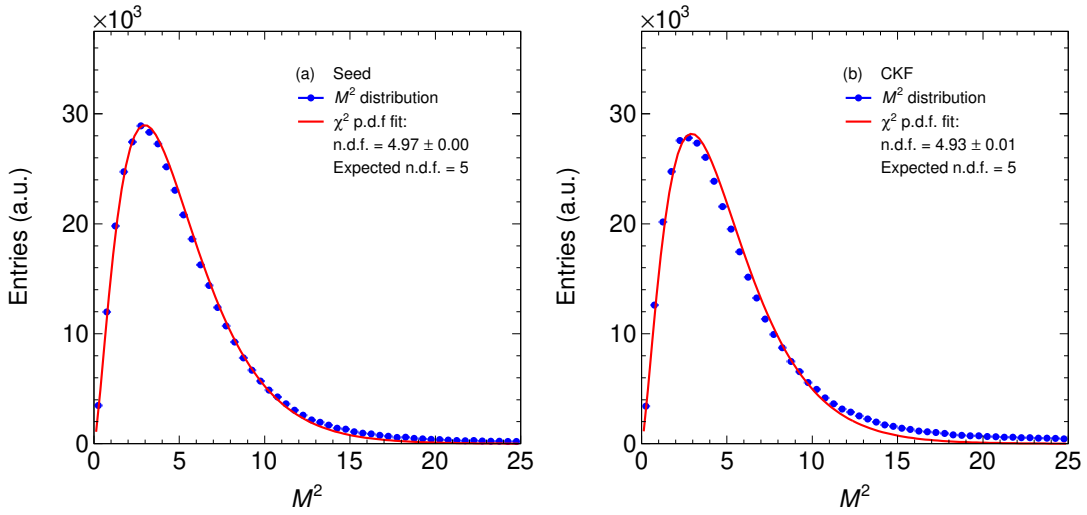

Figure 5.8: Square Mahalanobis distance M^2 distribution for the PS sample fitted by a standard χ^2 p.d.f. showing the results for the $n.d.f.$ parameter. The expected result for a 5-dimensional matrix is $n.d.f. = 5$. The results for the `Seed` and for the fully propagated `CKF` are shown in plots (a) and (b) respectively.

The σ_{H} component is determined by the point resolution and can be written as:

$$\sigma_{\mathrm{H}}(1/p_{\mathrm{T}}) = \frac{\sigma_{r\phi}}{0.3BL^2_{\mathrm{Arm}}}\sqrt{\frac{720}{N+4}}. \tag{5.22}$$

The multiple scattering component can be written as:

$$\sigma_{\mathrm{MS}}(1/p_{\mathrm{T}}) = \left\langle \frac{1}{\beta p_{\mathrm{T}}} \right\rangle \frac{0.016\ (\mathrm{GeV}/c)}{0.3Bl\cos\lambda}\sqrt{\frac{l}{X_0}}, \tag{5.23}$$

where l is the length of the track in the xy-plane. Note that the value of $1/(\beta p_{\mathrm{T}})$ is averaged along the trajectory to take into account energy loss. In Figs. 5.9, 5.10 and 5.11, the upper plots show the `CKF` covariance estimates, $\sqrt{C_{44}^{\mathrm{CKF}}}$, while the bottom plots show their ratios to the theoretical expectations, $\sqrt{C_{44}^{\mathrm{theo}}}$. The upper plots are shown to demonstrate how widely the values of $\sqrt{C_{44}^{\mathrm{CKF}}}$ vary and to highlight, in comparison, how stable the ratio with the theoretical expectation is. The points analysed are randomly taken along the reconstructed tracks and down-sampled to 10% of the total to avoid correlations.

In Fig. 5.9,the histograms are colour-scaled based on particle type, denoted as t_{ID}. Conversely, in Figs. 5.10 and 5.11, the colour scaling corresponds to gas pressure, P_{gas}, and point resolution $\sigma_{r\phi} = \sigma_z$ respectively. The `CKF` results

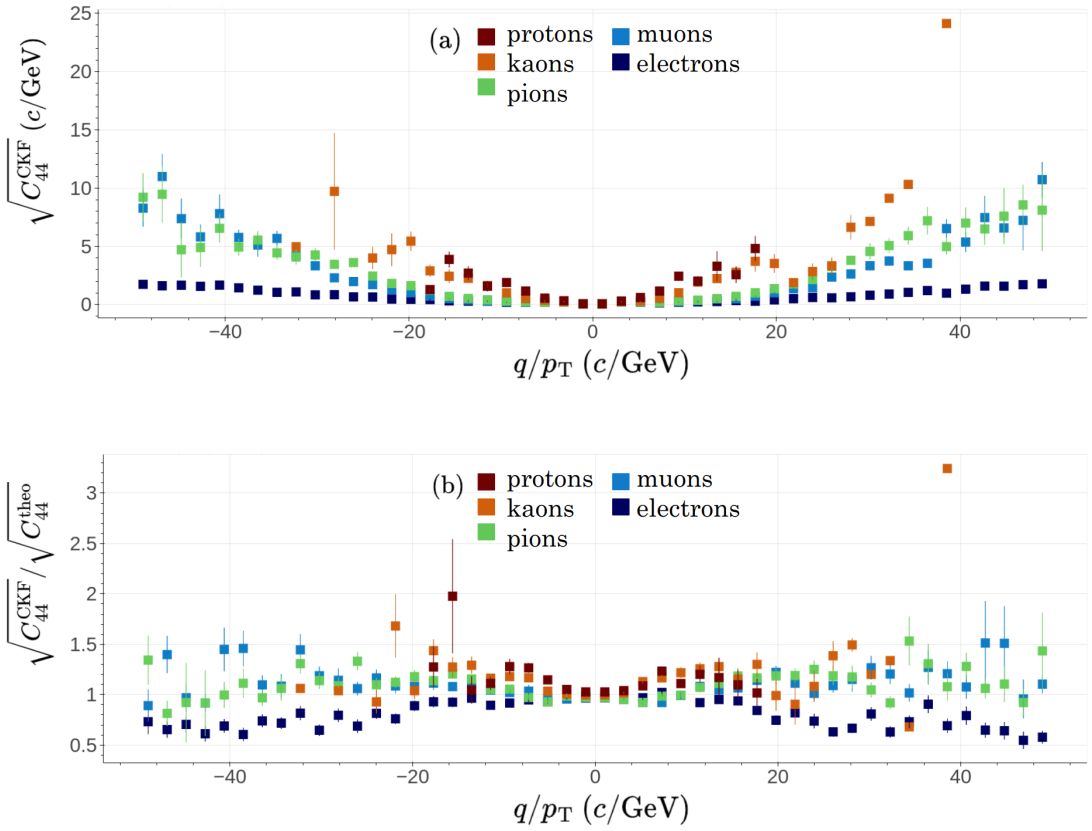

Figure 5.9: (a) `CKF` q/p_{T} resolution $\sigma_{\mathrm{CKF}}(q/p_{\mathrm{T}}) = \sqrt{C_{44}^{\mathrm{CKF}}}$ as a function of the true q/p_{T}. (b) Ratio of the `CKF` q/p_{T} resolution, over the theoretical expectations $\sigma_{\mathrm{theo}}(q/p_{\mathrm{T}}) = \sqrt{C_{44}^{\mathrm{theo}}}$, as a function of the true q/p_{T}. The histograms include all particles in the PS sample and are colour-coded according to the ALICE convention for particle types $t_{\mathrm{ID}} = (0, 1, 2, 3, 4) = (\mathrm{e}, \mu, \pi, K, \mathrm{p})$. These plots have been produced using the interactive analytical tool `ROOTInteractive` [163]. The error bars are statistical.

show overall good agreement with the theoretical expectation, with ratios ~ 1 for momenta down to 20 MeV/c within statistical uncertainties. In Fig. A.2 in the App. A.3 we present an alternative version of the plots in Fig. 5.10 focusing on the central region $q/p_{\mathrm{T}} \in [-5, 5]$ c/GeV which is more statistically significant.

The PS sample was further used to test the improvement in q/p_{T} resolution brought by the introduction of the "mirror rotation" technique in the `CKF`, compared to `BKF`. The fraction of the total tracks for which the mirroring technique was used $\epsilon_{\mathrm{Mirror}}$ is shown in Fig. 5.12 as a function of initial true p_{T} and P_{gas}. We show the fraction for the primaries in the first row and for the secondaries in the second. The

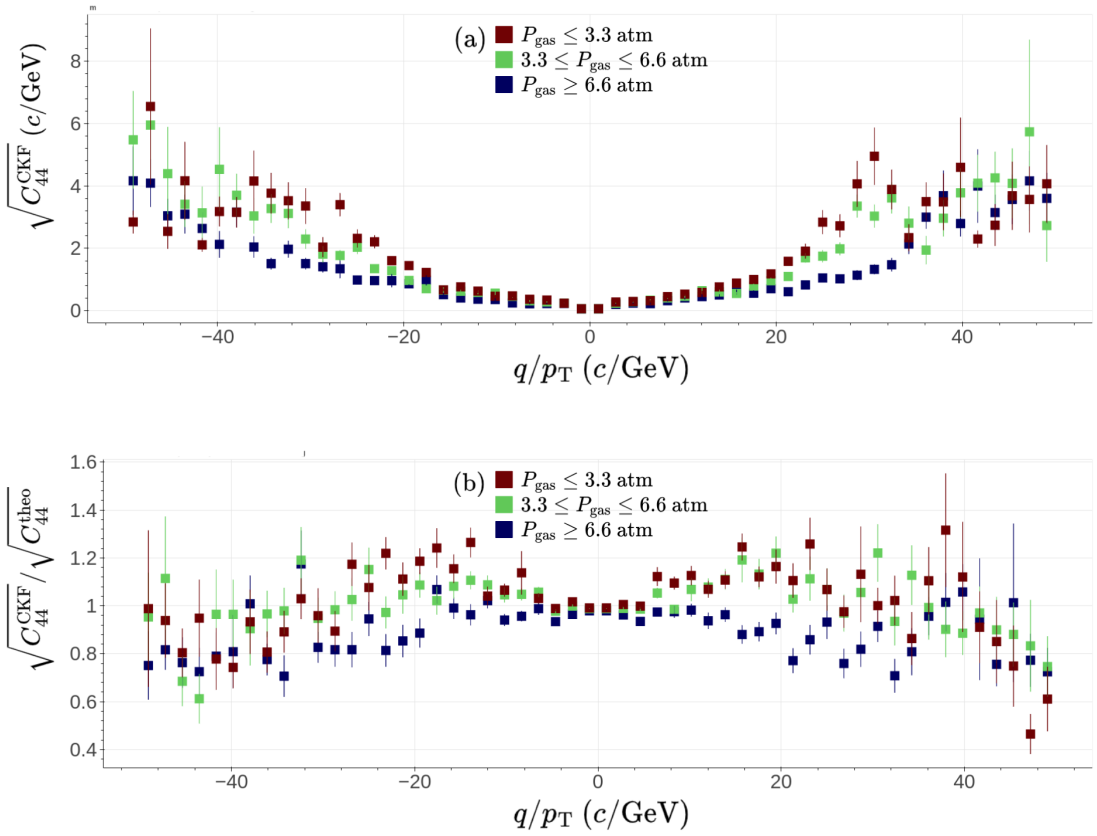

Figure 5.10: (a) `CKF` q/p_{T} resolution $\sigma_{\text{CKF}}(q/p_{\text{T}}) = \sqrt{C_{44}^{\text{CKF}}}$ as a function of the true q/p_{T}. (b) Ratio of the `CKF` q/p_{T} resolution, over the theoretical expectations $\sigma_{\text{theo}}(q/p_{\text{T}}) = \sqrt{C_{44}^{\text{theo}}}$, as a function of the true q/p_{T}. The histograms include all particles in the PS sample and are colour-coded according to the gas pressure P_{gas} used in the simulation. Only tracks with a minimum of 10 points are considered. These plots have been produced using the interactive analytical tool `ROOTInteractive` [163]. The error bars are statistical.

particle types are divided in order of mass between electrons in Figs. 5.12a and 5.12d, muons and pions in Figs. 5.12b and 5.12e, kaons and protons in Figs. 5.12c and 5.12f. We can see from the upper row plots and the low p_{T} component of the lower row plots that the likelihood of the particles producing looping trajectory drops significantly with mass, due to the higher $\mathrm{d}E/\mathrm{d}x$. At low momenta the pressure of the gas also becomes important. This is especially true for the higher mass particles such as protons and kaons, which at higher P_{gas} are stopped in the detector before producing any looping trajectory (see Fig. 5.12c). From Figs. 5.12a, 5.12b and 5.12c it can also be shown that the only primary particle that

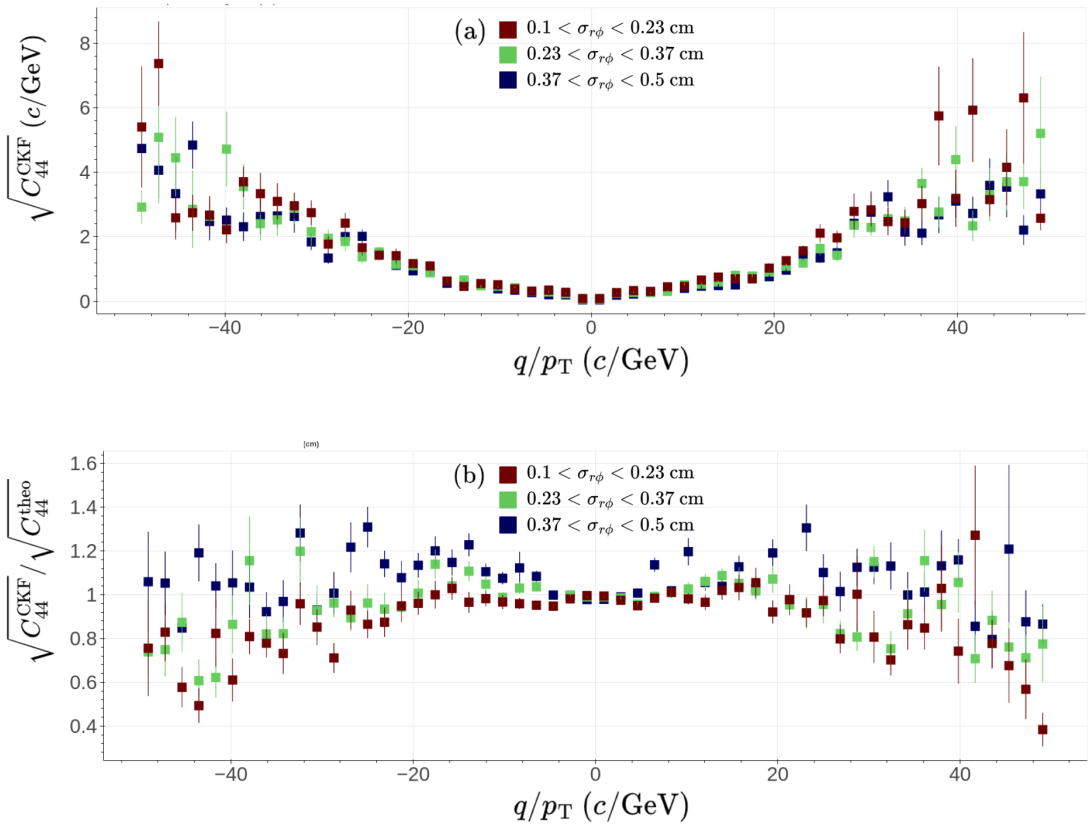

Figure 5.11: (a) `CKF` q/p_{T} resolution $\sigma_{\mathrm{CKF}}(q/p_{\mathrm{T}}) = \sqrt{C_{44}^{\mathrm{CKF}}}$ as a function of the true q/p_{T}. (b) Ratio of the `CKF` q/p_{T} resolution, over the theoretical expectations $\sigma_{\mathrm{theo}}(q/p_{\mathrm{T}}) = \sqrt{C_{44}^{\mathrm{theo}}}$, as a function of the true q/p_{T}. The histograms include all particles in the PS sample and are colour-coded according to the radial resoulution $\sigma_{r\phi}$ used in the simulation. Only tracks with a minimum of 10 points are considered. These plots have been produced using the interactive analytical tool `ROOTInteractive` [163]. The error bars are statistical.

necessitate the use of the mirroring operation are those that produce a looping trajectory in the detector, which is only possible at low initial transverse momenta $p_{\mathrm{T}} < 0.3$ GeV/c (see Eq. 4.15). Secondary particle trajectories, on the other hand, can cover more than a semi-plane even if they don't belong to loopers and can thus be produced at any momenta, as shown in Figs. 5.12d, 5.12e and 5.12f. At low transverse momenta, $\epsilon_{\mathrm{Mirror}}$ is still significantly higher for secondaries.

The reconstruction efficiency ϵ, defined as the fraction of the correctly simulated tracks for which the algorithm is fully propagated, was tested for `CKF` and `BKF`. It is shown as a function of the initial true p_{T} and the N of the total track in the

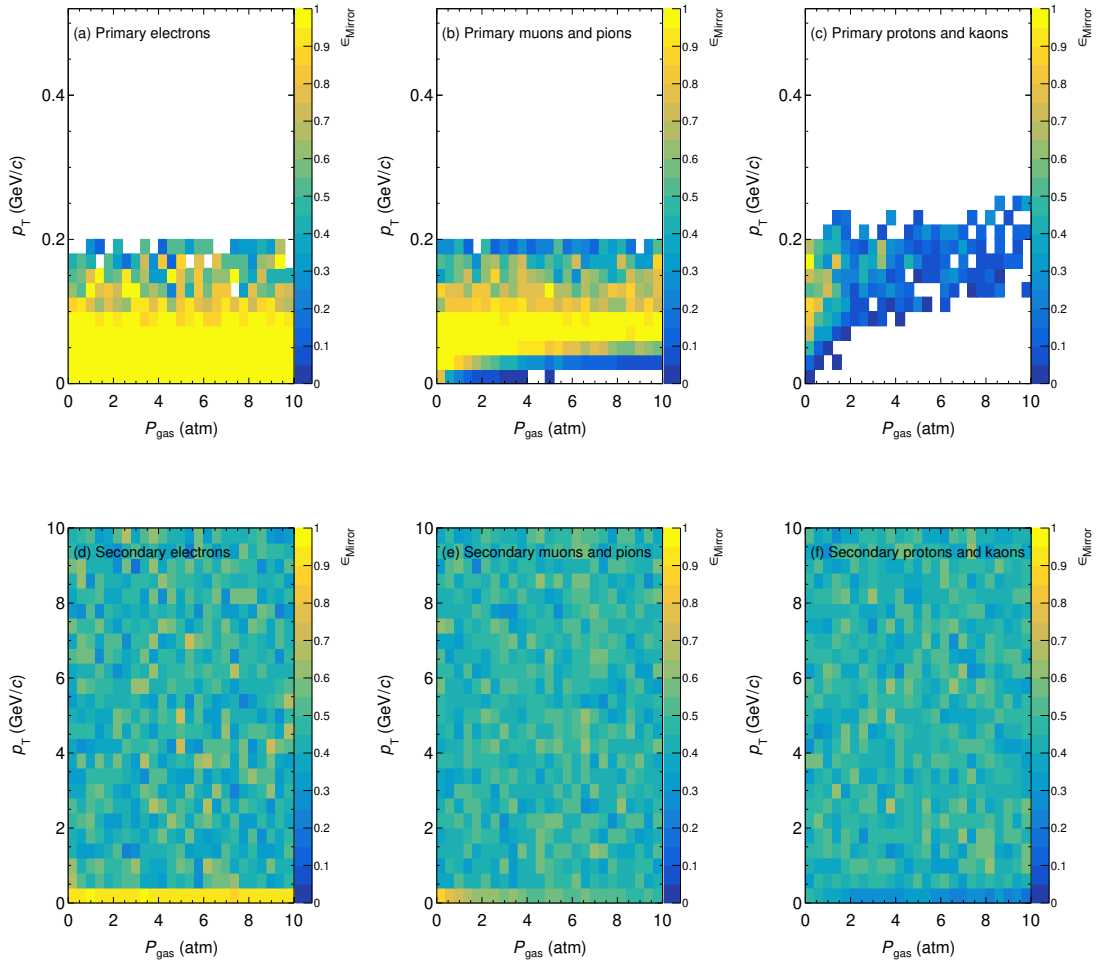

Figure 5.12: Portion of tracks in the PS sample for which the mirror rotation was applied, ϵ_{Mirror}, as a function of the gas pressure P_{gas} and the initial true transverse momentum p_{T} of the particle. The primaries are shown in the upper row, while the secondaries are shown in the lower row. The particle types are separated based on their mass: (a) and (d) contain only electrons, (b) and (e) muons and pions, (c) and (f) kaons and protons.

first and second column of Fig 5.13 respectively. In Figs. 5.13a and 5.13b only the tracks for which the mirroring technique is used are shown, while the other tracks are shown Figs. 5.13c and 5.13d. For the "non-mirrored" tracks the efficiency is essentially identical between the `BKF` and `CKF` algorithm and it is shown to be very close to 1 except for very low p_{T} and N, for which other approaches than a KF would most likely be used [171]. On the other hand ϵ is significantly improved by the `CKF` for low N "mirrored" tracks, in some cases going from an efficiency of

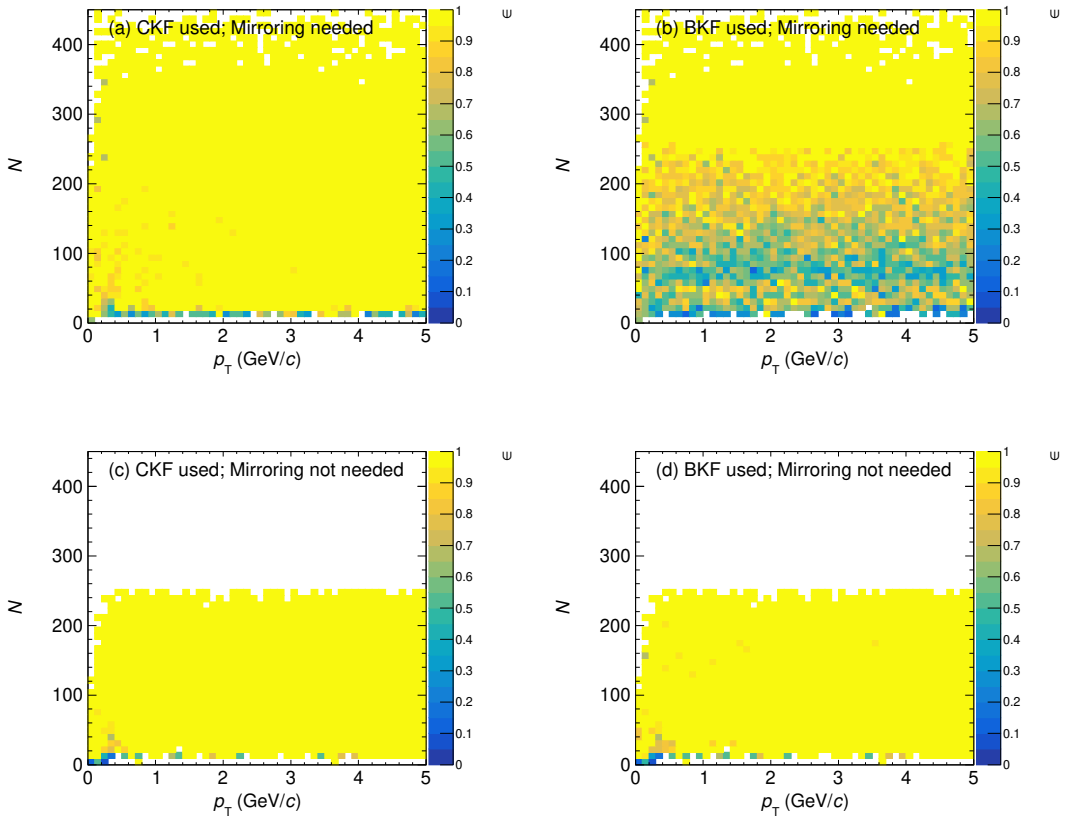

Figure 5.13: Reconstruction efficiency ϵ for the PS sample, as a function of the total number of points in the track N and the initial true transverse momentum p_{T}. The results for the tracks to which the mirroring technique was applied are shown in (a) and (b) for the `CKF` and `BKF` respectively. The results for the other tracks are shown in (c) for the `CKF` and (d) for the `BKF`.

~ 0.5 to $\epsilon > 0.9$. This is a direct consequence of the increased number of points becoming available through the use of the mirroring technique.

The difference in performance due to the mirror rotation can be quantified using the ratios between the full reconstruction resolution $\sqrt{C_{44}^{\mathrm{CKF}}}$ and the $\sqrt{C_{44}^{\mathrm{BKF}}}$ obtained with the basic reconstruction at a given point along the track. Figure 5.14 shows the ratios $\sqrt{C_{44}^{\mathrm{CKF}}}/\sqrt{C_{44}^{\mathrm{BKF}}}$ as a function of the true q/p_{T}, colour-coded according to the gas pressure P_{gas}. Figure 5.14a shows the results for a sample of only electrons, while Fig. 5.14b shows the results for a sample of muons and pions and Fig. 5.14c for a sample of protons and kaons. The points are again randomly taken along the reconstructed tracks and down-sampled to 10% of the total. For the electron sample, an overall relative improvement of $\sim 60\%$ is shown

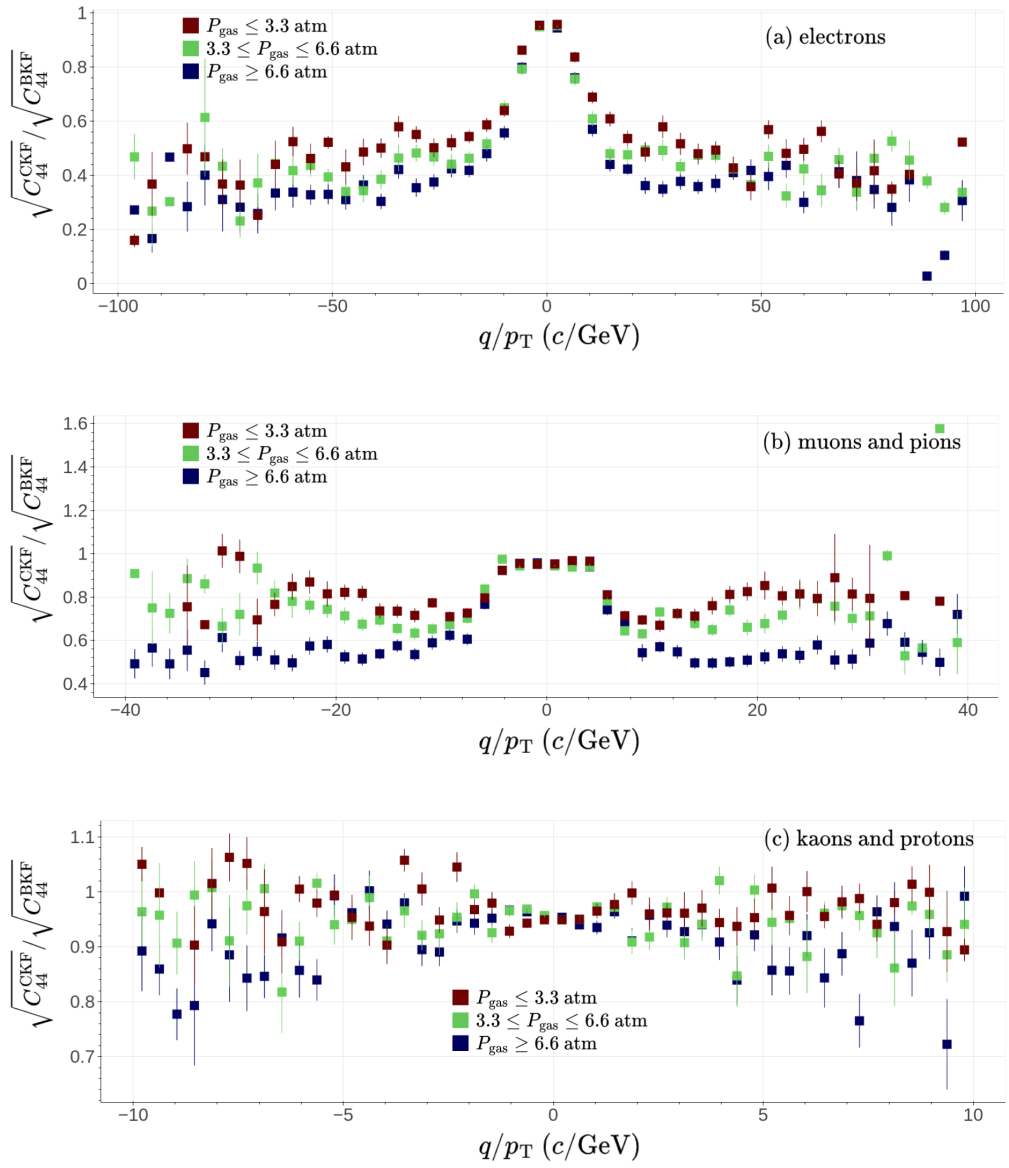

Figure 5.14: Ratios of the q/p_{T} resolutions obtained using the `CKF` algorithm $\sqrt{C_{44}^{\text{CKF}}}$, over the `BKF` $\sqrt{C_{44}^{\text{BKF}}}$. The plots were produced for the whole PS sample. The histograms are colour coded according to the gas pressure P_{gas}. Plot (a) contains only electrons, plot (b) contains pions and muons and plot (c) contains kaons and protons. Only tracks with a minimum of 30 points are considered. These plots have been produced using the interactive analytical tool `ROOTInteractive` [163]. The error bars are statistical.

at $p_{\text{T}} < 100$ MeV/c, with peaks of up to $\sim 80\%$ for the lowest momentum tracks in low pressure environments. This behaviour is in agreement with Eqs. 5.22 and 5.23 which show a dependency of the $1/p_{\text{T}}$ resolution on $1/\sqrt{N}$ and $1/\sqrt{L_{\text{Arm}}}$ respectively: using the mirroring technique, more space points of the tracks are

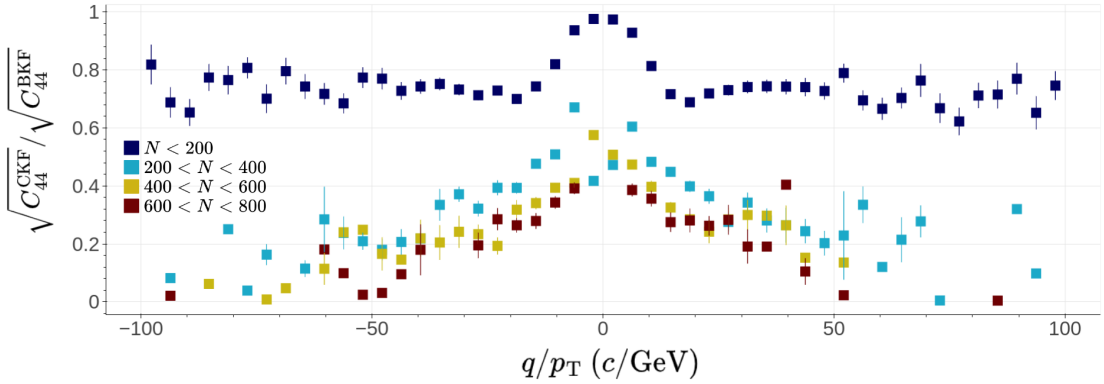

Figure 5.15: Ratios of the q/p_{T} resolutions obtained using the full `CKF` algorithm including the mirror rotation method $\sqrt{C_{44}^{\mathrm{CKF}}}$, over the reconstruction without mirror rotation $\sqrt{C_{44}^{\mathrm{BKF}}}$. The plots were produced for the whole PS sample. The histograms are colour coded according to number of points in the tracks N. These plots have been produced using the interactive analytical tool `ROOTInteractive` [163]. The error bars are statistical.

used, resulting in larger N and L_{Arm}. The dependence on the number of points is shown more clearly in Fig. 5.15, where the histograms are colour coded for total number of points in the track, including those only accessible through the mirroring technique. Tracks containing more than 800 points are excluded for easier legibility of the results. It is shown that for the longest tracks, relative improvements of up to 80% can be achieved.

The difference between the results is shown to be less dramatic in more pressurized environments, where particles tend to be absorbed sooner and tracks are generally shorter. This trend is confirmed looking at the results obtained for the muons and pions sample in Fig. 5.14b, for which $\mathrm{d}E/\mathrm{d}x$ will on average be higher due to their higher masses: the improvement in this case is by $\sim 20\%$ for $p_{\mathrm{T}} < 150$ MeV/c with peaks of up to $\sim 50\%$ for the lowest momentum tracks in low pressure environments. No improvements were found for the more massive particles shown in the sample, except for minor ones at lower pressures (Fig. 5.14c).

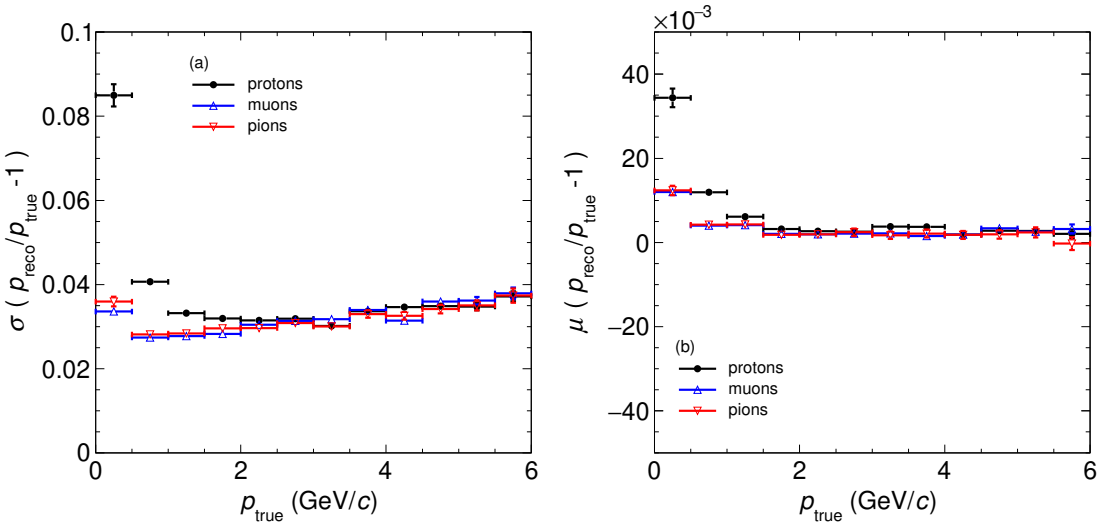

Figure 5.16: Relative momentum resolution (a) and bias (b) as function of the true momentum, p_{true}, for the HP sample. The two properties are defined as μ and σ of Gaussian fits of the momentum fractional residuals $p_{\text{reco}}/p_{\text{true}} - 1$. The three particle types (protons, muons and pions) are drawn separately.

5.5.3 The high pressure study

The HP sample is used to evaluate the detector performance of a HPgTPC similar to ND-GAr. We focus on the total momentum relative resolution and bias, defined as the σ and μ of a standard Gaussian fit applied to the momentum fractional residuals:

$$R = \frac{p_{\text{reco}}}{p_{\text{true}}} - 1. \tag{5.24}$$

The reconstruction efficiency ϵ was also tested. The results are shown in the App. A.3 in Fig. A.1 and are similar to the PS sample.

The dependencies of the total momentum resolution can be described using Eqs. 4.37 and 4.38. In Fig. 5.16 we show the relative momentum resolution and bias as a function of the true momentum for the three particle types present in the sample. At lower momenta ($p_{\text{true}} < 1\text{GeV}/c$) the resolution is close to 3% for pions and muons while it is closer to 8% for the protons. In this momentum region the multiple scattering component of the resolution is dominant. This component is inversely proportional to the β factor of the particle. With a given momentum,

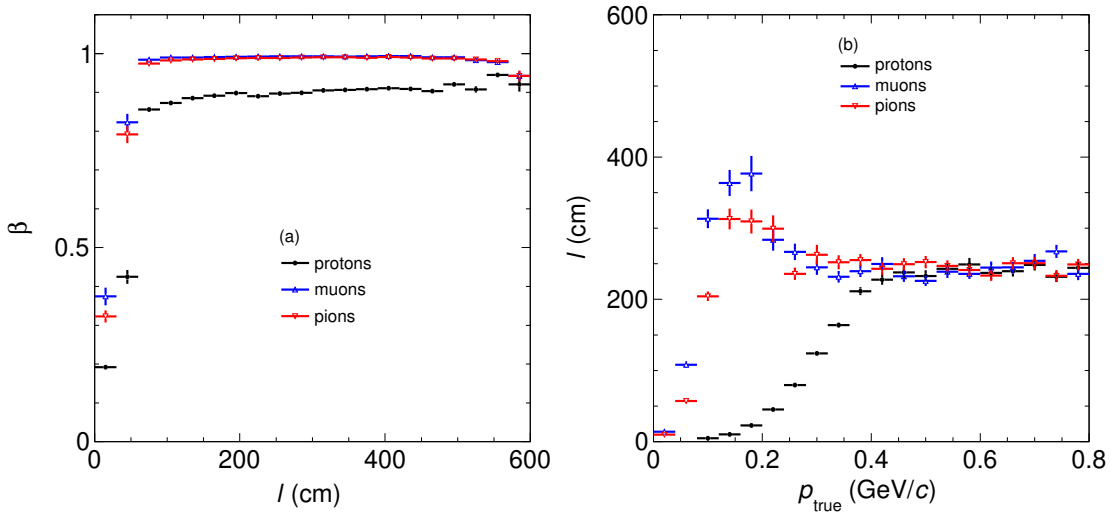

Figure 5.17: (a) Average β as a function of the track length l and (b) average track length as a function of the true momentum p_{true} for the HP sample.

the proton, having a higher mass, will always have a smaller β and thus a worse expected resolution. Furthermore, while muons and protons at lower energies have the chance to produce longer and even looping tracks inside the detector, protons will tend to loose their energy more quickly, again due to their masses. This is clearly shown in Fig. 5.17b where the average particle lengths as a function of their true momentum is shown. Somewhat significant biases are also shown at these lower momenta, especially for protons. For momenta $p_{\text{true}} > 1$ GeV/c, the resolution is comparable for the three particle types and increases slowly with the particle momentum. At higher momenta the point resolution component is dominant, so a direct proportionality on the momentum is expected, with no distinction between the particle types. An inverse dependency on the lever arm and number of points and thus indirectly on the length is also expected, but as shown in Fig. 5.17b, in this momentum range the average length of the track becomes roughly the same for all particle types.

In Fig. 5.18 we show the momentum resolution and bias as a function of the true track lengths l for the three particle types. As could be predicted from Eq. 4.38, an inverse proportionality of the relative resolution on l can be observed for all particle types. The worse performance observed for the protons can be explained by the

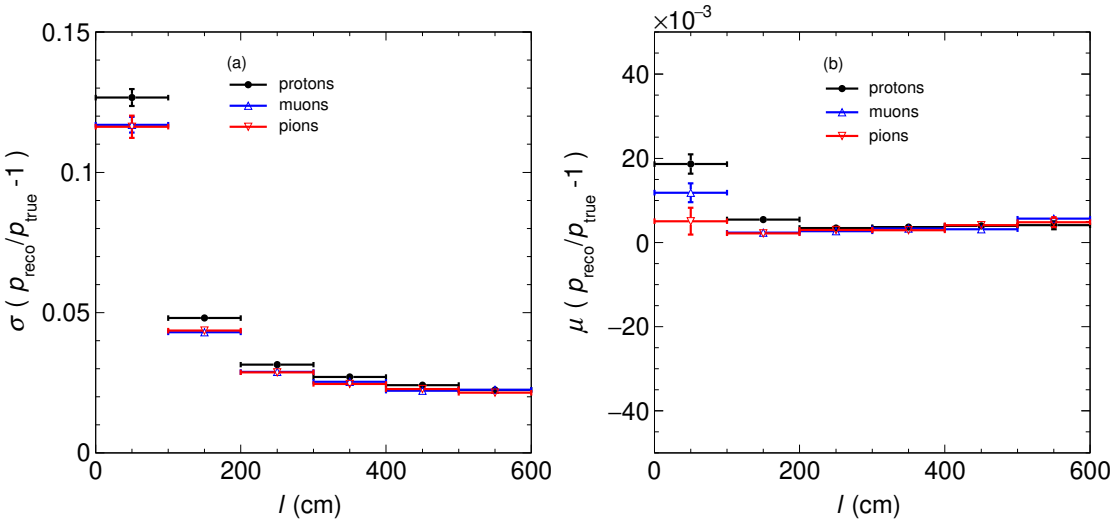

Figure 5.18: Similar plots to Fig. 5.16. In this case the relative momentum resolution (a) and bias (b) are shown as a function of the true track length l for the HP sample.

average β shown in Fig. 5.17a, which is always smaller for more massive particles regardless of the length of the tracks. For longer tracks the hit component of the resolution is dominant and the difference in β is not as impactful. A somewhat significant bias can be seen at lower lengths. Similar dependencies on lever arm L_{Arm} and number of points in the track N, which can be treated as a proxy for l in most cases, are shown in Figs. A.3 and A.4 in App. A.3. Similar plots have also been produced for the PS sample to allow for direct comparison in Figs. A.5 and A.6 also in App. A.3.

5.6 Implementation in `GArSoft`

The `GArSoft` software suite was used to produce samples of ν_μ CC interactions inside the ND-GAr TPC via the GENIE MC generator. A second sample of forward going muons was produced using the GEANT4 based particle gun feature of `GArSoft`.

The first sample was used to study the performance of the algorithm in the reconstruction of particle tracks produced by primary protons, muons and pions. The `CKF` algorithm was applied to the track candidates produced by `GArSoft` and

its performance was compared to that of the GKF in terms of total momentum and angle resolution. The sample was also used to confirm the internal consistency of the algorithm already demonstrated using fastMCKalman. We will refer to this as the interaction sample. The particle gun sample was used to estimate the performance of the new algorithm with particle tracks reproducing the conditions of muons coming from the ND-LAr detector, which is one of the key samples of study in ND-GAr.

The CKF algorithm which was tested on these GArSoft produced samples is identical to the one discussed in Sec. 5.2 and tested using fastMCKalman in Sec. 5.5 expect for the choice of the rotation center. While for the algorithm tested so far the rotation centre was chosen to be fixed at the centre of the TPC chamber, in this new application it is placed in front of the particle track. Specifically a simple linear fit is applied to the first 10 points of the track, and the rotation centre is chosen to be 30 cm away from the first point along the fitted line. This choice was made to avoid the unnecessary use of the mirroring technique, especially in the case of forward going tracks. In these scenarios the particle trajectories are often parallel to track pad layers for large portions of their trajectories and the application of the mirroring technique would produce large jumps, inducing the loss of hit clusters and a worse performance overall. This feature couldn't be seen when using the fastMCKalman toy MC generator, because in that case the mirroring technique was used in the simulation as well as in the reconstruction, producing gaps in the tracks themselves. Imposing that the rotation centre is put in front of the start of the track, we reduce the application of the mirroring technique to very "bendy" and often looping tracks, for which the method is always beneficial, adding hit clusters that wouldn't have been available otherwise.

Another less significant difference exists in the application of the Seed algorithm. While for the tests performed using the fastMCKalman algorithm, a limit of 60 points was imposed on the length of the track segment used for the seeding, in this case the entire track is always used. This choice was made in order to obtain the highest precision possible in the estimation of the state vector parameters, but it

has the side effect of making the estimation of the covariance matrix less reliable, especially when it comes to the energy loss and multiple scattering effects. However the additional precision in the state vector estimates yielded better results during the testing stage. Similarly to what was done for the HP sample in Sec. 5.5.3 the energy loss and multiple scattering corrections were evaluated by considering the characteristics of a 90-10 Ar-CH_4 gas mixture and then scaling them by a 10 atm pressure factor.

Once the `CKF` algorithm was fully mature and proven to outperform the `GKF`, it was implemented into `GArSoft` and set as the standard fitter. Additional tests were performed using two ν_μ CC interaction samples, produced entirely in `GArSoft`, using the same simulation up to the signal formation and digitization step but then using the two different fitters for the reconstruction. These samples were used to test that the integrated `CKF` fitter would behave identically to original independent code. Furthermore, they were utilized to compare aspects of the performance of the two fitters that would have been difficult to test prior to the full integration, such as reconstruction efficiency and vertexing resolution.

5.6.1 The interaction sample

To study the performance of the `CKF` we produced a sample composed of primary particles from 5×10^4 ν_μ CC interactions inside the ND-GAr TPC area. This was done using the GENIE neutrino interaction MC generator through `GArSoft`, propagating the particles using Geant4 and following all the simulation steps outlined in Sec. 5.4. We'll refer to this sample simply as the interaction sample. From the sample we selected protons, pions and muons and applied a fiducial cut on the true interaction vertices, imposing that they lie at least 20 cm from the barrel sides and 10 cm from the end-caps. This was done to eliminate many potentially problematic short tracks. The true vertex positions of all the events selected from the sample are shown in Fig. 5.19.

Some key features of the particle tracks are shown in Fig. 5.20. The histograms are separated between the different particle types (i.e. muons, pions and protons)

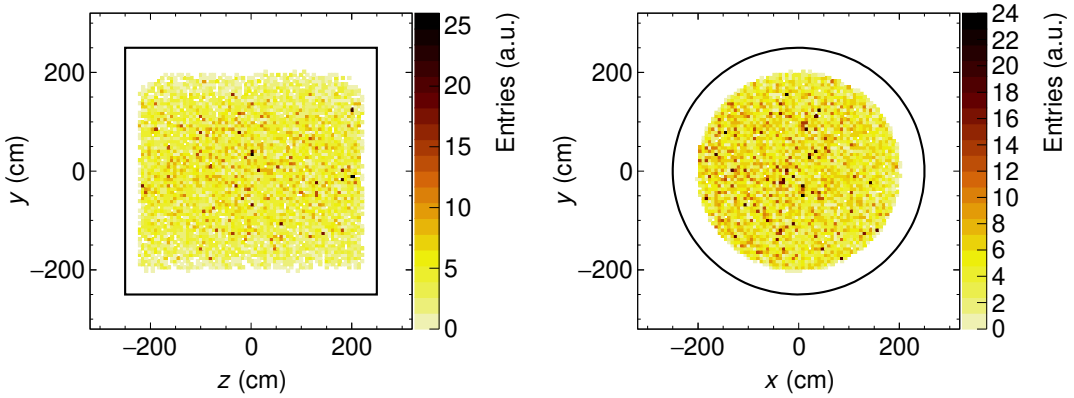

Figure 5.19: Starting positions for secondary particles in the interaction sample. The left plot shows the distribution in the zy plane, while the plot on the right shows the distribution in the xy plane. The edges of the TPC are drawn on top.

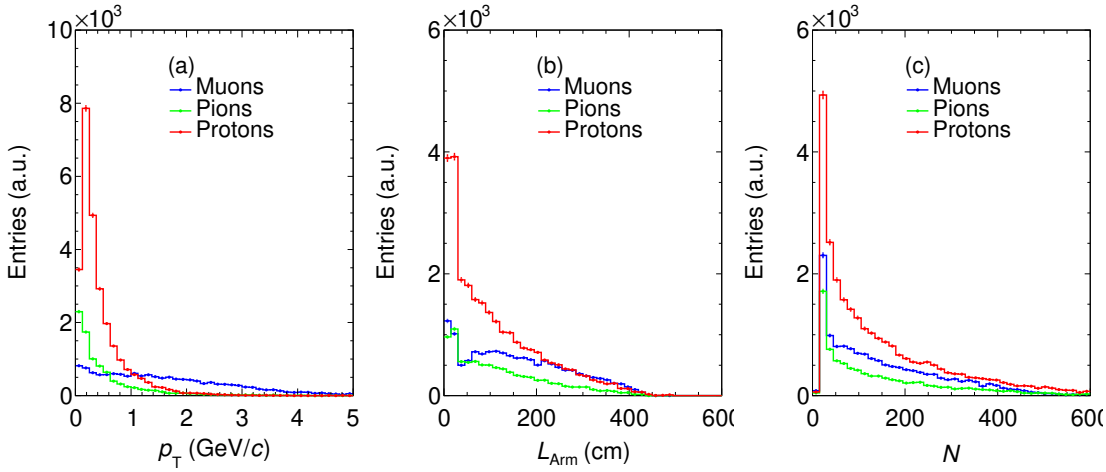

Figure 5.20: Distributions of (a) transverse momentum p_{T}, (b) lever arm L_{Arm} and (c) number of points per track N in the interaction sample sample. In all the plots the distributions for muons, pions and protons are shown separately.

of the true particles matched to the tracks by the `GArSoft` backtracker. We show the true initial transverse momentum p_{T} in the xy plane, the number of hit clusters belonging to the tracks N and the lever arm L_{Arm}, defined as the distance between the first and last track point in the xy plane. As expected from ν_μ CC interactions, where most of the initial neutrino momentum is transferred to the exiting muon,

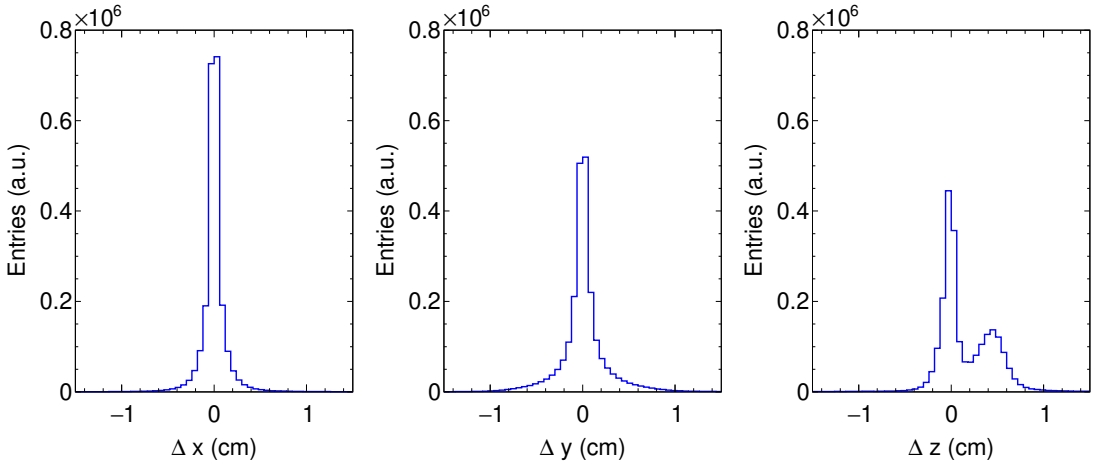

Figure 5.21: Position residuals in cm for the reconstructed hit clusters produced by `GArSoft`. (Left) Δx, (Center) Δy and (Right) Δz)

the muon sample has a higher momentum distribution compared to protons and pions. It is interesting to notice that significant L_{Arm} and N peaks are present in the lower regions of the spectra. While some of these shorter tracks are produced by particles stopping in the detector, especially in the case of protons, many of them are also the product of errors in the track formation stage of `GArSoft`. These errors include clumps of hits produced by δ rays that are wrongly assigned to a true MC particle by the backtracker or longer tracks that are cut into shorter segments.

In Fig. 5.21 we show the position residuals in 3 dimensions (Δx, Δy and Δz) for the reconstructed hit clusters. These are evaluated considering the closest true trajectory points to the hit-clusters by 3-dimensional distance. A very clear 2-peak structure is noticeable in the Δz distribution, pointing at an incorrect parameter choice in the `GArSoft` clustering method. A brief investigation of the problem seemed to point towards the clustering cut-off distance used in the z-direction being too short. This choice of parameter produced a split in hits that should have been joined together. However, this feature was discovered too late in the project's schedule to be corrected before the production of these studies. The Δx and Δy distributions are much closer to the expectations, but are non-Gaussian in their shape. These features are somewhat problematic when employing a KF algorithm,

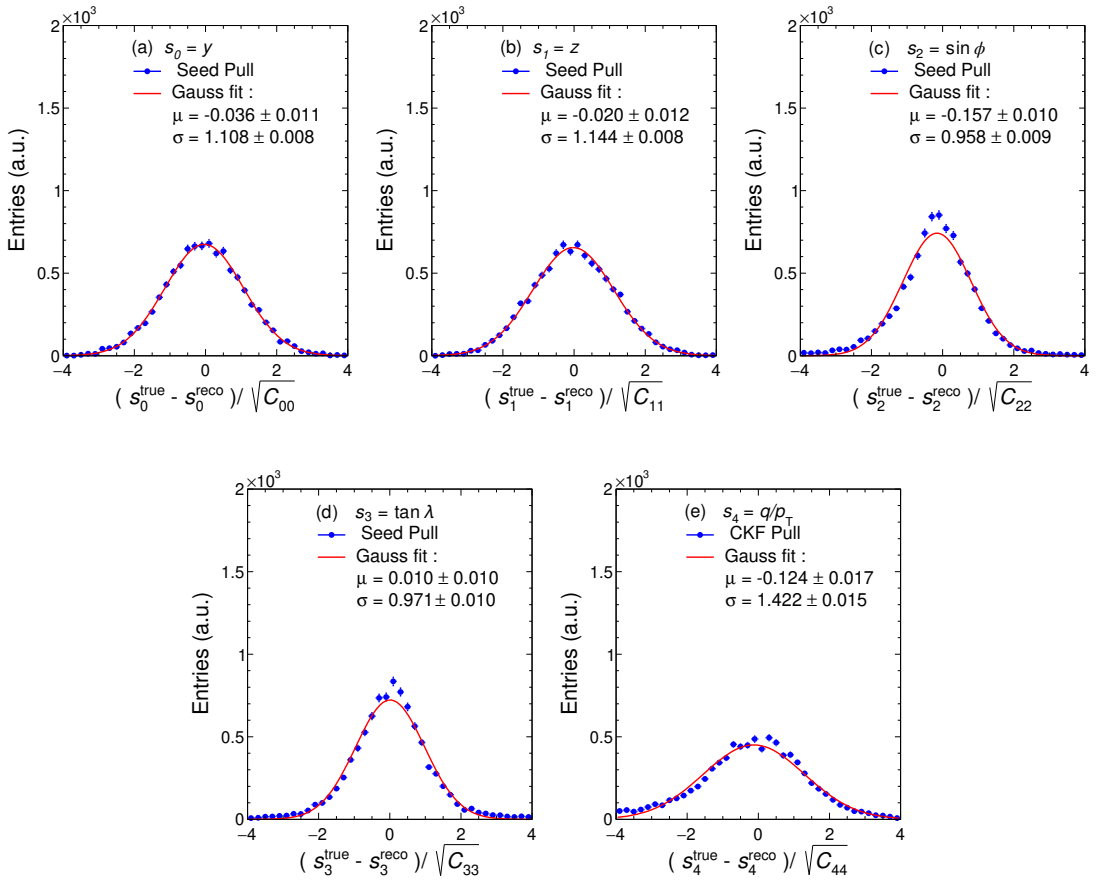

Figure 5.22: Pull distributions for the `Seed` algorithm over the whole interaction sample. All distributions were fitted to a Gaussian function. Results for parameters s_0 to s_4 (i.e. y, x, $\sin\phi$, $\tan\lambda$ and q/p_{T}) are shown from left to right and labelled from (a) to (e) accordingly.

since one of the assumptions that is made in the application of the technique is that the measurement noise is normally distributed.

In order to evaluate the internal consistency of the `CKF`, while separating its performance from the characteristics of `GArSoft`'s hit clustering algorithm, we devised a preliminary test using "fake tracks" built from the true MC particle trajectories associated to the tracks. These tracks were constructed by down-sampling the trajectory points, imitating the typical distances between hit clusters, and smearing their locations using Gaussian distributions in the x and y planes. The σs of the smearing distributions were randomly chosen particle by particle, within the range $\sigma_{xy} \in [0.05, 0.5]$ cm similarly to what was done in Sec. 5.5.2 for

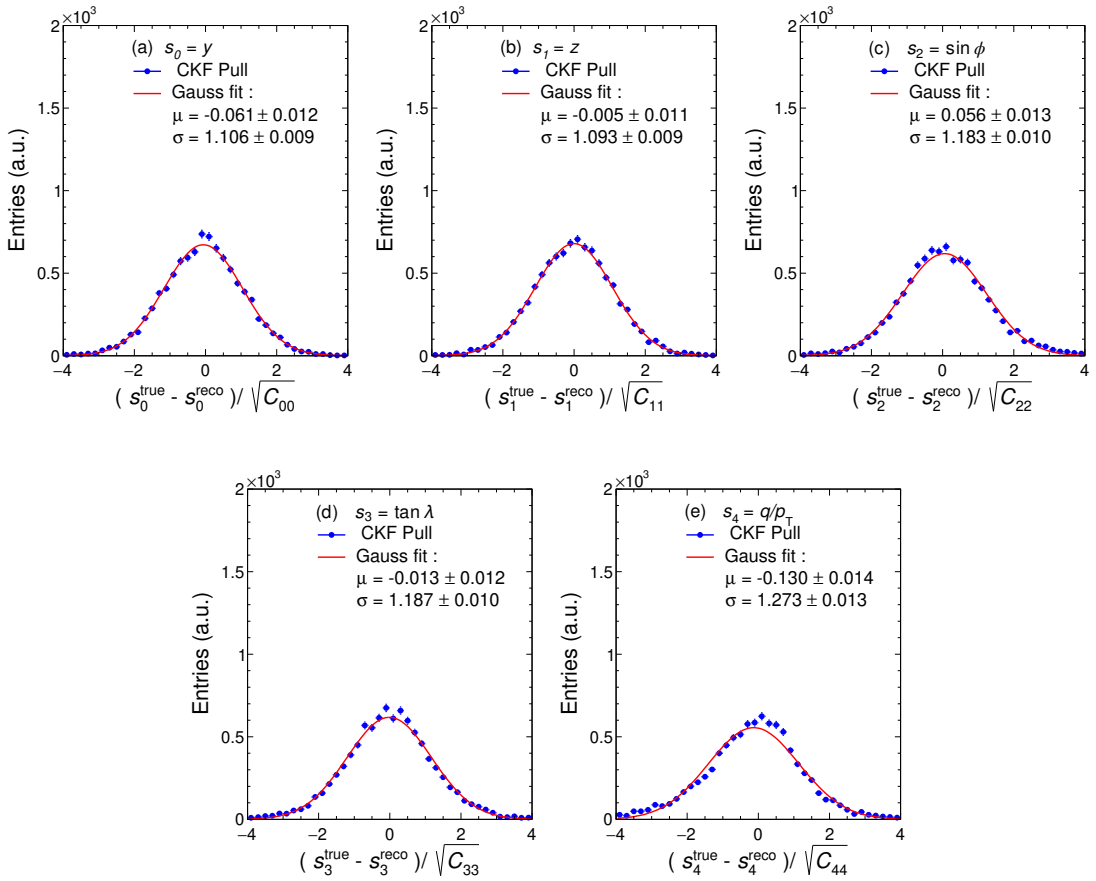

Figure 5.23: Pull distributions obtained after the full propagation of the `CKF` algorithm over the whole interaction sample. See Fig. 5.22 for comparison.

the PS sample. This construction ensures that the normality conditions for the measurement noise are respected. In order to test the internal consistency of the `CKF` and `Seed` algorithms, a pull test was applied to the parameter estimates, using all the particle tracks in the sample. The Π distributions for the `Seed` are shown in Fig. 5.22 and for the `CKF` in Fig. 5.23. Only the results for tracks that are formed by a minimum of 50 points are shown, in order to exclude problematic stopping short-tracks that would be reconstructed with methods different from a KF, such as range or dE/dx based algorithms [171]. For the `Seed` algorithm the pulls are all centred at 0 and have $\sigma \sim 1$,with the exception of $s_4 = q/p_{\mathrm{T}}$ for which there is a significant underestimation. This incorrect estimation could be caused by several factors. It could be that the gas properties used to evaluate the energy loss and multiple scattering corrections don't exactly match the ones

used in the Geant4 detector geometry. If this were the case however, an effect should be seen on the angle parameters $s_2 = \sin\phi$ and $s_3 = \tan\lambda$, which is not the case. Another option is an incorrect estimation of the c correction factor described in Eq. A.6. This would only have an impact on $s_4 = q/p_{\mathrm{T}}$, but such an error should have been spotted during the testing performed in `fastMCKalman`. Most likely this underestimation can be attributed to the choice of using the entire track during the application of the `Seed` algorithm, as mentioned in Sec. 5.6, which makes the estimation of the uncertainty connected to the energy loss less reliable. The underestimation present for the `Seed` algorithm is however partly corrected for by the application of the `CKF` as can be seen in Fig. 5.23, showing that the full algorithm produces reliable estimations.

Once the consistency of the estimations were tested using the ideal "fake tracks" sample, similar pull test were applied using the actual tracks produced by `GArSoft`. For this and all the other tests performed on the interaction sample, only tracks containing a minimum of 50 points were considered. This is done for similar reasons to the ones outlined in the "fake tracks" test, as well as eliminating tracks that were incorrectly assigned or formed by `GArSoft`. Given the highly non-Gaussian nature of the residuals shown in Fig. 5.21, the choice of the parameters to be used in the R matrix was non-trivial. While no formal calibration was conducted, the parameters shown to produce the best performance were $\sigma_{xy} = 0.4$ cm and $\sigma_{xy} = 0.3$ cm. The results for the `Seed` and `CKF` algorithms are shown in Figs. 5.24 and 5.25 respectively. Looking at the $s_0 = y$ and $s_1 = z$ the shape of the residual distributions shown in Figs. 5.21b and 5.21c imitate the ones of the corresponding hit clusters spatial residuals, with the first following a Cauchy-like distribution and the second one presenting a double-peak structure. The shape of the residuals distributions directly impacts the estimation of the other three parameters as well. The Π distributions for $s_2 = \sin\phi$, $s_3 = \tan\lambda$ and $s_4 = q/p_{\mathrm{T}}$ while being non-biased and having σs that are of the correct magnitude, are visibly non-normal. After the `CKF` is fully propagated, the pulls show much better results. The Π distribution for $s_1 = z$ is shown to produce a Gaussian distribution centred midway between the

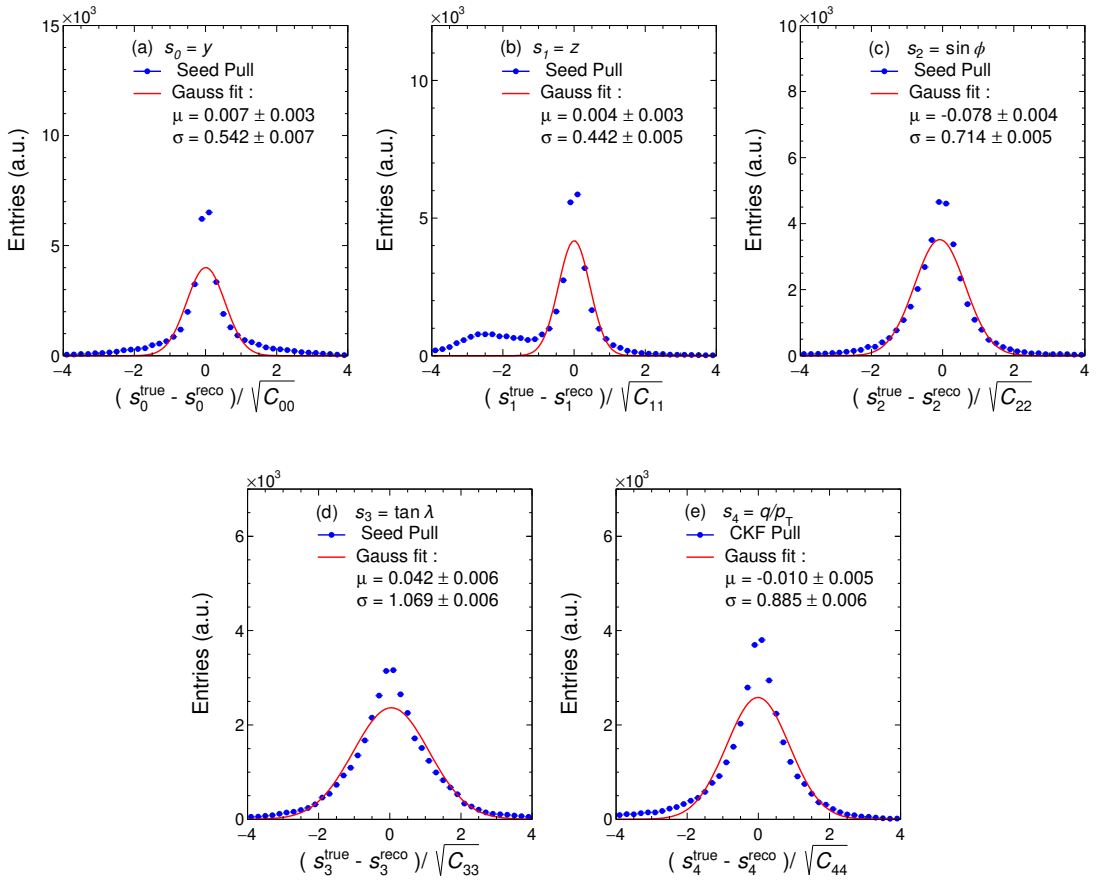

Figure 5.24: Pull distributions for the `Seed` algorithm applied to the "fake tracks" based on the MC trajectories constructed for the interaction sample. All distributions were fitted to a Gaussian function. Results for parameters s_0 to s_4 (i.e. y, x, $\sin\phi$, $\tan\lambda$ and q/p_{T}) are shown from left to right and labelled from (a) to (e) accordingly.

two peaks seen in the `Seed` distribution, demonstrating the smoothing qualities of the KF technique. The $s_0 = y$ distribution is Cauchy-like, but shows much less significant tails and a core distribution with a $\sigma \sim 1$ whereas for the `Seed` the σ was closer to 0.5. For parameters $s_2 = \sin\phi$ and $s_4 = q/p_{\mathrm{T}}$ the distributions are Gaussian, centred at 0 and with $\sigma \sim 1$, while the $s_3 = \tan\lambda$ is significantly underestimated. This was to be expected, since the estimation of $s_3 = \tan\lambda$ is the only one directly impacted by the measurement in the z direction.

The performance of the `CKF` algorithm was tested in terms of momentum resolution and bias and compared to the results obtained with the `GKF` algorithms. The two quantities were first measured by applying a double Gaussian fit to the

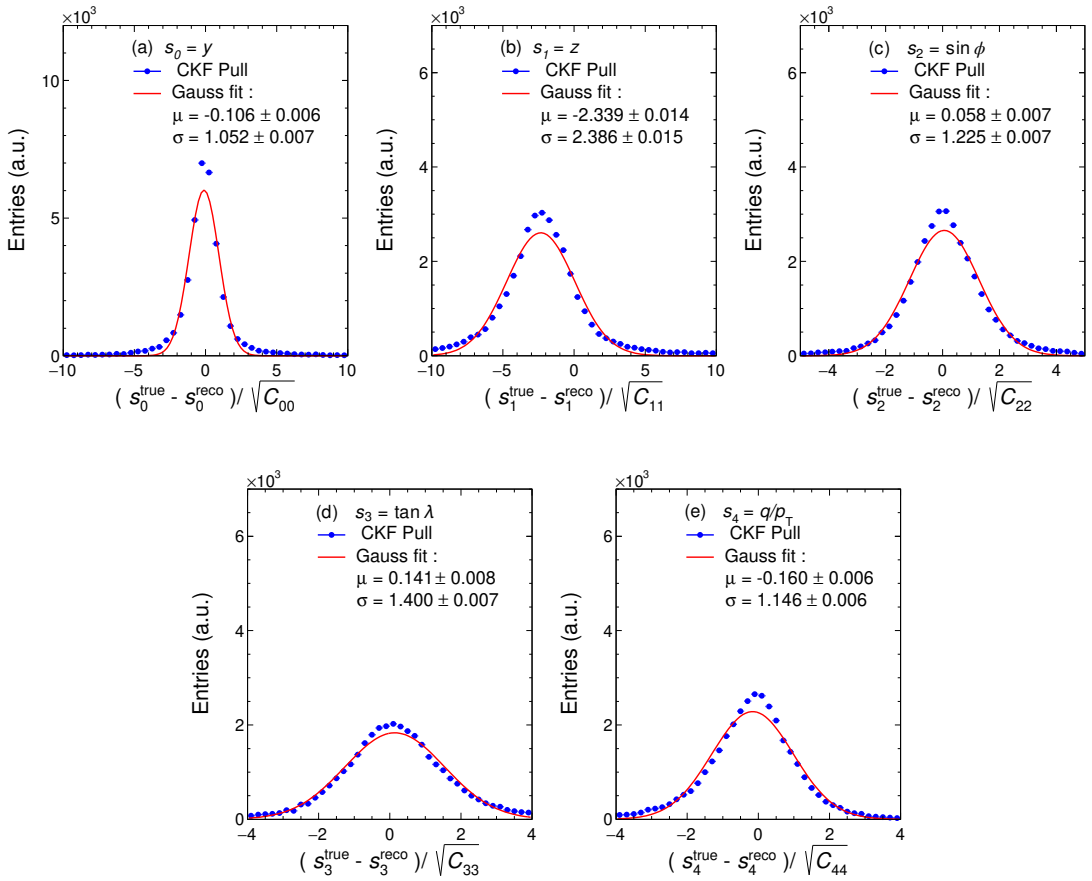

Figure 5.25: Pull distributions obtained after the full propagation of the CKF algorithm applied to the "fake tracks" based on the MC trajectories constructed for the interaction sample. See Fig. 5.6 for comparison.

momentum fractional residuals as defined in Eq. 4.35. This delineates a tail and a core distribution, similarly to what was done in Sec 4.7. The distributions, as well as the fit results, are shown in Fig. 5.26 and were separated by particle type in increasing order of mass from left to right. In the first row we show the results for the CKF algorithm and in the second for the GKF. For all particle types the new algorithm improves the performance both in terms of resolution and bias. The smallest differences can be seen for the muon sample. These are minimum ionizing particles (MIPs) at higher momenta than the other particle types in the sample (see Fig. 5.20a) and are thus the least impacted by the introduction of energy loss and multiple scattering corrections which are present in the CKF and not in the GKF. More significant improvements are seen in the pion sample where for the GKF, the

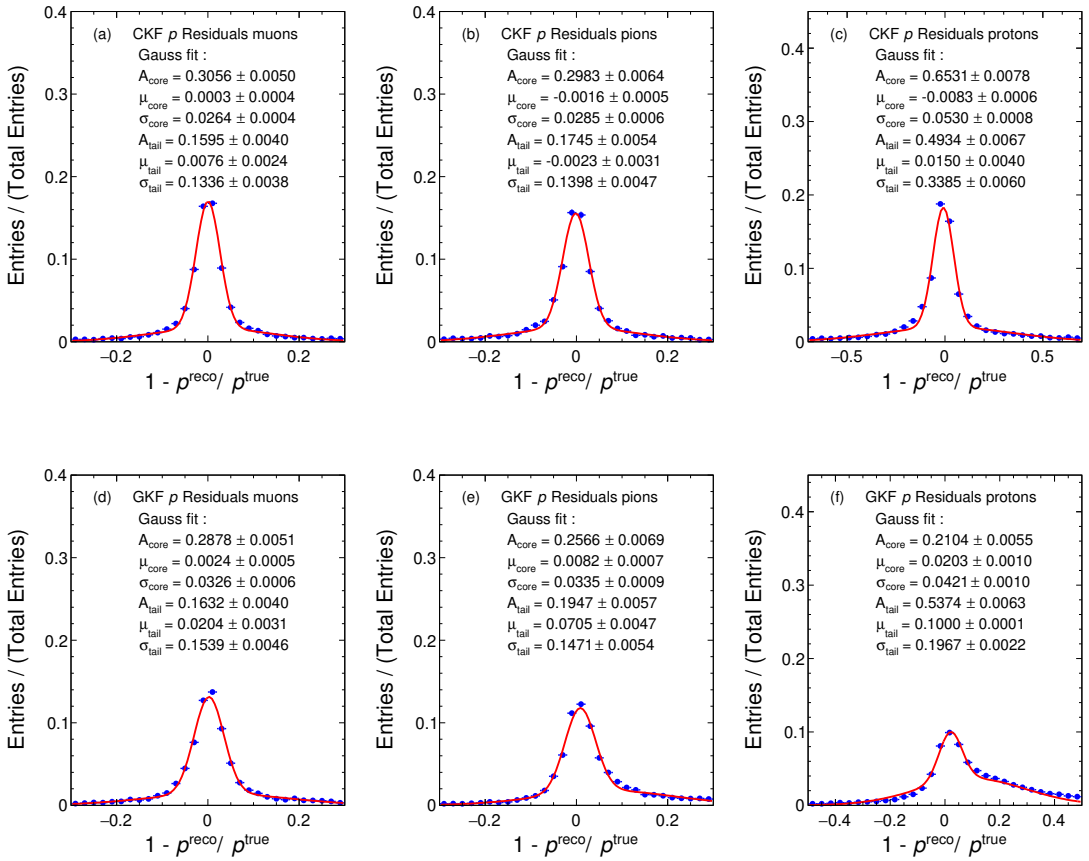

Figure 5.26: Momentum fractional residuals obtained with the `CKF` (top row) and `GKF` (bottom row) algorithms over the interaction sample. In the left column the (a) and (d) plots show the results for muons, in the centre column plots (b) and (e) show the results for pions and in the right column plots (c) and (f) show the results for protons. All distributions are fitted to a double Gaussian defining a core and tail distributions.

tail distribution is significantly biased, an issue which is fully corrected by the `CKF`. This was expected, since the pions are significantly lower energy than the muons in the sample and have thus higher dE/dx. This effect is even more pronounced for the protons, which have similar momenta to the pions but much larger masses and thus lower βs. In this sample the `GKF` produces a tails distribution which contains the majority of the particle tracks and has a bias of almost 10 %. This is not true for the `CKF` distribution where the tail distribution contains $\sim 2/5$ of the sample and is fully unbiased.

The momentum relative resolution and bias are also shown as a function of the total true momentum p_{true} and track length l in Figs 5.27 and 5.28 respectively.

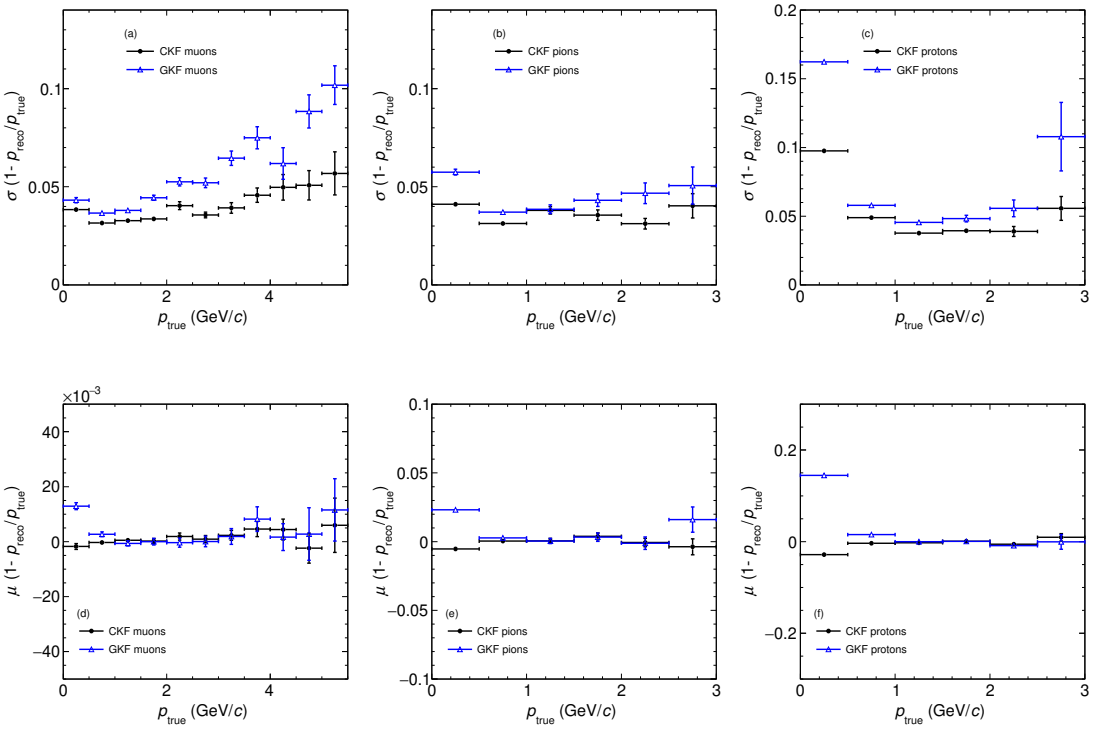

Figure 5.27: Momentum resolution (top row) and bias (bottom row) obtained with the `CKF` algorithm over the interaction sample, as a function of the particle initial true momentum p_{true}. In the left column the (a) and (d) plots show the results for muons, in the centre column plots (b) and (e) show the results for pions and in the right column plots (c) and (f) show the results for protons.

In this case, the relative bias and resolution are defined as the mean and standard deviation of simple Gaussian fits μ and σ applied to the momentum fractional residuals. The results for the `CKF` and `GKF` algorithm are shown in black and blue respectively. The resolutions are shown in the upper panels, while the biases are shown in the lower panels. The different particle types are shown in increasing order of mass from left to right. For both algorithms the resolution dependencies predicted by the formulas shown in Eqs. 4.37 and 4.38 are respected. The p_{true} dependency is characterized by an inverse proportionality on β at lower values where σ_{MS} is dominant and a direct proportionality at higher values where σ_{H} is dominant. The l dependency generally goes as $\sim 1/l$ over the entire spectrum. A general improvement on the resolution can be seen for all the particles over the whole p_{true} and l spectra, with the most significant being for the protons. The

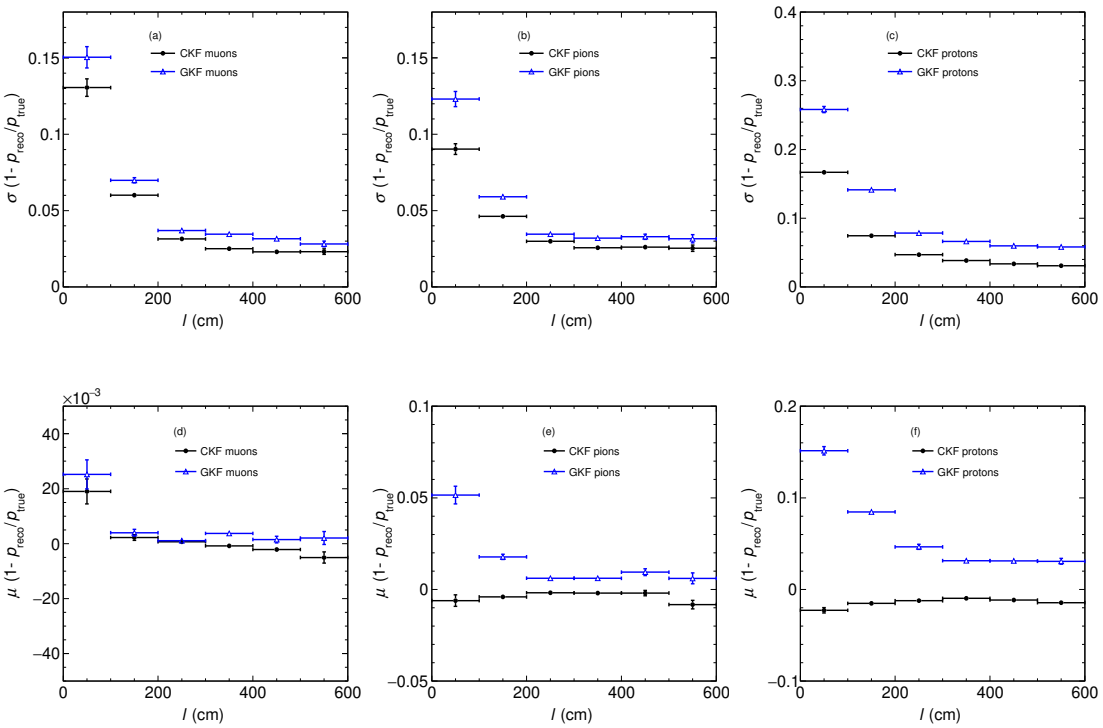

Figure 5.28: Momentum resolution (top row) and bias (bottom row) obtained with the `CKF` algorithm over the interaction sample, as a function of the particle track length l. In the left column the (a) and (d) plots show the results for muons, in the centre column plots (b) and (e) show the results for pions and in the right column plots (c) and (f) show the results for protons.

bias produced by the `GKF` is shown to be strongly momentum dependent, reaching values of up to $\sim$ 2% for muons, $\sim$ 3% for pions and $\sim$ 18% for protons having $p_{\text{true}} < 0.5$ GeV/c and being close to zero for higher momenta. The `CKF`, on the other hand, is shown to produce an un-biased momentum estimation over the whole spectrum, thanks mostly to the material budget corrections. A similar pattern is shown for the length dependency, with the `GKF` producing the most biased results for the shortest tracks. This is especially true for the proton sample for which the correlation between the production of short, mostly stopping tracks and lower momenta is especially direct (see Fig. 5.17b).

The performance of the `CKF` and the `GKF` was also tested in terms of angular resolution and bias. These were defined in terms of μ and σ of simple Gaussian

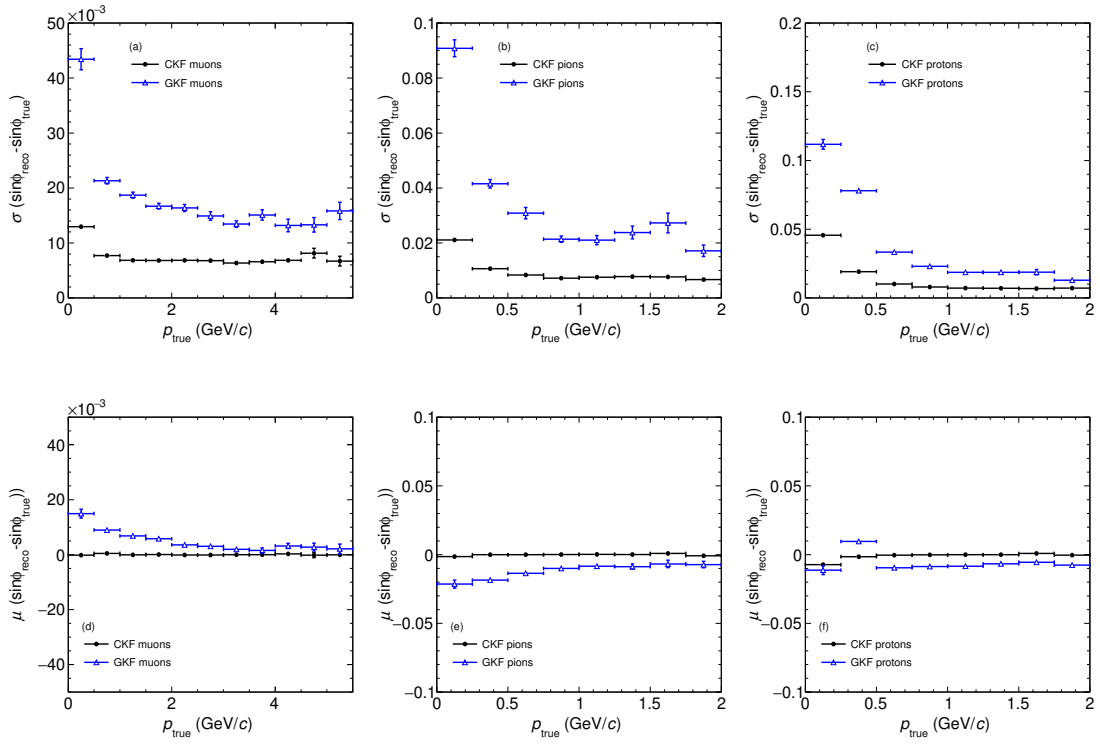

Figure 5.29: $\sin\phi$ resolution (top row) and bias (bottom row) obtained with the CKF algorithm over the interaction sample, as a function of the particle initial true momentum p_{true}. In the left column the (a) and (d) plots show the results for muons, in the centre column plots (b) and (e) show the results for pions and in the right column plots (c) and (f) show the results for protons.

fits of the residual distribution for $\sin\phi$ and $\tan\lambda$ defined as:

$$Res_{\sin\phi} = \sin\phi - \sin\phi_{\text{true}}, \tag{5.25}$$

$$Res_{\tan\lambda} = \tan\lambda - \tan\lambda_{\text{true}}. \tag{5.26}$$

We use absolute residuals instead of fractional, because both $\tan\lambda$ and $\sin\phi$ include 0 in their ranges. The resolution and biases for $\sin\phi$ and $\tan\lambda$ as a function of the particles true momenta p_{true} are shown in Fig. 5.29 and 5.30 respectively. Similarly to what was done for the momentum plots, the resolutions occupy the upper row, while the biases are in the lower row, the results for the GKF and CKF are shown in blue and black respectively and the particles types are shown in order of mass from left to right. Overall the CKF improves the angle resolution significantly for both $\sin\phi$ and $\tan\lambda$ over the whole p_{true} spectrum. A significant

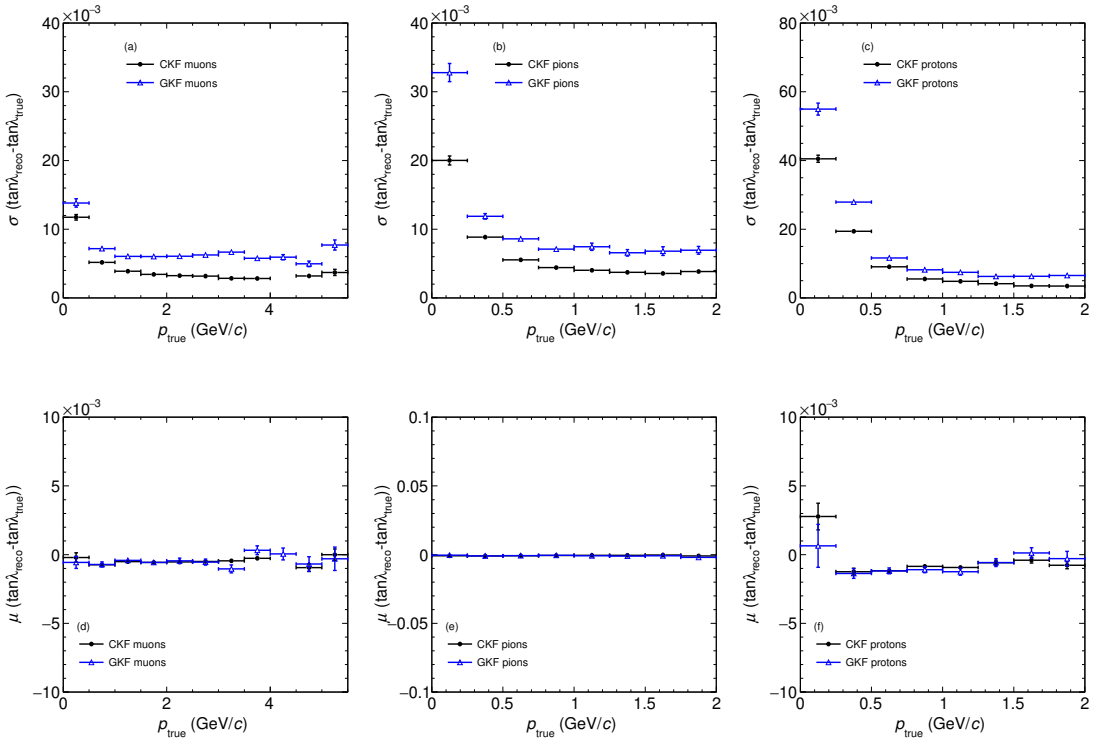

Figure 5.30: $\tan\lambda$ resolution (top row) and bias (bottom row) obtained with the `CKF` algorithm over the interaction sample, as a function of the particle initial true momentum p_{true}. In the left column the (a) and (d) plots show the results for muons, in the centre column plots (b) and (e) show the results for pions and in the right column plots (c) and (f) show the results for protons.

bias in the $\sin\phi$ estimation at lower momenta is also shown in the `GKF` results which is fully removed by the `CKF`.

5.6.2 The forward-going muon sample

In order to study the performance of the `CKF` algorithm for muons coming from ND-LAr we produced a sample of forward going muons using `GArSoft`'s particle gun functionality. The sample contained 10^5 muons, all having the same starting position, 10 cm in the x direction from the upstream wall of the TPC and with the same y and z coordinates as its center. The initial momenta of the muons were uniformly distributed between 0.5 GeV/c and 3 GeV/c, with the forward x component constituting a minimum of 80% of the total and the y and z being assigned a maximum of 10% each in either directions. We'll refer to this sample

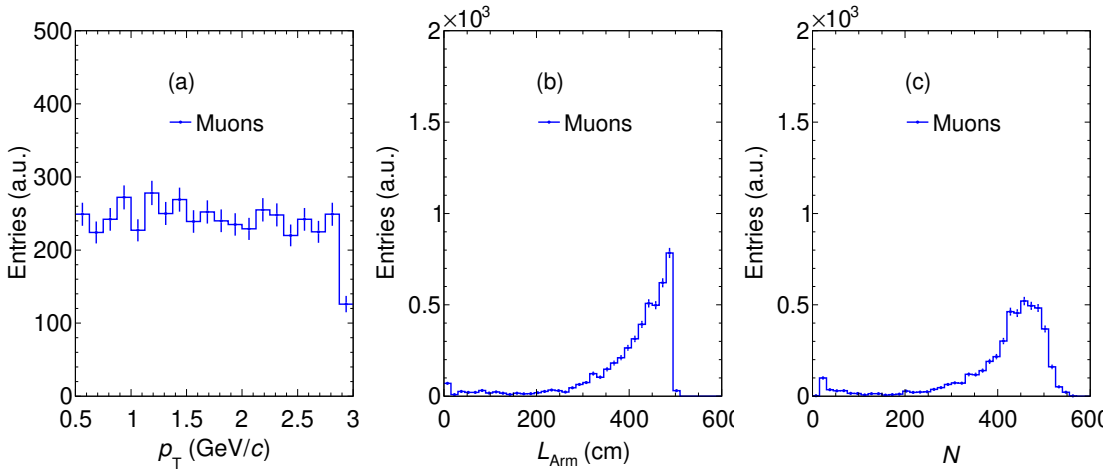

Figure 5.31: Distributions of (a) transverse momentum p_{T}, (b) lever arm L_{Arm} and (c) number of points per track N in the forward-going muon sample.

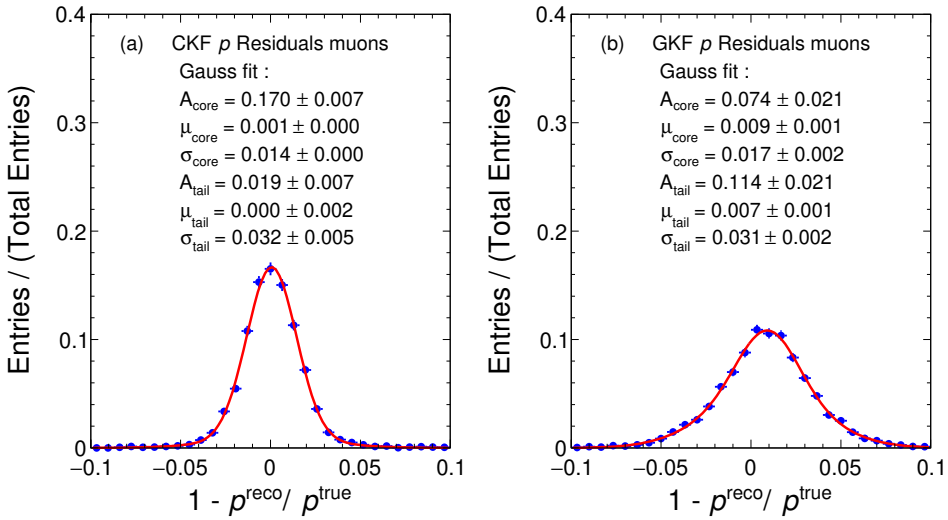

Figure 5.32: Momentum fractional residuals obtained with the `CKF` (a) and `GKF` (b) over the forward-going muon sample. All distributions are fitted to a double Gaussian defining a core and tail distributions.

as the forward-going muon sample.

The initial true momenta p_{true}, lever arm L_{Arm} and number of hit clusters N belonging to the muon tracks in the sample are shown in Fig. 5.31. Since all the muons were set to be forward going and coming from outside the TPC, the vast majority traverse the entire detector cylinder resulting in a L_{Arm} distribution whose peak is close to the full length of the diameter which is 500 cm. This is true for N

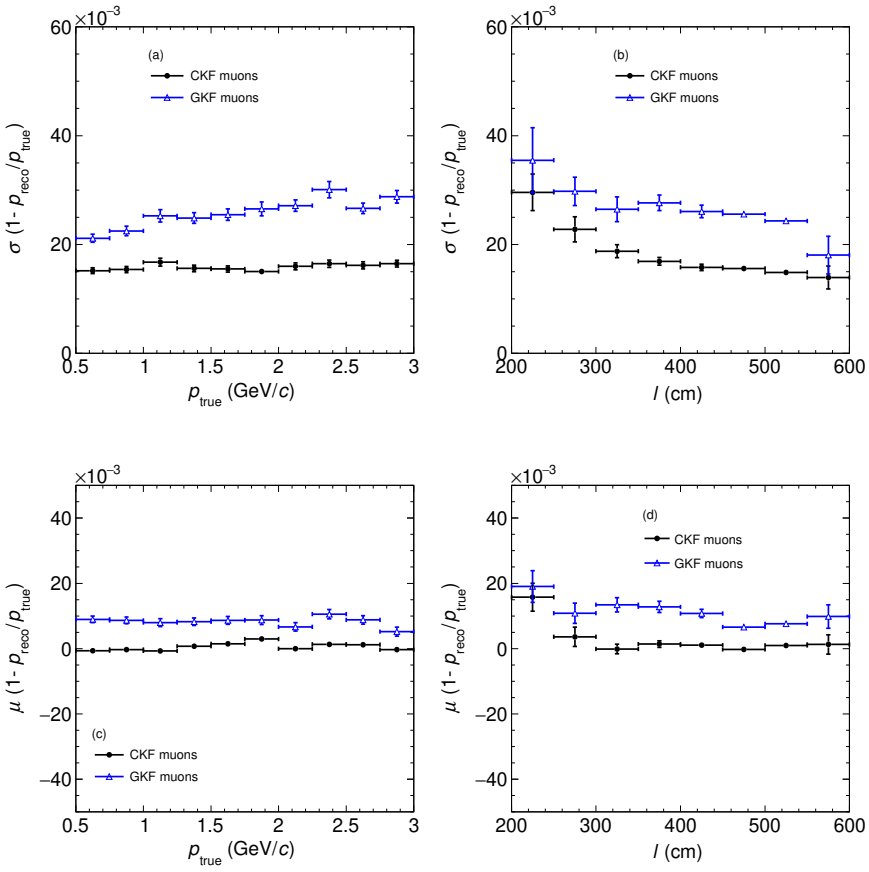

Figure 5.33: Momentum resolution (top row) and bias (bottom row) obtained with the `CKF` algorithm over the forward-going muon sample. The results are shown as a function of the particle initial true momentum p_{true} in (a) and (c), and as a function of track length in (b) and (d).

as well, since we expect to have about one hit cluster per cm of the trajectory.

The performance of the `CKF` algorithm was tested in terms of relative momentum resolution and compared with the results obtained with the `GKF`. The μ and σ for the whole samples were defined in the usual way, as the results of double Gaussian fits on the momentum fractional residuals distributions, obtaining a core and tail split (see Sec. 5.6.1). The fractional residuals distributions and the results of the fits are shown in Fig. 5.32. The `CKF` algorithm improves on the performance of the `GKF` algorithm both in terms of resolution and bias. Firstly, while the σ's of the core and tails distributions between the two algorithms is similar, the ratios between the number of entries is inverted. In the `CKF` the core distribution contains almost 9 times the number of entries of the tails $A_{core}/A_{tails} \simeq 8.94$, while for the

GKF the ratio is $A_{core}/A_{tails} \simeq 0.65$. The GKF distribution is also biased by a factor of about 1% in both the core and tail distribution, which is fully eliminated by the energy loss and multiple scattering corrections introduced by the CKF, as was already seen in the studies presented in the previous section. Using these fits, it is also possible to compare the CKF results with those obtained using the ND-GAr-Lite detector on a similar sample of forward-going muons as discussed in Sec. 4.7. Focusing on the results obtained with the best track fit configuration "3-point Seed + KF" we see an improvement using the CKF and the ND-GAr detector of a factor of $\sigma_{tails}/\sigma^{lite}_{tails} \simeq 0.57$ for the tails and $\sigma_{core}/\sigma^{lite}_{core} \simeq 0.73$ for the core. The ratio A_{core}/A_{tails} is also improved by a factor of ~ 2.

The resolution and bias are shown in Fig. 5.33 as a function of the muons' true initial momenta p_{true} and lengths l. In this case the resolution and bias are defined as the μ and σ of simple Gaussian fits, applied to the fractional residual distributions. We show the results for the CKF in black and for the GKF in blue. Improvements in resolution and bias are seen over the whole spectra and consistent with the previous results obtained with the Interaction sample.

5.6.3 Full implementation results

Once the CKF was considered to be sufficiently mature and it was demonstrated that the new algorithm outperformed the GKF, work was done to fully integrate the CKF into GArSoft. This was done by creating a new reconstruction module named ALICEKalmanTrackFit_module.cc that could replace all the functionalities of the old module hosting the GKF algorithm named tpctrackfit2_module.cc [172]. Both the CKF and GKF were left available in GArSoft, with the CKF being set as the new default reconstruction algorithm.

In order to verify the correct implementation of the CKF a sample of 10^6 ν_μ CC interactions was produced using the ALICEKalmanTrackFit_module.cc in GArSoft and re-reconstructing all the particle tracks locally, using the original fastMCKalman based code used in Sec. 5.6.1 and 5.6.2. The fit results for all the state vector parameters $s(x) = (y, z, \sin\phi, \tan\lambda, q/p_{\text{T}})$ as well as the free parameter x were then

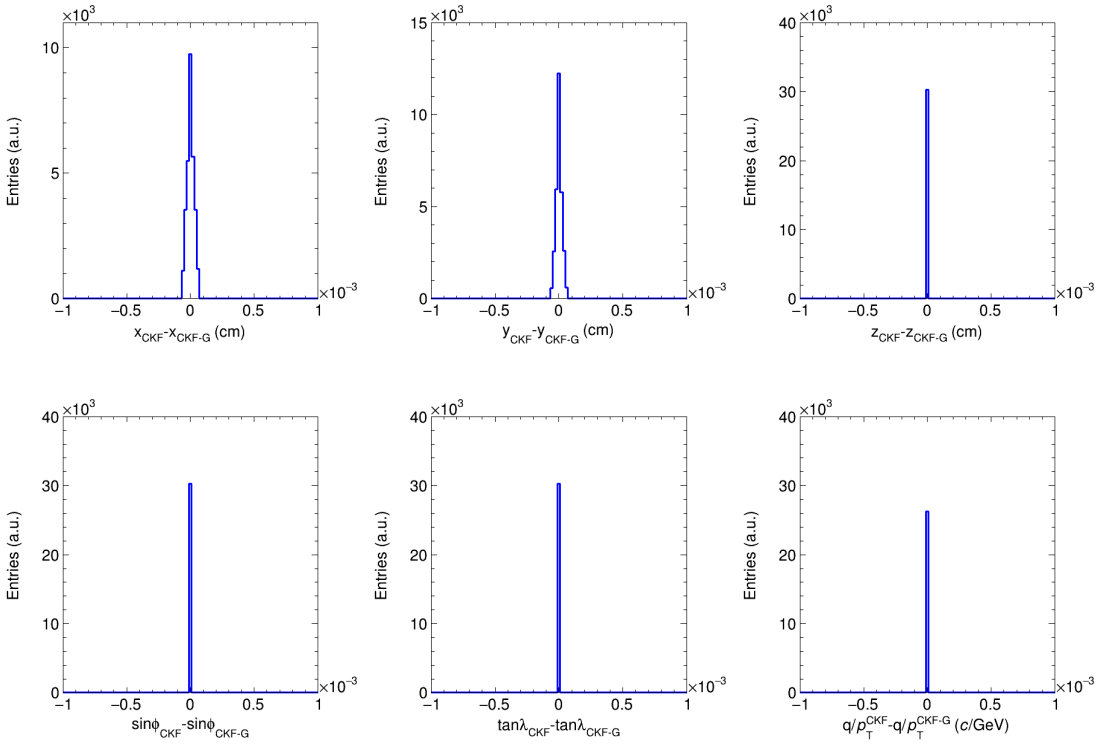

Figure 5.34: Residuals between fit results obtained with the implementation of the `CKF` in `GArSoft` and the re-reconstructed results from the original implementation in `fastMCKalman`. The results are shown for all the state vector parameters: (Top left) x; (Top center) y; (Top right) z; (Bottom left) $\sin\phi$; (Bottom center) $\tan\lambda$; (Bottom right) q/p_{T}.

directly compared by evaluating the residuals. The results of these comparisons are shown in Fig. 5.34. The residuals for all parameters never exceed 10^{-4}, a factor that can be attributed to rounding errors. These results demonstrate the consistency between the local code and the new `GArSoft` module, which can be considered to be properly implemented.

With the `CKF` fully implemented in `GArSoft`, additional tests could be performed to evaluate the performance of the `CKF` and compare it to the `GKF`. In order to do this, the ν_μ CC sample used for the implementation test, was also reconstructed through `GArSoft` using the `GKF`, producing two sets of analysis data files that could be directly compared. The first feature that was studied using these two data sets was the reconstruction efficiency ϵ_{reco}. We define ϵ_{reco} as the fraction of primary particles produced in the ν_μ CC interactions inside the TPC fiducial volume defined in Sec.

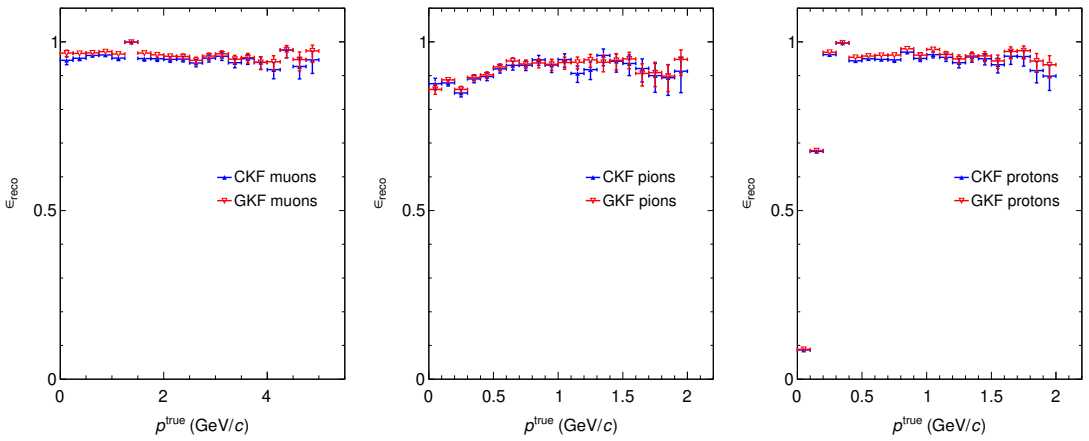

Figure 5.35: Reconstruction efficiencies as a function of the particles true momenta p_{true}. Muons pions and protons are shown in increasing order of mass from left to right and the results from the `CKF` are shown in blue, while the ones for the `GKF` are shown in red.

5.6.1 for which at least a reconstructed track with available fit results was produced. The reconstruction efficiencies as a function of the particles true momenta p_{true} are shown in Fig. 5.35. Muons pions and protons are shown in increasing order of mass from left to right and the results from the `CKF` are shown in blue, while the ones for the `GKF` are shown in red. The reconstruction efficiencies for the two algorithms are shown to be essentially equivalent for the two algorithms over the whole momentum spectrum and for all analysed particle types, being consistently above 90% for muons and pions, and reaching similar levels for protons for $p_{\text{true}} > 0.3$ MeV/c.

Another feature that could be tested and compared using the two data samples, was the quality of the interaction vertex fitting (see Sec. 5.4.4 for a brief description) using the reconstructions provided by the two algorithms. In Fig. 5.36 we show the vertex fit residual distributions in all three dimensions, fitted to a Cauchy distribution defined as:

$$C = \frac{K}{\pi} \frac{b}{(x-m)^2 + b^2}, \tag{5.27}$$

with K being a normalization factor, m being the centre of the distribution and b being the width. The `CKF` results are shown in the top row, while the `GKF` ones are shown in the bottom row. The resolutions obtained with the new algorithm,

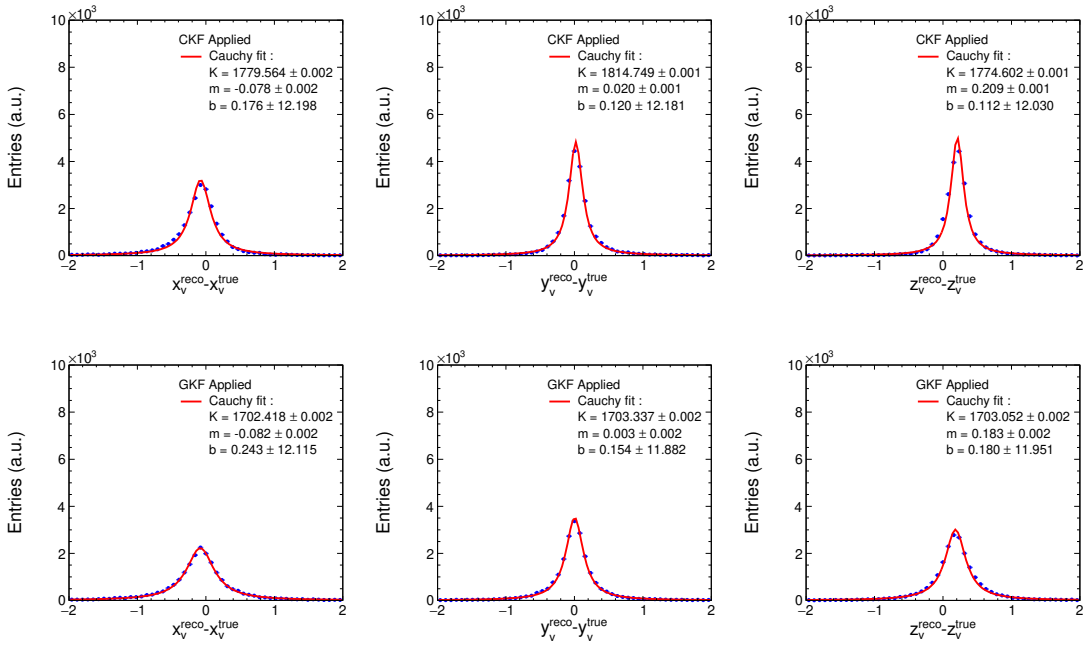

Figure 5.36: Vertex fit residual distributions for x (Left), y (Center) and z (Right) coordinates fitted to a Cauchy distribution. We show the results for the `CKF` and `GKF` in the top and bottom rows respectively.

which we can define as the width b of the Cauchy fits, consistently outperform the ones obtained with the `GKF`.

5.7 Results summary

In Sec. 5.2, we introduced `CKF`, a KF based algorithm tailored for homogeneous gas TPCs such as ND-GAr, adapted from the one used in the ALICE experiment. An inherent limitation in the original ALICE approach arises from its suitability only for tracks describing a semi-circle at most in the xy plane, perpendicular to the detector's magnetic field. We discovered that this challenge can be addressed by applying a mirror rotation to the state vector when reaching the semi-circle's boundaries. This adjustment is facilitated by introducing an xy plane rotation during the KF propagation step, converting the longitudinal x coordinate into the radial distance from the rotation center. By implementing this technique, the new algorithm can effectively track trajectories of any length, including multiple circular paths within the detector (loopers).

To test the new algorithm, we developed a toy MC simulation tool named `fastMCKalman` (Sec. 5.3) and generated a sample with diverse detector and particle properties to validate its performance across a wide parameter space (Sec. 5.5). Multiple tests conducted on this sample demonstrated that the algorithm's estimates for parameter covariance effectively describe the sample (Figs. 5.6, 5.7 and 5.8) and align closely with theoretical expectations, as defined in Eqs. 5.22 and 5.23. This last point is highlighted by Figs. 5.9, 5.11 and 5.10, where the theoretically expected resolution was first shown on its own for different particle types, gas densities and resolution and then directly compared with the `CKF` estimations by showing their ratios. Despite the wide resolution ranges shown for the theoretical expectations, the ratios are uniformly close to 1, demonstrating close agreement.

A significant improvement in the reconstruction efficiency for the low N and low p_{T} mirrored tracks was also shown in Fig. 5.13, in some cases going from $\epsilon \sim 0.5$ to $\epsilon > 0.5$. Furthermore, we examined the impact of the mirroring technique by comparing the ratios of q/p_{T} resolutions with and without its application, revealing relative improvements by up to 80% for low-energy electrons and up to 50% for muons and pions (Figs. 5.14 and 5.15). Additionally, we evaluated the `CKF` performance using a sample of particles propagated in a high material budget environment, simulating conditions akin to a HPgTPC like ND-GAr. Realistic assessments of relative momentum resolution and bias showed behaviours consistent with theoretical expectations (Figs. 5.16 and 5.18), affirming the viability of applying the method to a neutrino gas TPC.

Once the `CKF` algorithm was shown to be internally consistent, its performance was evaluated using the more sophisticated simulation provided by `GArSoft`, which was described in Sec. 5.4. The primary sample consisted of protons, muons, and pions produced in 5×10^4 ν_μ CC interactions within the ND-GAr TPC volume (Sec. 5.6.1). To assess the quality of the uncertainty estimates produced by `CKF`, an intermediate test was performed using "fake tracks" constructed from the true MC particle trajectories. These tracks were generated by down-sampling the trajectory points and smearing their positions with Gaussian noise in the

x and y planes. This approach decoupled the evaluation of `CKF` performance from `GArSoft`'s hit clustering, which was shown to produce highly non-Gaussian residuals (see Fig. 5.21). Pull tests were applied to both the `Seed` and the fully propagated `CKF` and the results were shown in Figs. 5.22 and 5.23. For the `Seed`, the pulls were centred at zero with $\sigma \sim 1$, except for q/p_{T}, where uncertainties were underestimated by approximately 40%. This discrepancy likely originated from the use of the entire track in the `Seed` algorithm, which reduces the reliability of the energy loss uncertainty estimate. The underestimation was shown to be largely corrected by the `CKF` propagation.

Pull tests were also performed using the actual tracks reconstructed by `GArSoft`, showing results consistent with the hit cluster residuals (Figs. 5.24 and 5.25). This sample was further used to evaluate the `CKF` reconstruction performance and compare it to `GKF`, the standard algorithm at the time, which lacked material budget corrections. The results of double Gaussian fits applied to the fractional momentum residuals for primary muons, pions, and protons are summarized in Tab. 5.1 and shown in Fig. 5.26. In all cases, `CKF` improved both resolution and bias. The smallest differences were observed for muons, which are MIPs at relatively high momenta (see Fig. 5.20a) and are thus less affected by energy loss and multiple scattering. Larger improvements were seen for pions, where the `GKF` tail was significantly biased, an issue fully corrected by `CKF`. The effect was even stronger for protons, which have similar momenta to pions but lower β. For protons, the `GKF` tail contained most tracks and exhibited a 10% bias, while the `CKF` tail contained only $\sim 2/5$ of the sample and was fully unbiased.

The momentum resolution and biases obtained for `CKF` and `GKF`, were also compared and shown as a function of some key track properties in Figs. 5.27 and 5.28. In all cases the `CKF` consistently outperformed the `GKF`. The resolutions produced by both algorithms followed the expected theoretical behaviours outlined in Eqs. 4.37 and 4.38. The $\tan\lambda$ and $\sin\phi$ resolutions were also consistently improved by the `CKF`, as shown in Figs. 5.29 and 5.30.

Particle	μ^-		$\pi^\pm$		p^+	
Reco	GKF	CKF	GKF	CKF	GKF	CKF
A_{core}	0.287 ± 0.005	0.306 ± 0.005	0.257 ± 0.007	0.298 ± 0.006	0.210 ± 0.006	0.653 ± 0.008
μ_{core} (%)	0.24 ± 0.05	0.03 ± 0.04	0.82 ± 0.07	-0.16 ± 0.05	2.0 ± 0.1	-0.83 ± 0.06
σ_{core} (%)	3.26 ± 0.06	2.64 ± 0.04	3.35 ± 0.09	2.85 ± 0.06	4.2 ± 0.1	5.30 ± 0.08
A_{tail}	0.163 ± 0.004	0.160 ± 0.004	0.195 ± 0.006	0.175 ± 0.005	0.537 ± 0.006	0.493 ± 0.007
μ_{tail} (%)	2.0 ± 0.3	0.8 ± 0.2	7.0 ± 0.5	-0.2 ± 0.3	10.00 ± 0.01	1.5 ± 0.4
σ_{tail} (%)	15.4 ± 0.5	13.4 ± 0.4	14.7 ± 0.5	14.0 ± 0.5	19.7 ± 0.2	33.9 ± 0.6

Table 5.1: Summary of the momentum reconstruction performance evaluated for the KF-Lite and ILRM algorithms, in the different test configurations described in the chapter. The key parameters arise from double Gaussian fits, defined in Eq. 4.36, applied to fractional momentum residual distributions.

An additional sample of forward-going muons with momenta uniformly distributed between 0.5 GeV/c and 3 GeV/c was generated using GArSoft's particle gun (Sec. 5.6.2). The CKF consistently outperformed the GKF. Applying a double Gaussian fit to the fractional momentum residuals (Fig. 5.32), also allowed for direct comparison with the ND-GAr-Lite performance (see Sec. 4.7). Comparing with the best-performing ND-GAr-Lite algorithm, "3-point Seed + KF-Lite", we showed that the ND-GAr detector with CKF achieved improvements of $\sigma_{tails}/\sigma_{tails}^{lite} \simeq 0.57$ and $\sigma_{core}/\sigma_{core}^{lite} \simeq 0.73$, along with a factor ~ 2 improvement in A_{core}/A_{tails}.

Once the CKF was shown to consistently outperform GKF, it was fully integrated into GArSoft (Sec. 5.6). Several checks were performed, confirming that the performance of the algorithm was preserved. The integration also enabled additional comparisons between CKF and GKF, which demonstrated comparable reconstruction efficiency (Fig. 5.35) and a slight improvement in vertex resolution (Fig. 5.36).

6

Accessing neutrino interactions via transverse kinematic imbalance

Contents

6.1 Introduction

Research into charged-current (CC) neutrino-nucleus interactions, which is essential for spectrum measurements in accelerator neutrino experiments, has primarily targeted inclusive and semi-inclusive observables, such as total cross sections and lepton kinematics. These observables are highly dependent on neutrino energy and are difficult to compare directly between experiments due to the broad energy range of the neutrino fluxes produced. To accurately interpret the data, theoretical models of fundamental interactions and nuclear effects must be integrated with estimated neutrino energy spectra. Consequently, accurately accessing nuclear effects is challenging, yet understanding these effects is crucial for determining the spectra.

Recently a novel method of investigating nuclear effects has been proposed, which involves a set of kinematic variables referred to as Transverse Kinematic Imbalance (TKI), which take inspiration from the "missing energy" concept in collider experiments. The technique has been introduced in the literature roughly 10 years ago through a series of seminal papers [8–11] and has been applied successfully to many accelerator experiments since, such as Minerνa [173–175], T2K [136, 176] and MicroBoone [177]. Some work has also been done to test the applicability of the TKI method to ND-GAr [2]. In particular the low detection threshold of the gas TPC combined with its 4π acceptance, make it an ideal candidate. Because of these favourable characteristics it has been suggested that it could be possible in a HPgTPC such as ND-GAr to use double-TKI variables to extract a sample of hydrogen interactions from a more complex multi-nuclear gas mixture [12]. A sample of hydrogen interactions would be especially beneficial to the measurement of neutrino spectra at the DUNE ND, because it would be completely devoid of nuclear effect systematics.

This chapter will be organized as follows: in Sec. 6.2 we introduce the concepts behind the TKI technique and we define some of the original variables used to apply it; in Sec. 6.3 we introduce the double-TKI variables and how they can be used to select for hydrogen events; in Sec. 6.4 we apply the technique to a ν_μ CC sample simulated for the ND-GAr detector, and we evaluate the detector performance, discussing the improvements brought by the `CKF` algorithm introduced in Chapter 5.

6.2 Single transverse kinematic imbalance

In this section we give a brief overview of single-TKI variables and how they can be used to study nuclear effects in a way that is largely neutrino energy independent [9]. Let's consider a neutrino CC interaction on a nucleus. At the most basic level this can be described as a neutrino ν interacting with a nucleon N. The neutrino transforms into a charged lepton ℓ' and the nucleon changes into a different hadronic state N':

$$\nu + N \rightarrow N' + \ell'. \tag{6.1}$$

In the rest frame of the nucleus, the bound nucleon has a Fermi motion (FM) induced momentum $\vec{p}_N$. The virtual W boson that carries the interaction, transfers its 4-momentum $(w, \vec{q})$ to the nucleon producing a new hadronic state with an exiting momentum $\vec{p}_{N'}$. Below the deep-inelastic scattering (DIS) region, especially in quasi-elastic (QE) and resonant (RES) interactions, the cross section is suppressed when $Q = \sqrt{q^2 - w^2}$ is larger than the mass of the nucleon m_N. Above the scale $Q^2/2m_N \sim \mathcal{O}(0.5)$ GeV, the hadron momentum saturates and most of the increase in momentum is absorbed by the exiting lepton. The momentum $\vec{p}_{N'}$ is only dependent on the initial neutrino energy via second order effects such as nucleon polarization and Pauli blocking.

Once the new hadronic state N' is produced, it starts propagating in the nuclear medium. Assuming that the original CC interactions and the propagation are not correlated, the momentum $\vec{p}_{N'}$ completely determines the interaction probability and the energy momentum transfer $(\Delta E, \Delta\vec{p})$. It is the latter that in turn determines the nuclear excitation and break-up probability, or in other worlds the probability of final state interactions to occur. It follows that the in-medium energy-momentum transfer $(\Delta E, \Delta\vec{p})$ would be an ideal observable, to measure nuclear effects in a neutrino-energy independent way. Unfortunately the quantities E_ν and $\vec{p}_N$ are unknown, which makes $(\Delta E, \Delta\vec{p})$ experimentally inaccessible. However, $\Delta\vec{p}$ can be inferred by measuring the following single TKI variables (see Fig. 6.1):

$$\delta\vec{p}_{\mathrm{T}} = \vec{p}_{\mathrm{T}}^{\,\ell'} + \vec{p}_{\mathrm{T}}^{\,N'}, \tag{6.2}$$

$$\delta\alpha_{\mathrm{T}} = \arccos\frac{-\vec{p}_{\mathrm{T}}^{\,\ell'}\cdot\delta\vec{p}_{\mathrm{T}}}{p_{\mathrm{T}}^{\ell'}\delta p_{\mathrm{T}}}, \tag{6.3}$$

where $p_{\mathrm{T}}^{\ell'}$ and $\vec{p}_{\mathrm{T}}^{\,N'}$ are the projections of the exiting charged lepton and hadron momenta on the plane transverse to the neutrino direction. $\delta\vec{p}_{\mathrm{T}}$ is called the transverse momentum imbalance and $\delta\alpha_{\mathrm{T}}$ is the boosting angle, defined as the angle between $\vec{q}_{\mathrm{T}}$ and $\delta\vec{p}_{\mathrm{T}}$. Note that $-p_{\mathrm{T}}^{\ell'} = \vec{q}_{\mathrm{T}}$ is the transverse component of the W-boson momentum. The momentum imbalance and the boosting angle can be defined both in the case of simple QE interactions as well as in the case of RES interactions. In the first case $\vec{p}_{\mathrm{T}}^{\,N'}$ is defined as the transverse momentum of the

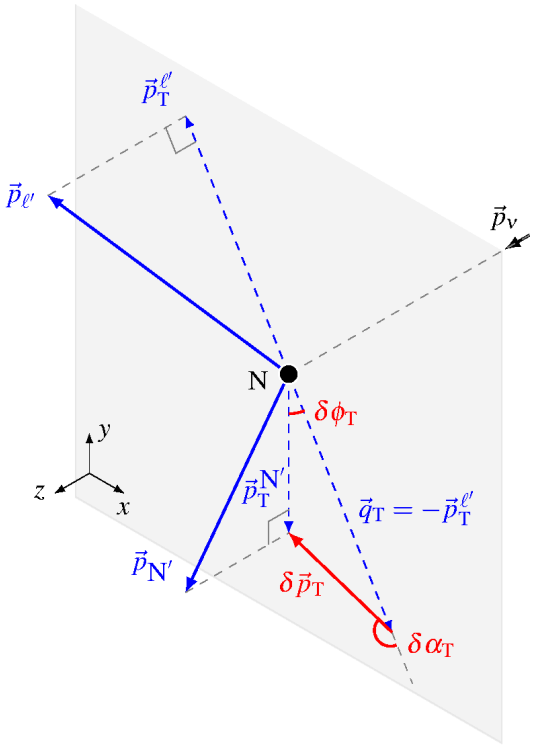

Figure 6.1: Schematic illustration of the single-transverse kinematic imbalance variables defined in the plane transverse to the neutrino direction [9].

exiting proton, while in the latter it is taken as the sum of the momenta of the exiting particles produced in the decay of the resonance.

To understand how $\delta\vec{p}_{\mathrm{T}}$ directly relates to the momentum transfer $\Delta\vec{p}$ one only needs to consider the kinematics of the interaction and the conservation of momentum in the transverse plane, which can be written as:

$$\vec{p}_T^{\,N} = \vec{p}_{\mathrm{T}}^{\,\ell'} + \vec{p}_{\mathrm{T}}^{\,N'} + \Delta\vec{p}_T, \tag{6.4}$$

where the neutrino momentum in the transverse plane is 0 by construction, $\vec{p}_T^{\,N}$ is the transverse component of the initial bound nucleon momentum, and $\vec{p}_T$ is the transverse component of the momentum transfer. From this the transverse momentum imbalance can be re-written as:

$$\delta\vec{p}_{\mathrm{T}} = \vec{p}_{\mathrm{T}}^{\,N} - \Delta\vec{p}_T. \tag{6.5}$$

It is clear from this expression that in the case of an interaction on a free nucleon (as it would the case for an hydrogen nucleus), $\delta\vec{p}_{\mathrm{T}}$ would be equal to 0. Conversely,

in the case of an interaction with a bound nucleon where FSI effects were switched off, $\delta\vec{p}_{\mathrm{T}}$ would be equal to the transverse projection of $\vec{p}_{\mathrm{T}}^{N}$. This would produce a distribution of δp_{T} with a FM peak independent of neutrino energy, and a flat distribution in $\delta\alpha_{\mathrm{T}}$. The FSI-induced acceleration (deceleration) of the propagating N instead pushes $\delta\vec{p}_{\mathrm{T}}$ forward (backward) to $(-)q_{\mathrm{T}}$, inducing a long tail in its distribution, and making $\delta\alpha_{\mathrm{T}} \to 0^{\circ}$ (180°).

6.3 Double transverse kinematic imbalance

The double-TKI variables and their proposed used in neutrino physics can be traced back to [9]. The paper proposes to use this TKI quantity to extract a sample of neutrino interactions on hydrogen using final state kinematics in CC RES production. Hydrogen is an ideal target for reconstructing the neutrino energy, since it's unaffected by nuclear effects, which are a major source of systematic uncertainty in the measurement of neutrino spectra.

The traditional measurement of the energy spectra of neutrino beams is done using CC QE interactions on bound nuclei. The neutrino energy can be reconstructed by measuring the exiting lepton momentum vector. This is done under the assumption that the initial nucleon is static and thus the measurement's accuracy is strongly limited by the uncertainty brought by FM and the binding energy. In order to take into account the properties of the nucleon, the final state momenta of all the exiting particles can be measured and summed up instead. However, FSIs can strongly modify the kinematics of the final state nucleon, bringing further uncertainties. An additional calorimetric approach is to reconstruct the neutrino energy by summing all the visible energy of the exiting particles. The precision of this method is, however, still limited, although to a lesser degree, by an influence from nucleon initial state uncertainties and by the systematics related to measuring the energy of neutral particles. Furthermore, FSI can modify the visible kinematics of the interactions to such a degree that, for example, resonant interactions can be misidentified as CC QE due to the reabsorption of pions into the nuclear medium.

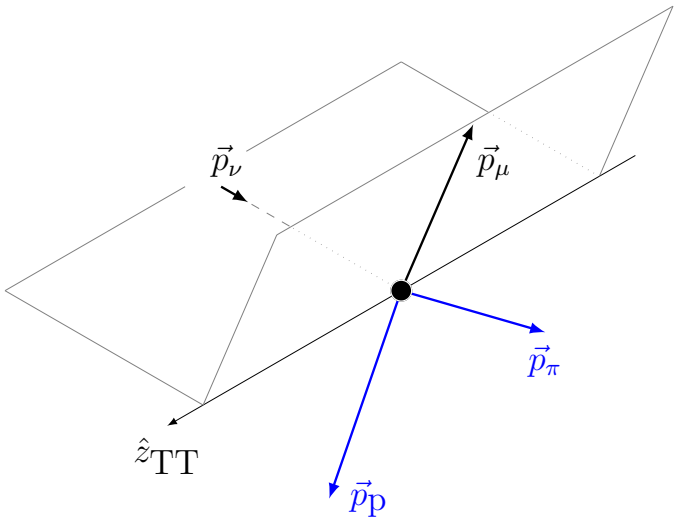

Figure 6.2: Schematic diagram for the particle kinematics of Eq. 6.6. The neutrino and muon momentum vectors, $\vec{p}_\nu$ and $\vec{p}_\mu$, define the double-transverse axis $\vec{z}_{\mathrm{TT}}$ from Eq. 6.7, onto which the proton and pion momentum vectors, $\vec{p}_{\mathrm{p}}$ and $\vec{p}_\pi$, are projected. The sum of these projections defines δp_{TT} in Eq. 6.8 [12].

All these difficulties are avoided by using an hydrogen sample. However, producing an experiment with a high enough mass of pure hydrogen to study neutrino interactions is highly impractical. Using the double-TKI variable $\delta\vec{p}_{\mathrm{TT}}$ one can in principle extract hydrogen interactions from a sample of various nuclear targets.

We define $\delta\vec{p}_{\mathrm{TT}}$ in the specific case of a CC RES interaction, where a Δ^{++} resonance is produced and decays into a pion and a proton:

$$\nu + p \to \ell^- + (\Delta^{++}) \to \ell^- + p + \pi^+ \tag{6.6}$$

We define a double transverse axis $\vec{z_{\mathrm{TT}}}$ which is perpendicular to both the neutrino momentum $\vec{p}_\nu$ and the charged lepton momentum $\vec{p}_{\ell^-}$:

$$\vec{z}_{\mathrm{TT}} = \frac{\vec{p}_\nu \times \vec{p}_{\ell^-}}{|\vec{p}_\nu \times \vec{p}_{\ell^-}|} \tag{6.7}$$

A schematic diagram showing the particle kinematics in Eq. 6.6 and the definition of $\vec{z}_{\mathrm{TT}}$ in Eq. 6.7 can be found in Fig. 6.2. Note that in this case the exiting lepton is assumed to be a muon $\ell^- = \mu^-$.

The momentum of the pion $\vec{p}_\pi$ and the proton $\vec{p}_{\mathrm{p}}$ can be projected on the double transverse axis obtaining $p^\pi_{\mathrm{TT}} = \vec{p}_\pi \cdot \vec{z}_{\mathrm{TT}}$ and $p^{\mathrm{p}}_{\mathrm{TT}} = \vec{p}_p \cdot \vec{z}_{\mathrm{TT}}$. The double-TKI is

defined as the sum of these two quantities:

$$\delta p_{\mathrm{TT}} = p^{\pi}_{\mathrm{TT}} + p^{\mathrm{p}}_{\mathrm{TT}} \tag{6.8}$$

For an hydrogen target, similarly to δp_{T}, δp_{TT} is equal to zero and the spread of its distribution is fully determined by detector response. For a nuclear target where FM and FSI play a role, δp_{TT} has the following characteristics: it is distributed symmetrically around zero, since the proton motion and the decay kinematics of the resonance are not correlated to $\vec{z}_{\mathrm{TT}}$; since FM is isotropic in nature, the spread of the distribution is mainly determined by the magnitude of the average FM momentum ($\sim$ 200 MeV/c for carbon); additional smearing effects are brought by FSI of the resonance and the decay products. In both cases this is independent from the neutrino energy and decay kinematics. The drastic difference between the δp_{TT} distribution in hydrogen, which is, for a perfect detector equal to a Dirac delta peaked in 0, and the distribution for other nuclear targets where an intrinsic spread of $\sim$ 200 MeV/c exists, can allow to distinguish between the bound and free nucleon interactions event by event.

6.4 Hydrogen sample in ND-GAr

HPgTPCs such as ND-GAr are ideal detectors for the application of the δp_{TT} technique described in the previous section. The low tracking thresholds of a gas detector, combined with the full angular acceptance brought by the fact that the neutrinos interact directly in the gas, are particularly advantageous when measuring δp_{TT}. Additionally, the momentum resolution of the ND-GAr detector is expected to be much improved compared to previously available near detectors. For example, the ND280 detector at T2K offers a transverse momentum resolution of the order of $\sim \mathcal{O}(10\%)$. In the original study presented in Ref. [9], the reconstructed δp_{TT} distribution for hydrogen target events using the ND280 detector was found to have a Cauchy spread of $\sigma(\delta p_{\mathrm{TT}}) \simeq 20$ MeV/c. Using the current reconstruction available for ND-GAr, we estimated that the total momentum resolution available for the detector is of about 3%-6%, depending

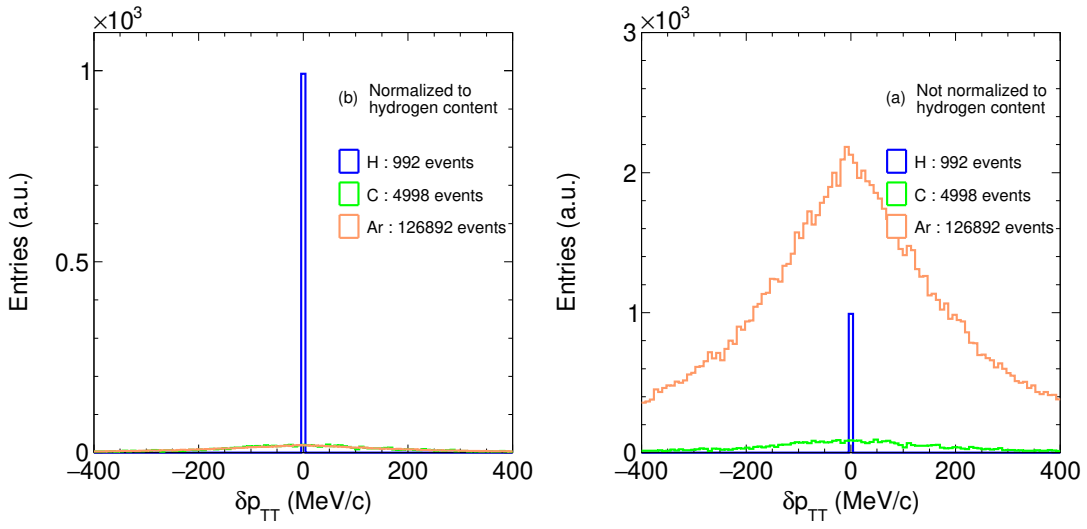

Figure 6.3: δp_{TT} distributions for a sample of ν_μ CC interactions in the ND-GAr TPC, calculated using true momentum quantities taken at the neutrino interaction vertex. The different atomic targets (H,C and Ar) are separated by colour. In the left plot the argon and carbon histograms are normalized to the content of the hydrogen one, while in the right plot they aren't.

on the particle type and the track's characteristics (see Sec. 5.7). Given that the spread of the δp_{TT} distribution on hydrogen is fully determined by the detector response, we can expect, in first approximation, to obtain a $\sigma(\delta p_{\mathrm{TT}})$ of the order of $6 - 12$ MeV/c.

In order to determine the δp_{TT} resolution of the ND-GAr detector, we produced a ν_μ CC interaction sample containing a total of 3×10^6 events. We followed the same procedure outlined for the interaction sample in 5.6.1, applying the same fiducial cuts on the interaction vertices. The gas with which the TPC is filled, is the nominal one, having a 90-10 Ar-CH_4 mix. As an initial sanity check, using the MC truth information, we selected all those events with have the same exiting particles of the event topology shown in Eq. 6.6. For ν_μ CC events, specifically, the exiting charged lepton is a negative muon. Using these events we calculated the δp_{TT} for both hydrogen targets and bound nucleon targets, specifically carbon and argon. For the calculation we used the true momenta of the exiting particles at the production vertex as well as the true neutrino direction.

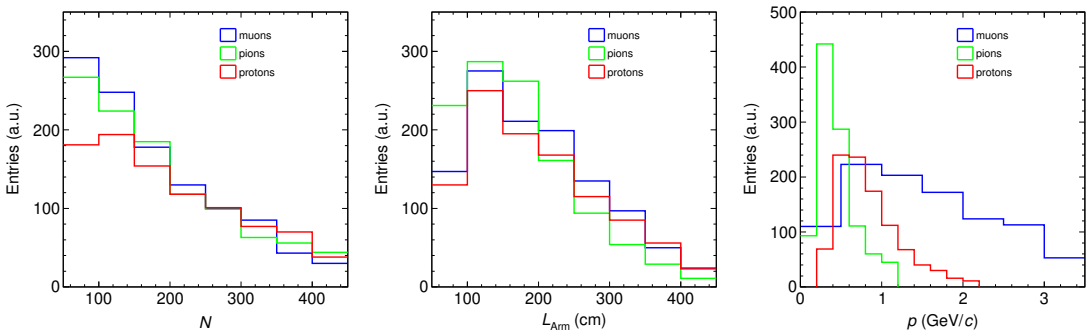

Figure 6.4: Lever arm, L_{Arm}, number of points, N, and true total initial momentum ,p^{true}, of the particle tracks belonging to the ND-GAr TKI study. The properties for the `CKF` and `GKF` reconstructed samples are identical, as they are based on the same underlying MC sample. Protons, muons and pions are separated by colour.

The δp_{TT} distributions divided by nuclear target are shown in Fig. 6.3: in the left plot the heavy nuclear target distributions are scaled to the content of the hydrogen one, while in the right plot they are not. As expected, we see that the hydrogen distribution presents as a Dirac delta peaked in 0, while the carbon and argon backgrounds have symmetric spreads of the order of ~ 200 MeV/c, mainly due to the isotropic smearing effect of FM as well as additional contributions from FSI. From Fig. 6.3b we can see that using the nominal ND-GAr gas mixture, the argon background is overwhelming, making the application of the δp_{TT} technique impractical. However, as it is pointed out in Ref. [12], a gas TPC has the unique advantage of being able to swap the gas target with relative ease. It has been suggested that other gas mixtures with a much more favourable argon content could be used in a HPgTPC such as ND-GAr, while still maintaining a similar detector performance and making the application of the δp_{TT} technique much more realistic. As an initial proof-of-concept study, however, we decided to focus our attention on the nominal gas mixture. This had the obvious advantage of using the unmodified `GArSoft` simulation which has been thoroughly validated, as well as matching the conditions in which the `CKF` algorithm was tested and its performance evaluated.

In order to evaluate the impact of the new `CKF` reconstruction in improving the precision of the δp_{TT} measurement, we applied both the `GKF` and the `CKF` reconstruction, creating two separate samples. Out of these reconstructed events,

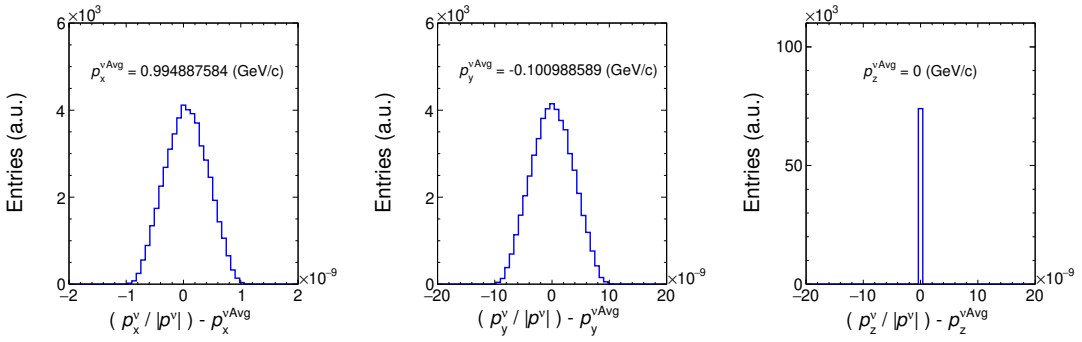

Figure 6.5: Distributions of the differences between the true normalized momentum components $p_i^\nu/|p_i^\nu|$ of the interacting muon neutrinos in the ND-GAr TKI sample and their average values $p_i^{\nu\text{Avg}} = (0.995,\ -0.101, 0.00)$ GeV/c

we selected the ones which contained exactly three tracks. This was done in order to match the topology of RES events as closely as possible, as outlined in Eq. 6.6. Note that MC-truth information on the interaction type was used. Additionally, some quality cuts on the reconstructed properties of the tracks were applied. We selected only events for which all the tracks respected the following criteria: their reconstructed initial kinetic energy K.E. had to be 3 MeV or higher; the three momentum components p_i with $i = (x, y, z)$ higher than 0.001 GeV/c; the lever arm $L_{\text{Arm}} > 50$ cm; the number of hit clusters belonging to the track $N > 50$. The cut on the K.E. was reproduced from the original study in [9], while the cut on p_i was made to eliminate events for which the reconstruction had failed. The two redundant cuts on the track lengths were made to eliminate the reconstructions for which the Kalman filter technique is not suited, but for which at the moment other reconstructions are not available, as explained in Sec. 5.6.1. The L_{Arm}, N and true total initial momentum p^{true} for the particle tracks selected for the `CKF` and `GKF` reconstructed samples are shown in Fig. 6.4. The three charged particle types relevant for the RES interactions, which are protons, muons and pions are separated by colour. All the selected particles show to have produced similarly long tracks, while having significantly different momentum distributions. As expected from resonant events, the charged leptons μ^- has on average the highest momenta, the pions the lowest and the protons are in between.

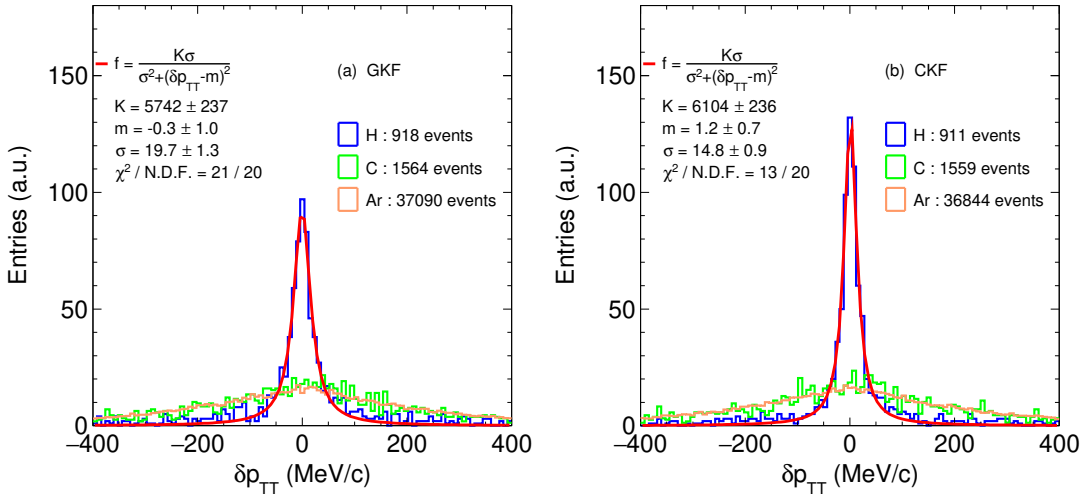

Figure 6.6: δp_{TT} distributions for a sample of ν_μ CC interactions in the ND-GAr TPC, calculated using reconstructed momentum quantities taken at the start of the reconstructed tracks. The different atomic targets (H,C and Ar) are separated by colour. The C and Ar distributions are normalized to the content of the H one. The `GKF` and `CKF` reconstructions have been used in the left (a) and right (b) plot respectively. The results of a Cauchy fit applied to the hydrogen distributions are shown directly on the plots.

The neutrino direction was taken as the average values of the true normalized momentum components $p_i^\nu/|p_i^\nu|$ which were: $p_i^{\nu\mathrm{Avg}} = (0.995,\ -0.101, 0.00)$ GeV/c. The distributions of the differences between $p_i^\nu/|p_i^\nu|$ and $p_i^{\nu\mathrm{Avg}}$ are shown on Fig. 6.5. As can be seen from the spread of the distributions, which are of the order of 10^{-6} GeV/c for the x and y components and 10^{-16} GeV/c for the z components, no significant beam spread was simulated. This makes the impact of the uncertainty on the neutrino direction in this study impossible to evaluate.

The hydrogen target δp_{TT} distributions obtained using the `CKF` and `GKF` reconstruction are shown in Fig. 6.6. The argon and carbon distributions are also shown, scaled to the content of the hydrogen one. In both cases the reconstructed momentum was taken at the start of the track, rather than at the interaction vertex, as it was done for the MC results. The hydrogen distributions were fitted with a Cauchy probability density function as defined in Eq. 5.27. For the `GKF` the distribution is unbiased, having $m = (-0.3 \pm 1.0)$ MeV/c and has a spread of $\sigma = (19.7 \pm 1.3)$ MeV/c, which is comparable with the results obtained for the T2K

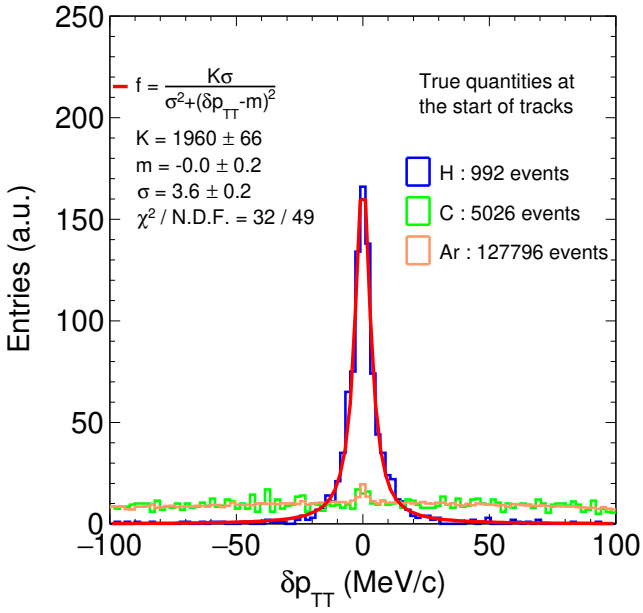

Figure 6.7: δp_{TT} distributions for a sample of ν_μ CC interactions in the ND-GAr TPC, calculated using true momentum quantities taken at the start of the reconstructed tracks. The different atomic targets (H,C and Ar) are separated by colour. The C and Ar distributions are normalized to the content of the H one. The results of a Cauchy fit applied to the hydrogen distributions are shown directly on the plots.

ND280 detector. Better results are obtained with the `CKF` algorithm, for which we obtain an unbiased $m = (1.2 \pm 0.7)$ MeV/c but a $\sigma = (14.8 \pm 0.9)$ MeV/c, showing an improvement which is compatible with the momentum reconstruction performance demonstrated for the algorithm in Sec. 5.6.1.

Additional performance improvements can be obtained by propagating the reconstruction of the 3 tracks to the interaction vertex. This can be easily done with a Kalman filter by simply adding the interaction vertex as an additional point to the start of each track. In order to gauge how much resolution is lost exclusively by the misplacement of the track starting point, we can calculate the δp_{TT} spread using the true momentum components associated with the closest trajectory points to the starting hit clusters of each track. We show the distribution resulting from this calculation in Fig. 6.7. We again fitted the distribution using a Cauchy p.d.f. obtaining a spread of $\sigma = (3.6 \pm 0.2)$ MeV/c. This implies that if the propagation to the interaction vertex is done perfectly, the resolution can be improved by up to $\sim$ 3.6 MeV/c.

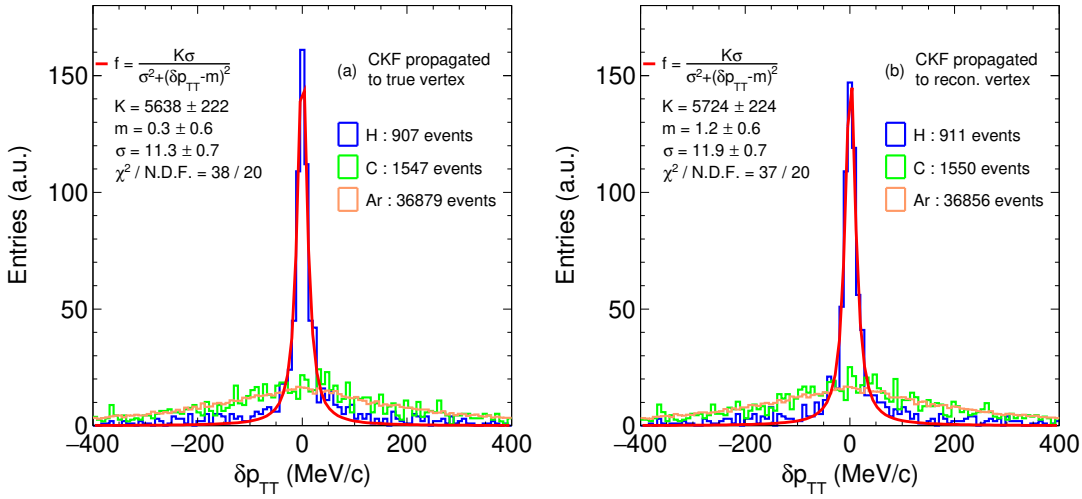

Figure 6.8: δp_{TT} distributions for a sample of ν_μ CC interactions in the ND-GAr TPC, calculated using reconstructed momentum quantities propagated to the true (a) and reconstructed (b) interaction vertex. In both cases the `CKF` has been used for the reconstruction. The results of a Cauchy fit applied to the hydrogen distributions are shown directly on the plots. The different atomic targets (H,C and Ar) are separated by colour. The C and Ar distributions are normalized to the content of the H one.

We applied the propagation to the `CKF` algorithm, using both the true coordinates of the interaction vertex, as well as the reconstructed ones from `GArSoft`. The results are shown in Figs. 6.8a and 6.8b respectively. When using the true position of the vertex, the `CKF` is capable of fully recovering the 3.6 MeV/c smearing, reaching a Cauchy spread of $\sigma = (11.3 \pm 0.7)$ MeV/c. If the reconstructed vertex is used instead, the smearing is still mostly corrected for, reaching a Cauchy spread of $\sigma = (11.9 \pm 0.7)$ MeV/c. This result is compatible with our original expectations derived from the momentum reconstruction performance of the `CKF`.

The improvement in resolution obtained after the vertex propagation of the `CKF` can mostly be attributed to a better estimation of the momentum angles at the interaction point. To illustrate this in Fig. 6.9 we show the resolution and bias of the $\sin\phi$ parameter in the hydrogen sample, as a function of the number of points in the tracks. In black we show the results obtained with the `CKF` before the propagation, and in blue we show them after. The results for the three different particle types are shown from left to right in increasing order of mass (i.e. μ^-, π^+

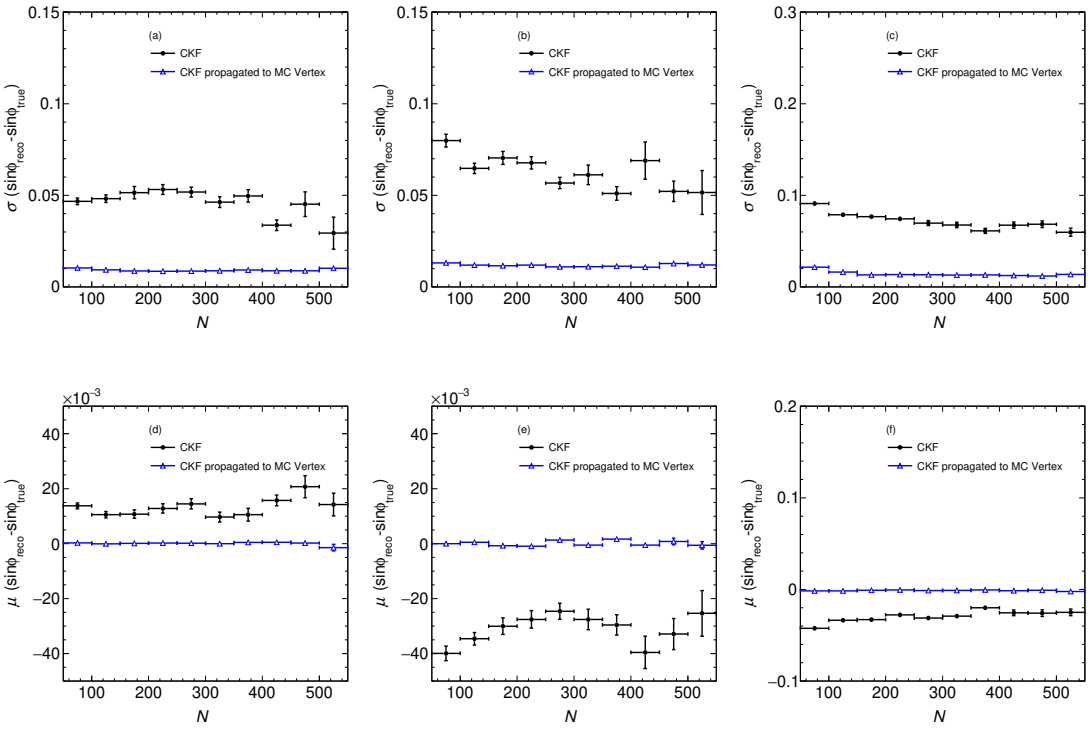

Figure 6.9: Resolution and bias of the $\sin\phi$ parameter in the hydrogen ν_μ CC ND-GAr sample, as a function of the number of points in the tracks N. In black we show the results obtained with the `CKF` before the propagation, and in blue we show them after. The results for the three different particle types are shown from left to right in increasing order of mass (i.e. μ^-, π^+ and p) with the resolution on top ((a),(b) and (c)) and the bias at the bottom ((a),(b) and (c)). The bias and resolution are defined as the μ and σ of simple Gaussian fits applied to the $\sin\phi$ residuals. The residuals are taken in comparison to the $\sin\phi$ true values at the interaction vertex.

and p) . As done previously the bias and resolution are defined as the μ and σ of simple Gaussian fits applied to the $\sin\phi$ residuals. In this case the residuals are taken in comparison to the $\sin\phi$ true values at the interaction vertex. Note that this is different from what was done previously, where the closest trajectory point was always considered. For all particle types, both the resolution and bias are significantly improved. It is interesting to note that the direction of the $\sin\phi$ bias is opposite for particles of opposite charge: negative for the p and π^+ and positive for the μ^-. This is consistent with the opposite direction of circular motion that we expect for particles of opposite charge in a magnetic field.

In Figs. 6.10 and 6.11 we show the dependency of the δp_{TT} resolution as a

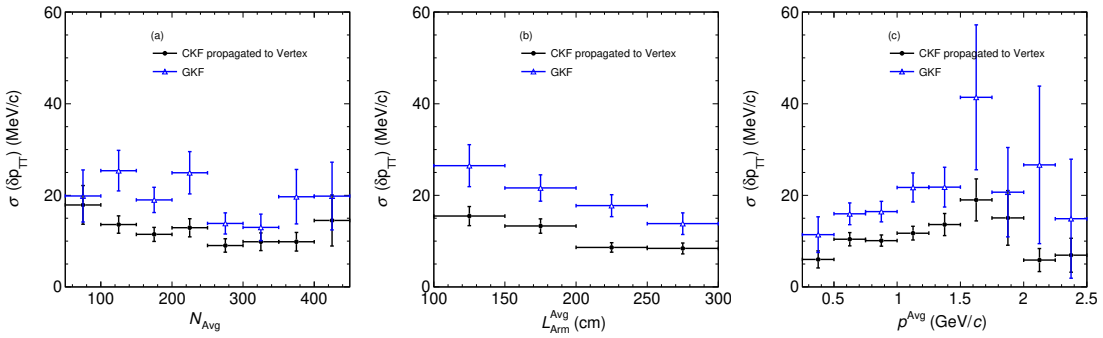

Figure 6.10: Dependency of the δp_{TT} Cauchy spread hydrogen resolution as a function of average number of points N_{Avg}, lever arm L_{Arm}^{Avg} and true initial momentum p^{Avg}, calculated between the three tracks in the event. In blue we show the results obtained with the `GKF`, while in black we show the results for the `CKF` propagated to the reconstructed vertex.

function of number of points N, lever arm L_{Arm} and true initial momentum p. In Fig.6.10 we show the dependency on the average values calculated among the three tracks in each event, while in 6.11 we show the dependency on the characteristics of each particle type. In all cases the resolution is defined again as the Cauchy spread of the δp_{TT} distribution for hydrogen. In blue we show the results obtained with the `GKF`, while in black we show the results for the `CKF` propagated to the reconstructed vertex. It is clear that the `CKF` outperforms the old algorithm, regardless of the track characteristics. Since the δp_{TT} resolution on hydrogen solely depends on the detector response, we should expect for the dependencies to follow similar patterns to the ones described by the Gluckstern formulas in Eqs. 4.37 and 4.38. Indeed, looking at the dependencies on the average properties of the tracks, we see an inverse proportionality on L_{Arm} and N and a direct proportionality on p, which is in agreement with expectations. The dependencies are less clear but still visible when looking at the particle types separately.

Using the δp_{TT} resolution found for the `CKF` algorithm after the reconstructed vertex propagation (see Fig. 6.8b), which is $\sigma(\delta p_{\mathrm{TT}}) = (11.9 \pm 0.7)$ MeV/c, we can impose the cuts $|\delta p_{\mathrm{TT}}| \leq n\sigma$. We identify the signal as the hydrogen target sample and the background as either the carbon target sample, the argon target sample or the combination of both. We define the cut efficiency $\epsilon_{\delta p_{\mathrm{TT}}}$ as the ratio between

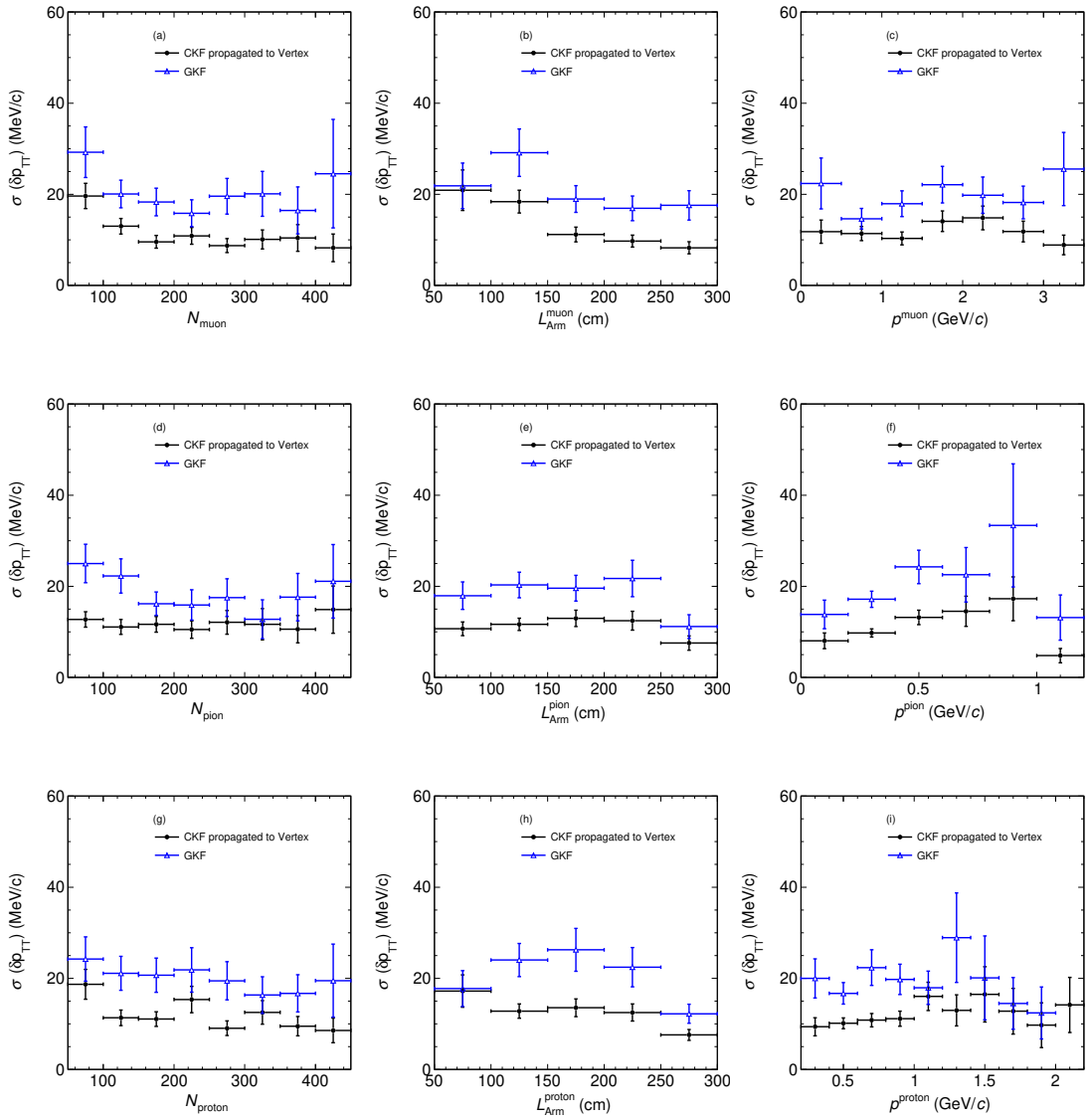

Figure 6.11: Dependency of the δp_{TT} Cauchy spread hydrogen resolution as a function of number of points N, lever arm L_{Arm} and true initial momentum p for the three particle types in increasing order of mass from top to bottom: muons, pions and protons. In blue we show the results obtained with the `GKF`, while in black we show the results for the `CKF` propagated to the reconstructed vertex.

signal and background events passing the cut and the total number of events:

$$\epsilon_{\delta p_{\mathrm{TT}}} = \frac{N_{\mathrm{sig}}^{\mathrm{pass}} + N_{\mathrm{bkg}}^{\mathrm{pass}}}{N_{\mathrm{sig}}^{\mathrm{tot}} + N_{\mathrm{bkg}}^{\mathrm{tot}}} \tag{6.9}$$

We can also define the purity $\rho_{\delta p_{\mathrm{TT}}}$ as the ratio between the number of signal events

(%)	ρ (1σ)	ρ (2σ)	ρ (3σ)	ϵ (1σ)	ϵ (2σ)	ϵ (3σ)
C	81 ± 6	76 ± 4	69 ± 4	19 ± 1	26 ± 1	33 ± 1
Ar	17.6 ± 0.9	13.0 ± 0.6	10.2 ± 0.4	5.7 ± 0.1	10.5 ± 0.2	15.0 ± 0.2
Ar+C	16.9 ± 0.9	12.5 ± 0.6	9.7 ± 0.4	5.7 ± 0.1	10.5 ± 0.2	15.0 ± 0.2

Table 6.1: Efficiency $\epsilon_{\delta p_{\mathrm{TT}}}$ and purity $\rho_{\delta p_{\mathrm{TT}}}$ for the $|\delta p_{\mathrm{TT}}| \leq n\sigma$ cut for $n = 1, 2, 3$ for a signal of hydrogen events, considering as the background the carbon and argon events both separately and in total. The σ used is the Cauchy spread estimated for the `CKF` algorithm after vertex propagation.

that passed the cut and the number of total events that passed the cut:

$$\rho_{\delta p_{\mathrm{TT}}} = \frac{N_{\mathrm{sig}}^{\mathrm{pass}}}{N_{\mathrm{sig}}^{\mathrm{pass}} + N_{\mathrm{bkg}}^{\mathrm{pass}}} \tag{6.10}$$

We calculated the efficiency and purity for the $|\delta p_{\mathrm{TT}}| \leq n\sigma$ cut for $n = 1, 2, 3$ considering as the background the carbon and argon events both separately and in total. The results are summarized in Tab. 6.1. As previously discussed, using the nominal gas mixture, the argon background completely dominates and makes the application of the technique not practical. If we just consider the carbon background however, the results are much more encouraging, showing a purity of at a 1σ cut of $\rho_{\delta p_{\mathrm{TT}}} = (81 \pm 6)\%$. It's clear that in order to reap the benefits of the δp_{TT} technique in ND-GAr, other gas mixtures should be considered, as it was originally pointed out in Ref. [12]. It is important to remember that ND-GAr is a gas TPC, which offers the unique opportunity of switching the target material during data taking. In the original paper many potential gas mixtures are explored and it is demonstrated that it is possible for several of them to maintain a similar detector performance, while offering a much more favourable argon ratio. This study demonstrates that the performance of the ND-GAr detector, as it stands right now, is already sufficient to reach levels of δp_{TT} resolution which surpass all other neutrino detectors tested so far and is consistent with the original expectations. This results motivate a more comprehensive program of studies into the use of other gas mixtures for ND-GAr with which measurements of neutrino on hydrogen would become available. This would expand the reach of the detector into the field of nuclear effects, improving the precision of the DUNE experiment as a whole.

7 Conclusions

The main goal of this thesis was to describe the development of a novel Kalman filter algorithm for the ND-GAr detector and show its impact in achieving the detector's physics goals, specifically in the study of neutrino interactions and nuclear effects. In Ch. 4 we introduced the Kalman filter technique and its application to particle tracking and we described the development and testing of a KF for the ND-GAr-Lite detector named `KF-Lite`. The ND-GAr-Lite detector was a proposed temporary muon spectrometer designed to substitute ND-GAr in the early days of DUNE experiment's data tacking. The testing of `KF-Lite` started with the production of a toy Monte Carlo Tool, which allowed each component of the algorithm to be validated individually. Once the algorithm was demonstrated to be mature and internally consistent, it was applied to data simulated with `GArSoft`, the software tool developed by the ND-GAr collaboration. The performance of `KF-Lite` was tested on a sample of mono-energetic forward-going muons and was compared with the previously available reconstruction algorithm which consisted of an iterative linear regression method `ILRM`. `KF-Lite` was shown to significantly outperform the `ILRM`, fully removing a $\sim 4\%$ momentum bias present in the original reconstruction.

In Ch. 5 we described a novel Kalman filter constructed for the ND-GAr detector and based on the parametrisation and the infrastructure originally developed

by the ALICE experiment. The new algorithm, which we named the Complete Kalman filter or `CKF`, includes a novel feature which allows for the reconstruction of very long "looping" tracks produced by low energy light particles. The impact of this technique and the internal consistency of the algorithm was demonstrated in a toy Monte Carlo study using a wide range of detector and particle characteristics. In particular it was shown that the novel "loop-following" method has the potential of improving both the detection efficiency and the resolution significantly for light particles such as electrons, muons and pions. Once the algorithm was demonstrated to be fully mature, it was integrated in `GArSoft`. Two studies were produced which employed a sample of primary particles from ν_μ CC interactions and a sample of forward-going muons respectively. In both cases it was shown that the `CKF` improves the performance of the ND-GAr detector. Direct comparison were done with the previous reconstruction algorithm, which we named the GArSoft Kalman filter `GKF` , showing improvement in angular and momentum resolution and bias for all particle types and especially protons.

The impact of the `CKF` was demonstrated in Ch. 6. In this final chapter we described a study designed to evaluate the feasibility of using transverse kinematic imbalance (TKI) techniques to isolate a sample of neutrino-hydrogen interactions in the ND-GAr detector. The performance was evaluated in terms of double transverse kinematic imbalance resolution $\sigma(\delta p_{\mathrm{TT}})$, which is the TKI variable used to separate the hydrogen interactions from the rest. The study was performed on a sample of ν_μ CC interactions simulated with `GArSoft` and showed that the new `CKF` algorithm was capable of producing a resolution of $\sigma(\delta p_{\mathrm{TT}}) = (11.9 \pm 0.7)$ MeV/c. This result represents an improvement of a factor of ~ 2 compared to the resolution found for `GKF`, which was is $\sigma(\delta p_{\mathrm{TT}}) = (19.7 \pm 1.3)$ MeV/c, and is consistent with the original expectations. Finally, the efficiency and purity for the hydrogen sample cut on the nominal ND-GAr gas mixture were evaluated. The results of the study indicate that ND-GAr is an ideal candidate for the application of the TKI technique offering an unprecedented level of δp_{TT} resolution. This strongly motivates the need for

further exploration into gas mixtures with more favourable hydrogen content that would allow a fuller realisation of the benefits of the technique.

Appendices

A
Appendices

Contents

A.1 ILRM numerical methods

As described in Section 4.3.1 the `ILRM` method consists in minimizing the functional $K(x_C, y_C, r)$ which is shown in Eq. 4.33 and can be written more fully as:

$$K(x_C, y_C, r) = \sum_{i=1}^{n} \left(\frac{x_i + y_i}{r} - 2\frac{x_C}{r} - 2\frac{y_C}{r} + \frac{x_C^2 + y_C^2 - r^2}{r} \right)^2 \tag{A.1}$$

The numerical process with which this functional is minimized is not straightforward. The first step in the minimization is to find the normal equations by imposing that the derivatives of K in x_C, y_C and r are equal to zero. Doing this we find the system of equations:

$$\begin{cases} Fx_C + Hy_C - x_C\gamma = P, \\ Hx_C + Gy_C - y_C\gamma = Q, \\ 2Px_C + 2Qy_C + \gamma^2 = T \end{cases} \tag{A.2}$$

where $\gamma = r^2 - x_C^2 - y_C^2$ as above. To write the expression for the coefficients we use the Gauss brackets convention as :

$$\sum_{i=1}^{n} x^p y^q = [x^p y^q]. \tag{A.3}$$

Using this convention we can write the coefficients as:

$$\begin{aligned} F &= \frac{1}{n}[3x^2 + y^2], & G &= \frac{1}{n}[x^2 + 3y^2] \\ H &= \frac{2}{n}[xy], & P &= \frac{1}{n}[x(x^2 + y^2)], \\ Q &= \frac{1}{n}[y(x^2 + y^2)], & T &= \frac{1}{n}[(x^2 + y^2)^2], \end{aligned} \tag{A.4}$$

By excluding the pair x_C, y_C from the system of equations in Eq. A.2 one can find the single fourth order equation:

$$\gamma^4 + A\gamma^3 + B\gamma^2 + C\gamma + D = 0 \tag{A.5}$$

where the coefficients derive directly from Eq. A.4 and can be written as:

$$\begin{aligned} A &= -F - G, & B &= FG - T - H^2, \\ C &= T(F + G) - 2(P^2 + Q^2), & D &= T(H^2 - FG) + 2(P^2 G + Q^2 F) - 4PQH, \end{aligned} \tag{A.6}$$

Eq. A.5 has 4 roots, but to obtain a good approximation of the first one one can do:

$$\gamma_0 = \frac{1}{n}([x^2] + [y^2]). \tag{A.7}$$

By dividing Eq. A.5 by γ_0^4 round-off errors can be minimized and we obtain the new equation:

$$\Gamma^4 + A_0\Gamma^3 + B_0\Gamma^2 + C_0\Gamma + D = 0, \tag{A.8}$$

where $\Gamma = \gamma/\gamma_0$, $A_0 = A/\gamma_0$, $B_0 = B/\gamma_0^2$, $C_0 = C/\gamma_0^3$ and $A_0 = A/\gamma_0^4$. After calculating all the coefficients, the roots of Eq. A.8 can be found iteratively with Newton's method using the starting value $\Gamma_0 = 1$. Once Γ is found we get $\gamma = \gamma_o\Gamma$, we derive x_C and y_C from Eq. A.2 and finally we get r as:

$$r = \sqrt{x_C^2 + y_C^2 + \gamma}. \tag{A.9}$$

A.2 Summary tables

All the sample simulation/reconstruction conditions tested for ND-GAr and ND-GAr-Lite are summarized in Table A.2 and A.1 respectively. All test samples are identified by a code composed of up to three numbers and a letter. The main number n identifies a specific set of simulation conditions, while the other numbers and letters or lack thereof characterize the reconstruction:

- **n:** the seeding step is "cheated" i.e. the KF is applied using MC true values as initial guesses
- **n.5:** the seeding is done using the `Seed` 3-point circumference method
- **n.6:** the seeding is done using the `ILRM` method
- **n.x.1:** the energy loss correction is applied to the seeding
- **n.x.2:** the energy loss and multiple scattering correction are both applied to the seeding
- **n.x.3:** the multiple scattering correction is applied to the seeding
- **n.x.y a:** the KF is applied to a realistic seed
- **n.x.y b:** the KF is applied to a realistic seed, with additional energy loss corrections
- **n.x.y c:** the KF is applied to a realistic seed, with additional energy loss and multiple scattering corrections
- **n.x.y d:** the KF is applied to a realistic seed, with additional multiple scattering corrections

	Monte Carlo						Seed							Kalman Filter		Spectrum		Geometry	
	σ_{yz}	dE/dx	Gauss σ_E	Landau σ_E	MS	Garsoft	Alone	ALICE	ILRM	dE/dx	MS	Cheated	Realistic	dE/dx Corr	MS Corr	Fixed p	Random	5 planes	6 planes
0												✓					✓	✓	
0.5							✓	✓									✓	✓	
0.5a								✓					✓				✓	✓	
1	✓											✓					✓	✓	
1.5	✓						✓	✓									✓	✓	
1.5a	✓							✓					✓				✓	✓	
2		✓										✓					✓	✓	
2b		✓										✓		✓			✓	✓	
2.5		✓					✓	✓									✓	✓	
2.5a		✓						✓					✓				✓	✓	
2.5b		✓						✓					✓	✓			✓	✓	
3		✓	✓					✓				✓					✓	✓	
3b		✓	✓					✓				✓		✓			✓	✓	
3.5		✓	✓				✓	✓									✓	✓	
3.5a		✓	✓					✓					✓				✓	✓	
3.5b		✓	✓					✓					✓	✓			✓	✓	
4		✓		✓				✓				✓					✓	✓	
4b		✓		✓				✓				✓		✓			✓	✓	
4.5		✓		✓			✓	✓									✓	✓	
4.5a		✓		✓				✓					✓				✓	✓	
4.5b		✓		✓				✓					✓	✓			✓	✓	
5.5		✓					✓	✓								✓		✓	
5.5a		✓						✓					✓			✓		✓	
5.5b		✓						✓					✓	✓		✓		✓	
6.5		✓					✓	✓								✓			✓
6.5a		✓						✓					✓			✓			✓
6.5b		✓						✓					✓	✓		✓			✓
7.5		✓	✓				✓	✓								✓			✓
7.5a		✓	✓					✓					✓			✓			✓
7.5b		✓	✓					✓					✓	✓		✓			✓
8.5		✓		✓			✓	✓								✓			✓
8.5a		✓		✓				✓					✓			✓			✓
8.5b		✓		✓				✓					✓	✓		✓			✓
9.5	✓	✓	✓				✓	✓								✓			✓
9.5a	✓	✓	✓					✓					✓			✓			✓
9.5b	✓	✓	✓					✓					✓	✓		✓			✓
10.5	✓	✓		✓			✓	✓								✓			✓
10.5a	✓	✓		✓				✓					✓			✓			✓
10.5b	✓	✓		✓				✓					✓	✓		✓			✓
11.5		✓			✓		✓	✓								✓			✓
11.5a		✓			✓			✓					✓			✓			✓
11.5b		✓			✓			✓					✓	✓		✓			✓
11.5c		✓			✓			✓					✓	✓	✓	✓			✓
12.5	✓	✓			✓		✓	✓								✓			✓
12.5a	✓	✓			✓			✓					✓			✓			✓
12.5b	✓	✓			✓			✓					✓	✓		✓			✓
12.5c	✓	✓			✓			✓					✓	✓	✓	✓			✓
13.5	✓	✓	✓		✓		✓	✓								✓			✓
13.5a	✓	✓	✓		✓			✓					✓			✓			✓
13.5b	✓	✓	✓		✓			✓					✓	✓		✓			✓
13.5c	✓	✓	✓		✓			✓					✓	✓	✓		✓		✓
13.5.2c	✓	✓	✓		✓	✓	✓	✓					✓	✓	✓		✓		✓
14.5	✓	✓		✓	✓		✓	✓								✓			✓
14.5a	✓	✓		✓	✓			✓					✓			✓			✓
14.5b	✓	✓		✓	✓			✓					✓	✓		✓			✓
14.5c	✓	✓		✓	✓			✓					✓	✓	✓	✓			✓
15.5						✓	✓	✓								✓			✓
15.5a						✓		✓					✓			✓			✓
15.5b						✓		✓					✓	✓		✓			✓
15.5c						✓		✓					✓	✓	✓	✓			✓
15.5.1						✓	✓	✓		✓						✓			✓
15.5.1a						✓		✓		✓			✓			✓			✓
15.5.1b						✓		✓		✓			✓	✓		✓			✓
15.5.1c						✓		✓		✓			✓	✓	✓	✓			✓
15.5.2						✓	✓	✓		✓	✓					✓			✓
15.5.2a						✓		✓		✓	✓		✓			✓			✓
15.5.2b						✓		✓		✓	✓		✓	✓		✓			✓
15.5.2c						✓		✓		✓	✓		✓	✓	✓	✓			✓
15.6						✓	✓		✓							✓			✓
15.6a						✓			✓				✓			✓			✓
15.6b						✓			✓				✓	✓		✓			✓
15.6c						✓			✓	✓			✓	✓	✓	✓			✓
15.6.1						✓	✓		✓	✓						✓			✓
15.6.1a						✓			✓	✓			✓			✓			✓
15.6.1b						✓			✓	✓			✓	✓		✓			✓
15.6.1c						✓			✓	✓	✓		✓	✓	✓	✓			✓
15.6.2						✓	✓		✓	✓	✓					✓			✓
15.6.2a						✓			✓	✓	✓		✓			✓			✓
15.6.2b						✓			✓	✓	✓		✓	✓		✓			✓
15.6.2c						✓			✓	✓			✓	✓	✓	✓			✓

Table A.1: Summary of all sample conditions used for ND-GAr-Lite modular tests

	Monte Carlo				**Seed**						**Kalman Filter**		**Spectrum**		**Geometry**	
	σ_{yz}	dE/dx	pidCode	MS	Standalone	ALICE	dE/dx Corr	MS Corr	Cheated	Realistic	dE/dx Corr	MS Corr	Fixed p	Random	densScaling	resScaling
0.5	✓		1		✓	✓							✓		10	1
0.5a	✓		1			✓				✓			✓		10	1
1.5	✓	✓	1		✓	✓							✓		10	1
1.5a	✓	✓	1			✓				✓			✓		10	1
1.5b	✓	✓	1			✓				✓	✓		✓		10	1
1.5.1	✓	✓	1		✓	✓							✓		10	1
1.5.1a	✓	✓	1			✓	✓			✓			✓		10	1
1.5.1b	✓	✓	1			✓	✓			✓	✓		✓		10	1
2.5	✓		1	✓	✓	✓							✓		10	1
2.5a	✓		1	✓		✓				✓			✓		10	1
2.5d	✓		1	✓		✓				✓		✓	✓		10	1
2.5.3	✓		1	✓	✓	✓		✓					✓		10	1
2.5.3a	✓		1	✓		✓		✓		✓			✓		10	1
2.5.3d	✓		1	✓		✓		✓		✓		✓	✓		10	1
3.5	✓	✓	1	✓	✓	✓							✓		10	1
3.5a	✓	✓	1	✓		✓				✓			✓		10	1
3.5b	✓	✓	1	✓		✓				✓	✓		✓		10	1
3.5c	✓	✓	1	✓		✓				✓	✓	✓	✓		10	1
3.5d	✓	✓	1	✓		✓				✓		✓	✓		10	1
3.5	✓	✓	1	✓	✓	✓	✓						✓		10	1
3.5a	✓	✓	1	✓		✓	✓			✓			✓		10	1
3.5b	✓	✓	1	✓		✓	✓			✓	✓		✓		10	1
3.5c	✓	✓	1	✓		✓	✓			✓	✓	✓	✓		10	1
3.5d	✓	✓	1	✓		✓	✓			✓		✓	✓		10	1
3.5.2	✓	✓	1	✓	✓	✓	✓	✓					✓		10	1
3.5.2a	✓	✓	1	✓		✓	✓	✓		✓			✓		10	1
3.5.2b	✓	✓	1	✓		✓	✓	✓		✓	✓		✓		10	1
3.5.2c	✓	✓	1	✓		✓	✓	✓		✓	✓	✓	✓		10	1
3.5.2d	✓	✓	1	✓		✓	✓	✓		✓		✓	✓		10	1
4.5.2c	✓	✓	1	✓		✓	✓	✓		✓	✓	✓		✓	10	1
5.5.2c	✓	✓	[0,4]	✓		✓	✓	✓		✓	✓	✓		✓	[0.01,10]	[0.01,2]

Table A.2: Summary of all sample conditions used for ND-GAr modular tests

A.3 Additional material for the ND-GAr toy MC study

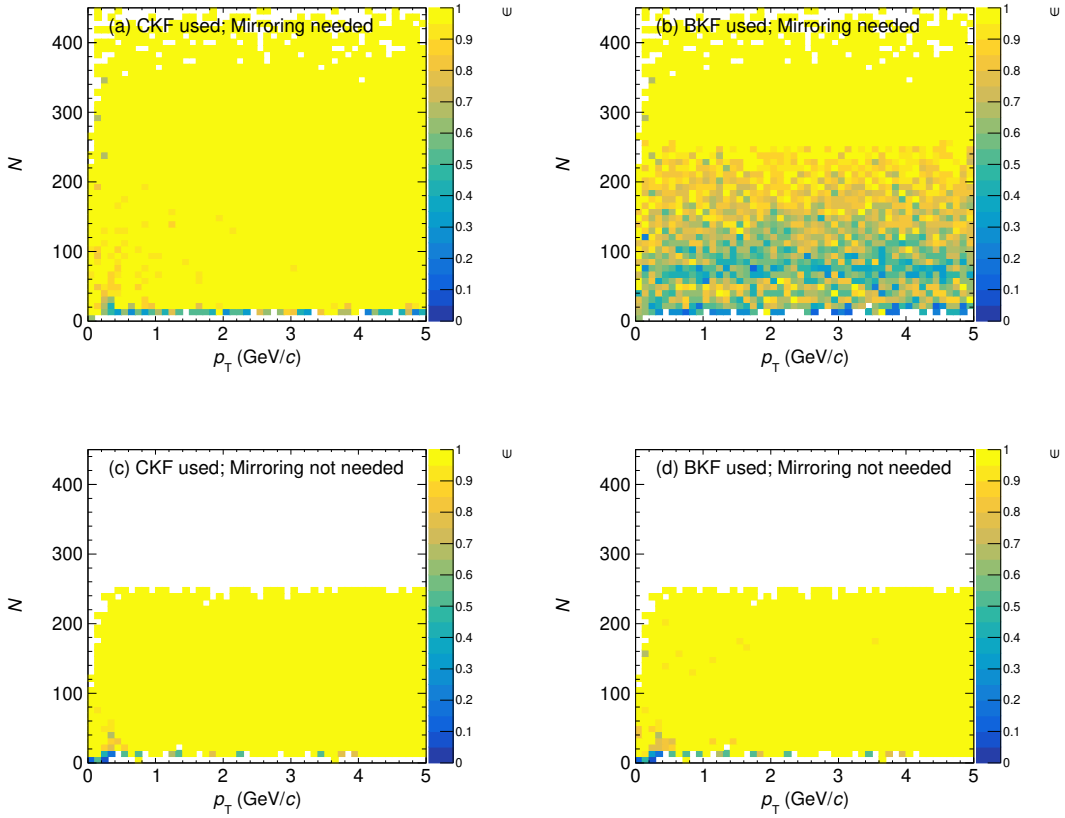

Figure A.1: Reconstruction efficiency ϵ for the HP sample, as a function of the total number of points in the track N and the initial true transverse momentum p_{T}. Analogous to Fig. 5.13

In this Appendix we include some additional plots produced for the ND-GAr toy MC study discussed in Sec. 5.5 to allow for more direct comparisons between the HP and PS samples and to provide additional insight. The reconstruction efficiency for the HP sample is shown in Fig. A.1. Analogously to what was shown in Fig. 5.13 ϵ is plotted as a function of the initial true p_{T} and the N. The results for the `CKF` and `BKF` are shown in the first and second column respectively. In the plots occupying the first row only the tracks for which the mirroring technique is used are shown, while the other tracks are shown in the plots in the second row. The results are analogous to what was shown for the PS sample in Fig. 5.13.

In Fig. A.2 we show an alternative version of the plot in Fig.5.10 which focuses on the more statistically rich central region. In Figs. A.3 and A.4, we show the relative momentum resolution and bias for the three particle types present in the HP sample, as a function of L_{Arm} and N, respectively. These are analogous to Fig. 5.18 in the main text. Similar plots are produced for the PS sample to allow for a direct comparison. In Figs. A.5 and A.6, we show the relative momentum resolution and bias for the particles in the PS sample as a function of p and l respectively. The particle types are divided by mass into protons and kaons, pions and muons and finally electrons. Note that in this case the resolution and material properties are not uniform in the sample.

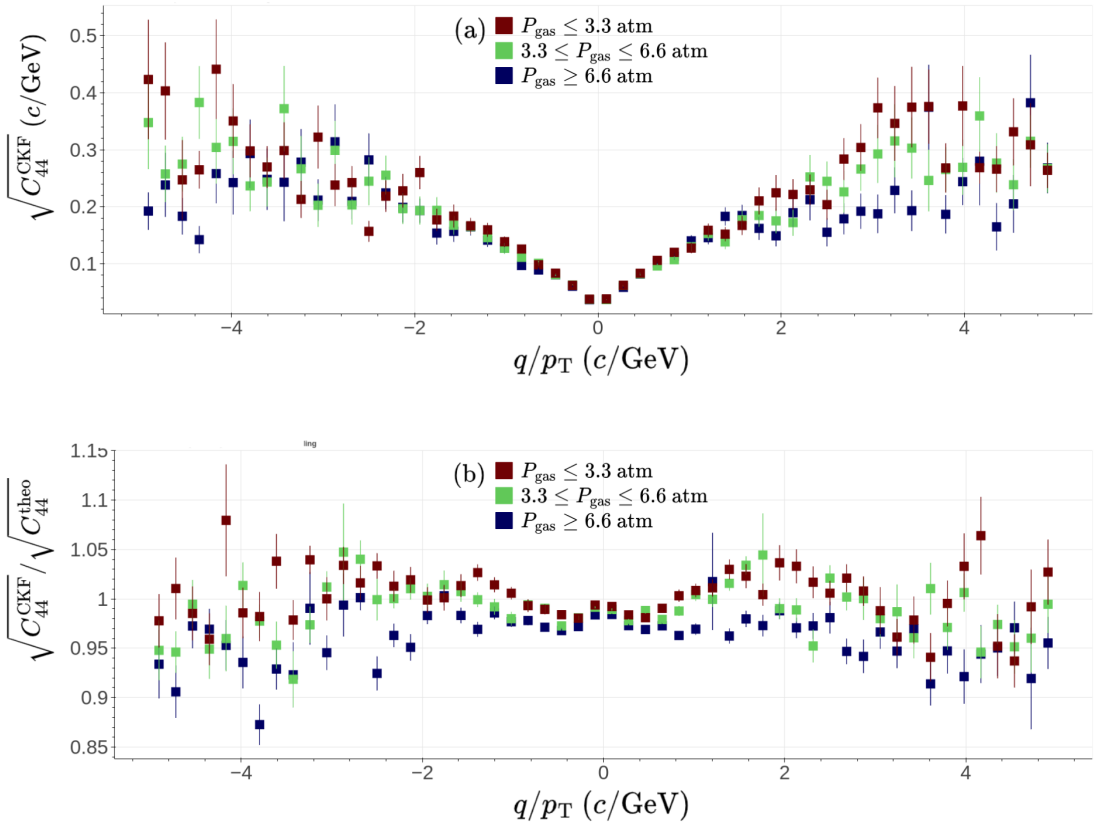

Figure A.2: (a) `CKF` q/p_{T} resolution $\sigma_{\text{CKF}}(q/p_{\text{T}}) = \sqrt{C_{44}^{\text{CKF}}}$ as a function of the true q/p_{T}. (b) Ratio of the `CKF` q/p_{T} resolution, over the theoretical expectations $\sigma_{\text{theo}}(q/p_{\text{T}}) = \sqrt{C_{44}^{\text{theo}}}$, as a function of the true q/p_{T}. The histograms include all particles in the PS sample and are color-coded according to the gas pressure P_{gas} used in the simulation. Only tracks with a minimum of 10 points are considered. These plots have been produced using the interactive analytical tool `ROOTInteractive` [163]. The error bars are statistical.

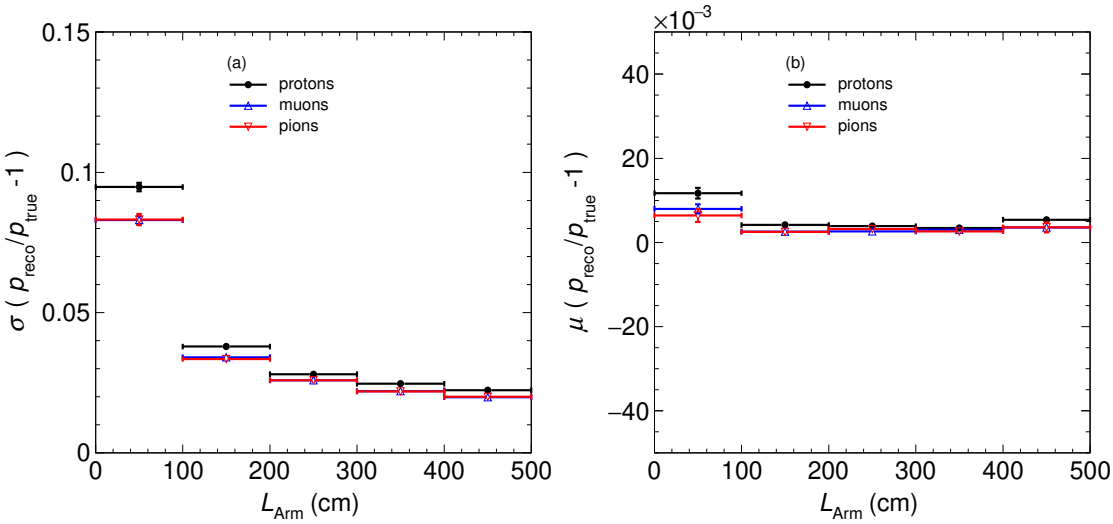

Figure A.3: Similar plots to Fig. 5.16. In this case the relative momentum resolution (a) and bias (b) are shown as a function of the tracks' lever arm L_{Arm} for the HP sample.

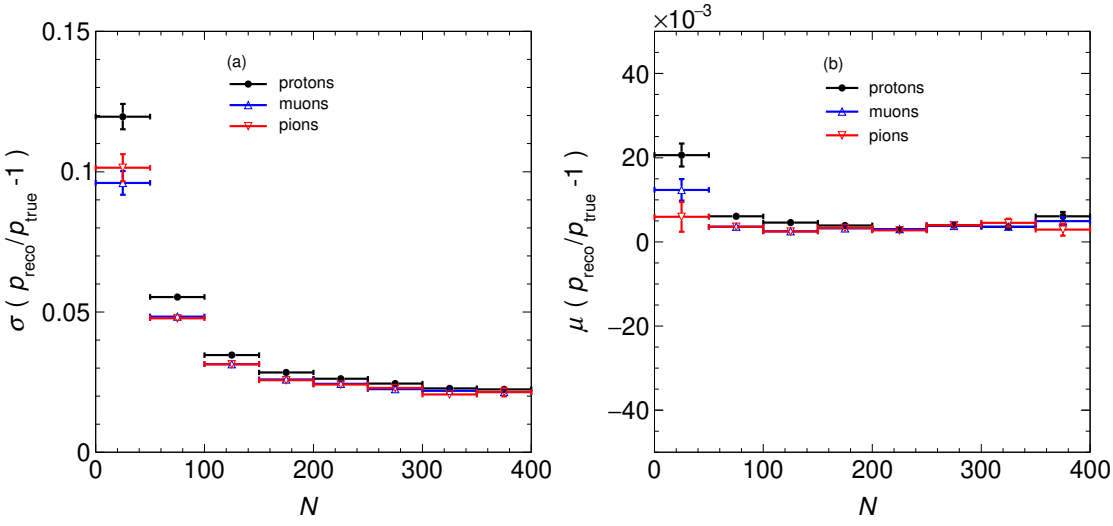

Figure A.4: Similar plots to Fig. 5.16. In this case the relative momentum resolution (a) and bias (b) are shown as a function of the number of points in the track N for the HP sample.

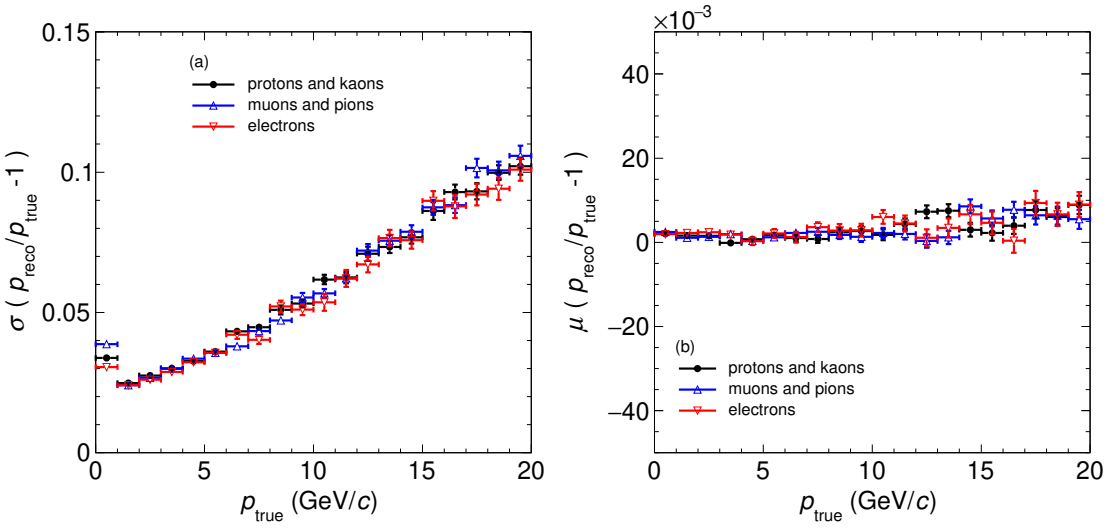

Figure A.5: Relative momentum resolution (a) and bias (b) as function of the true momentum, p_{true}, for the PS sample. The two properties are defined as μ and σ of Gaussian fits of the momentum fractional residuals $p_{\text{reco}}/p_{\text{true}} - 1$. The particle types are divided based on their mass (protons and kaons, muons and pions, electrons) are drawn separately.

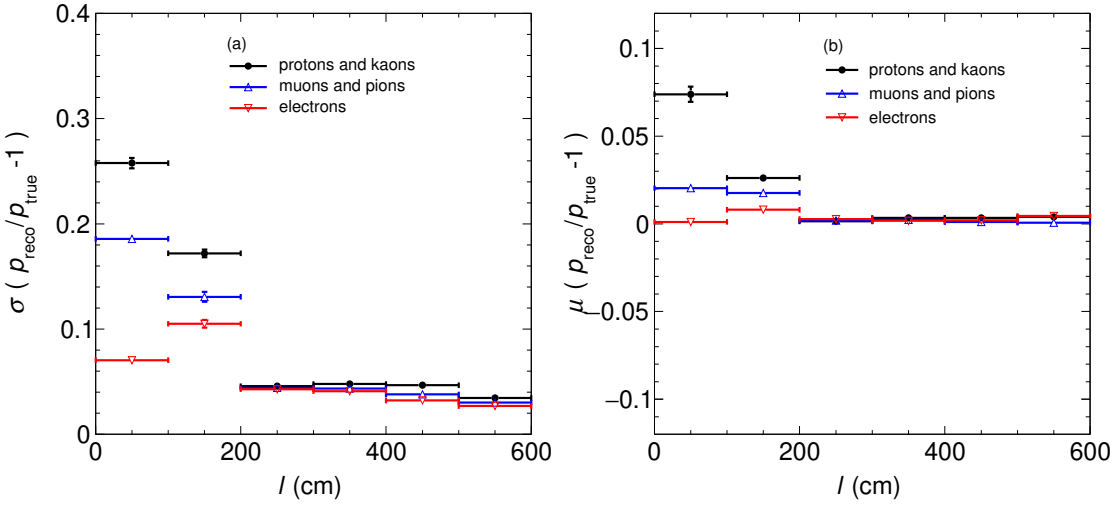

Figure A.6: Relative momentum resolution (a) and bias (b) as function of the track length, l, for the PS sample. The two properties are defined as μ and σ of Gaussian fits of the momentum fractional residuals $p_{\text{reco}}/p_{\text{true}} - 1$. The particle types are divided based on their mass (protons and kaons, muons and pions, electrons) are drawn separately.

References

[1] Babak Abi et al. “Deep Underground Neutrino Experiment (DUNE), Far Detector Technical Design Report, Volume I Introduction to DUNE”. In: *JINST* 15.08 (2020), T08008. arXiv: 2002.02967 [physics.ins-det].

[2] V. Hewes et al. “Deep Underground Neutrino Experiment (DUNE) Near Detector Conceptual Design Report”. In: *Instruments* 5.4 (2021), p. 31. arXiv: 2103.13910 [physics.ins-det].

[3] D. Nygren. “Time-projection chamber”. In: *LBL–4800* (1975).

[4] D. Attie. “TPC review”. In: *Nucl. Instrum. Meth. A* 598 (2009). Ed. by A. Buzulutskov, pp. 89–93.

[5] H. J. Hilke. “Time projection chambers”. In: *Rept. Prog. Phys.* 73 (2010), p. 116201.

[6] K. Aamodt et al. “The ALICE experiment at the CERN LHC”. In: *JINST* 3 (2008), S08002.

[7] “ALICE upgrades during the LHC Long Shutdown 2”. In: (Feb. 2023). arXiv: 2302.01238 [physics.ins-det].

[8] X.-G. Lu et al. “Reconstruction of Energy Spectra of Neutrino Beams Independent of Nuclear Effects”. In: *Phys. Rev. D* 92.5 (2015), p. 051302. arXiv: 1507.00967 [hep-ex].

[9] X.-G. Lu et al. “Measurement of nuclear effects in neutrino interactions with minimal dependence on neutrino energy”. In: *Phys. Rev. C* 94.1 (2016), p. 015503. arXiv: 1512.05748 [nucl-th].

[10] X.-G. Lu and Jan T. Sobczyk. “Identification of nuclear effects in neutrino and antineutrino interactions on nuclei using generalized final-state correlations”. In: *Phys. Rev. C* 99.5 (2019), p. 055504. arXiv: 1901.06411 [hep-ph].

[11] Tejin Cai, X.-G. Lu, and Daniel Ruterbories. “Pion-proton correlation in neutrino interactions on nuclei”. In: *Phys. Rev. D* 100 (2019), p. 073010. arXiv: 1907.11212 [hep-ex].

[12] Philip Hamacher-Baumann, Xianguo Lu, and Justo Martìn-Albo. “Neutrino-hydrogen interactions with a high-pressure time projection chamber”. In: *Phys. Rev. D* 102.3 (2020), p. 033005. arXiv: 2005.05252 [physics.ins-det].

[13] Mark Thomson. *Modern Particle Physics*. Cambridge University Press, 2013.

[14] Carlo Giunti and Chung W. Kim. *Fundamentals of Neutrino Physics and Astrophysics*. Oxford University Press, 2007.

[15] J. L. Hewett et al. “Fundamental Physics at the Intensity Frontier”. In: (May 2012). arXiv: 1205.2671 [hep-ex].

[16] M. Tzanov et al. "Precise measurement of neutrino and anti-neutrino differential cross sections". In: *Phys. Rev. D* 74 (2006), p. 012008. arXiv: hep-ex/0509010.

[17] J. A. Formaggio and G. P. Zeller. "From eV to EeV: Neutrino Cross Sections Across Energy Scales". In: *Rev. Mod. Phys.* 84 (2012), pp. 1307–1341. arXiv: 1305.7513 [hep-ex].

[18] Daniel Ivan Scully. "Neutrino induced coherent pion production." PhD thesis. Warwick U., 2013.

[19] O. Benhar et al. "Spectral function of finite nuclei and scattering of GeV electrons". In: *Nucl. Phys. A* 579 (1994), pp. 493–517.

[20] R. Subedi et al. "Probing Cold Dense Nuclear Matter". In: *Science* 320 (2008), pp. 1476–1478. arXiv: 0908.1514 [nucl-ex].

[21] Evgeny Akhmedov. "Majorana neutrinos and other Majorana particles:Theory and experiment". In: Dec. 2014. arXiv: 1412.3320 [hep-ph].

[22] Andrea Giuliani. "Neutrinoless double-beta decay: Where we are and where we are going". In: *Frascati Phys. Ser.* 64 (2017). Ed. by R. Fusco Femiano et al., pp. 147–155.

[23] S. Abe et al. "Search for Majorana Neutrinos with the Complete KamLAND-Zen Dataset". In: (June 2024). arXiv: 2406.11438 [hep-ex].

[24] S. F. King. "Neutrino mass models". In: *Rept. Prog. Phys.* 67 (2004), pp. 107–158. arXiv: hep-ph/0310204.

[25] M. Aker et al. "Direct neutrino-mass measurement with sub-electronvolt sensitivity". In: *Nature Phys.* 18.2 (2022), pp. 160–166. arXiv: 2105.08533 [hep-ex].

[26] S. Gariazzo. "Neutrino masses in cosmology". In: *21st Lomonosov Conference on Elementary Particle Physics*. Jan. 2024. arXiv: 2401.11976 [astro-ph.CO].

[27] Boyde S. *Lecture notes on Neutrino Oscillations*. Nov. 2005. URL: https://warwick.ac.uk/fac/sci/physics/staff/academic/boyd/stuff/neutrinolectures/lec_oscillations.pdf.

[28] Marcella Bona et al. "Overview and theoretical prospects for CKM matrix and CP violation from the UTfit Collaboration". In: *PoS* WIFAI2023 (2024), p. 007.

[29] Luca Stanco. "The next challenge for neutrinos: the mass ordering". In: *EPJ Web Conf.* 164 (2017). Ed. by L. Bravina, Y. Foka, and S. Kabana, p. 01031. arXiv: 1610.05533 [hep-ph].

[30] S. P. Mikheyev and A. Yu. Smirnov. "Resonance Amplification of Oscillations in Matter and Spectroscopy of Solar Neutrinos". In: *Sov. J. Nucl. Phys.* 42 (1985), pp. 913–917.

[31] A. Yu. Smirnov. "The MSW effect and solar neutrinos". In: *10th International Workshop on Neutrino Telescopes*. May 2003, pp. 23–43. arXiv: hep-ph/0305106.

[32] L. Wolfenstein. "Neutrino Oscillations in Matter". In: *Phys. Rev. D* 17 (1978), pp. 2369–2374.

[33] Ricciardi S. *Lecture notes on Neutrino oscillations in matter*. Oct. 2003. URL: https://hepwww.pp.rl.ac.uk/users/Ricciardi/Lectures/MSW-1.pdf.

[34] W. Pauli. *Letter to a physicists gathering at Tubingen reprinted in Wolfgang Pauli Collected Scientific Papers*. Vol. 2. R. Kronig and V. Weisskopf (Interscience New York 1964), Dec. 1930.

[35] E. Fermi. "Tentativo di una Teoria Dei Raggi Beta". In: *Il Nuovo Cimento* 11 (Jan. 1934).

[36] H. Bethe and R. Peierls. "The 'neutrino'". In: *Nature* 133 (1934), p. 532.

[37] B. Pontecorvo. "Inverse beta process". In: *Camb. Monogr. Part. Phys. Nucl. Phys. Cosmol.* 1 (1991), pp. 25–31.

[38] Frederick Reines and Clyde L. Cowan. "The neutrino". In: *Nature* 178 (1956), pp. 446–449.

[39] C. S. Wu et al. "Experimental Test of Parity Conservation in β Decay". In: *Phys. Rev.* 105 (1957), pp. 1413–1414.

[40] M. Goldhaber, L. Grodzins, and A. W. Sunyar. "Helicity of Neutrinos". In: *Phys. Rev.* 109 (1958), pp. 1015–1017.

[41] G. Danby et al. "Observation of High-Energy Neutrino Reactions and the Existence of Two Kinds of Neutrinos". In: *Phys. Rev. Lett.* 9 (1962), pp. 36–44.

[42] Martin L. Perl et al. "Evidence for Anomalous Lepton Production in e+ - e- Annihilation". In: *Phys. Rev. Lett.* 35 (1975), pp. 1489–1492.

[43] D. Decamp et al. "A Precise Determination of the Number of Families With Light Neutrinos and of the Z Boson Partial Widths". In: *Phys. Lett. B* 235 (1990), pp. 399–411.

[44] K. Kodama et al. "Observation of tau neutrino interactions". In: *Phys. Lett. B* 504 (2001), pp. 218–224. arXiv: `hep-ex/0012035`.

[45] B. Pontecorvo. "Inverse beta processes and nonconservation of lepton charge". In: *Zh. Eksp. Teor. Fiz.* 34 (1957), p. 247.

[46] D. D'Angelo et al. "Recent Borexino results and prospects for the near future". In: *EPJ Web Conf.* 126 (2016). Ed. by Larisa Bravina, Yiota Foka, and Sonja Kabana, p. 02008. arXiv: `1405.7919 [hep-ex]`.

[47] K. Lande and P. Wildenhain. "The Homestake chlorine solar neutrino experiment: Past, present and future". In: *Nucl. Phys. B Proc. Suppl.* 118 (2003). Ed. by F. von Feilitzsch and N. Schmitz, pp. 49–54.

[48] M. Altmann et al. "Complete results for five years of GNO solar neutrino observations". In: *Phys. Lett. B* 616 (2005), pp. 174–190. arXiv: `hep-ex/0504037`.

[49] J. N. Abdurashitov et al. "Solar neutrino flux measurements by the Soviet-American Gallium Experiment (SAGE) for half the 22 year solar cycle". In: *J. Exp. Theor. Phys.* 95 (2002), pp. 181–193. arXiv: `astro-ph/0204245`.

[50] S. Fukuda et al. "Solar B-8 and hep neutrino measurements from 1258 days of Super-Kamiokande data". In: *Phys. Rev. Lett.* 86 (2001), pp. 5651–5655. arXiv: `hep-ex/0103032`.

[51] Q. R. Ahmad et al. "Direct evidence for neutrino flavor transformation from neutral current interactions in the Sudbury Neutrino Observatory". In: *Phys. Rev. Lett.* 89 (2002), p. 011301. arXiv: `nucl-ex/0204008`.

[52] Y. Fukuda et al. "Evidence for oscillation of atmospheric neutrinos". In: *Phys. Rev. Lett.* 81 (1998), pp. 1562–1567. arXiv: hep-ex/9807003.

[53] K. Eguchi et al. "First results from KamLAND: Evidence for reactor anti-neutrino disappearance". In: *Phys. Rev. Lett.* 90 (2003), p. 021802. arXiv: hep-ex/0212021.

[54] M. H. Ahn et al. "Indications of neutrino oscillation in a 250 km long baseline experiment". In: *Phys. Rev. Lett.* 90 (2003), p. 041801. arXiv: hep-ex/0212007.

[55] D. G. Michael et al. "Observation of muon neutrino disappearance with the MINOS detectors and the NuMI neutrino beam". In: *Phys. Rev. Lett.* 97 (2006), p. 191801. arXiv: hep-ex/0607088.

[56] M. Apollonio et al. "Limits on neutrino oscillations from the CHOOZ experiment". In: *Phys. Lett. B* 466 (1999), pp. 415–430. arXiv: hep-ex/9907037.

[57] F. Boehm et al. "Final results from the Palo Verde neutrino oscillation experiment". In: *Phys. Rev. D* 64 (2001), p. 112001. arXiv: hep-ex/0107009.

[58] Y. Abe et al. "Indication of Reactor $\bar{\nu}_e$ Disappearance in the Double Chooz Experiment". In: *Phys. Rev. Lett.* 108 (2012), p. 131801. arXiv: 1112.6353 [hep-ex].

[59] F. P. An et al. "Observation of electron-antineutrino disappearance at Daya Bay". In: *Phys. Rev. Lett.* 108 (2012), p. 171803. arXiv: 1203.1669 [hep-ex].

[60] K. Abe et al. "Observation of Electron Neutrino Appearance in a Muon Neutrino Beam". In: *Phys. Rev. Lett.* 112 (2014), p. 061802. arXiv: 1311.4750 [hep-ex].

[61] K. Abe et al. "Indication of Electron Neutrino Appearance from an Accelerator-produced Off-axis Muon Neutrino Beam". In: *Phys. Rev. Lett.* 107 (2011), p. 041801. arXiv: 1106.2822 [hep-ex].

[62] N. Agafonova et al. "Discovery of τ Neutrino Appearance in the CNGS Neutrino Beam with the OPERA Experiment". In: *Phys. Rev. Lett.* 115.12 (2015), p. 121802. arXiv: 1507.01417 [hep-ex].

[63] K. Abe et al. "Combined Analysis of Neutrino and Antineutrino Oscillations at T2K". In: *Phys. Rev. Lett.* 118.15 (2017), p. 151801. arXiv: 1701.00432 [hep-ex].

[64] R. L. Workman et al. "Review of Particle Physics". In: *PTEP* 2022 (2022), p. 083C01.

[65] Sacha E. Kopp. "Accelerator-based neutrino beams". In: *Phys. Rept.* 439 (2007), pp. 101–159. arXiv: physics/0609129.

[66] M. Wurm, F. von Feilitzsch, and Jean-Come Lanfranchi. "Neutrino Detectors". In: *Handbook of Particle Detection and Imaging*. Ed. by Ivor Fleck et al. Cham: Springer International Publishing, 2021, pp. 371–412. URL: https://doi.org/10.1007/978-3-319-93785-4_14.

[67] *T2K notes on neutrino physics*. URL: https://t2k-experiment.org/neutrinos/.

[68] L. Aliaga et al. "Design, Calibration, and Performance of the MINERvA Detector". In: *Nucl. Instrum. Meth. A* 743 (2014), pp. 130–159. arXiv: 1305.5199 [physics.ins-det].

[69] D. S. Ayres et al. “The NOvA Technical Design Report”. In: (Oct. 2007).

[70] Georges Charpak et al. “The Use of Multiwire Proportional Counters to Select and Localize Charged Particles”. In: *Nucl. Instrum. Meth.* 62 (1968), pp. 262–268.

[71] F. Sauli. “GEM: A new concept for electron amplification in gas detectors”. In: *Nucl. Instrum. Meth. A* 386 (1997), pp. 531–534.

[72] K. Abe et al. “The T2K Experiment”. In: *Nucl. Instrum. Meth. A* 659 (2011), pp. 106–135. arXiv: 1106.1238 [physics.ins-det].

[73] A. Simón. “Status of the NEXT experiment”. In: *J. Phys. Conf. Ser.* 2374.1 (2022), p. 012033.

[74] C. Rubbia. “The Liquid Argon Time Projection Chamber: A New Concept for Neutrino Detectors”. In: (May 1977).

[75] R. Acciarri et al. “Design and Construction of the MicroBooNE Detector”. In: *JINST* 12.02 (2017), P02017. arXiv: 1612.05824 [physics.ins-det].

[76] Pedro AN Machado, Ornella Palamara, and David W Schmitz. “The Short-Baseline Neutrino Program at Fermilab”. In: *Ann. Rev. Nucl. Part. Sci.* 69 (2019), pp. 363–387. arXiv: 1903.04608 [hep-ex].

[77] B. Abi et al. “First results on ProtoDUNE-SP liquid argon time projection chamber performance from a beam test at the CERN Neutrino Platform”. In: *JINST* 15.12 (2020), P12004. arXiv: 2007.06722 [physics.ins-det].

[78] C. Patrignani et al. “Review of Particle Physics: Passage of particles through matter”. In: *Chin. Phys. C* 40.10 (2016), p. 100001.

[79] Frass W. and Walczak R. *Lecture notes on the passage of particles though matter*. 2009. URL: https://www2.physics.ox.ac.uk/sites/default/files/Passage.pdf.

[80] Gerald R. Lynch and Orin I. Dahl. “Approximations to multiple Coulomb scattering”. In: *Nucl. Instrum. Meth. B* 58 (1991), pp. 6–10.

[81] A. Abed Abud et al. “Snowmass Neutrino Frontier: DUNE Physics Summary”. In: (Mar. 2022). arXiv: 2203.06100 [hep-ex].

[82] Adam Abed Abud et al. “The DUNE Far Detector Vertical Drift Technology, Technical Design Report”. In: (Dec. 2023). arXiv: 2312.03130 [hep-ex].

[83] Babak Abi et al. “Deep Underground Neutrino Experiment (DUNE), Far Detector Technical Design Report, Volume IV: Far Detector Single-phase Technology”. In: *JINST* 15.08 (2020), T08010. arXiv: 2002.03010 [physics.ins-det].

[84] Federico Battisti. “The DUNE Near Detector”. In: *PoS* ICHEP2022 (2022), p. 615.

[85] *DUNE at LBNF official page*. URL: https://lbnf-dune.fnal.gov/how-it-works/neutrino-beam/.

[86] James Strait et al. “Long-Baseline Neutrino Facility (LBNF) and Deep Underground Neutrino Experiment (DUNE): Conceptual Design Report, Volume 3: Long-Baseline Neutrino Facility for DUNE June 24, 2015”. In: (Jan. 2016). arXiv: 1601.05823 [physics.ins-det].

[87] Vaia Papadimitriou et al. "Design of the LBNF Beamline". In: *7th International Particle Accelerator Conference*. 2016, TUPMR025. arXiv: 1704.04471 [physics.acc-ph].

[88] P. Adamson et al. "The NuMI Neutrino Beam". In: *Nucl. Instrum. Meth. A* 806 (2016), pp. 279–306. arXiv: 1507.06690 [physics.acc-ph].

[89] Babak Abi et al. "Deep Underground Neutrino Experiment (DUNE), Far Detector Technical Design Report, Volume II: DUNE Physics". In: (Feb. 2020). arXiv: 2002.03005 [hep-ex].

[90] B. Abi et al. "The DUNE Far Detector Interim Design Report, Volume 3: Dual-Phase Module". In: (July 2018). arXiv: 1807.10340 [physics.ins-det].

[91] E. Segreto et al. "Liquid Argon test of the ARAPUCA device". In: *JINST* 13.08 (2018), P08021. arXiv: 1805.00382 [physics.ins-det].

[92] D. A. Dwyer et al. "LArPix: Demonstration of low-power 3D pixelated charge readout for liquid argon time projection chambers". In: *JINST* 13.10 (2018), P10007. arXiv: 1808.02969 [physics.ins-det].

[93] Damian Göldi. "A Novel Liquid Argon Time Projection Chamber Detector: The ArgonCube Concept". PhD thesis. Bern U., 2018.

[94] Andrea Bersani et al. "SPY: A Magnet System for a High-pressure Gaseous TPC Neutrino Detector". In: (Nov. 2023). arXiv: 2311.16063 [hep-ex].

[95] J. Alme et al. "The ALICE TPC, a large 3-dimensional tracking device with fast readout for ultra-high multiplicity events". In: *Nucl. Instrum. Meth. A* 622 (2010), pp. 316–367. arXiv: 1001.1950 [physics.ins-det].

[96] A. Ferretti. "The ALICE Experiment Upgrades". In: *32nd Rencontres de Blois on Particle Physics and Cosmology*. Jan. 2022. arXiv: 2201.08871 [physics.ins-det].

[97] Christian Lippmann. "Performance of the ALICE Time Projection Chamber". In: *Phys. Procedia* 37 (2012). Ed. by Ted Liu, pp. 434–441.

[98] Claus Grupen. "Physics of particle detection". In: *AIP Conf. Proc.* 536.1 (2000). Ed. by S. Kartal, pp. 3–34. arXiv: physics/9906063.

[99] C. Adloff et al. "Construction and Commissioning of the CALICE Analog Hadron Calorimeter Prototype". In: *JINST* 5 (2010), P05004. arXiv: 1003.2662 [physics.ins-det].

[100] D. Allan et al. "The Electromagnetic Calorimeter for the T2K Near Detector ND280". In: *JINST* 8 (2013), P10019. arXiv: 1308.3445 [physics.ins-det].

[101] V. Golovatyuk et al. "The Multi-Purpose Detector (MPD) of the collider experiment". In: *Eur. Phys. J. A* 52.8 (2016), p. 212.

[102] A. Abed Abud et al. "Snowmass Neutrino Frontier: DUNE Physics Summary". In: (Mar. 2022). arXiv: 2203.06100 [hep-ex].

[103] DUNE ND-GAr working group. "A Conceptual Design for ND-GAr-Lite". In: (Sept. 2021). URL: https://indico.fnal.gov/event/51215/attachments/147873/189770/ND_GAr_Lite_CDR_20210930.pdf.

[104] Milind V. Diwan. "The Case for a super neutrino beam". In: *Frascati Phys. Ser.* 35 (2004). Ed. by A. Lopez, pp. 89–109. arXiv: hep-ex/0407047.

[105] B. Abi et al. "Long-baseline neutrino oscillation physics potential of the DUNE experiment". In: *Eur. Phys. J. C* 80.10 (2020), p. 978. arXiv: 2006.16043 [hep-ex].

[106] Ivan Esteban et al. "Global analysis of three-flavour neutrino oscillations: synergies and tensions in the determination of θ_{23}, δ_{CP}, and the mass ordering". In: *JHEP* 01 (2019), p. 106. arXiv: 1811.05487 [hep-ph].

[107] Stephen F. King et al. "Neutrino Mass and Mixing: from Theory to Experiment". In: *New J. Phys.* 16 (2014), p. 045018. arXiv: 1402.4271 [hep-ph].

[108] W. de Boer. "Grand unified theories and supersymmetry in particle physics and cosmology". In: *Prog. Part. Nucl. Phys.* 33 (1994), pp. 201–302. arXiv: hep-ph/9402266.

[109] Paul Langacker. "Grand Unified Theories and Proton Decay". In: *Phys. Rept.* 72 (1981), p. 185.

[110] K. Abe et al. "Search for proton decay via $p \to \nu K^+$ using 260 kilotonůyear data of Super-Kamiokande". In: *Phys. Rev. D* 90.7 (2014), p. 072005. arXiv: 1408.1195 [hep-ex].

[111] K. Abe et al. "Search for proton decay via $p \to e^+\pi^0$ and $p \to \mu^+\pi^0$ in 0.31 megatonůyears exposure of the Super-Kamiokande water Cherenkov detector". In: *Phys. Rev. D* 95.1 (2017), p. 012004. arXiv: 1610.03597 [hep-ex].

[112] K. Abe et al. "Search for nucleon decay into charged antilepton plus meson in 0.316 megaton·years exposure of the Super-Kamiokande water Cherenkov detector". In: *Phys. Rev. D* 96.1 (2017), p. 012003. arXiv: 1705.07221 [hep-ex].

[113] K. Abe et al. "Hyper-Kamiokande Design Report". In: *HAL* (May 2018). arXiv: 1805.04163 [physics.ins-det].

[114] Zelimir Djurcic et al. "JUNO Conceptual Design Report". In: *CERN Document Server* (Aug. 2015). arXiv: 1508.07166 [physics.ins-det].

[115] Christoph A. Ternes et al. "Neutrino mass ordering at DUNE: An extra ν bonus". In: *Phys. Rev. D* 100.9 (2019), p. 093004. arXiv: 1905.03589 [hep-ph].

[116] Kevin James Kelly et al. "Sub-GeV Atmospheric Neutrinos and CP-Violation in DUNE". In: *Phys. Rev. Lett.* 123.8 (2019), p. 081801. arXiv: 1904.02751 [hep-ph].

[117] R. Abbasi et al. "Search for a Lorentz-violating sidereal signal with atmospheric neutrinos in IceCube". In: *Phys. Rev. D* 82 (2010), p. 112003. arXiv: 1010.4096 [astro-ph.HE].

[118] M. G. Aartsen et al. "Neutrino Interferometry for High-Precision Tests of Lorentz Symmetry with IceCube". In: *Nature Phys.* 14.9 (2018), pp. 961–966. arXiv: 1709.03434 [hep-ex].

[119] K. Abe et al. "Test of Lorentz invariance with atmospheric neutrinos". In: *Phys. Rev. D* 91.5 (2015), p. 052003. arXiv: 1410.4267 [hep-ex].

[120] Animesh Chatterjee et al. "Testing nonstandard neutrino matter interactions in atmospheric neutrino propagation". In: *Phys. Rev. D* 93.9 (2016), p. 093017. arXiv: 1409.8472 [hep-ph].

[121] K. Abe et al. "Limits on sterile neutrino mixing using atmospheric neutrinos in Super-Kamiokande". In: *Phys. Rev. D* 91 (2015), p. 052019. arXiv: 1410.2008 [hep-ex].

[122] R. M. Bionta et al. "Observation of a Neutrino Burst in Coincidence with Supernova SN 1987a in the Large Magellanic Cloud". In: *Phys. Rev. Lett.* 58 (1987), p. 1494.

[123] K. Hirata et al. "Observation of a Neutrino Burst from the Supernova SN 1987a". In: *Phys. Rev. Lett.* 58 (1987). Ed. by K. C. Wali, pp. 1490–1493.

[124] S. Gariazzo et al. "Updated Global 3+1 Analysis of Short-BaseLine Neutrino Oscillations". In: *JHEP* 06 (2017), p. 135. arXiv: 1703.00860 [hep-ph].

[125] Mona Dentler et al. "Updated Global Analysis of Neutrino Oscillations in the Presence of eV-Scale Sterile Neutrinos". In: *JHEP* 08 (2018), p. 010. arXiv: 1803.10661 [hep-ph].

[126] Y. Farzan and M. Tortola. "Neutrino oscillations and Non-Standard Interactions". In: *Front. in Phys.* 6 (2018), p. 10. arXiv: 1710.09360 [hep-ph].

[127] Wolfgang Altmannshofer et al. "Neutrino Tridents at DUNE". In: *Phys. Rev. D* 100.11 (2019), p. 115029. arXiv: 1902.06765 [hep-ph].

[128] N. Aghanim et al. "Planck 2018 results. VI. Cosmological parameters". In: *Astron. Astrophys.* 641 (2020). [Erratum: Astron.Astrophys. 652, C4 (2021)], A6. arXiv: 1807.06209 [astro-ph.CO].

[129] Marco Battaglieri et al. "US Cosmic Visions: New Ideas in Dark Matter 2017: Community Report". In: *U.S. Cosmic Visions: New Ideas in Dark Matter*. July 2017. arXiv: 1707.04591 [hep-ph].

[130] A. A. Aguilar-Arevalo et al. "Dark Matter Search in Nucleon, Pion, and Electron Channels from a Proton Beam Dump with MiniBooNE". In: *Phys. Rev. D* 98.11 (2018), p. 112004. arXiv: 1807.06137 [hep-ex].

[131] Kaustubh Agashe et al. "(In)direct Detection of Boosted Dark Matter". In: *JCAP* 10 (2014), p. 062. arXiv: 1405.7370 [hep-ph].

[132] M. A. Acero et al. "First Measurement of Neutrino Oscillation Parameters using Neutrinos and Antineutrinos by NOvA". In: *Phys. Rev. Lett.* 123.15 (2019), p. 151803. arXiv: 1906.04907 [hep-ex].

[133] A. Bodek et al. "Methods to Determine Neutrino Flux at Low Energies:Investigation of the Low ν Method". In: *Eur. Phys. J. C* 72 (2012), p. 1973. arXiv: 1201.3025 [hep-ex].

[134] T. Le et al. "Measurement of $\bar{\nu}_\mu$ Charged-Current Single π^- Production on Hydrocarbon in the Few-GeV Region using MINERvA". In: *Phys. Rev. D* 100.5 (2019), p. 052008. arXiv: 1906.08300 [hep-ex].

[135] A. A. Aguilar-Arevalo et al. "Measurement of Neutrino-Induced Charged-Current Charged Pion Production Cross Sections on Mineral Oil at $E_\nu \sim 1$ GeV". In: *Phys. Rev. D* 83 (2011), p. 052007. arXiv: 1011.3572 [hep-ex].

[136] K. Abe et al. "Measurement of the muon neutrino charged-current single π^+ production on hydrocarbon using the T2K off-axis near detector ND280". In: *Phys. Rev. D* 101.1 (2020), p. 012007. arXiv: 1909.03936 [hep-ex].

[137] A. Mislivec et al. "Measurement of total and differential cross sections of neutrino and antineutrino coherent $\pi^{\pm}$ production on carbon". In: *Phys. Rev. D* 97.3 (2018), p. 032014. arXiv: 1711.01178 [hep-ex].

[138] Adam Abed Abud et al. "DUNE Phase II: scientific opportunities, detector concepts, technological solutions". In: *JINST* 19.12 (2024), P12005. arXiv: 2408.12725 [physics.ins-det].

[139] Gregory F. Welch. "Kalman Filter". In: *Computer Vision: A Reference Guide*. Ed. by Katsushi Ikeuchi. Boston, MA: Springer US, 2014, pp. 435–437.

[140] R. Fruhwirth. "Application of Kalman filtering to track and vertex fitting". In: *Nucl. Instrum. Meth. A* 262 (1987), pp. 444–450.

[141] Federico Battisti, Marian Ivanov, and Xianguo Lu. "A Kalman filter for track reconstruction in very large time projection chambers". In: *Comput. Phys. Commun.* 308 (2025), p. 109443. arXiv: 2404.08614 [physics.ins-det].

[142] Y. Belikov et al. "TPC tracking and particle identification in high density environment". In: *eConf* C0303241 (2003), TULT011. arXiv: physics/0306108 [physics].

[143] Mesut Arslandok et al. "Track Reconstruction in a High-Density Environment with ALICE". In: *Particles* 5.1 (2022), pp. 84–95. arXiv: 2203.10325 [physics.ins-det].

[144] R. M. Sternheimer, M. J. Berger, and S. M. Seltzer. "Density Effect for the Ionization Loss of Charged Particles in Various Substances". In: *Atom. Data Nucl. Data Tabl.* 30 (1984), pp. 261–271.

[145] David F. Griffiths and Desmond J. Higham. "Euler's Method". In: *Numerical Methods for Ordinary Differential Equations: Initial Value Problems*. London: Springer London, 2010. Chap. 2, pp. 19–31.

[146] F. Carminati and A. Morsch. *Simulation in ALICE*. 2003. arXiv: physics/0306092 [physics.comp-ph].

[147] Yu Belikov, K. Safarík, and B. Batyunya. "Kalman Filtering Application for Track Recognition and Reconstruction in ALICE Tracking System". In: *ALICE-INT-1997-24, CERN-ALICE-INT-1997-24* (1997).

[148] Joel Tellinghuisen. "Statistical Error Propagation". In: *The Journal of Physical Chemistry A* 105 (2001), pp. 3917–3921.

[149] N.I. Chernov and G.A. Ososkov. "Effective algorithms for circle fitting". In: *Computer Physics Communications* 33.4 (1984), pp. 329–333. URL: https://www.sciencedirect.com/science/article/pii/0010465584901371.

[150] *GArSoft*. https://github.com/DUNE/garsoft. Accessed: 2024-03-29.

[151] Eric D. Church. "LArSoft: A Software Package for Liquid Argon Time Projection Drift Chambers". In: (Nov. 2013). arXiv: 1311.6774 [physics.ins-det].

[152] *LArSoft*. https://larsoft.org/. Accessed: 2024-06-17.

[153] C. Green et al. "The Art Framework". In: *J. Phys. Conf. Ser.* 396 (2012). Ed. by Michael Ernst et al., p. 022020.

[154] C. Andreopoulos et al. “The GENIE Neutrino Monte Carlo Generator”. In: *Nucl. Instrum. Meth. A* 614 (2010), pp. 87–104. arXiv: 0905.2517 [hep-ph].

[155] R. Brun and F. Rademakers. “ROOT: An object oriented data analysis framework”. In: *Nucl. Instrum. Meth. A* 389 (1997). Ed. by M. Werlen and D. Perret-Gallix, pp. 81–86.

[156] R. Chytracek et al. “Geometry description markup language for physics simulation and analysis applications.” In: *IEEE Trans. Nucl. Sci.* 53 (2006), p. 2892.

[157] S. Agostinelli et al. “GEANT4–a simulation toolkit”. In: *Nucl. Instrum. Meth. A* 506 (2003), pp. 250–303.

[158] C. Patrignani et al. “Review of Particle Physics: Particle detectors and accelerators”. In: *Chin. Phys. C* 40.10 (2016), p. 100001.

[159] K. H. Ackermann et al. “STAR detector overview”. In: *Nucl. Instrum. Meth. A* 499 (2003), pp. 624–632.

[160] *AliRoot*. https://github.com/alisw/AliRoot. Accessed: 2024-04-04.

[161] *fastMCKalman*. https://github.com/miranov25/fastMCKalman. Accessed: 2024-03-29.

[162] D.C. Lay. *Linear Algebra and Its Applications*. Pearson Education, 2003. Chap. 1.9 - The matrix of a linear transformation, pp. 71–81. URL: https://books.google.com/books?id=v8Zls26Y0wkC.

[163] Marian Ivanov, Marian Ivanov, and Giulion Eulise. “RootInteractive tool for multidimensional statistical analysis, machine learning and analytical model validation”. In: (Mar. 2024). arXiv: 2403.19330 [hep-ex].

[164] John Allison et al. “Geant4 developments and applications”. In: *IEEE Trans. Nucl. Sci.* 53 (2006), p. 270.

[165] J. Allison et al. “Recent developments in Geant4”. In: *Nucl. Instrum. Meth. A* 835 (2016), pp. 186–225.

[166] G. Dellacasa et al. “ALICE: Technical design report of the time projection chamber”. In: (Jan. 2000).

[167] J. B. Birks. “Scintillations from Organic Crystals: Specific Fluorescence and Relative Response to Different Radiations”. In: *Proc. Phys. Soc. A* 64 (1951), pp. 874–877.

[168] Christian Lippmann. “Performance of the ALICE Time Projection Chamber”. In: *Phys. Procedia* 37 (2012). Ed. by Ted Liu, pp. 434–441.

[169] Rand Wilcox. “Chapter 6 - Some Multivariate Methods”. In: *Introduction to Robust Estimation and Hypothesis Testing*. third. Statistical Modeling and Decision Science. Boston: Academic Press, 2012, pp. 215–289.

[170] R. L. Gluckstern. “Uncertainties in track momentum and direction, due to multiple scattering and measurement errors”. In: *Nucl. Instrum. Meth.* 24 (1963), pp. 381–389.

[171] Are Strandlie and Rudolf Fruhwirth. “Track and vertex reconstruction: From classical to adaptive methods”. In: *Rev. Mod. Phys.* 82 (2010), pp. 1419–1458.

[172] *Pull request for new module implementation in GArSoft*. `https://github.com/DUNE/garsoft/pull/4`. Accessed: 2024-07-4.

[173] X. G. Lu et al. "Measurement of final-state correlations in neutrino muon-proton mesonless production on hydrocarbon at $E_\nu = 3$ GeV". In: *Phys. Rev. Lett.* 121.2 (2018), p. 022504. arXiv: `1805.05486 [hep-ex]`.

[174] T. Cai et al. "Nucleon binding energy and transverse momentum imbalance in neutrino-nucleus reactions". In: *Phys. Rev. D* 101.9 (2020), p. 092001. arXiv: `1910.08658 [hep-ex]`.

[175] D. Coplowe et al. "Probing nuclear effects with neutrino-induced charged-current neutral pion production". In: *Phys. Rev. D* 102.7 (2020), p. 072007. arXiv: `2002.05812 [hep-ex]`.

[176] K. Abe et al. "Characterization of nuclear effects in muon-neutrino scattering on hydrocarbon with a measurement of final-state kinematics and correlations in charged-current pionless interactions at T2K". In: *Phys. Rev. D* 98.3 (2018), p. 032003. arXiv: `1802.05078 [hep-ex]`.

[177] P. Abratenko et al. "First Double-Differential Measurement of Kinematic Imbalance in Neutrino Interactions with the MicroBooNE Detector". In: *Phys. Rev. Lett.* 131.10 (2023), p. 101802. arXiv: `2301.03706 [hep-ex]`.